Heat Transfer Mechanism and Thermal Performance of a Channel with Baffles having Open Wings

Eiamsa-ard Smith

A thesis submitted for the degree of

Doctor of Engineering

Division of System Engineering

Graduate School of Engineering

Mie University, Japan

March 2024

Abstract

For more than a century, heat exchangers have been widely used in cooling/heating systems in many commercial applications such as solar air heating, refrigeration, gas turbines, vehicle manufacturing, chemical engineering, and power plant industries. The major challenge in producing a heat exchanger is to intensify its heat transfer rate with a minimum friction loss penalty. Several heat transfer augmentation techniques have been applied and developed. One of the most widely used techniques is employing transverse baffles/ribs to alter flow structures by generating a recirculation and reattachment. The former separates the fluid from heat transfer surfaces while the latter facilitates the contact between fluid and heat transfer surfaces and thus the heat transfer rate. The thesis seeks ways to minimize the recirculation and intensify the flow reattachment by forming wings on the baffles.

In the first part of this thesis, heat transfer augmentation of newly designed perforated V-type baffles with semi-circular wings (SCW-PVBs) was examined. For a better understanding of the reasons behind the heat transfer by the baffles, a numerical analysis of the heat transfer mechanism and flow topology of channels was carried out. The effects of geometric parameters: pitch ratios (PR = 0.5, 1.0, 1.5 and 2.0), blockage ratios (BR = 0.1, 0.15 and 0.2), wing attack angles ($\theta = 5^o$, 10° and 15°) on heat transfer of air flow were studied in the turbulent region. The results of the channel installed with SCW-PVBs were compared with those of a smooth channel and the one with solid V-type baffles (VBs). The numerical results showed that the application of the SCW-PVBs having smaller pitch ratios and larger blockage ratios resulted in better heat transfer enhancement and higher pressure drop. The maximum heat transfer enhancement of 5.57 times over the smooth channel was found at a pitch ratio of 0.5, a blockage ratio of 0.2, wing attack angle of 10°. In addition, SCW-PVBs gave higher heat transfer and thermal performance factors (TPF) and lower pressure losses than VBs by around 1.73-8.98%, 5.41-26.84% and 4.51-15.22%, respectively depending on Reynolds number, blockage ratio, pitch ratio and wing attack angle. The maximum TPF of 2.6 was achieved by the SCW-PVBs having a blockage ratio of 0.1, a pitch ratio of 0.5 and wing attack angle of 10°.

The second part of the thesis aimed to experimentally investigate heat transfer enhancement in the channels installed with (1) perforated transverse baffles with square wings (SW-PBs) and (2) perforated V-type baffles with semi-oval/square/delta wings (SOW-PVBs/SW-PVBs/DW-PVBs). The effects of wing attack angles ($\theta = 0°$ (solid baffles), 22.5°, 45°, 67.5°, and 90°) and Reynolds numbers on the heat transfer performance characteristics were examined. All channels had an aspect ratio ($W:H$) of 3.75:1. All baffles had a width (w) of 150 mm and a perforated cross-sectional area of 64 mm^2. During experiments, the lower walls of the channels were evenly heated, while the other walls were insulated.

The temperature contours on the heated surface were acquired via a thermochromic liquid crystal (TLC) image-processing method. At the proper attack angles ($\theta = 22.5°$ and 45°), the modified baffles offered greater heat transfer rates and caused lower friction losses, resulting in higher TPFs than the solid baffles. In the current thesis, the greatest TPF was found at θ of 45°. The Nusselt number contours indicated that the modified baffles introduced multiple impinging jets which suppressed the size of the recirculation flow and allowed better contact between the fluid flow and the channel walls as compared to the solid ones. The jets impinged on the wall in different ways depending on the shapes of the wings and attack angles. Experimental results also suggested that the SW-PVBs gave TPF over those of the other modified baffles (SW-TBs/DW-PVBs/SOW-PVBs), owing to the higher heat transfer rate and lower pressure losses. The findings in this thesis are applicable to improving solar air heaters also other thermal systems.

Acknowledgements

First of all, I would like to express my deepest gratitude to Professor Naoki Maruyama for providing me with the opportunity to work in such an inspiring environment and for his guidance. Under his tutelage, I was able to pursue my research with a sense of excitement and adventure in both my research and my teaching. I have no hesitation in indicating that this investigation couldn't have been done without his guidance.

In conducting the experiments, I am indebted to Professor Masafumi Hirota of the Department of Mechanical Engineering, Faculty of Engineering, Aichi Institute of Technology, for their helpful suggestions. Their modest approach to research and engineering is illuminating.

I am indebted to Professor Koich Tsujimoto and Professor Takao Maeda of the Division of Mechanical Engineering, and Professor Takane Terashima of the Division of Architecture, Graduate School of Engineering, Mie University gave me valuable advice. Their unassuming approach to research and engineering is a source of inspiration.

I'd additionally like to take this occasion to thank the merit power for their virtuous deed: the utmost concentration of their creative, energetic, and dynamic potentiality in the form of insightful criticism and helpful guidance. I was exposed to the tremendous reality of information, particularly outside the bounds of textbooks, and instructed and counseled on its value inside them as well. They helped me so much and taught me so many things, that I can honestly say that I am who I am now because of them. This was the single most important breakthrough in my engineering education, and it had a profound impact on my personal growth. Their assistance broadens my mental understanding.

During my time here at Mie University, the students in the Thermal Energy System Laboratory were really helpful, and I would like to extend my deepest gratitude to every one of them.

In addition, I want to convey my deep gratitude to the people who have helped me and given me the strength to keep going.

Smith Eiamsa-ard

March, 2024

Table of contents

Chapter 3. Heat transfer enhancement in channel: Numerical investigation

Chapter 4. Heat transfer enhancement in channel: Experimental investigation

Chapter 5. Conclusions

List of figures

Figures **Page**

List of tables

Tables

Page

CHAPTER 1
Introduction

1.1 Background of heat transfer enhancement

Reduced global resources and environmental considerations have necessitated the development of more efficient heat-transfer devices with higher heat transfer rates. Engineers responsible for the design and operation of such systems must now prioritize both the reduction of energy lost due to inefficient use and the enhancement of energy transfer in the form of heat in light of the global increase in energy demand. Improvements in heat transfer have been suggested using a variety of methods. The methods can be classified into two categories: those that do not need any external power sources, known as "passive," and those that do, known as "active," which do require such sources.

The major technique of passive heat transfer enhancement is modifying heat transfer surfaces through different forms/designs. The viable approaches include installing baffles, ribs, fins and blocks, or forming grooves, dimpled and rough surfaces. Heat-transfer enhancement is achieved by increased surface area (surface extension) and also by increasing turbulence (mixing). Modified surfaces are applicable in numerous equipment including heat exchangers, solar air heaters, nuclear reactor fuel elements, turbine blades, electronic boards and various components, among others. Improved heat-transfer rates are normally accompanied by increased pressure losses in the flow over such surfaces. A practical use requires a reasonable tradeoff between augmented heat transfer rate and raised pressure drop.

One important application of modified heat transfer surfaces is that of cooling channels for gas turbine blades. One of the main criteria for aircraft engine design is to have a high thrust-to-weight ratio. To meet this requirement, the thermal performance/efficiency of gas turbine blades must be improved. An efficient strategy is raising the turbine's intake temperature. However, this approach may damage the turbine blades. To prevent damage and avoid blade melting, efficient cooling of turbine blades is essential. In turbine blade cooling, different techniques are applied to the various areas of the turbine blade. As demonstrated in Fig. 1 . 1 (a-c), rib turbulators are often installed in serpentine passages and fin cooling is often applied in trailing edge sections. Impingement cooling is often used at the leading edge areas and dimples are normally placed in the tip areas of the blade. The relevant research concerning modified heat transfer surfaces was reported by Han [1].

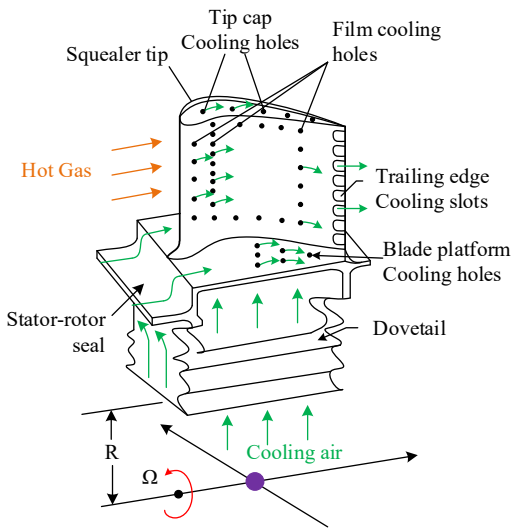

(a) Outside view

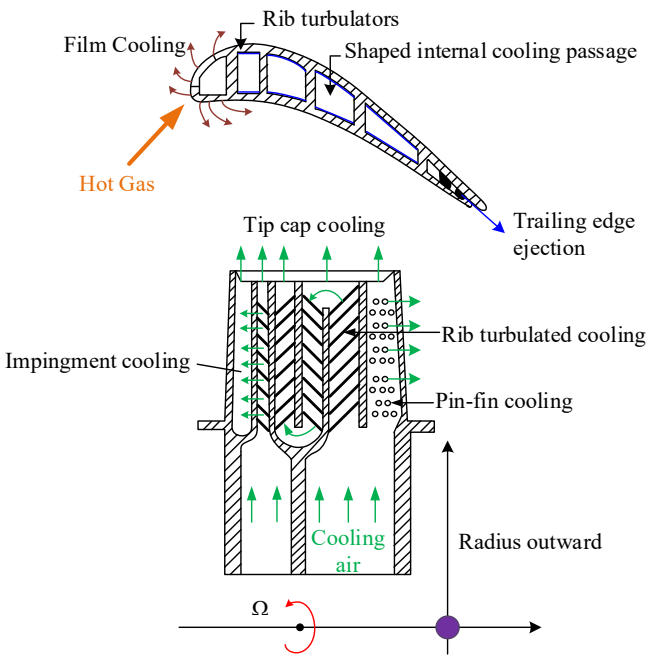

(b) Internal view

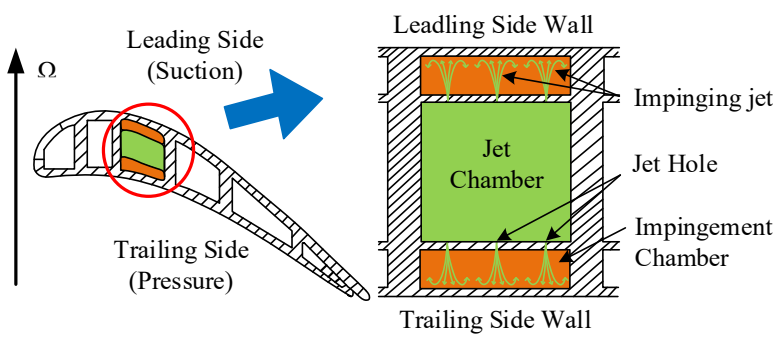

(c) Internal view of a blade

Figure 1.1. Cooling of a gas turbine blade.

Due to the absorber plate and duct's poor heat transfer capabilities, the thermal performance of solar air heaters is commonly low compared to that of solar water heaters. Improvements in heat transfer coefficients will increase the performance of solar air heaters, making them more cost-effective. Rough elements should be placed only on the wall that collects solar radiation, since this is the only heated wall in solar air heaters, to maximize heat transfer. Solar air heaters are thus represented by a rectangular duct with one rough wall and three smooth side walls.

One way to collect the sun's warmth is with a solar air heater (Fig. 1.2). These systems have been used in a variety of heat transfer applications, including solar-powered agricultural drying processes, indoor heating and cooling, nighttime cooling, preheating ventilation makeup air, and timber seasoning. Laminar sublayers often develop above absorber plates and other heat-transfer surfaces to limit the amount of heat lost to the surrounding medium. The creation of a laminar sublayer reduces the energy-collecting performance of a solar air heating system because it causes poor air-side heat transfer ability. Heat transfer coefficients are a crucial parameter in solar air heating system design. Heat transfer augmentation can be accomplished by incorporating artificial surface roughness on the solar collector at various orientations and shapes of the roughness. There are two strategies for maximizing heat convection from an absorber plate to the surrounding air. The primary method does not affect the heat transfer coefficient. It involves expanding the area of heat transfer through the utilization of corrugated/grooved or extended surfaces known as fins. The second approach generates surface turbulence, which improves heat transfer coefficient. The bottom surface of an absorber plate might be purposefully roughened for this purpose. Several researchers have worked to minimize frictional losses while increasing convective heat transfer using a roughened element.

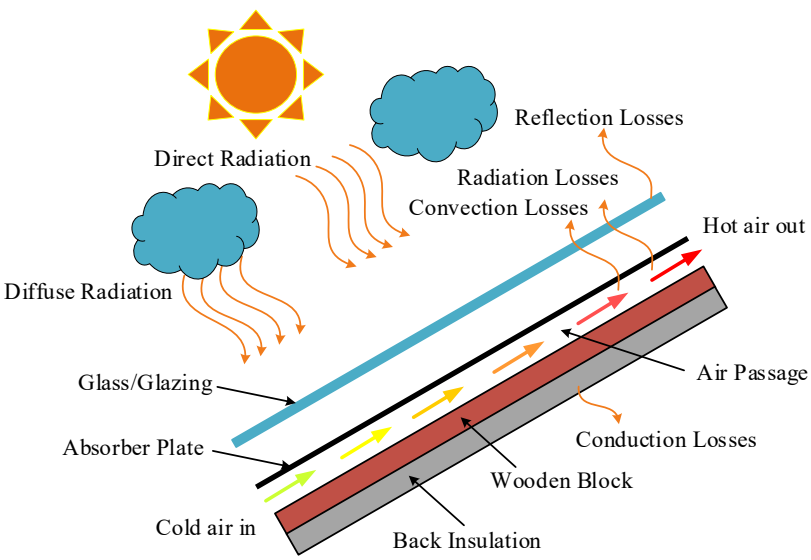

Figure 1.2. Solar air heater.

Ribs and baffles are the major types of rough surfaces that have been widely developed and modified by many researchers. Flow through the ribs/baffles is extremely complex. There are several factors affecting heat transfer and pressure drop. In general, experimentation is time-consuming and expensive since it requires researchers to repeatedly test variations in a variety of variables. Another option is using the numerical method which allows researchers to examine issues that cannot be studied experimentally while permitting deeper research to investigate whether two or more variables are related. As previously stated, heat-transfer enhancement is obtained at the expense of an increased pressure loss. The energy lost due to pressure losses may sometimes exceed that gained by heat-transfer enhancement. For many practical applications, it is necessary to determine the net economic benefit arising from a heat-transfer enhancement.

Figure. 1.3 shows a review of the heat transfer enhancement technique relating to the use of ribs and baffles turbulators with varying geometric characteristics. The literature review focuses on the effect of shape parameters on heat transfer mechanisms, flow structure, pressure losses, and thermal performance characteristics. All articles cited in the present work are available on the Scopus and Google databases.

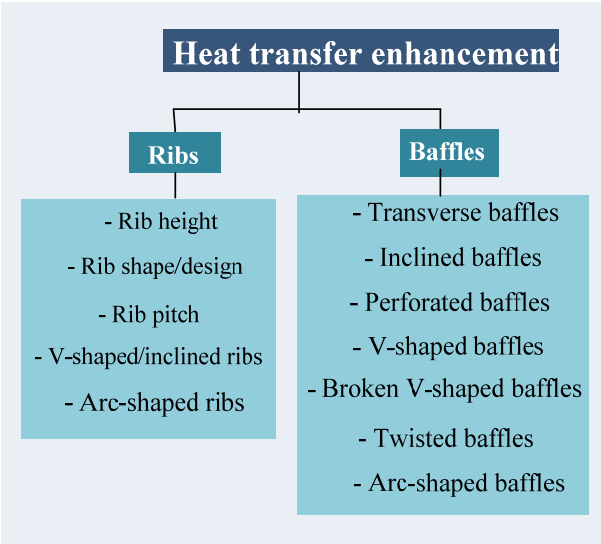

Figure 1.3. Review of the heat transfer enhancement relating to the use of ribs and baffles turbulators.

1.2 Guidelines for designing roughened surfaces within channels

Applications of rib/baffle rows can greatly increase the convection coefficient over that of smooth surfaces since rough surfaces create recirculation/longitudinal-vortex flows that reduce the thin thermal layer thickness. This leads to a higher convection coefficient in the reattachment flow region. Optimization of ribs/baffles geometries plays a major part in enhancing the thermal performance factor which is significantly influenced by geometric parameters including rib thickness, rib arrangement and various designs adjusting the angle of flow attack (α), rib width (w), rib height (e) distance between ribs (p) and the rough surface shape. The major configurations of rough surfaces are shown in Fig. 1.4.

Three basic roughness groups can be identified, 3-dimensional, ridge type 2-dimensional and groove type 2-dimensional roughness. In designing ribs/baffles, geometric parameters are usually based on dimensionless variables such as the rib height ratio (*e/d*, BR), rib spacing ratio (*p/e*, PR), the ratio of the rib width (*w/e*) and the shape of the surface roughness.

Rough surface Types	Three-dimensional roughened surface (consistency rough surface)	Two-dimensional roughened surface with protruding or convex surface	Two-dimensional roughened surface with grooves or holes
Common basic shapes	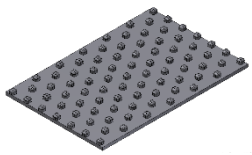	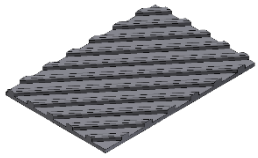	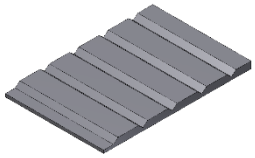
Basic roughness shapes with modified distances between the rough protrusions	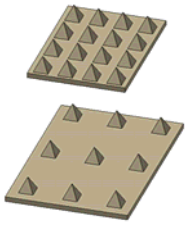	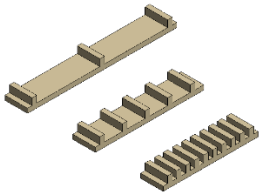	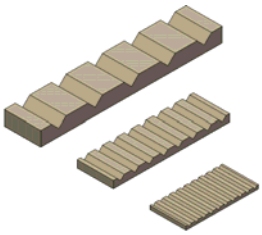
Various rough surface shapes	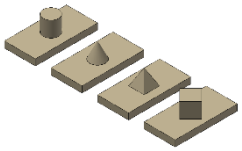	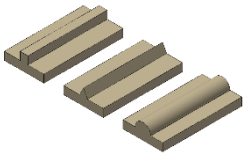	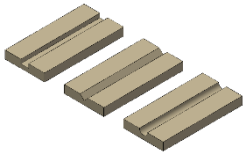

Figure 1.4. Basic geometry of roughened surfaces [4].

1.3 Hypothesis

Vortex generator, designated as VG, is a device used to produce streamwise vortices which are effective in boosting the rate of heat transfer and mixing with only a moderate amount of loss due to friction. Since the vortices are induced by the secondary flows rather than being manipulated or altered by the mainstream flow, the VG helps increase the turbulence intensity and improves the convection heat transfer with lower pressure loss penalty. In addition to this, the vortices created by the VG cause a transfer of momentum to occur between the region of the mainstream flow and the region close to the wall. This is also beneficial for enhancing the speed at which fluids are mixed. In particular, the

counter-rotation vortices have a rise in the heat transfer rate that is more efficient than the co-rotation ones [5, 6]. The primary reason for this phenomenon is that the counter-spinning vortices can rise the amount of momentum that is transferred. While the fluid with lower momentum moves upwards to the mainstream, the fluid with higher momentum moves downwards to the wall that surrounds each vortex generator [7].

Numerous researchers have attempted to improve a solar air collector efficiency by modifying baffles installed on heated plates. The modification of baffles as vortex generator (VG) can cause fluid flow path changes and promote interference and boundary-layer destruction which consequently diminish thermal resistance [8-13]. In general, baffles show promising performance in heat transfer augmentation with a moderate pressure loss drawback. Various baffles were offered to create different flow structures to increase heat transfer.

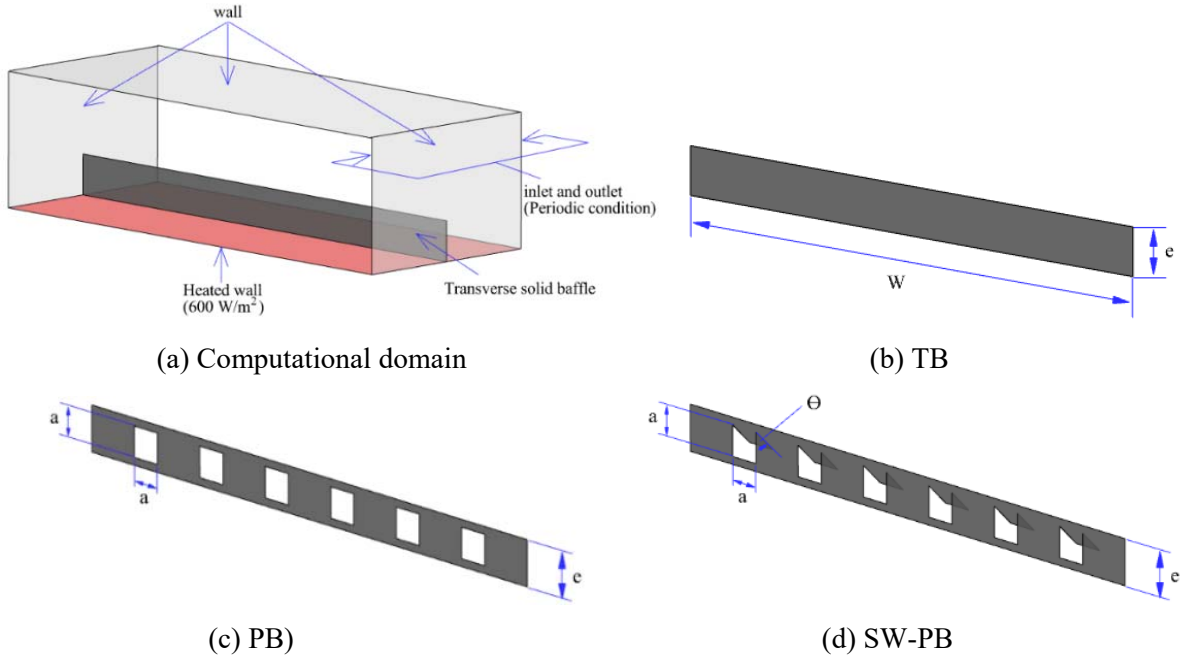

Figure 1.5. Computational domain of channel with transverse solid baffle (TB), perforated-baffle (PB), and perforated-baffle with square wing (SW-PB).

Figure 1.5(a-d) demonstrate the computational domain of a channel with transverse solid baffle (TB), perforated-baffle (PB) and perforated-baffle with square wing (SW-PB). Numerical results include flow/temperature field and local heat transfer distributions of the channels installed with the transverse solid baffle (TB), perforated-baffle (PB), and perforated-baffle with square wings (SW-PB). The simulation results demonstrated that TB brought a large recirculation flow, PB induced small recirculation and SW-PB produced several impinging jets as well as recirculation flows. Figures 1.6(a-c) and 1.7 present the flow structures and local wall temperature distributions and turbulent kinetic energy fields (TKE) in the channels with TB, PB and SW-PB at Re = 9,000. The TB primarily created

a recirculation flow. The wall temperature was dramatically lowered as a result of the primary recirculation attack since it severely disrupted a thermal boundary layer and boosted thermal transfer through the wall. However, the created vortex flow was unable to reach the areas behind the baffles, dead zones (high wall/fluid temperatures) emerged. In cases of the PB and SW-PB, multiple impinging jets were created by the fluid flow through square spaces. The jets helped in washing dead zones behind the baffles. The square wings of the SW-PB brought the fluid very close to the baffles. Therefore, dead zones behind the baffles were completely removed. Moreover, the square wings also promoted turbulence intensity and fluid mixing. The SW-PB, however, provided weaker TKE than TB because the square holes and wings suppressed recirculation flow strength. The flow separation was also observed further downstream of both PB and SW-PB.

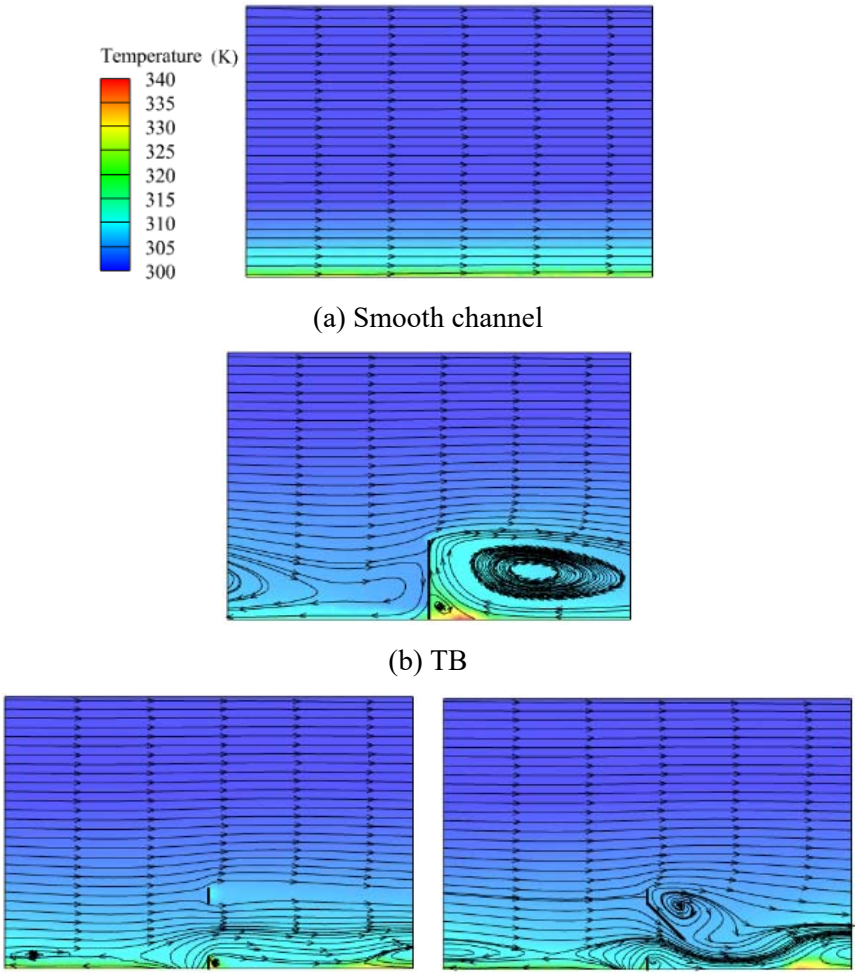

(a) Smooth channel

(b) TB

(c) PB

(d) SW-PB

Figure 1.6. Flow structures in the channels with solid baffles (TB), perforated-baffles (PB), and perforated-baffles with square wings (SW-PB).

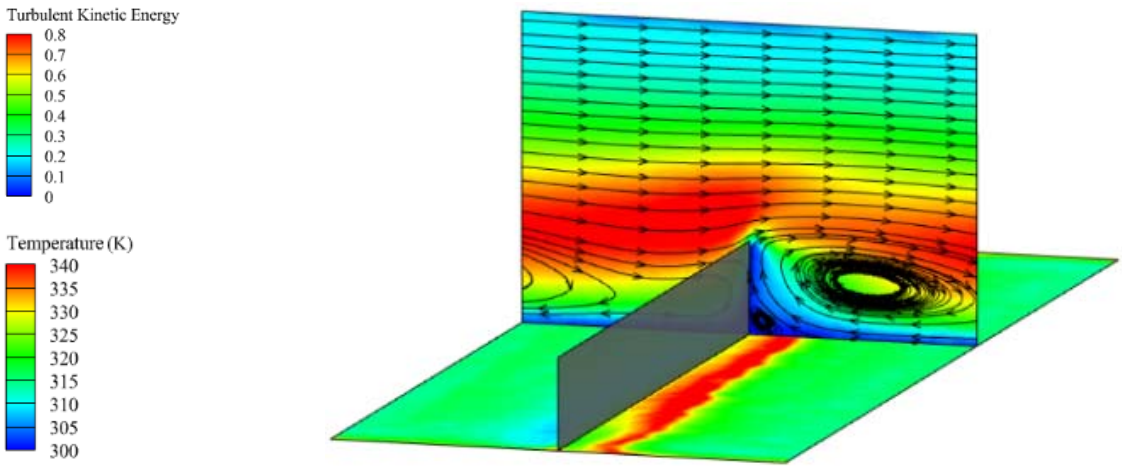

(a) TB

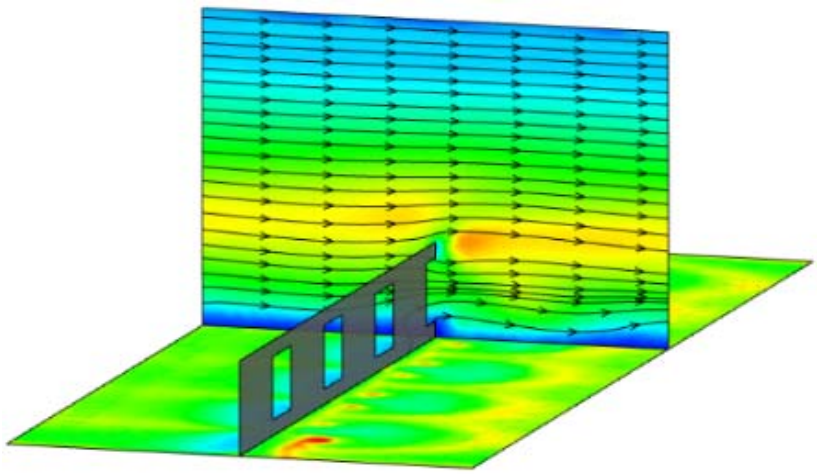

(b) PB

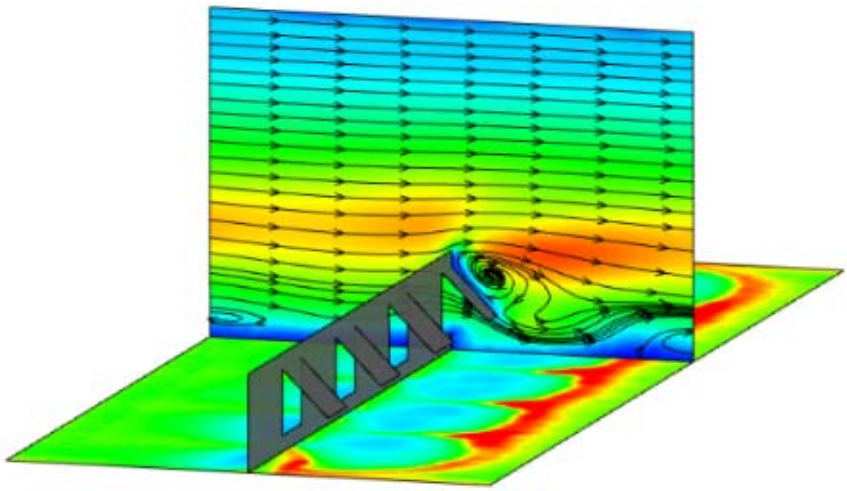

(c) SW-PB

Figure 1.7. Local wall temperature distributions and turbulent kinetic energy fields (TKE) in the channels with various baffles.

Figure 1.8(a-d) present local Nusselt number distributions at the Reynolds number of 9,000. As expected, heat transfer adjacent to the TB was low due to the presence of dead zones. Nusselt numbers further downstream of the TB were moderate and the distribution was quite uniform. On the other hand, heat transfer adjacent to the SW-PB was high due to the impingement of the fluid. It is noteworthy that heat transfer improvement by the SW-PB was marginal as compared to that by the TB owing to the suppressed recirculation flow strength as mentioned above. Nusselt numbers further downstream of the SW-PB were low due to the flow separation. Heat transfer in the channel with PB was similar to that of the one with SW-PB but with lower Nusselt numbers because of the weaker flow impingement.

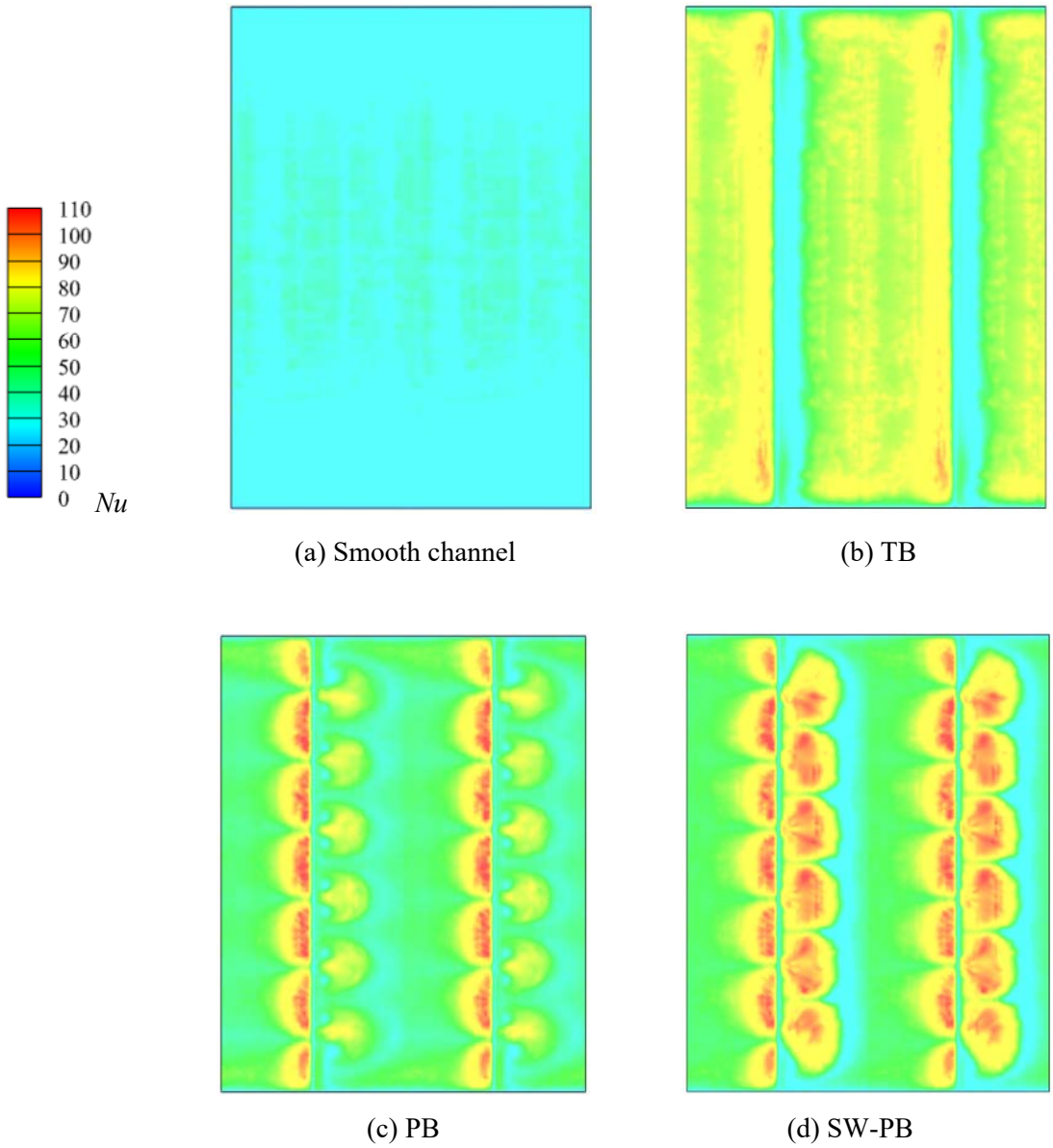

Figure 1.8. Distributions of local Nusselt numbers (*Nu*) on the heated walls of the channels with various baffles.

Due to the extreme pressure loss, the common winglet turbulator was discretely placed [14, 15] or perforated/punched [5, 16-18] to lower pumping or blowing energy. The influence of inserting a louver-punched trapezoidal winglet (LPTW) into a uniform heat-fluxed tube to create a longitudinal vortex generator as seen in Fig. 1.9. The LPTW was designed to maximize both the thermal performance to improve energy savings capability, and the Nusselt number ratio to reduce heat exchanger sizes. The results suggested that LPTWs introduced strong vortex flow and increased Nusselt number and friction loss above the smooth tube by 5.5 and 29.1 times, respectively. It was concluded that the perforated/ punched approach could lessen the pressure drop as compared to the typical ones. In addition, the vortex was also created by the ribbed twisted-oval tubes as seen in Fig. 1.10. The vortex flow separation is followed by flow reattachment behind the ribs. The combined effects resulted in a higher flow strength (higher TKE). Consequently, the disruption of the thermal boundary layer and fluid mixing between the core and near wall region were facilitated (indicated by the thinning of the high fluid temperature layer around the wall), leading to better heat transfer through the tube wall. Additionally, with a greater number of ribs, the TKE distribution became more uniform, indicating more consistent turbulence intensity.

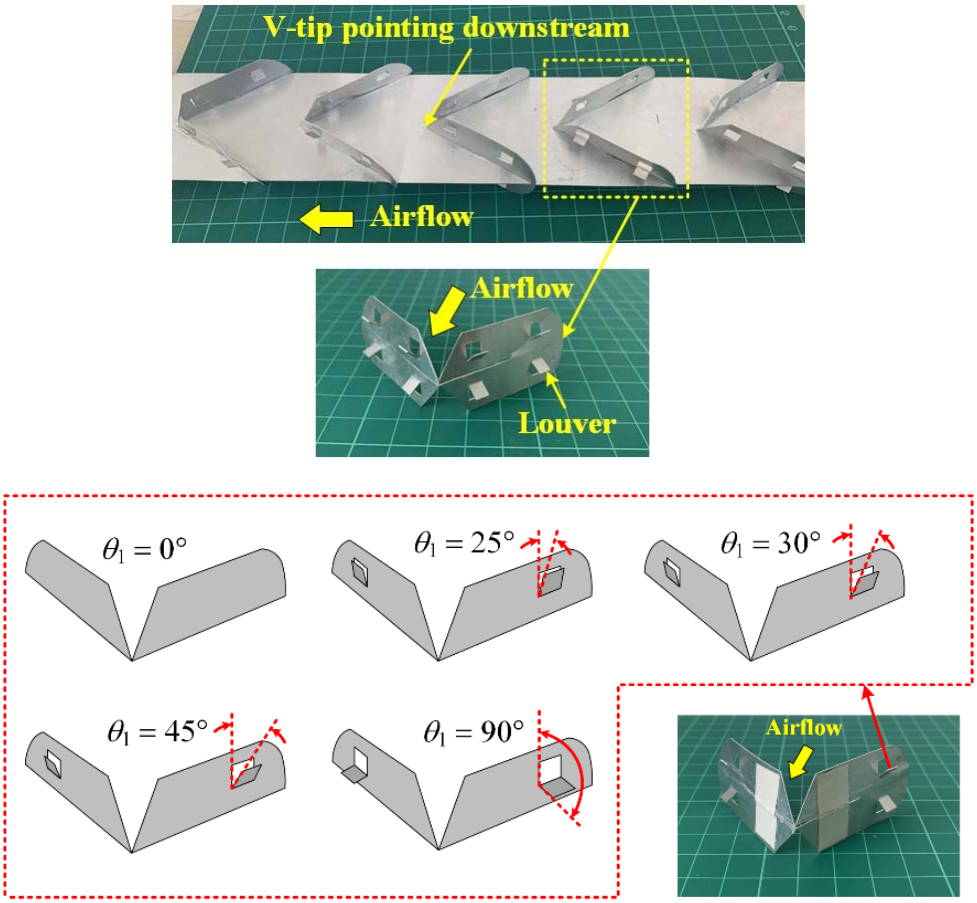

Figure 1.9. Louver-punched trapezoidal-winglet (LPTW) tape.

The primary goal of this thesis is to introduce a novel vortex generator application that effectively boosts heat transfer while lowering pressure loss and consequently facilitating thermal performance. Several researchers [19-24] attempted to modify baffles to enhance the heat transfer rate and reduce pressure losses as shown in Fig. 1.11. According to earlier research, holes and perforations in baffles significantly helped to reduce pressure losses thus improving the thermal performance factor. This concept has been adopted for newly designed baffles, namely, square-wing perforated transverse baffles (SW-PBs), delta-wing perforated V-type baffles (DW-PVBs), semi-oval wing perforated V-type baffles (SOW-PVBs) and square-wing perforated V-type baffles (SW-PVBs). The square-wing perforated transverse baffles and wing perforated V-type baffles are utilized to form (a) recirculation and vortex flows, which creates flow reattachment between the baffles; and (2) multiple impinging flows behind the baffles, to diminish the dead zone. The combination is expected to enhance the fluid wall contact, and thus the heat transfer rate. In addition, various geometric parameters of the perforated V-type baffles are studied to find the optimum condition.

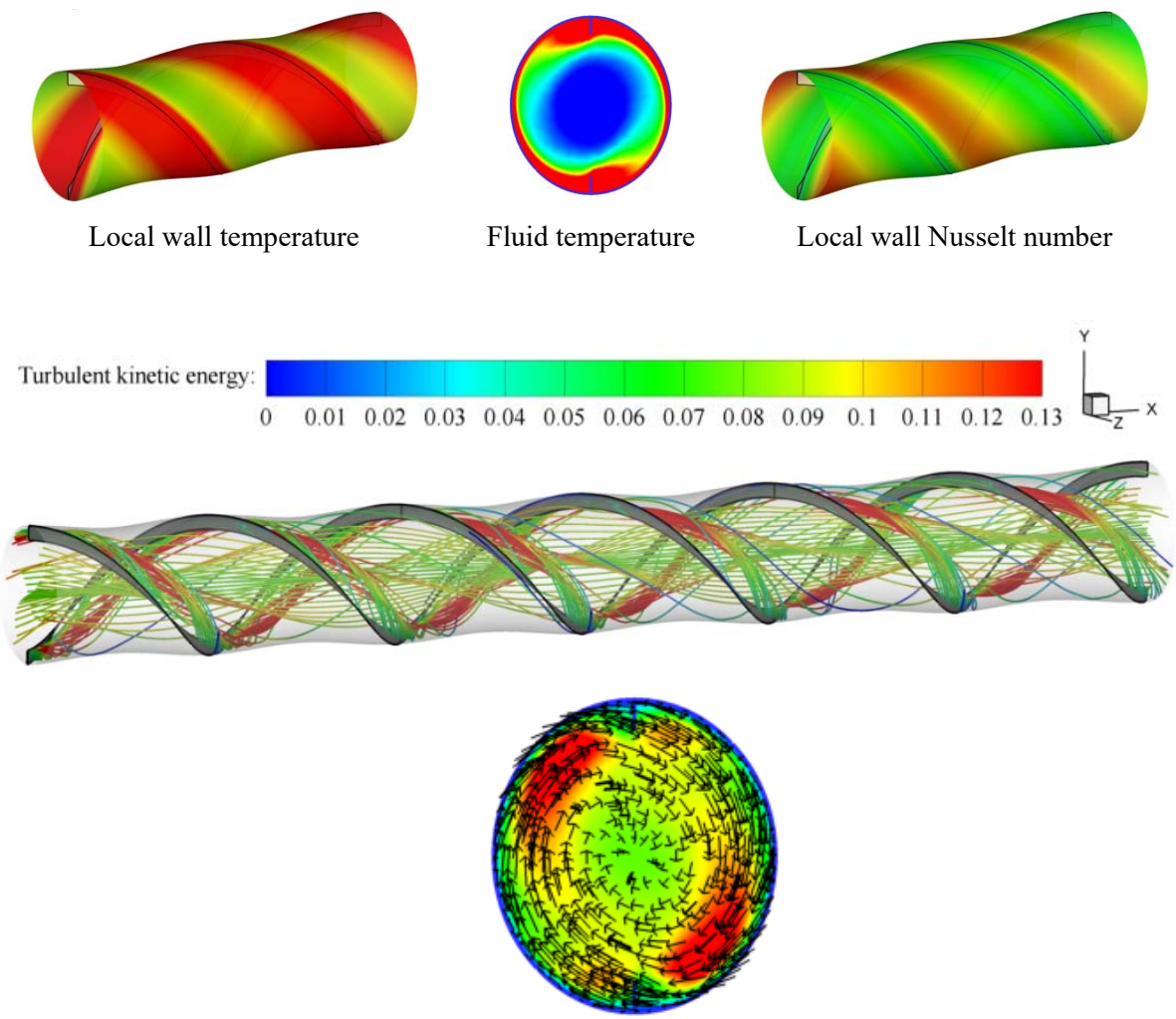

Figure 1.10. Flow behaviors and turbulent kinetic energy (TKE) fields in a ribbed twisted-oval tube.

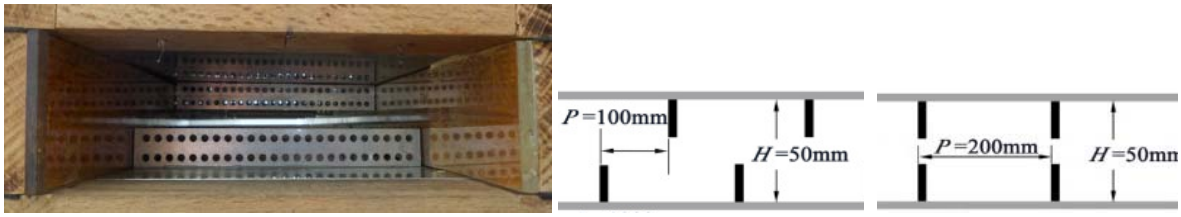

Staggered Inline

(a) Inline/staggered perforated baffles [19]

(b) Inclined perforated baffles [20]

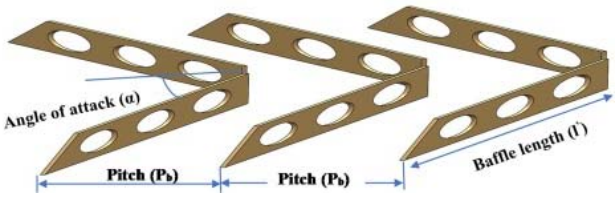

(c) V-down pattern perforated baffles [21]

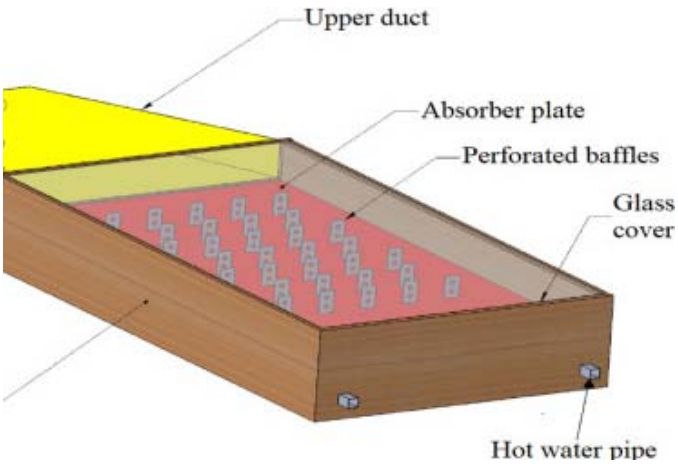

(d) Perforated baffles [22]

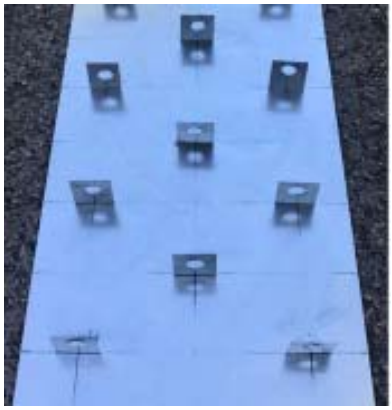

(e) Perforated baffles [23]

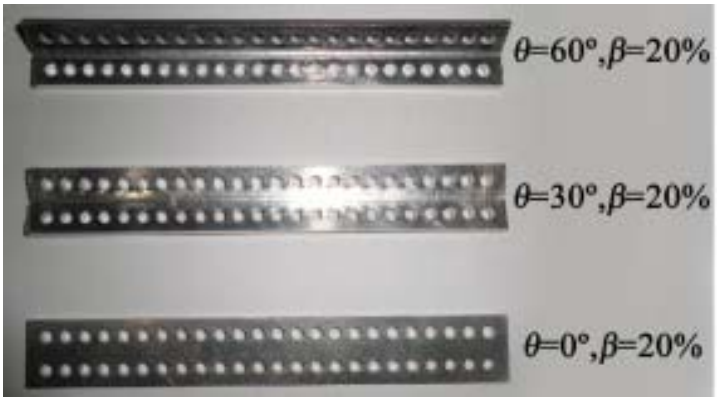

(f) Staggered and partially tilted perforated baffles [24]

Figure 1.11. Perforated baffles utilized in previously published works.

1.4 Objectives

1.4.1 To modify the typical transverse baffles (TB) into perforated V-type baffles with different shapes which are square-wing perforated transverse baffles (SW-PBs), delta-wing perforated V-type baffles (DW-PVBs), semi-oval wing perforated V-type baffles (SOW-PVBs) and square-wing perforated V-type baffles (SW-PVBs) to improve the thermal performance and heat transfer rate of the channel.

1.4.2 To examine heat transfer, pressure losses and thermal performance behaviors in the presence of the modified baffles.

1.4.3 To develop empirical correlations of Nusselt number, friction factor and thermal performance factor of channel installed with square-wing perforated transverse baffles (SW-PBs), square-wing perforated transverse baffles (SW-PBs), delta-wing perforated V-type baffles (DW-PVBs), semi-oval wing perforated V-type baffles (SOW-PVBs).

1.5 Scopes

1.5.1 The visualization of heat transfer behaviors by perforated baffles having different wing attack angles (θ = 0° (solid V-type baffle), 22.5°, 45°, 67.5° and 90°), using a thermochromic liquid crystal sheet. The technique gives the local thermal distributions on the wall surfaces for a better understanding of the heat transfer enhancement mechanism and fills a gap in the body of knowledge.

1.5.2 All the perforated baffles were located on the bottom of the channel which had an aspect ratio ($W:H$) of 3.75:1. The baffles were installed with a constant pitch length (p) of 60 mm or a pitch ratio (p/H) of 1.5 (60 mm). The baffles were 150 mm wide (W). The cross-sectional area of the perforated part was 64 mm^2.

1.5.3 The experiment was tested by permitting air to flow through a channel at Reynolds numbers (Re) ranging from 6,000 to 24,000 that examined to identify the optimal conditions.

1.5.4 Measuring the temperature distributions on the heated surface, thermochromic liquid crystal sheet (TLC).

1.5.5 The heat transfer region was a bottom wall that was maintained under a steady heat flux condition. During experiments, the bottom wall was heated using a thin heater sheet (0.254 mm) under a heat flux of 600 W/m^2, while the other three walls were insulated.

1.6 Outlines of thesis

The thesis consists of 5 chapters. The first chapter addresses the background of heat transfer enhancement, as well as the basic idea, hypothesis, objective, scopes, and thesis outline. Chapter 2 describes an evaluation of the thermal performance criteria and a literature review of rib and baffle turbulators. In Chapter 3, the numerical method, mathematical model, computational domain, and the configuration of semi-circular wing perforated V-type baffles are addressed. Additionally, the chapter

presents the numerical findings for (1) fully developed periodic velocity and heat transfer conditions, and (2) the analysis of the heat transfer mechanism and flow topology. Chapter 4 presents a comprehensive overview of the experimental systems and techniques utilized in this study. It encompasses four major parts: (1) the experimental facility, (2) the thermochromic liquid crystal setup, (3) the details of the channel equipped with various baffle vortex generators and their respective geometries, and (4) the analysis and discussion of the findings of heat transfer, friction factor, and thermal performance factor characteristics. Chapter 5 presents the conclusions drawn from the major findings of the current research.

References in chapter 1

1 Han JC, Chandra PR, Lau SC. Local heat/mass transfer distributions around sharp 180 deg turns in two-pass smooth and rib-roughened channels. Journal of Heat Transfer - Transactions of ASME. 1988;110:91-98.

2 Nikuradse J. Laws of flow in rough pipes. NACA. Technical Memorandum 1292. Nov 1950.

3 Varun Saini RP, Singal SK. A review on roughness geometry used in solar air heaters. Solar Energy. 2007;81:1340-1350.

4 Webb RL, Haman LL, Hui TS. Enhanced channels in electric utility stream condensers. Heat transfer in Heat Rejection Systems - ASME Symposium. 1984;37:17-26.

5 Skullong S, Promthaisong P, Promvonge P, Thianpong C, Pimsarn M. Thermal performance in solar air heater with perforated-winglet-type vortex generator. Solar Energy. 2018;170:1101-1117.

6 Promvonge P, Promthaisong P, Skullong S. Experimental and numerical thermal performance in solar receiver heat exchanger with trapezoidal louvered winglet and wavy groove. Solar Energy. 2022;236:153-174.

7 Godard G, Stanislas M. Control of a decelerating boundary layer Part 1: Optimization of passive vortex generators. Aerospace Science and Technology. 2006;10: 181-191.

8 Liang CH, Zhang XS, Li XW, Zhu X. Study on the performance of a solar assisted air source heat pump system for building heating. Energy Building. 2011;43:2188-2196.

9 Abdullah AH, Abou-Ziyan HZ, Ghoneim AA. Thermal performance of flat plate solar collector using various arrangements of compound honeycomb. Energy Conversion and Management. 2003;44:3093-3112.

10 Li SL, Meng XR, Wei XL. Heat transfer and friction factor correlations for solar air collectors with hemispherical protrusion artificial roughness on the absorber plate. Solar Energy. 2015;118:460-468.

11 Ravi RK, Saini RP. Experimental investigation on performance of a double pass artificial roughened solar air heater duct having roughness elements of the combination of discrete multi V shaped and staggered ribs. Energy. 2016;116: 507-516.

12 Alam T, Saini RP, Saini JS. Experimentally investigation on heat transfer enhancement due to V-shaped perforated blocks in a rectangular duct of solar air heater. Energy Conversion and Management. 2014;81:374-383.

13 Promvonge P, Kwankaomeng S. Periodic laminar flow and heat transfer in a channel with 45° staggered V-baffles. International Communications in Heat and Mass Transfer. 2010;37:841-849.

14 Skullong S, Promvonge P, Thianpong C, Jayranaiwachira N, Pimsarn M. Thermal performance of heat exchanger tube inserted with curved-winglet tapes. Applied Thermal Engineering. 2018;129:1197-1211.

15 Bhuiya MMK, Chowdhury MSU, Saha M, Islam MT, Heat transfer and friction factor characteristics in turbulent flow through a tube fitted with perforated twisted tape inserts. International Communications in Heat and Mass Transfer. 2013;46:49-57.

16 Promvonge P, Promthaisong P, Skullong S. Experimental and numerical heat transfer study of turbulent tube flow through discrete V-winglets. International Journal of Heat and Mass Transfer. 2020;151:119351.

17 Skullong S, Promvonge P, Thianpong C, Jayranaiwachira N. Thermal behaviors in a round tube equipped with quadruple perforated-delta-winglet pairs. Applied Thermal Engineering. 2017;115:229-243.

18 Wang J, Fu T, Zeng L, Lien FS, Chen G. Thermal-hydraulic performance in a tube with punched delta winglets inserts in turbulent flow. International Journal of Thermal Sciences. 2022;172:107326.

20 Kumar R, Nadda R, Kumar S, Razak A, Sharifpure M, Aybar HS, Saleel, CA, Afzal A. Influence of artificial roughness parametric variation on thermal performance of solar thermal collector: An experimental study, response surface analysis and ANN modelling. Sustainable Energy Technologies and Assessments. 2022;52:102047.

19 El Habet MA, Ahmed SA, Saleh MA. Thermal/hydraulic characteristics of a rectangular channel with inline/staggered perforated baffles. International Communications in Heat and Mass Transfer. 2021;128:105591.

21 Faujdar S, Agrawal M. Computational fluid dynamics based numerical study to determine the performance of triangular solar air heater duct having perforated baffles in V-down pattern mounted underneath absorber plate. Solar Energy. 2021;52:235-252.

22 Tandel HU, Modi KV. Experimental assessment of double-pass solar air heater by incorporating perforated baffles and solar water heating system. Renewable Energy. 2022;183:385-405 .

23 Khanlari A, Tuncer AD, Sözen A, Aytaç İ, Çiftçi E, Variyenli Hİ. Energy and exergy analysis of a vertical solar air heater with nano-enhanced absorber coating and perforated baffles. Renewable Energy. 2022;187:586-602.

24 El Habet MA, Ahmed SA, Saleh MA. The effect of using staggered and partially tilted perforated baffles on heat transfer and flow characteristics in a rectangular channel. International Journal of Thermal Sciences. 2022;174:107422.

Publication lists

1) Smith Eiamsa-ard, Somchai Sripattanapipat, Anucha Saysroy, Pongjet Promvonge, Naoki Maruyama, Masafumi Hirota, Heat transfer distribution and flow characteristics in a channel with perforated-baffles, *The 5th International Conference on Renewable Energy and Environment Engineering (REEE 2022)*, Paper ID: RE1031, Brest, France, 24-26 August 2022, pages 420-426.
2) Smith Eiamsa-ard, Somchai Sripattanapipat, Anucha Saysroy, Pongjet Promvonge, Naoki Maruyama, Masafumi Hirota, Heat transfer distribution and flow characteristics in a channel with perforated-baffles, *Energy Reports*, Vol. 8, Supplement 15, November 2022, pages 420-426, DOI: 10.1016/j.egyr.2022.10.079.
3) Pongjet Promvonge, Smith Eiamsa-ard, Sompol Skullong, Naoki Maruyama, Masafumi Hirota, Thermal performance and exergy analysis in a round tube with louvered trapezoidal winglets, *International Journal of Heat and Mass Transfer*, Vol. 212, Article no. 124261, 15 September 2023, pages 1-17, DOI: 10.1016/j.ijheatmasstransfer.2023.124261.
4) Smith Eiamsa-ard, Naoki Maruyama, Masafumi Hirota, Sompol Skullong, Pitak Promthaisong, Heat transfer mechanism in ribbed twisted-oval tubes, *International Journal of Thermal Sciences*, Vol. 193, July 2023 (Online), 20 pages, DOI: doi.org/10.1016/j.ijthermalsci.2023.108532.

CHAPTER 2

Thermal performance evaluation and literature review

2.1 Thermal performance assessment

Many performance evaluation criteria (PECs) have been suggested by researchers for relative evaluation of heat transfer enhancement, but it is important to note that applicability varies depending on the specifics of the application [1-14]. Table 2.1 provides a preliminary listing based on the classification established by Bergles *et al.* [8] and its following revisions [5, 9]. Two of the most popular figures of merit for thermal hydrodynamic performance in the chemical and process industries are reviewed here to demonstrate this trade-off and provide optimization guidelines.

1) FG-2a: In the absence of enhancement, quantify the additional heat load Q induced by the technique when the geometry of the heat exchanger (N and L), the temperature difference across the approach (ΔT_i), and the pumping power P are all the same as the case with no enhancement. Heat load and pumping power can both be determined by reference to their commonly accepted definitions.

$$Q = \varepsilon(\dot{m}C_p)\Delta T_i \approx hA\Delta T = (\pi kLN\Delta T_i)Nu \tag{2.1}$$

$$P = (\dot{m}/\rho)\Delta p = (\pi\mu^2 L/2\rho^2 d^2)(fRe^3) \tag{2.2}$$

2) VG-1: When the mass flow rate, pumping power P, heat load Q, and approach temperature differential (ΔT_i) remain unchanged, as in the case with no enhancement, the surface area (A) of the heat exchanger is lowered by a quantifiable amount for the enhancement technique. It is noteworthy that the condition of a fixed pressure drop remains constant under the constraints of constant $\dot{m}$ and P values.

$$\Delta p = f(4L/d)(\rho V_o^2/2) = (2\mu^2 L/\rho d^3)(fRe^2) \tag{2.3}$$

In most enhancement technology applications, these figures of merit highlight the key design issues, which are maintaining greater heat loads in a given heat exchanger or decreasing the size of the heat exchanger for an offered heat load. Evaluating the enhanced thermal performance (or improvement in Q) owing to enhanced tubes in a heat exchanger under the constraint of fixed shape and equal pumping

power is desirable in many applications involving chemical processing heat transfer or thermal manufacture of various fluid media. To do so, we can apply the FG-2a criterion described above and shown in Table 2.1, by writing the heat transfer rate for a duct/tube (Q_{tt}), with an insert, as a fraction of the heat transfer rate for a plain or unaugmented tube (Q_{st}).

$$(Q_{tt} / Q_{st}) = (Nu_{tt} / Nu_{st})_{N,L,d,P,\Delta T_i} \tag{2.4}$$

The following constraint is imposed by Eq. (2.2) on the operation of a heat exchanger under the given conditions when using constant pumping power:

$$(fRe^3)_{tt} = (fRe^3)_{st} \tag{2.5}$$

The presence of ribs or rough surfaces always simultaneously causes a desired heat transfer enhancement and an unwanted friction loss penalty. Increased friction losses lead to a need for higher pumping power, which impacts the economics of operation. Therefore, both effects need to be considered for evaluation of overall performance. Generally, improved heat transfer is determined in terms of a normalized parameter, the Nusselt ratio (Nu/Nu_s), where Nu is the Nusselt number in roughed channels/pipes and Nu_s is the Nusselt number in smooth channels/pipes. Similarly, increased friction losses are presented in term of a dimensionless friction factor ratio (f/f_s), where f is the friction factor in roughed channels/pipes and f_s is the friction factor in smooth channels/pipes. The overall performance of the operation is evaluated in terms of a thermal performance factor (*TPF*). Fundamentally, the *TPF* is a ratio of the convection coefficient in roughened channels/pipes (h) to that of smooth channels/pipes (h_s). Under identical pumping power conditions, the convection coefficient ratio can be written in terms of the Nusselt number and friction factor ratios as shown in Eq. (2.6) [10-14].

$$\eta = \left.\frac{h}{h_s}\right|_{pp} = \left.\frac{Nu}{Nu_s}\right|_{pp} = (Nu / Nu_s) / (f / f_s)^{1/3} \tag{2.6}$$

According to Eq. (2.6), a high thermal performance factor (*TPF*) can be achieved by enhancing heat transfer while controlling friction losses to be as low as possible.

Table 2.1: Standards for evaluating performance of tubular heat exchangers utilizing single-phase forced convection [6].

Case	Shape	Parameter				Aim
		W	P	Q	ΔT_i	
FG-1a	N,L^a	x			x	$\uparrow Q$
FG-1b	N,L	x		x		$\downarrow \Delta T_i$
FG-2a	N,L		x		x	$\uparrow Q$
FG-2b	N,L		x	X		$\downarrow \Delta T_i$
FG-3	N,L			x	x	$\downarrow P$
FN-1	N	x	x	x	x	$\downarrow L$
FN-2	N	x		x	x	$\downarrow L$
FN-3	N	x		x	x	$\downarrow P$
VG-1		x	x	x	x	$\downarrow NL$
VG-2a	N,L^b	x	x		x	$\uparrow Q$
VG-2b	N,L^b	x	x	x		$\downarrow \Delta T_i$
VG-3	N,L^b	x	x	x	x	$\downarrow P$

† According to Bergles's [5] classification. * The product of N and L.

2.2 Enhancing heat transfer with ribs

The flow of a viscous fluid in a plain pipe will result in a non-uniform velocity distribution across the pipe cross-section. The fluid velocity near the wall of the pipe is very low, which is significantly different from that at the pipe core. Alternatively, the flow of non-viscous fluid (inviscid flow) usually shows a uniform velocity distribution. In case the fluid flows through a two- or three-dimensional rough pipe, different velocity distribution patterns are generated depending on the base geometry of surface roughness. Flow behaviors affect the heat transfer rate in the pipe or channel. Figure 2.1 illustrates the flow behavior through single rib and continuous ribs by the hydrogen bubble technique in a channel at the low Reynolds number [15]. The flow pattern at the inlet of the channel is a fully developed flow. Flow velocity is dependent on the radial distances from the pipe wall. Flow velocity is zero at the wall. The flow reaches maximum velocity at the pipe core. A collision between the fluid and ribs results in flow separation and eddy motion or vortices behind the rib. The size and shape of the vortices are dependent on surface roughness. For a single rib, the flow begins to develop into a fully developed flow after passing the rib at a certain distance, as displayed in Fig. 2.1(a). To maintain the secondary flow or flow disturbance, a series of ribs must be applied as demonstrated in Fig. 2.1(b). This results in a decreased thickness of the velocity boundary layer and increased heat transfer [16] as depicted in Fig. 2.2. However, the spacing between the ribs must be appropriately designed to obtain a reasonable

trade-off between heat transfer enhancement and increased pressure drop (see details in the next section).

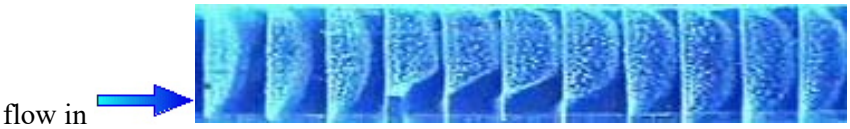

(a) Flow behavior over a single rib at a Reynolds number of 490

(b) Flow behavior over a pair rib in series at a Reynolds number of 490

Figure 2.1. Flow behavior aver rib (s) observed *via* the hydrogen bubble technique [15].

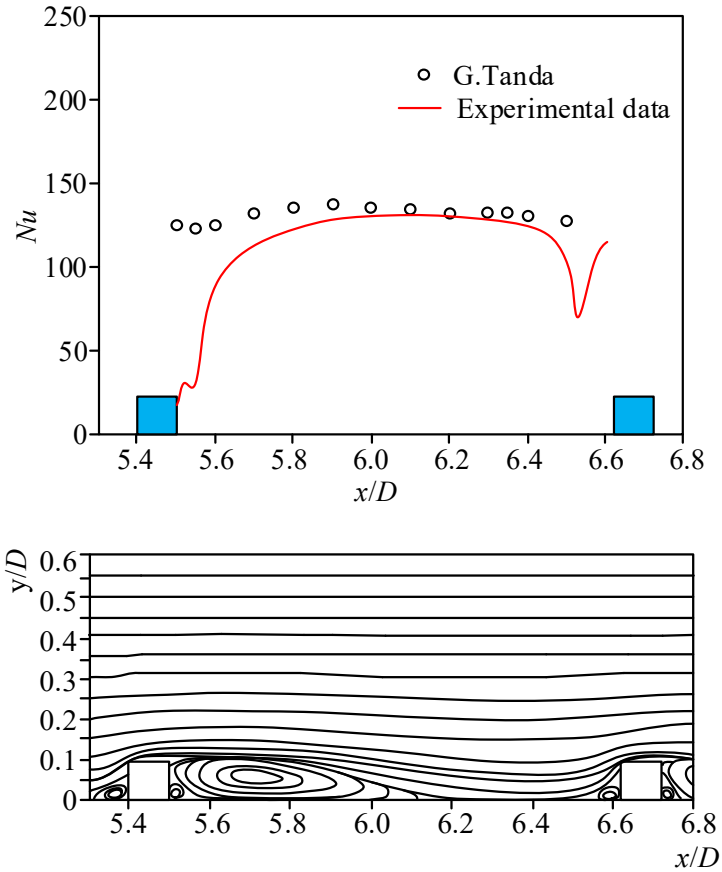

Figure 2.2. Local Nusselt number distribution (upper figure) and streamline distribution (lower figure) in a channel with continuous ribs [16].

The flow pattern is dependent on the shapes/geometries of the rough surfaces. Generally, recirculation flow (eddy motion) usually takes place adjacent to the rear of modified surfaces, followed by flow reattachment, which directly promotes heat transfer [17, 18], as shown in Fig. 2.3(a). Figures 2.3(b) and 2.3(c) illustrate the temperature and Nusselt number gradients throughout the direction of flow, respectively. The temperature of the fluid increases as a result of the heat transfer from the channel

wall. Here, the Nusselt number reaches a periodic condition at around the 5th rib. The number of ribs within the channel also has a role in the onset of a periodic condition. The major parameters that affect the heat transfer rate and pressure loss in a system with ribs are the Reynolds number, rib shape/design, attack angle of the ribs, rib height, rib arrangement, and ribs with special design (baffles).

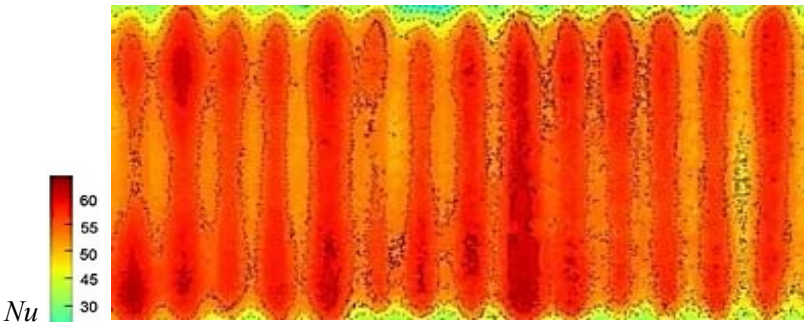

(a) Nusselt number contour in the channel with continuous baffles [17]

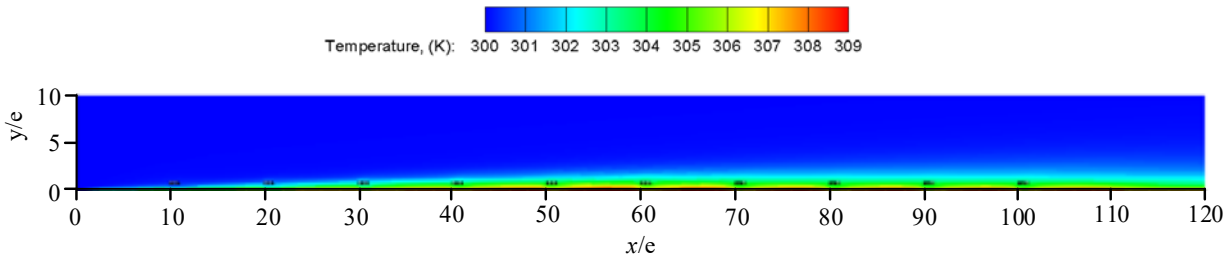

(b) Temperature contours in a channel with continuous ribs [18]

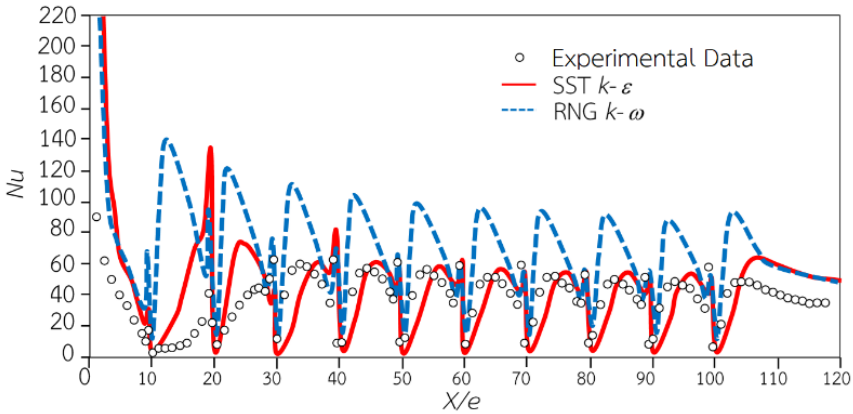

(c) Nusselt number distributions in a channel with continuous ribs [18].

Figure 2.3. Nusselt number and temperature contours in a channel with continuous ribs.

2.2.1 Effect of Reynolds number

The Nusselt numbers grow as the Reynolds numbers rise due to the thinning thermal boundary layer and thus, reduction of convective resistance. Simultaneously, an increased Reynolds number helps to decrease the friction factor since a greater Reynolds number diminishes the viscous boundary layer. Recirculation behaviors between ribs at Reynolds numbers (*Re*) of 100 and 1000 are shown in Fig. 2.4.

The greater the Reynolds number, the size and amplitude of the eddy currents are promoted and the thermal boundary layer becomes thinner [19]. As shown in Fig. 2.5, the Nusselt numbers at *Re* = 20,000 are significantly higher than those at *Re* = 4000 [17]. Additionally, Fig. 2.5 also indicates that a high Nusselt number region is located midway between each pair of ribs, where flow reattachment takes place.

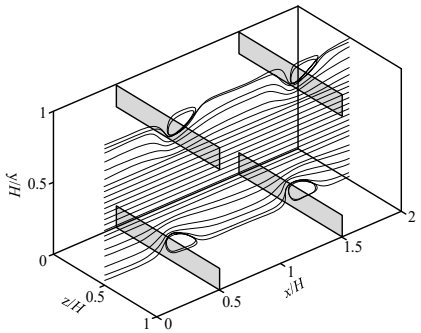

(a) *Re* = 100

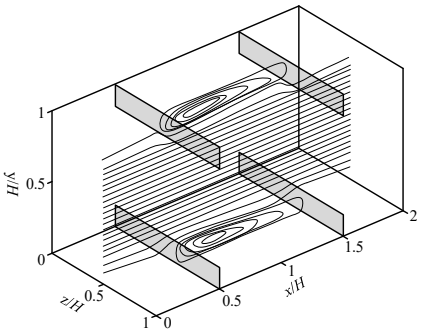

(b) *Re* = 1000

Figure 2.4. Recirculation flow behavior between ribs at various Reynolds numbers [19].

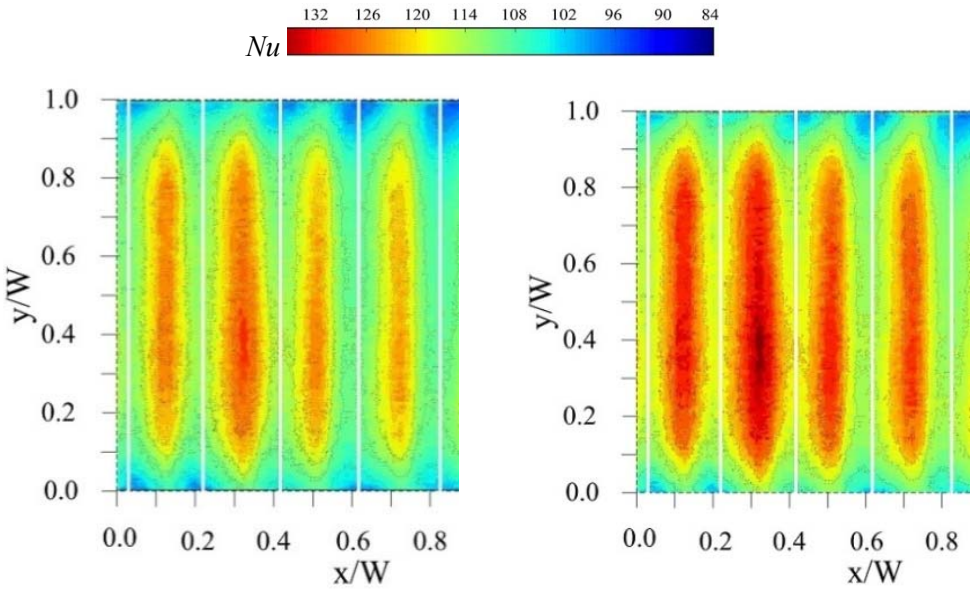

(a) *Re* = 4000 (b) *Re* = 20,000

Figure 2.5. Effect of Reynolds number on heat transfer behavior in a ribbed channel [17].

2.2.2 Effect of rib shape/design

Rib shape and design significantly influence the heat transfer behavior and flow structure in ribbed pipes and channels. Generally, ribs cause separation and reattachment on heat transfer surfaces. The phenomena have an antagonistic effect (improving heat transfer rate and causing higher pressure loss). Numerous researchers have modified ribs for better tradeoffs between these effects. Nuntadusit *et al.* [20] developed the straight perforated rib shown in Fig. 2.6(b), and an inclined perforated rib shown in Fig. 2.6(c). They compared their performance with that of a conventional solid rib (Fig. 2.6(a)).

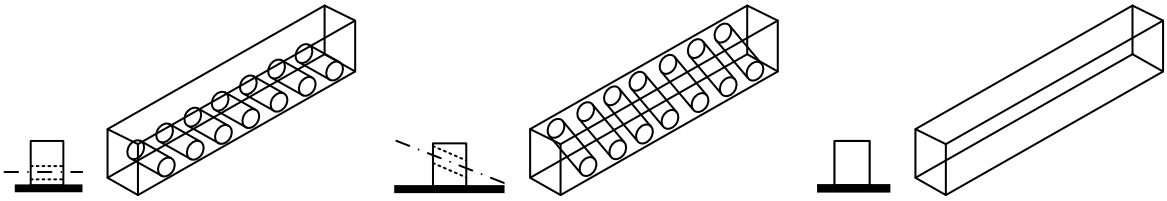

(a) Straight perforated rib (b) Inclined perforated rib (c) Solid rib

Figure 2.6. A conventional solid rib and modified ribs [20].

The numerical results in Fig. 2.7 suggest that a solid rib causes a long separation flow behind the rib. Alternatively, the holes as part of the straight perforated ribs and inclined perforated ribs direct jets on the heat transfer surfaces behind the ribs as depicted in Figs. 2.7(b-c). This allows for more efficient local heat transfer compared to the conventional solid rib design. Additionally, an inclined perforated rib gives a stronger attack angle and thus higher Nusselt number than an uninclined rib.

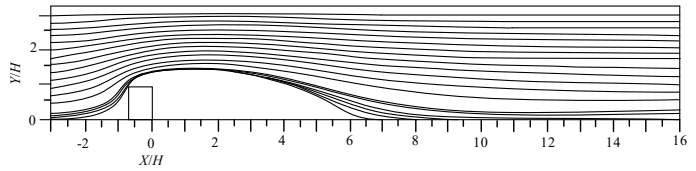

(a) Solid rib

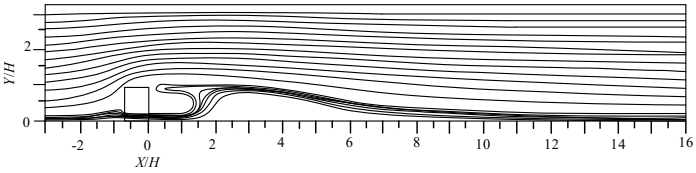

(b) Straight perforated rib

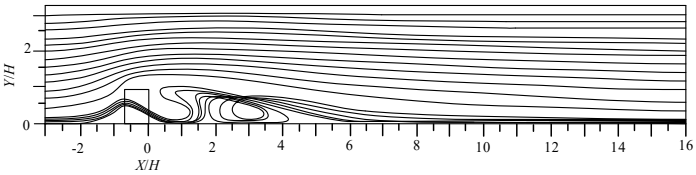

(c) Inclined perforated rib

Figure 2.7. Post-rib flow and heat transfer behavior at a Reynolds number of 60,000 [20].

In Fig. 2.8, shows effects of rib shape and geometry on Nusselt number distribution. Clearly, inclined perforated ribs with a larger perforation angle (30°) yield better heat transfer adjacent to a rib than is observed with a smaller angle (15°). However, all perforated ribs yield comparable heat transfer in the reattachment region.

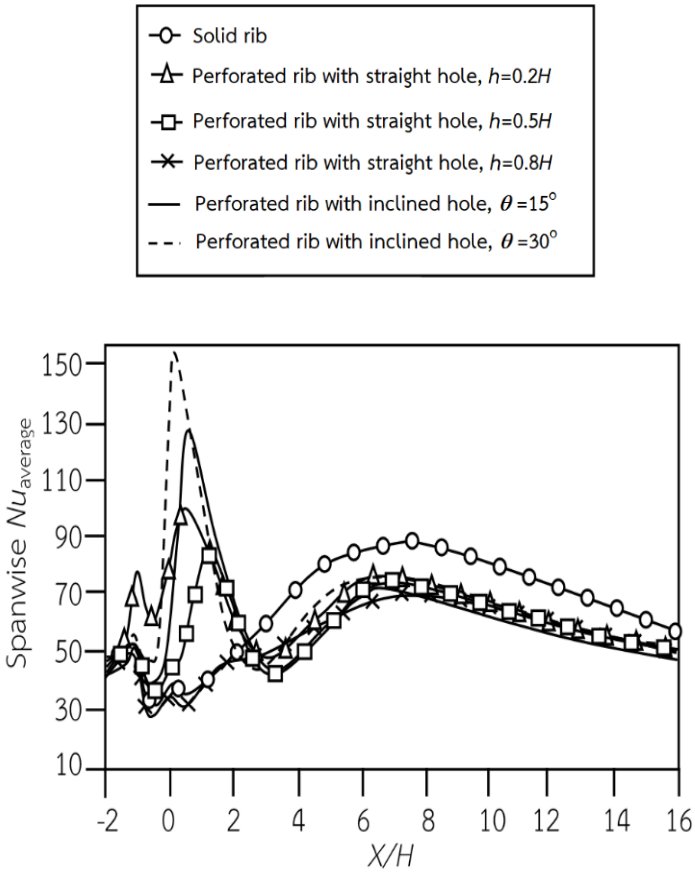

Figure 2.8. Nusselt numbers distribution in the channels with different types of ribs [10].

Additionally, Changcharoen and Eiamsa-ard [21] reported the flow behavior of uplifted ribs (detached ribs), as shown in Fig. 2.9. Rib detachment had a substantial influence on the flow pattern. Figure 2.10 presents that the flow has an immediate effect on the thickness of the thermal boundary layer, which in turn increased heat transfer. Subsequent flow reattachment led to a maximal heat transfer area. Yongsiri *et al.* [18] developed ribs with various inclination angles. The fluid flow direction corresponded to the inclination angles, as shown in Fig. 2.11. The presence of rib gaps also helped in decreasing the pressure loss of the system. Jiang and Gao [22] reported the heat transfer mechanism and flow pattern in ducts with 45°/60°/75° V-shaped and 45°/60°/75°/90° parallel ribs. They showed that the duct rough with 45° V-shaped ribs was found to have the greatest longitudinal secondary flow regions and the largest mainstream secondary flow regions.

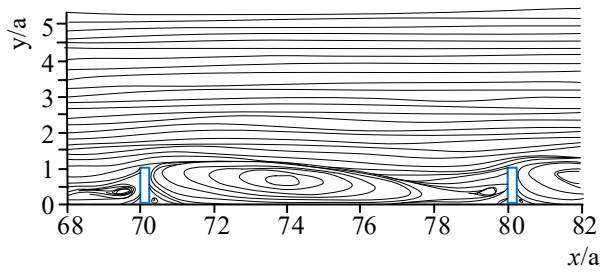

(a) $c/a = 0.0$

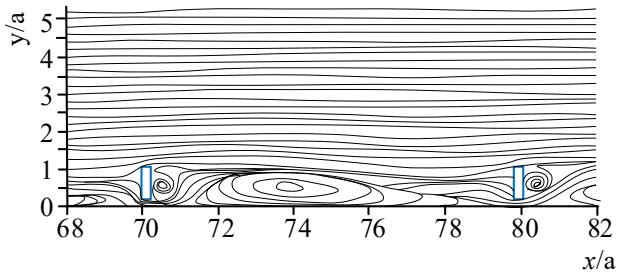

(b) $c/a = 0.2$

Figure 2.9. Flow behavior in the channel with uplifted (detached) ribs at a Reynolds number of 8000 [21].

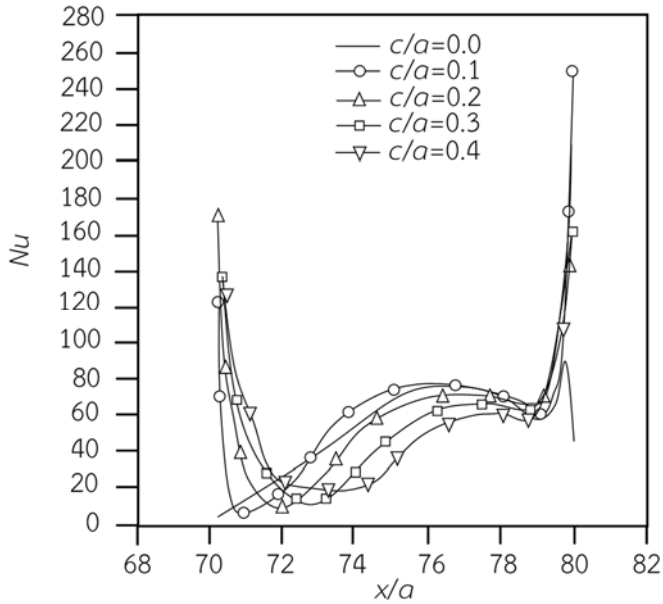

Figure 2.10. Heat transfer distribution (*Nu*) in a channel with detached ribs at *Re* = 8000 [21].

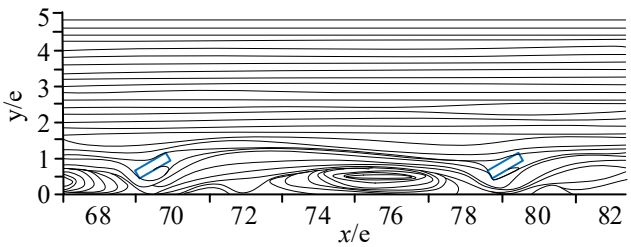

Figure 2.11. Flow behavior in a channel between the 7th and 8th ribs for detached ribs with a 150° attack angle [18].

Ribs commonly have two major forms, protruding and grooved (or a combination of these two types of roughness), as shown in Fig. 2.12. Their geometries can be varied by changing the height (or depth) and width of the protrusion or groove. A change of rib geometry directly affects the heat transfer mechanism and flow pattern of enhanced systems as the sample numerical results in Fig. 2.13. Generally, the surface friction coefficient increases as the groove width decreases, as depicted in Fig. 2.14.

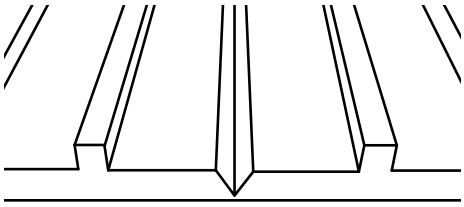

Figure 2.12. Illustration and imagery of grooved ribs [23].

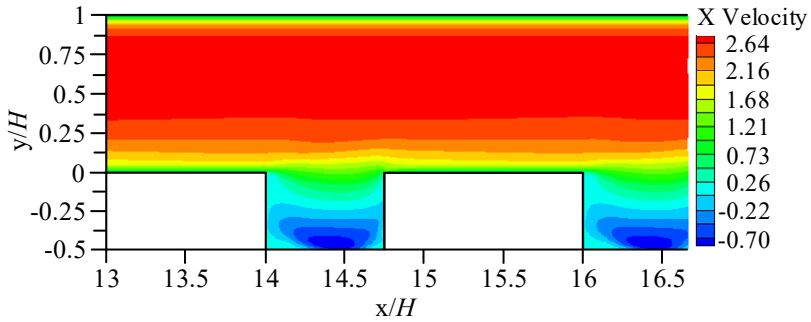

(a) $B/H = 0.75$

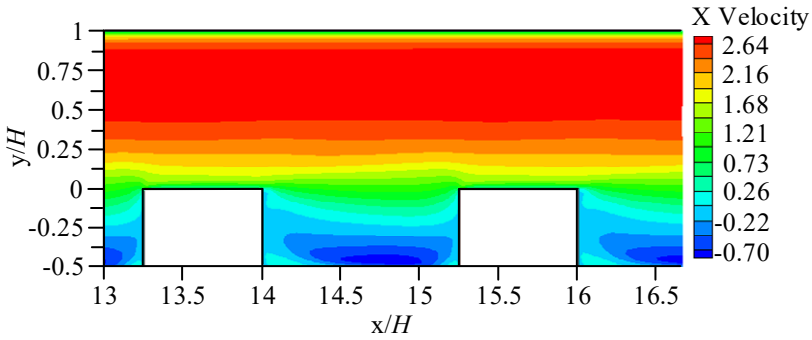

(b) $B/H = 1.25$

Figure 2.13. Influence of groove width on heat transfer [24].

Triangular prism ribs are another type of rib that are applied for heat transfer augmentation. Numerical results by Eiamsa-ard *et al.* [25] revealed that triangular prism ribs introduced turbulent eddy flows as display in Fig. 2.15. Adjusting the location of the prism affects the distribution of the Nusselt numbers, as depicted in Fig. 2.16. Prism ribs with a small clearance ratio (CR = 1.5) induced a high Nusselt number area near the ribs, according to the location of the reattachment flow [25]. However, ribs with

a large clearance ratio (*CR* = 3.0) caused long flow separation behind the ribs. Therefore, the high Nusselt number area related to the reattachment location shifted downstream. It is notable that at *CR* = 3.0, the reattachment area was larger than that found at *CR* = 1.5.

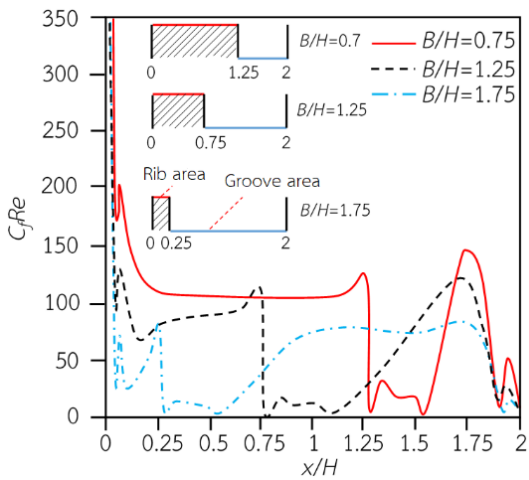

Figure 2.14. Influence of groove width on surface friction coefficient distribution [24].

Ribs with various shapes/arrangements lead to different attack angles of flows, which directly affect flow and heat transfer characteristics. Numerical results of Eiamsa-ard and Changcharoen [16] revealed that a reduction of rib sharpness helped in suppressing sudden changes of the main flow and flow separation, as displayed in Fig. 2.17. Consequently, the hot spots behind the ribs became smaller, especially with concave-concave ribs, as demonstrated in Fig. 2.18. Additionally, the results of Eiamsa-ard and Chuwattanakul [17] indicated that the utilization of inclined ribs with a low *p/w* yielded greater heat transfer than for a higher *p/w* as seen in Fig. 2.19.

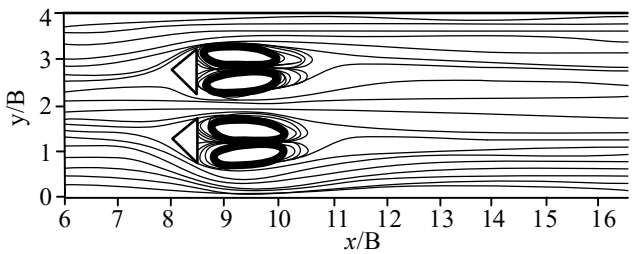

(a) CR = 1.5

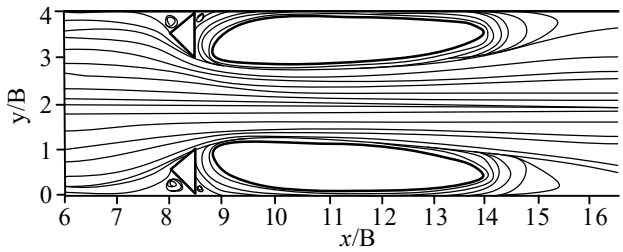

(b) CR = 3.0

Figure 2.15. Streamlines in channels equipped with a triangular prism at various clearance ratios [25].

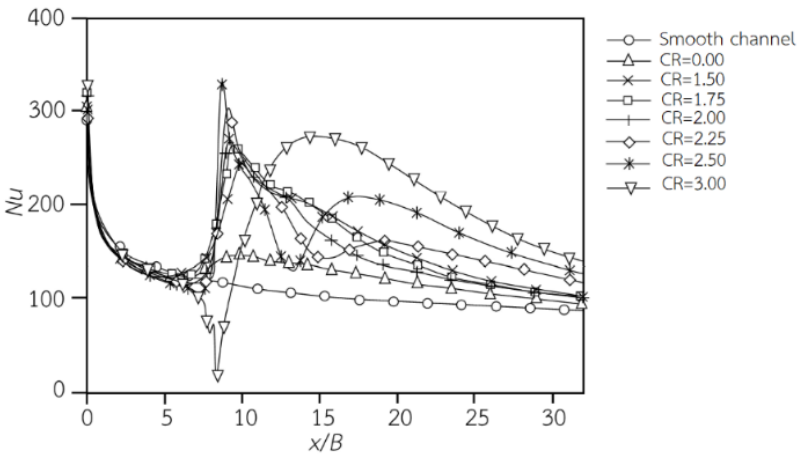

Figure 2.16. Axial distribution of *Nu* on the bottom wall surface of the channel at *Re* = 20,000 [25].

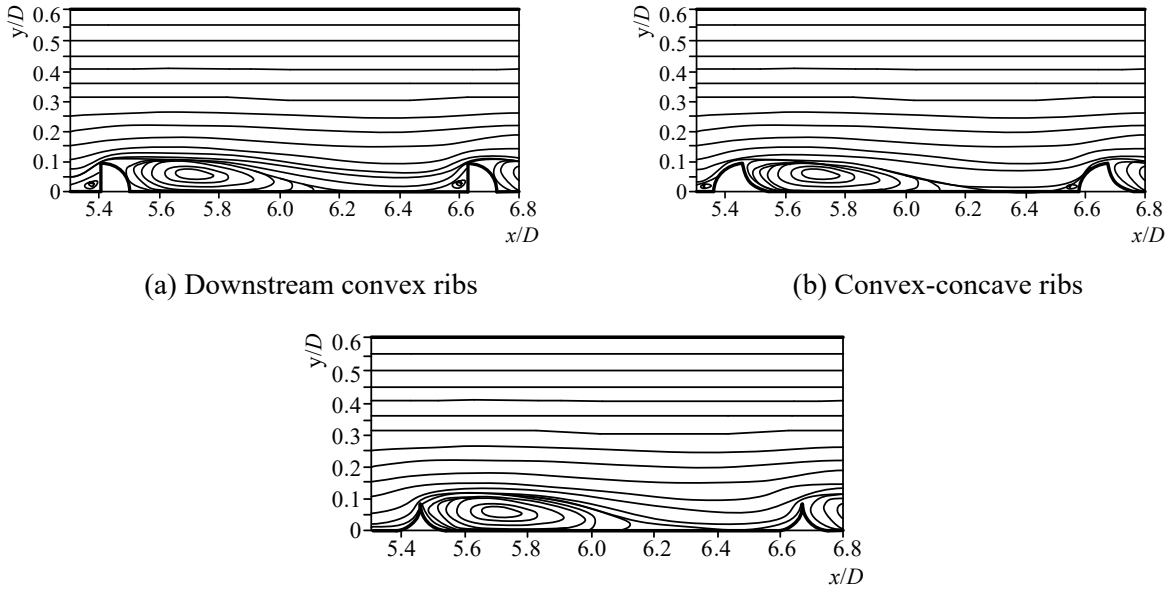

(a) Downstream convex ribs (b) Convex-concave ribs

(c) Concave-concave ribs

Figure 2.17. Effects of various curved ribs on flow characteristics at *Re* = 25,000 [16].

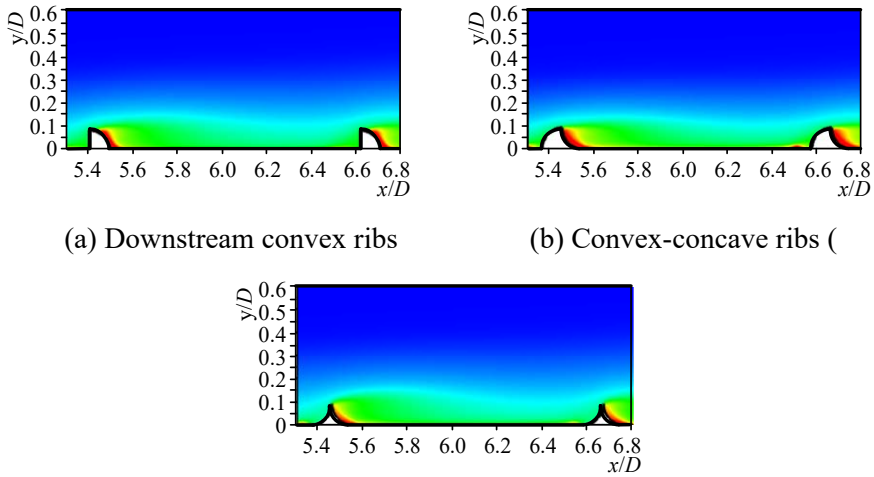

(a) Downstream convex ribs (b) Convex-concave ribs (

c) Concave-concave ribs

Figure 2.18. Effects of various curved ribs on temperature distributions at *Re* = 25,000 [16].

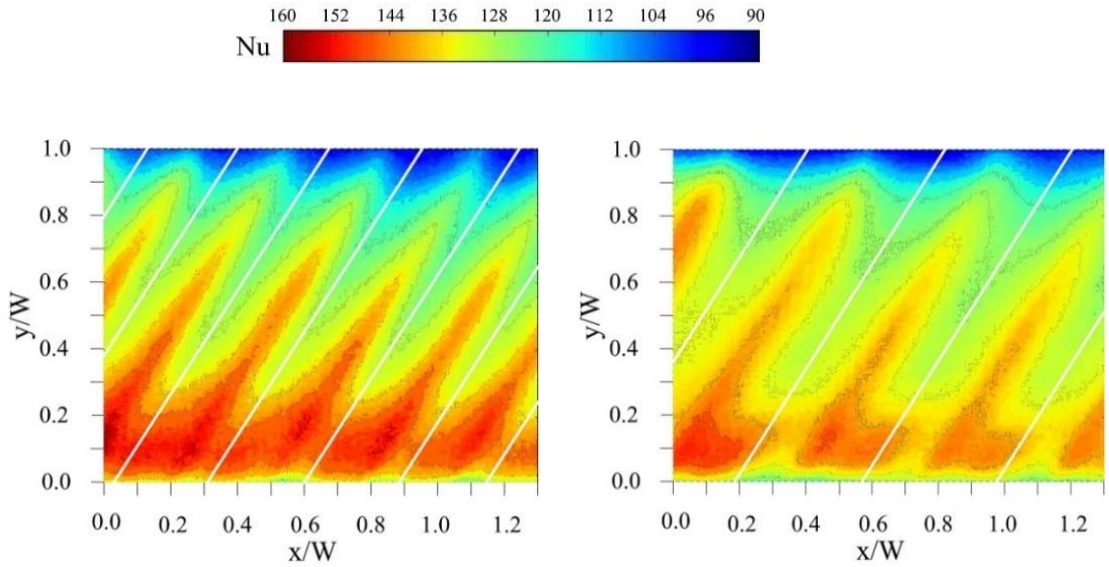

(a) p/w = 8.0 (b) p/w = 12

Figure 2.19. Nusselt number distribution in an inclined baffled channel at Re = 20,000 [17].

Heat transfer in a channel with a wide range of rib shapes was studied by Wang and Sundén [26]. The pitch-to-height ratios of these ribs ranged from 8.0 to 15.0. Real-time Laser Holographic Interferometry tests were performed in 8,000 ≤ Re ≤ 20,000 to measure the average and local heat transfer. They discovered that ribs with a trapezoidal shape transferred heat more effectively than ribs of other shapes. Heat transfer and pressure drop characteristics were investigated by Xie *et al.* [27], who evaluated the influence of truncated rib and mid-truncated rib, offset position, and angles. They found that the pressure loss was minimal when the ribs were truncated at 90 degrees in the middle and placed without any offset, while 135° mid-truncated ribs provided the greatest heat transfer coefficient. The enhanced heat transfer rate was tested by Iacovides *et al.* [28] in a duct with staggered ribs. Local heat transfer was demonstrated utilizing a thermochromic liquid crystal (TLC) sheet. Average fluid motion and its fluctuations were estimated using laser Doppler Anemometry. They noticed that the structure of the flow and the local heat transfer varied considerably over the length. Secondary flows and recirculation influenced flow and thermal developments. According to Mahanand and Senapati [29], quarter-circular ribs (Fig. 2.20) offered the highest thermal enhancement factor, 1.88. Triangular ribs performed the best heat transfer rate, according to Ekiciler and Çetinkaya [30], who used elliptical, square, and triangular shaped transverse ribs (Fig. 2.21) for heat transfer enhancement. Liu *et al.* [31] improved heat transfer and the thermal enhancement by altering conventional transverse ribs to create truncated ribs (Fig. 2.22). They revealed that the truncated ribs promoted reduced pressure losses without negatively impacting heat transfer. According to Liu *et al.* [32], perforated transverse ribs (Fig. 2.23) can increase heat transfer by 4-8% while decreasing pressure losses by 12-24% compared to traditional ribs.

Figure 2.20. Quarter-circular ribs [29].

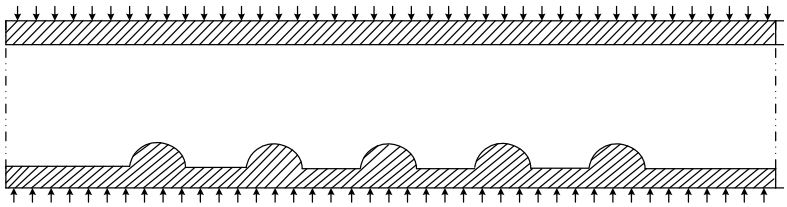

Figure 2.21. Transverse ribs with ellipses [30].

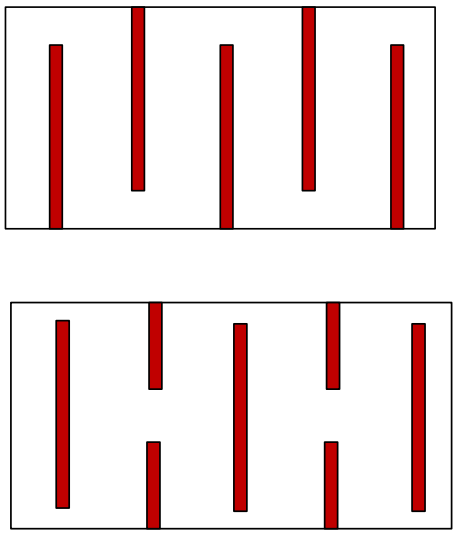

Figure 2.22. Truncation ribs [31].

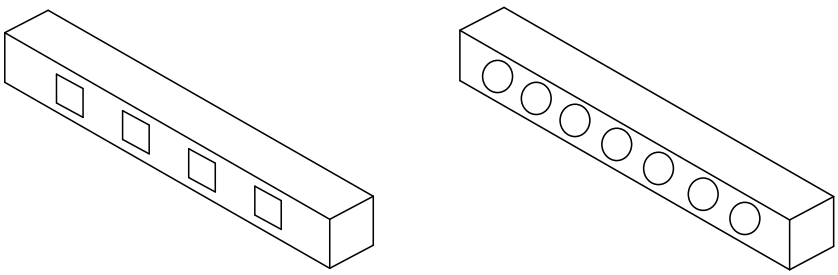

(a) Square perforated (b) Circular perforated

Figure 2.23. Perforated transverse ribs [32].

2.2.3 Effect of rib height

The thickness of the boundary layer and the rate of heat transfer are both directly affected by rib height. Generally, increased rib height introduces stronger turbulence/reattachment and superior heat transfer. However, further increased rib height beyond the appropriate level leads to the absence of reattachment

(Fig. 2.24) and thus, poorer heat transfer rate due to the flow patterns [33]. The analysis by Prasad and Saini [34], suggests that the optimum rib height is slightly larger than the transition sublayer thickness. Under this condition, ribs noticeably enhance heat transfer with moderate pressure losses since they do not protrude into the turbulent core. An over-height rib causes a high-pressure drop penalty that directly degrades thermal performance. Figures 2.25 and 2.26 show that eddy currents or recirculation flow occur adjacent to the rear of a rib. As the rib height to channel height ratio (BR) grows larger, the size and shape of the eddy currents become larger. Consequently, the reattachment areas shrink. Therefore, excessively high ribs are used, leading to inefficient heat transfer [19, 35].

e/D	Flow pattern between ribs
e_1/D	
e_2/D	
e_3/D	
e_4/D	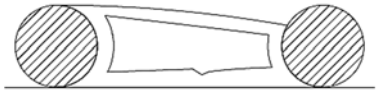
e_5/D	

Figure 2.24. Effect of rib height in terms of rib height ratio on flow patterns [33].

Promvonge *et al.* [36] investigated the turbulent flow in a duct with thin discrete inline 60° V-shaped ribs. According to their findings, a pair of counter-rotating vortices (P-vortices) were created by the ribs, and these P-vortices triggered impingement flows that improved heat transfer. With increasing blockage ratio, pressure losses and heat transfer increased. Ribs with a blockage ratio value of 0.0725 at Re = 10,000 produced the highest thermal performance factor, 1.8. As much as four times as much heat was transferred in this configuration as in a square, smooth duct. According to Bahiraei *et al.* [37], the increase in the heat transfer coefficient was caused by reducing rib pitch and increasing rib height. It can be concluded from the above results that there is an appropriate range of rib height which

offers efficient heat transfer with a reasonable pressure loss penalty. Since it is related to the reattachment flow [38-40], the roughness height ratio (e/D_h) has a substantial influence on the flow and heat transfer of enhanced thermal systems.

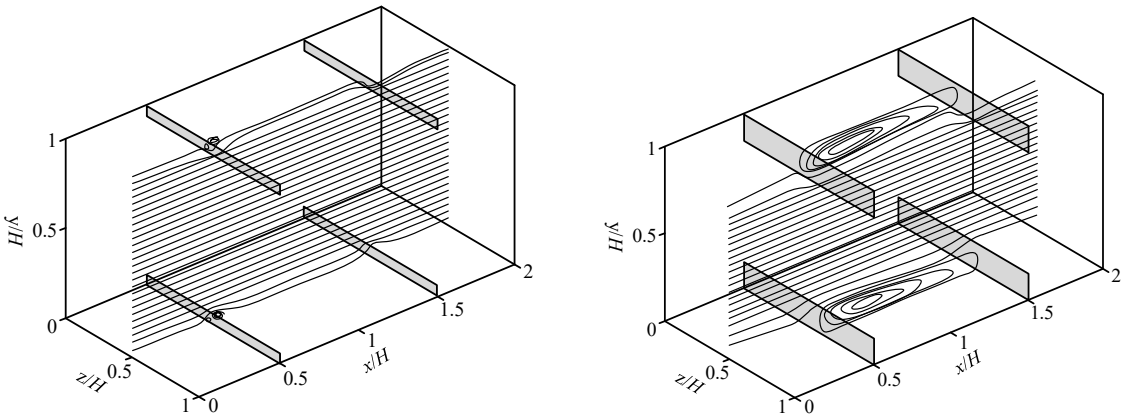

(a) BR = 0.05 (b) BR = 0.15

Figure 2.25. Flow patterns in a ribbed channel with different rib heights [19].

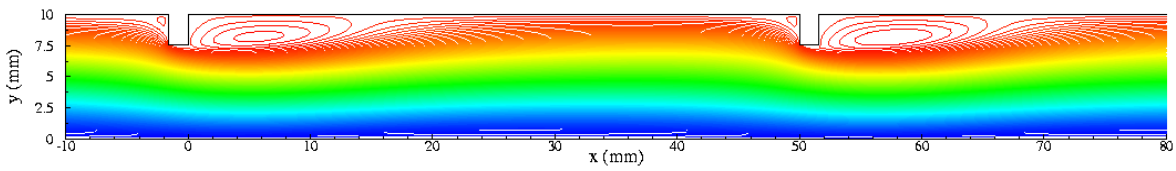

(a) BR = 0.125

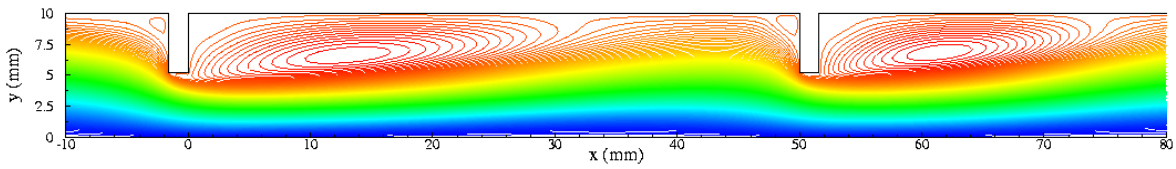

(b) BR = 0.25

Figure 2.26. Prediction of flow in a ribbed channel with different rib heights [35].

2.2.4 Effect of rib pitch

Creating an artificially rough absorber plate bottom for a solar air heater duct, the heat transfer coefficient between the absorber plate and the air can be significantly enhanced. The effect of relative pitch (p/e) on heat transfer rate and pressure loss in a roughened duct of varying form roughness geometries was investigated experimentally [41-45]. Prasad and Saini [34] present the flow patterns associated with ribs having different pitch ratios (p/e) as seen in Fig. 2.27. Reattachment of a free shear layer appeared at 6e-8e, behind each rib. Therefore, installing ribs at pitch ratios (p/e) values smaller than 6, reattached flow did not occur. Consequently, the heat transfer rate was reduced to levels even poorer than that of smooth surface in some cases. Additionally, decreasing rib pitch monotonically increased friction losses. Therefore, ribs having p/e values less than 6.0 yielded extremely low thermal

performance. On the other hand, ribs with too large pitch yielded low heat transfer and thus, low thermal performance due to inconsistent reattachment. Generally, optimal rib pitches producing maximal thermal performance, are in the range of 6.0 to 10.

p/e	Flow pattern between ribs
∞	
10	
6.0	
5.0	
2.0	
0.75-1.25	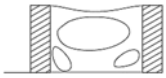

Figure 2.27. Effect of rib pitch on downstream flow [33].

Yadav and Bhagoria found that the transverse ribs significantly boosted the degree of turbulent flow closer to the heat transfer surface [46-48] as shown Figs. 2.28-2.30. Aharwal *et al.* [49] examined the effect of ribs on heat transfer of a solar air heater. They reported that the pressure loss and heat transfer rate rose over those of a smooth channel by 2.6% and 2.9%, respectively. Results suggested that the optimum location and width ratios for thermal performance were 0.25 and 1.0, respectively. Influences of gap width and gap position on heat transfer and flow were also studied by Aharwal *et al.* [50]. They found that the pressure losses increased up to 3.6 times greater than that of a smooth channel, with a maximum increase in heat transfer of 2.83 times that of a small channel at corresponding gap positions and pitch ratios of 1.0 and 8.0.

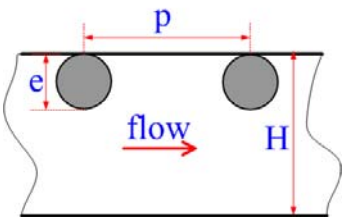

Figure 2.28. Circular ribs at *p/e* = 7.14-35.71, *e/D* = 0.021-0.042 [46].

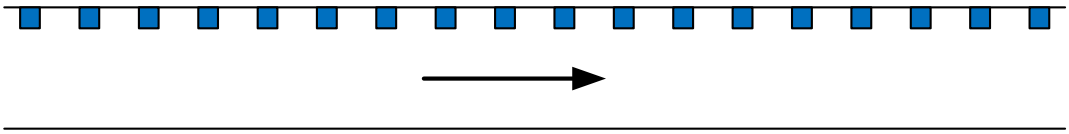

Figure 2.29. Rectangular ribs at *p/e* = 7.14-35.71, *e/D* = 0.021-0.042 [47].

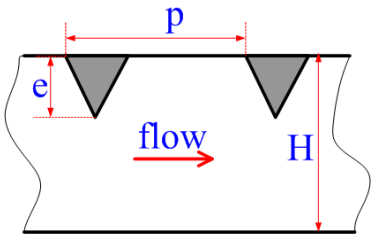

Figure 2.30. Triangular ribs at *p/e* = 7.14-35.71, *e/D* = 0.021-0.042 [48].

2.2.5 Effect of V-shaped/inclined ribs

There are two major categories of ribs: (1) transverse ribs, which are arranged perpendicular to the flow, and (2) V-shaped/inclined ribs, which are angled to the flow as shown in Fig. 2.31. Owing to their lower pressure losses, V-shaped ribs usually yield higher thermal performance (evaluated from $(Nu/Nu_s)/(f/f_s)^{1/3}$) than transverse ribs. Furthermore, V-shapes ribs have been modified for a better performance. The modified ones in the form of multiple V-shaped ribs (Fig. 2.31(c)), introduce multiple pairs of eddy flows downstream of the ribs. These flows help in disrupting thermal layers and blending cold and hot fluids, resulting in enhanced heat transfer [51-53]. Generally, multiple V-shaped ribs cause fluid to impinge at the rear of ribs producing counter-vortex-flow as shown in Fig. 2.32. Flow leads to strong turbulence signified by high kinetic energy dissipation in the transverse flow plane. The impinged area shows excellent heat transfer since the cold fluid near the upper wall is induced by a recirculation stream to absorb heat from the hot lower wall and vice versa.

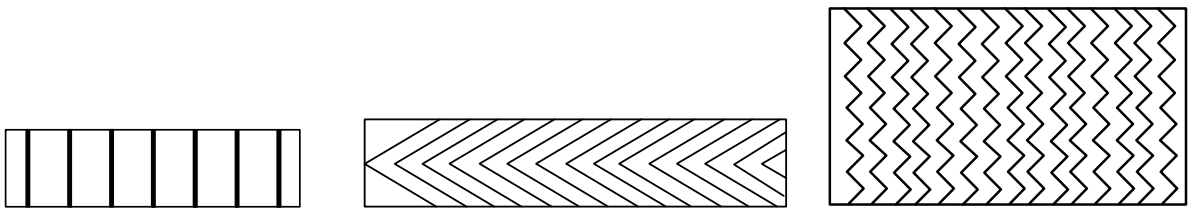

(a) Transverse ribs (b) V-shaped ribs (c) Multiple V-shaped ribs

Figure 2.31. Transverse rib and V-shaped ribs/multiple V-shapes ribs [53].

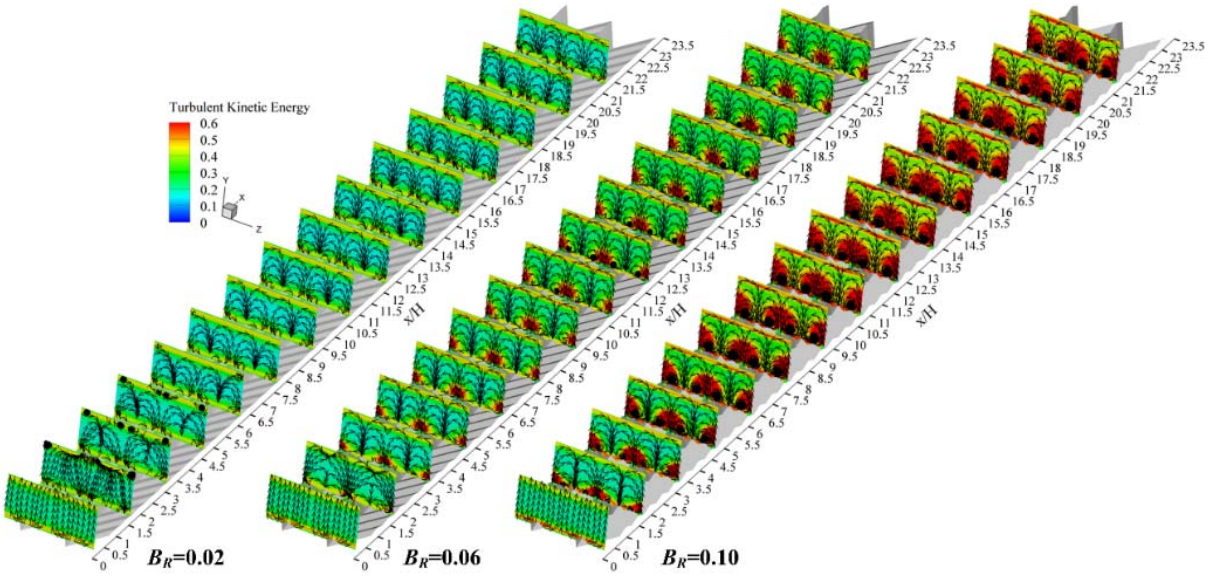

(a) Streamlines and kinetic energy dissipation in the transverse flow plane

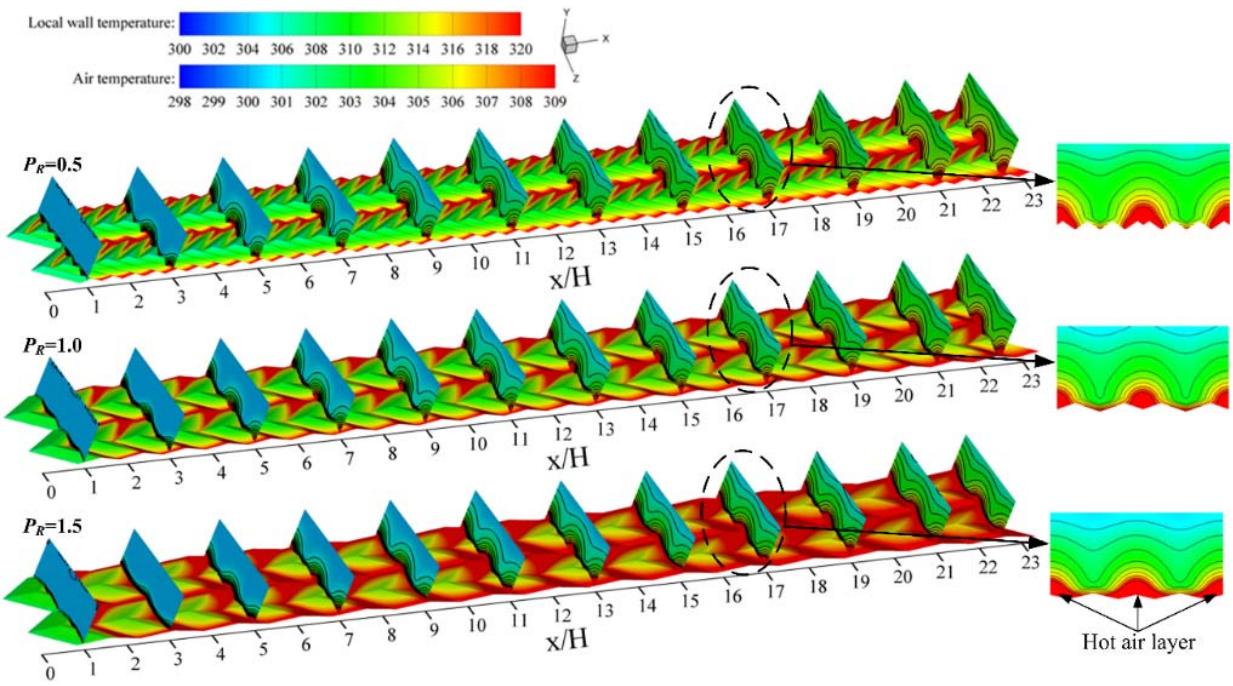

(b) Fluid and surface temperatures

Figure 2.32. Flow behaviors and temperature distributions in a duct with multiple V-shaped ribs [54].

Chaube *et al.* [55] fabricated and employed inclined ribs with various attack angles, widths and configurations for heat transfer enhancement. The ribs with an attack angle of 60 degrees, a position and a width ratio of 0.33 and 0.33 generated the highest heat transfer and pressure losses. Kaewchoothong *et al.* [56] examine how different arrangements of inclined angle ribs in a duct

influenced local heat transfer. Based on their experimental findings, heat transfer by transverse ribs was respectively enhanced by about 20%, 25%, and 30% for inclination angles of 60°, 45°, and 60°. Experiments on heat transfer in a square channel with ribs on two walls were undertaken by Han *et al.* [57] to examine how rib configuration affected performance. Heat was transported more efficiently with 'V' and angled ribs compared with continuous ribs. Among the angled ribs, the 60° angle ribs had the highest pressure loss and heat transfer rates. Han *et al.* [58] also reported that heating only one or both of the ribbed walls increased heat transfer comparable to heating all four channel walls. Xie *et al.* [59] undertook a numerical analysis of the influence of rib arrangement on heat transfer and pressure losses. They compared a variety of configurations: continuous ribs of the same size, half-sized and same-size ribs below greater ribs, and half-size ribs between two larger nearby ribs. Their findings demonstrated that positioning the downstream ribs was an effective way to reduce pressure losses and enhance the flow structure. The thermal performance and heat transfer augmentation by different V-pattern ribs including V-shaped ribs, protruding V-shaped ribs, dimpled V-shaped ribs, and grooved V-shaped ribs were evaluated by Kumar and HoeKim [60]. Among the examined ribs, the grooved V-shaped ribs yielded the best thermal performance.

Using a square channel with either V-ribs (V-shaped ribs with a 45° apex angle, with the apex pointing in the upstream and downstream directions) or W-ribs (W-shaped ribs with a 45° apex angle, with the central apex pointing in the upstream and downstream directions), Abraham and Vedula [61] investigated the characteristics of pressure drop and heat transfer enhancement. The experiments were carried out at three relative pitch ratios (p/e = 6, 10, and 17.5). They found that compared to W-rib turbulators, V-rib turbulators offered higher heat transfer coefficients. Based on the thermal performance criteria for constant pumping power, the optimal condition was found using W-rib turbulators with a pitch ratio of 10. Han and Zhang [62] investigated the effects of broken V-ribs and continuous ribs in a square channel. They discovered that V-ribs with breaks at a 60-degree angle outperformed continuous ribs. A duct installed with 60° broken V-ribs provided up to 4.5 times more heat transfer than a channel without ribs.

Using attack angles of 0°-165°, Yongsiri *et al.* [18] studied how incorporating inclined detached ribs into a channel improved heat transfer. Attack angles of 60° and 120° on the ribs were used in the testing. They generated the highest heat transfer and thermal performance indices. Karwa [63] evaluated how V-discrete ribs to a channel's wall increased heat transfer. The V-down discrete arrangement was found to have the best thermal performance. Tanda and Abram [64] observed that the inclined ribs placed on one or both channel walls raised the transfer of heat rates. They noticed that the Nusselt number was 29% higher when inclined ribs were inserted on both sides of the channel, and the pressure loss was 3.0 times higher than in a smooth channel.

2.2.6 Summary of Rib Applications

The important characteristics of ribs that affect their performances are shape, configuration, height, and pitch. Several types of ribs (solid ribs, straight perforated, inclined perforated, detached, grooved, triangular prism, downstream convex, convex-concave, concave-concave, downstream convex, convex-concave, concave-concave, staggered, truncated, elliptical shaped transverse, triangular shaped transverse, circular, V-shaped, and multiple V-shaped ribs, as well as V-pattern ribs with dimples, V-pattern ribs with a combination of grooves, W-ribs, and V-discrete ribs) were utilized. Creation of flow separation areas has the greatest influence on the flow behavior of a rib. This recirculation/vortex flow accounts for turbulence, which promotes both heat transfer and pressure losses. More specifically, perforations on ribs and V-shaped ribs can improve thermal performance and minimize pressure losses.

2.3 Enhancing heat transfer with baffles

For heat transfer in compact heat exchangers, special baffles with appropriate sizes are needed. Baffles of several designs have been proposed.

2.3.1 Effect of transverse baffles

Heat transfer and flow structure in a channel with inline baffles were predicted numerically by Bazdid-Tehrani and Naderi-Abadi [65]. They claimed that baffles with high blockage ratios were ineffective in improving heat transfer. Oils were used as the working fluids in Mousavi and Hooman [66] investigated the influence of segmented baffles on the top and bottom channel walls to improve heat transfer rate. Chang *et al.* [67] examined at how oblique baffles affected thermal performance. Their results suggested that the baffles significantly improved the rates of heat transfer and pressure loss over those determined by the Dittus-Boelter and Blasius correlations. Additionally, the maximum thermal performance reached 3.4. Al_2O_3/water nanofluid heat transfer behaviors in a channel with baffles were investigated in experiments by Mashaei *et al.* [68]. Nanofluid flow reduced length of the recirculation regions over that of base fluid (water) flow.

2.3.2 Effect of inclined baffles

Promvonge *et al.* [69, 70] evaluated the effect of installing 45° angled baffles in a duct on its heat transfer. They noticed that pressure drop and heat transfer rose as baffle height increased. The baffle having 45° angle offered the greatest thermal performance. Kwankaomeng and Promvonge [71] examined the thermal characteristics of a channel with inclined baffles. They discovered that the vortex flow produced by a baffle introduced impinging flows, which greatly boosted heat transfer throughout the channel. The greatest Nusselt number ratio and thermal performance were identified to be 7.9 and 3.1, respectively. Promvonge *et al.* [72] analyzed thermal behavior and fluid flow in a channel with inclined baffles on the top and bottom walls. The numerical results revealed that the inter-baffle cavity walls substantially boosted thermal performance.

2.3.3 Effect of perforated baffles

Perforated baffles can create jets impinging on exchanger surfaces to improve heat transfer. Additionally, the presence of holes also helps in reducing pressure losses. This results in better thermal performance. The report by Dutta *et al.* [73], shows that installing perforated baffles improves heat transfer by up to 5 times compared to that of a bare channel. Moreover, the jets introduced by perforated ribs gave superior transfer to that given by the common secondary flow provided by non-perforated ribs [74]. Sahel *et al.* [75] measured the thermal performance of a channel with fitted perforated baffles. They revealed that perforated baffles with pore axis ratios of 0.19 produced approximately 65% greater heat transfer than traditional baffles. El Habet *et al.* [76] examined the impact of baffle perforation ratios and tilt angles (as seen in Fig. 2.33) on heat transfer rate and thermal performance. The highest thermal performance was achieved at a tilt angle of 60º and a perforation ratio of 10%.

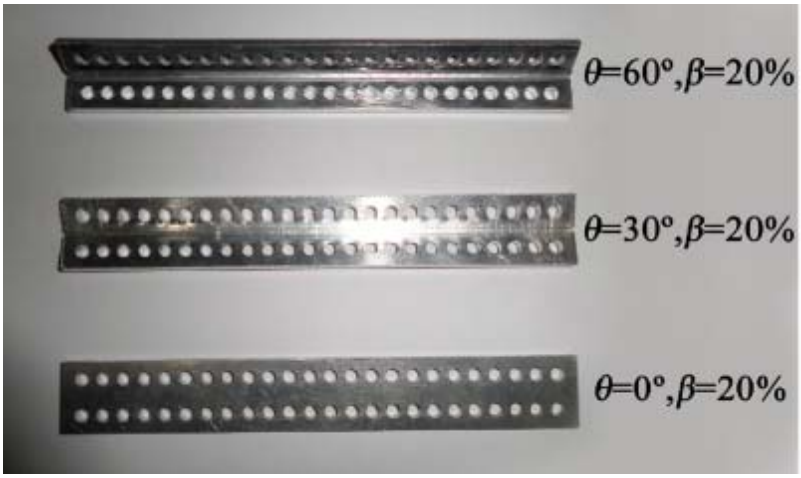

Figure 2.33. Transverse and V-shaped ribs [76].

Alam *et al.* [77], reported that perforated V-shaped baffles (Figs. 2.34-2.36) could boost heat transfer and thermal enhancement while decreasing pressure losses as compared to a conventional V-shaped baffle. Chamoli [78] and Chamoli and Thakur [79, 80] investigated numerically the geometry of V-down shaped perforated baffles in order to obtain minimal pressure losses and maximum heat transfer. Evidently, the maximum Nusselt number and pressure losses were obtained at a 12% open area. Promvonge and Skullong [81] studied the thermal performance of a duct with V-shaped flapped baffles with a chamfered groove, depicted in Fig. 2.37. According to their findings, baffles with a tilt angle of 90° had the lowest heat transfer because they produced the least powerful counter-rotating vortices among those of four flap angles (30°, 45°, 60°, and 90°) placed in the central area of the baffle.

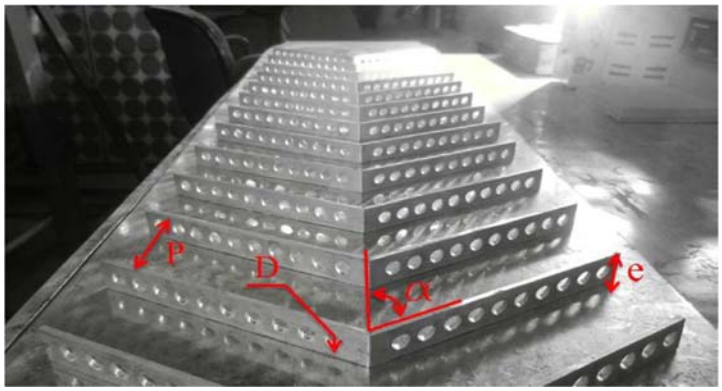

Figure 2.34. Perforated V-shaped baffles [77].

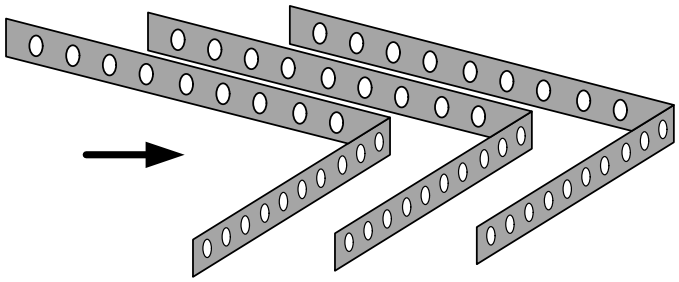

Figure 2.35. V-down shaped perforated baffles [78].

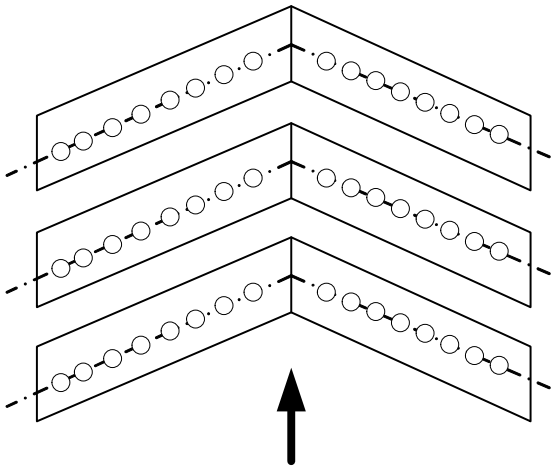

Fig. 2.36. V-down shaped perforated baffles [79].

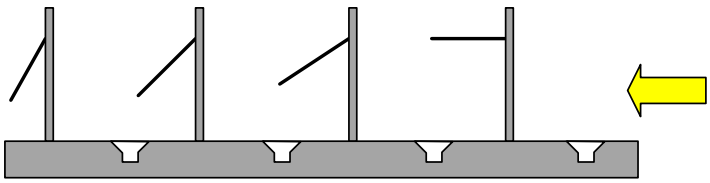

Figure 2.37. V-shaped flapped baffles combined with chamfered groove [81].

2.3.4 Effect of V-shaped baffles

Generally, V-shaped ribs induce axial vortices which cause collision of low temperature fluid with both the upper and lower walls, and subsequently improve fluid mixing and heat transfer. The results by Eiamsa-ard *et al.* [82] revealed that each pair of thin V-shaped ribs induces four longitudinal vortices. Two were induced by the top rib and the other two by the bottom one. The vortices assisted in the transfer of heat from a heated surface to the fluid (Fig. 2.38). In addition, the V-shaped ribs with an angle of attack of 45° are more effective at enhancing heat transfer than those with attack of 60°, as indicated by a thinner high temperature layer (red layer).

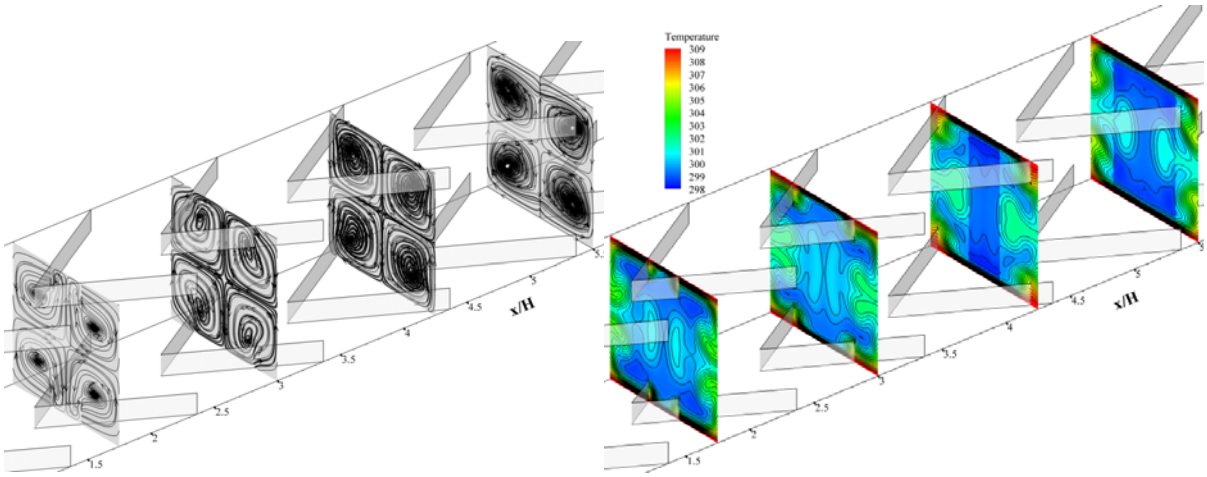

(a) α = 45° at Re = 1,000 and BR = 0.15

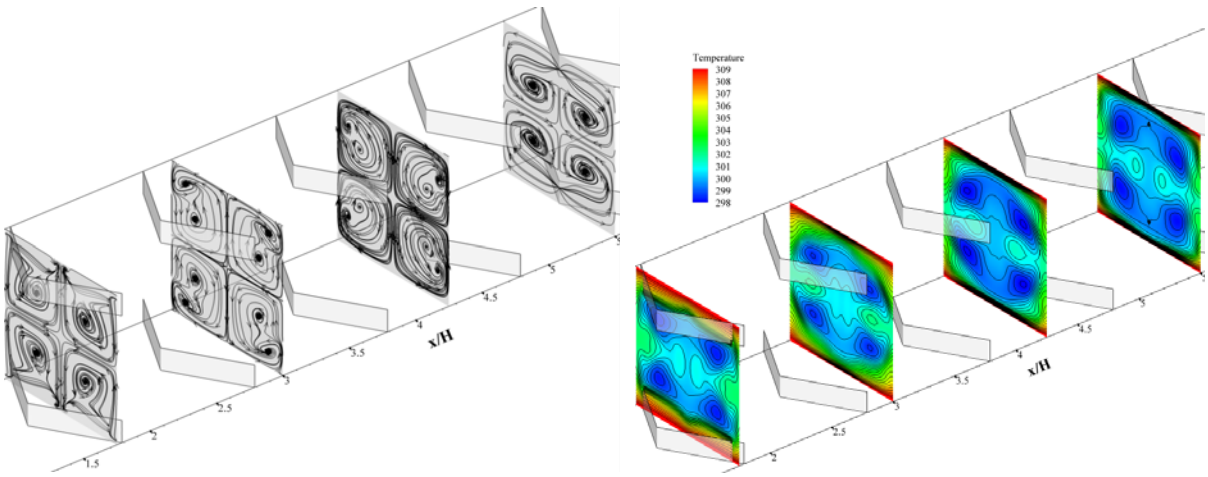

(b) α = 60° at Re = 1,000 and BR = 0.15

Figure 2.38. Axial vortex flows on the vertical planes and temperature distributions on the vertical planes in a square channel equipped with thin V-shaped ribs [82].

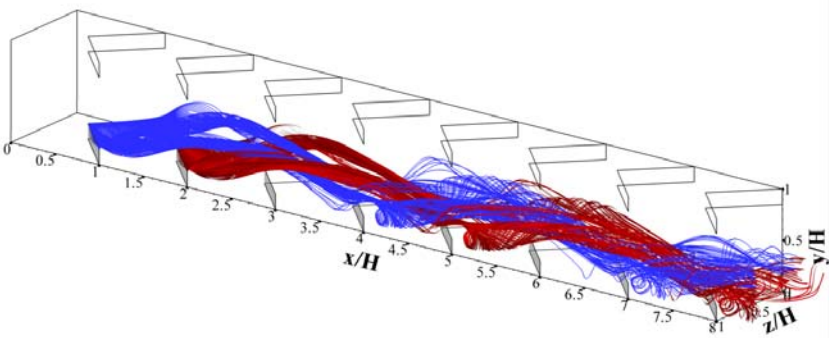

(a) α = 45°

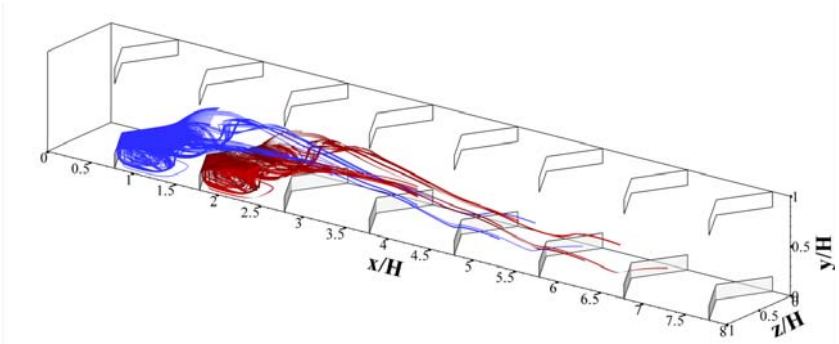

(b) α = 60°

Figure 2.39. Discharge current line from V-shaped ribs at *Re* = 1000 and *BR* = 0.15 [82].

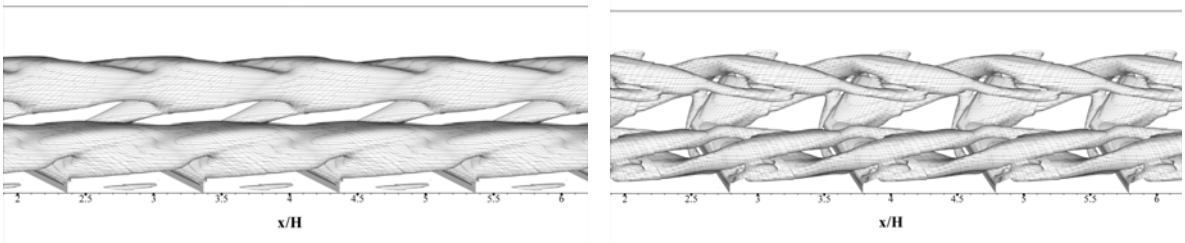

(a) α = 45° (b) α = 60°

Figure 2.40. The 3D surface flow (iso-surface) introduced by V-shaped ribs at *Re* = 1000 and *BR* = 0.15 [82].

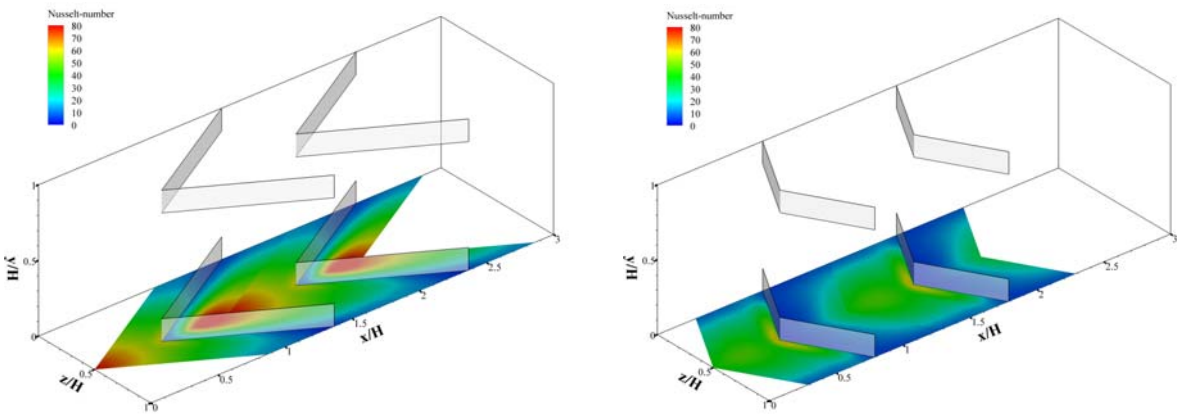

(a) α = 45° (b) α = 60°

Figure 2.41. Nusselt number contours yielded by V-shaped ribs at *Re* = 1000 and *BR* = 0.15 [82].

Figure 2.39 shows that V-shaped ribs with $\alpha = 45^o$ introduced reattachment flow that cover a larger area than those having $\alpha = 60^o$. The ribs at $\alpha = 45^o$ cause reattached flow from the whole bodies of the ribs while the ones with $\alpha = 60^o$ cause reattahment only around the rib center. The 3D iso-surface flow patterns in Fig. 2.40 supports the observation that the V-shaped ribs with $\alpha = 45^o$ introduce vortices with higher strength (observed from the larger ring diameter) than the ones with $\alpha = 60^o$. Figure 2.41 confirms that V-shaped ribs with $\alpha = 45^o$ provide a high Nusselt number area closer the the rib rear with higher intensity than the ones with $\alpha = 60^o$.Multiple V-shaped ribs, including the V/W-shaped rib, the multi V-shaped rib, the arch-shaped rib, the broken V-shaped rib, the broken multi V-shaped rib, and double V baffles, are illustrated in Figs. 2.42 to 2.59. In accordance to research by Abraham and Vedula [61], Thakur *et al.* [83], Li *et al.* [84], and Jiang *et al.* [85], angled ribs (V- and W-shaped ribs) were able to generate counter-rotating flows and provide better heat transfer than transverse ribs (Fig. 2.42). A study by Thakur *et al.* [83] and Li *et al.* [84], V- and W-shaped ribs give a greater rate of heat transfer than inclined ribs (Figs. 2.43-2.45). Tanda and Satta [86] mentioned that angled ribs generate a vortex flow that helped in reducing wall temperature and improving heat transfer. Jin *et al.* [87, 88] and Li *et al.* [89] revealed that the arrangement of multiple V-shaped ribs (Figs. 2.46-2.47) on one wall of a solar air radiator generated a pair of counter-rotating vortices. The V-shaped ribs (Fig. 2.45) placed on the upper and lower walls produced four counter-rotating vortices, as reported by Fawaz *et al.* [90] and Bahiraei *et al.* [37]. This flow disrupted a thermal boundary layer and increased heat transfer on the impinged surface. In the work of Ebrahim Momin *et al.* [39], V-shaped ribs with a larger rib height caused higher pressure losses and heat transfer. Dong *et al.* [91] used solar air heaters with inclined groove rolling surfaces. They noted that the number of counter-rotating flows on the transverse plane and heat transfer tended to increase with an incresing number of rolling surfaces (*N*). Singh *et al.* [92] discovered that raising the number of arc-shaped ribs increased the heat transfer rate and friction factor by as much as 5.07 and 3.71 times, respectively, compared to a plain channel. Angled baffles and ribs have been altered in a variety of ways, including adding discrete/broken perforations. This was done to improve the thermal performance factor. Discrete V-down ribs offer lower pressure losses and greater heat transfer than the continuous V-down ribs, according to Singh *et al.* [93, 94], who investigated the effects of discrete baffles/ribs. According to Kumar *et al.* [95], disruption of the boundary layer by air passing through a gap increased heat transfer behind the rib. Furthermore, it was claimed that powerful secondary stream jets were produced by broken multiple V-type baffles (in the form of counter-rotating vortices). Maithani and Saini [96] also mentioned that broken V-type baffles with smaller gaps provided the greater heat transfer rates. Kumar *et al.* [97] analyzed the thermal performance of the channel using multiple broken V-shaped baffles. According to their findings, the baffles having a relative baffle width of 5.0 offered superior thermal performance overall to others ribs. In addition, the results suggested that the thermal performance of the broken multiple V-type baffles was more beneficial than that of the other baffles.

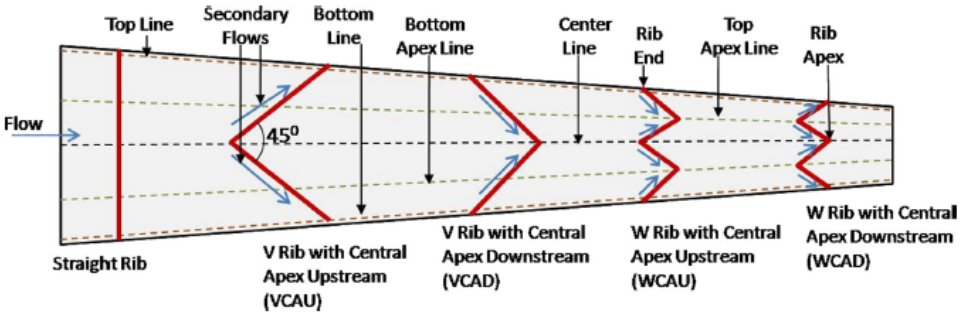

Figure 2.42. V- and W-shaped ribs [61].

Figure 2.43. V-shaped ribs [83].

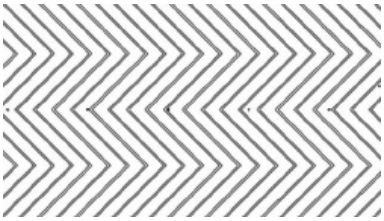

Figure 2.44. W-shaped ribs [84].

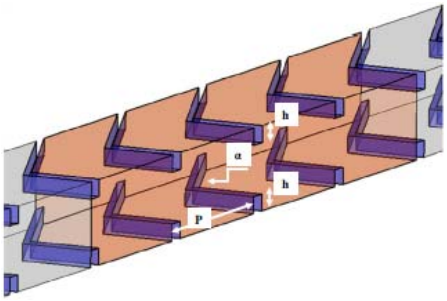

Figure 2.45. Multi V-shaped ribs [90].

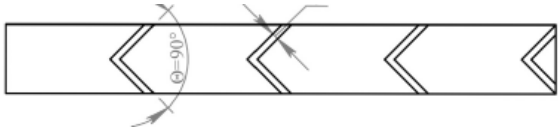

Figure 2.46. V-shaped ribs [37]

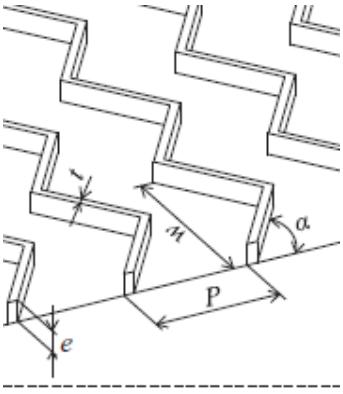

Figure 2.47. Multi V-shaped ribs [88].

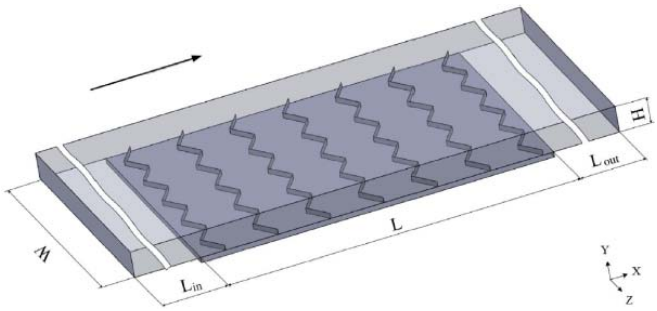

Figure 2.48. Multi V-shaped ribs [89].

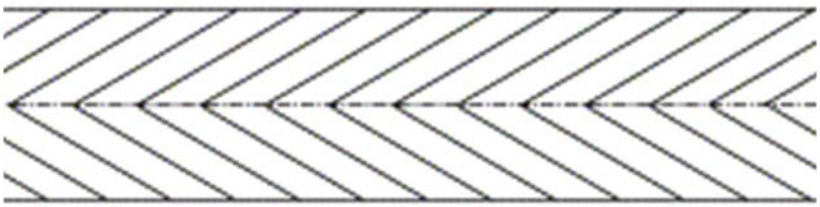

Figure 2.49. V-shaped ribs with the greater rib height [39].

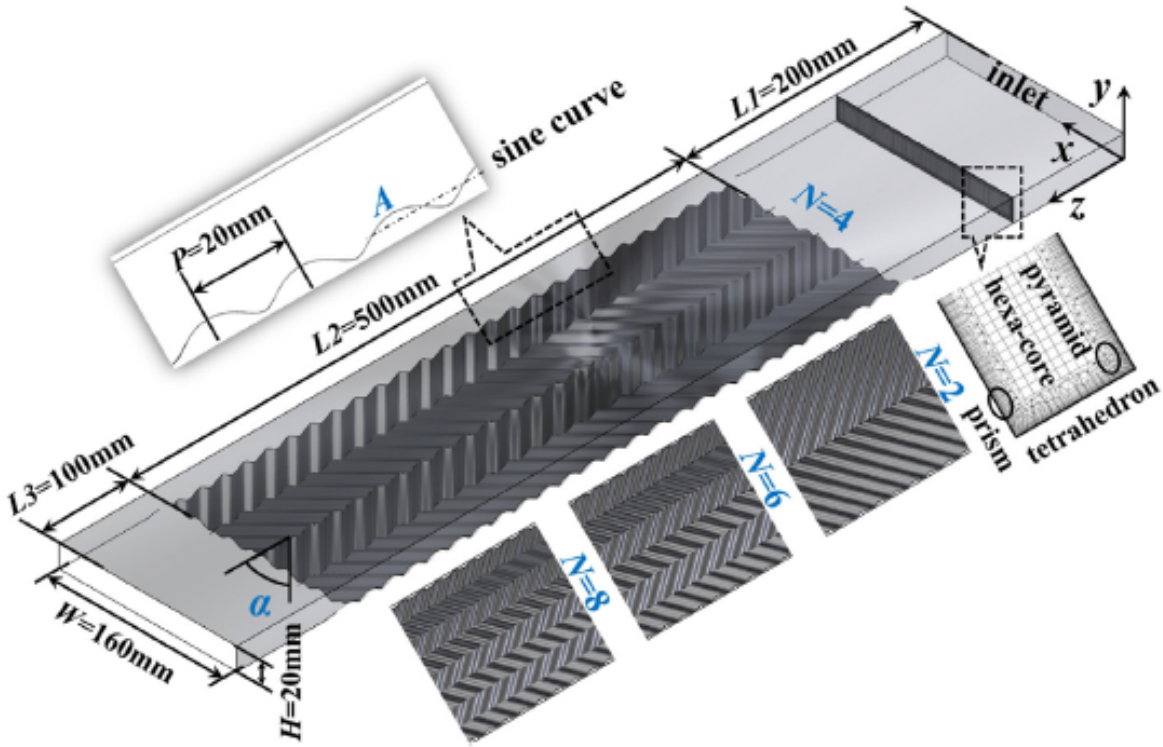

Figure 2.50. Inclined groove ripple surfaces [91].

Figure 2.51. Arc-shaped ribs [92].

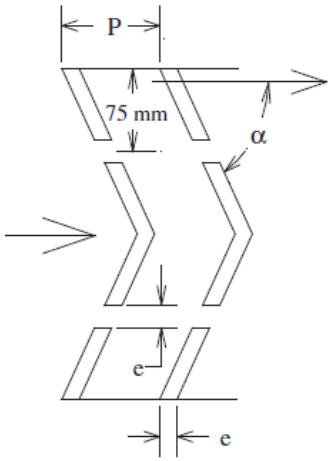

Figure 2.52. Continuous V-down ribs [93].

Figure 2.53. Broken V-type baffles [96].

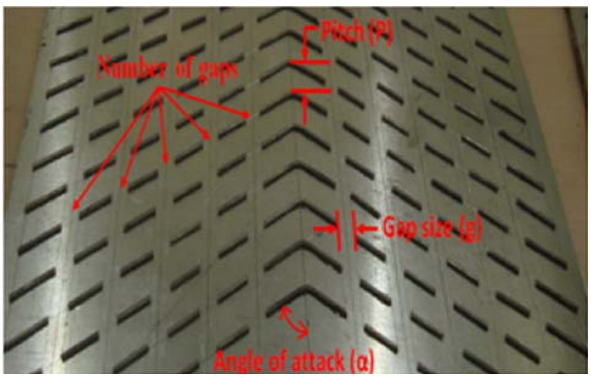

Figure 2.54. Broken multiple V-type baffles [97].

Jedsadaratanachai and Boonloi [98] examined heat transfer of the channels with 30° double V-baffles and different blockage ratios (0.05-0.25) and pitch ratios (1.0-2.0) (Fig. 2.55). It was found that increasing the blockage ratio while reducing the pitch ratio led to the rises of pressure losses and heat transfer. The greatest thermal performance, 3.2, was found at blockage and pitch ratios of 0.1 and 1.0. Jedsadaratanachai and Boonloi [99] examined the heat transfer, pressure losses, and thermal performance of a duct with hybrid discrete baffles or V-baffle/orifice (Fig. 2.56), in the turbulent flow regime. At a blockage ratio of 0.1, the baffles boosted the heat transfer rate and thermal performance up to 6.0 and 1.7 times, respectively. A variety of V-type baffles with 60° splits and various width ratios (Fig. 2.57) were presented by Kumar *et al.* [97]. According to their research, broken multiple V-type baffles surpassed other baffles in terms of thermal performance. Kumar *et al.* [100] utilized discretized broken V-pattern baffles with attack angles of 30°-70°, blockage ratios of 0.25-0.8, pitch ratios of 0.5-2.5, and baffle gap width ratios of 0.5-1.5 to improve heat transfer. The discretized broken V-pattern baffle gave better than other baffles in terms of thermal performance. The heat transfer behaviors of a channel with discretized broken V-pattern baffles with different baffle gap ratios (0.26 to 0.83) and baffle gap width ratios were also tested by Kumar *et al.* [101]. The baffles yielded the greatest thermal performance as high as 3.14. Fawaz *et al.* [90] numerically investigated flow topology and heat transfer mechanisms in a duct with V-baffles inserted at a 45° attack angle with varying blockage (0.2-0.6) and pitch ratios (0.5-1.5). They predicted that the four counter-rotating vortices produced by the V-baffle would result in chaotic mixing between the wall and core flow areas.

Promvonge and Skullong [102] proposed straight tapes with double-sided V-baffles installed with various blockage and pitch ratios for enhancing heat transfer. In their experiments, the tapes were arranged in two different configurations, with the V-apex pointing upstream and downstream. The ones with the V-apex pointing upstream underperformed the ones with the V-apex pointing downstream by about 1.4%. The greatest thermal performance factor, 2.07, was attained at a blockage ratio of 0.15 and a pitch ratio of 1.0. Promvonge and Skullong modified V-shaped baffles with the blockage and pitch ratios varied between 0.1-0.2 and 0.5-2.0 while the attack angle of the baffles remained constant at 30°. [103]. Manifestly, the V-shaped baffles with a blockage ratio of 0.15 and a pitch ratio of 0.1 yielded the maximum thermal performance factors of 2.34. Promvonge and Skullong [81] examined the thermal performance of a channel with a coupled V-shaped flapped baffle and chamfered groove. The study encompassed four different flap angles installed on the central region of the baffle (30°, 45°, 60°, and 90°), baffle pitch ratios of 1.0-2.0, and groove pitch ratios of 1.0-2.0. The optimal baffle geometric parameters were a 1.5 pitch ratio and a 45° flap angle placed in the baffle center region. The baffles provided the thermal performance factor as high as 2.68.

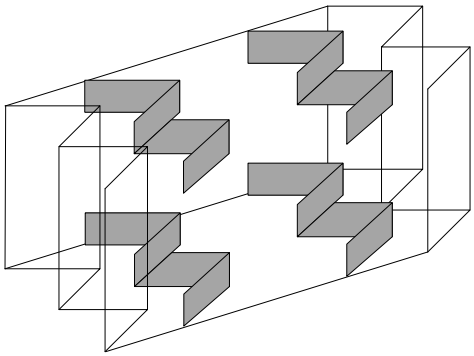

Figure 2.55. 30° double V-baffles [98].

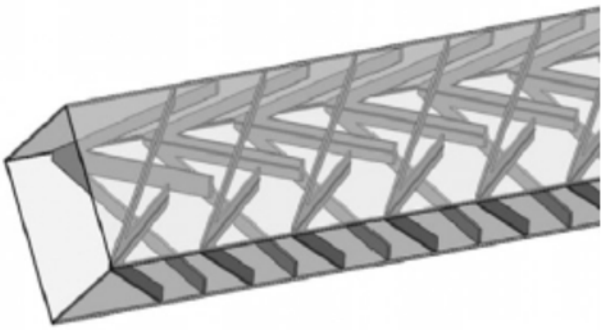

Figure 2.56. Discrete Combined V-baffle and V-orifice [99].

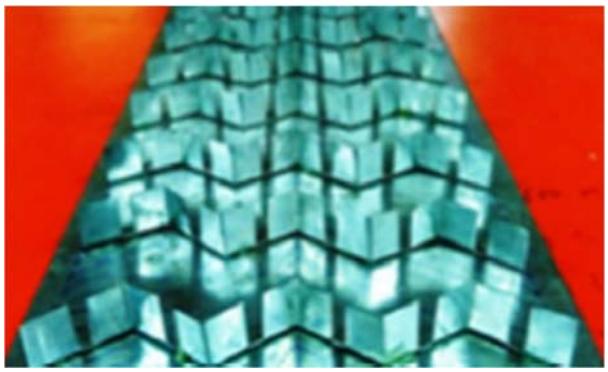

Figure 2.57. Broken Multiple V-type baffle [97].

2.3.5 Effect of broken V-shaped baffles

Segregated V-shaped baffles can generate secondary vortex flows as well as longitudinal vortex flows. The results by Promvonge *et al.* [36] showed velocity, temperature and pressure fields as well as Nusselt number contours associated with the use of segregated V-shaped baffles (Fig. 2.57). Clearly, counter longitudinal eddy currents appeared at the lower wall near each V-shaped rib. Low pressure at the rib rear induced fluid movement from the main flow down to the hot wall. Then, the fluid moved upward with transferred heat. The process was continuously repeated at each rib. Since baffles have smaller pitch ratios (*PR*) than square ribs, they therefore show different heat transfer behaviors, as depicted in Fig. 2.59. This figure suggests that the density and intensity of eddy currents and Nusselt numbers for baffles, were greater than square ribs, owing to their smaller pitch ratio. Consequently, heat transfer with baffles was superior to that of the square baffles, especially around the middle of the channel and

in front of the ribs. However, heat transfer along the lateral region by the baffles was slightly lower than that of square baffles. Kumar *et al*. [101] evaluated the heat transfer rates in a channel with discretized broken V baffles installed. Thermal performance indices reached 3.14 with up to 4.47 times greater heat transfer over that of a smooth channel. The thermal performance of a solar air heater with multiple broken V-shaped baffles installed was compared to those of a channel with conventional baffles by Kumar *et al.* [97]. According to their findings, broken multiple V-shaped baffles outperformed conventional baffles in terms of thermal performance.

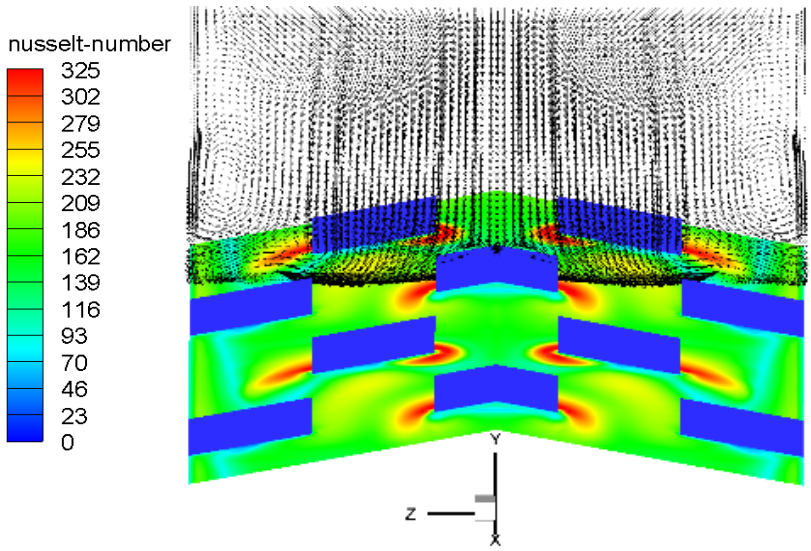

(a) Fluid velocity field and surface Nusselt number contour

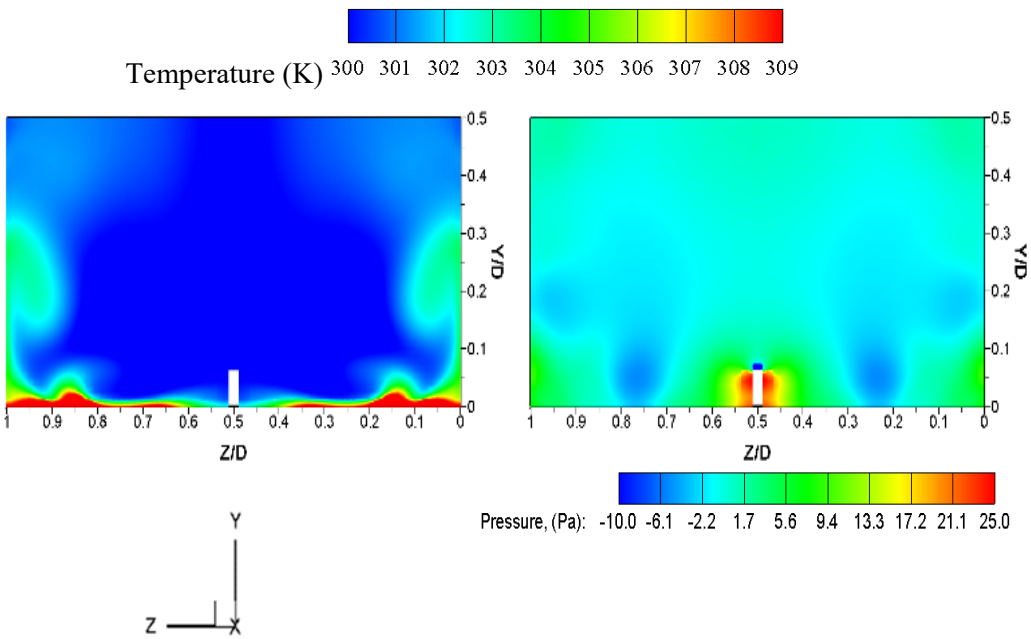

(b) Temperature and pressure fields

Figure 2.58. Velocity field, surface Nusselt number contour, temperature and pressure fields in the channel with segregated V-shaped baffle at BR = 0.0625, PR = 0.625 and Re = 15,000 [36].

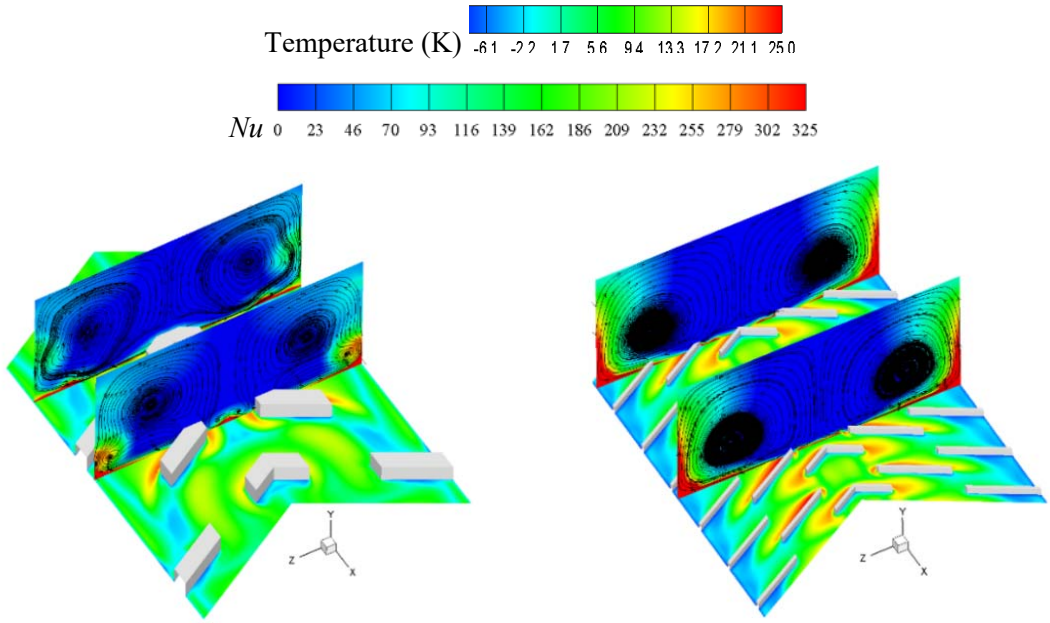

(a) Square rib PR = 0.6250, BR = 0.0625 (b) PR = 0.1875, BR = 0.0250

Figure 2.59. Perpendicular flow lines in each cross-section and contour of the Nusselt numbers on the surface at *Re* = 15,000 and α = 60° [36].

2.3.6 Effect of twisted baffles

Two types of twisted ribs [104] have been proposed for application in a ribbed channel. They are typical twisted ribs and an alternating axis twisted ribs, as depicted in Fig. 2.60. Flow patterns and Nusselt number contours associated with the application of typical thin and common/alternating axis twisted baffles are displayed in Figs. 2.61 and 2.62, respectively. The fluid flow across a typical baffle shows common reattachment, while that across the common/alternating axis twisted baffles (Fig. 2.62) is slightly diffracted, leading to spiral flow prior to reattachment. Subsequently, the Nusselt number on the wall surface varies. However, the mean Nusselt numbers in all cases are comparable. Among all ribs, a typical baffle generates the highest friction losses. The twisted baffles and alternating axis twisted baffles facilitate fluid flow in a spiral pattern which potentially promotes thermal performance. Eiamsa-ard [105] investigated how multiple twisted tapes improved heat transfer in a duct. The influences of free-spacing ratios and tape twist ratios were determined. According to experimental findings, multiple twisted tapes could improve transfer heat up to 167% compared to that of a smooth channel. As free-spacing ratio and tape twist ratio decreased, heat transfer and pressure losses increased. The thermal performance of a solar air heater equipped with twisted ribs was investigated by Kumar and Layek [106-107]. The effects of pitch ratio (*p/e*), rib inclination angle (30°-90°), and twist ratio (*y/e* = 3.0-7.0) were examined. When twisted rib turbulators (Fig. 2.63) were utilized, heat transfer and pressure drop increased up to 2.58 and 1.78 times, respectively, compared to a plain channel. Rashidi *et al*. [108] explored the thermal performance of a square duct attached with transverse twisted baffles. The baffle with a pitch intensity of 540° caused the lowest pressure losses,

whereas the baffle with a pitch intensity of 360° gave the maximum heat transfer. Thermal enhancement was studied by Eiamsa-ard and Chuwattanakul [17] in a channel with inclined twisted baffles having different pitch ratios and baffle twist ratios (Fig. 2.64). The highest thermal performance factors, up to 1.98, were provided by inclined twisted baffles (p/w = 6.0 and y/w = 5.0). The thermal performance factor produced by the channel containing the baffles reached 1.98. The thermal performance of a micro/mini-channel heat sink with twisted ribs installed was studied by Zhang *et al.* [109]. Their results demonstrated that twisted or inclined ribs in mini-channels simultaneously promoted both flow resistance and heat transfer. Thermal efficiency was enhanced by increasing twist angle and decreasing height of the twisted ribs. The micro/mini-channel heat sink with twisted ribs had an overall maximum thermal performance factor of 1.34. According to Sawhney *et al.* [110], heat transfer from wavy delta winglets (Fig. 2.65) was about 223% higher than that of a smooth channel.

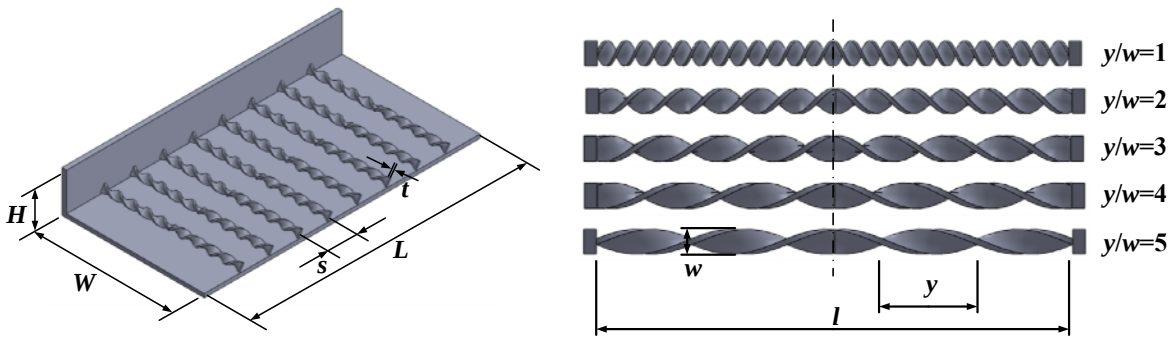

Figure 2.60. Twisted baffles [104].

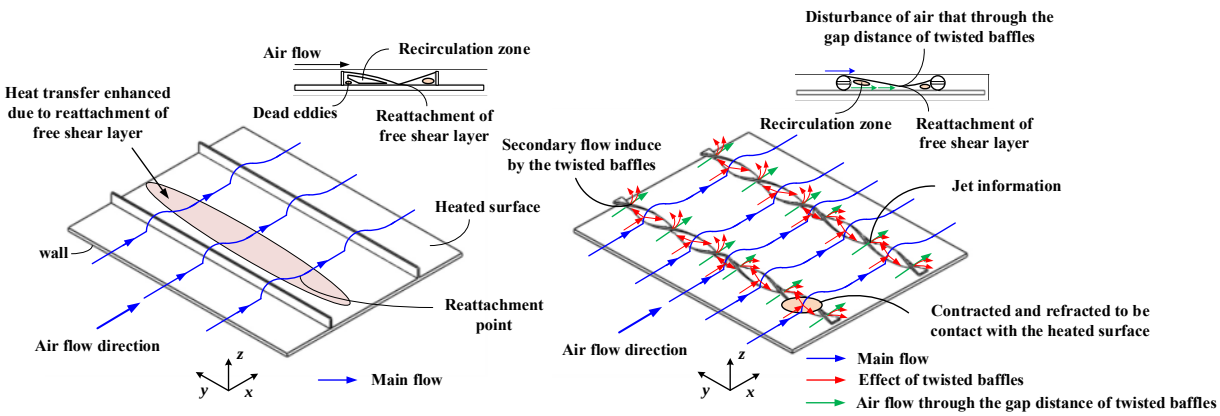

(a) Transverse baffles (b) Alternate axis twisted baffles

Figure 2.61. Flow patterns through transverse baffles and alternate axis twisted baffles [104].

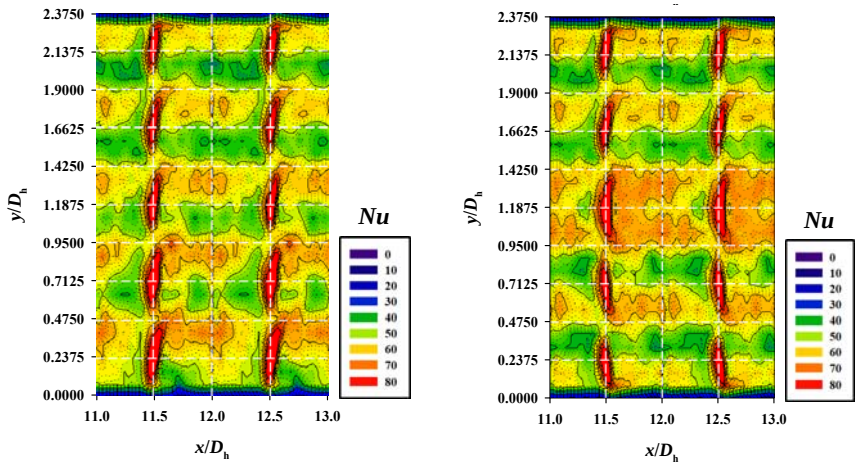

(a) Transverse baffles (b) Alternate axis twisted baffles

Figure 2.62. Nusselt number distributions in the channels installed with a typical baffle, common twisted rib and alternating axis twisted ribs at a Reynolds number of 9 ,0 0 0 [104].

Figure 2.63. Twisted ribs [106-107].

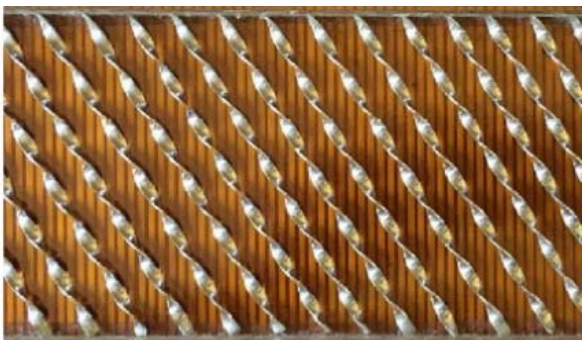

Figure 2.64. Inclined twisted-baffles [17].

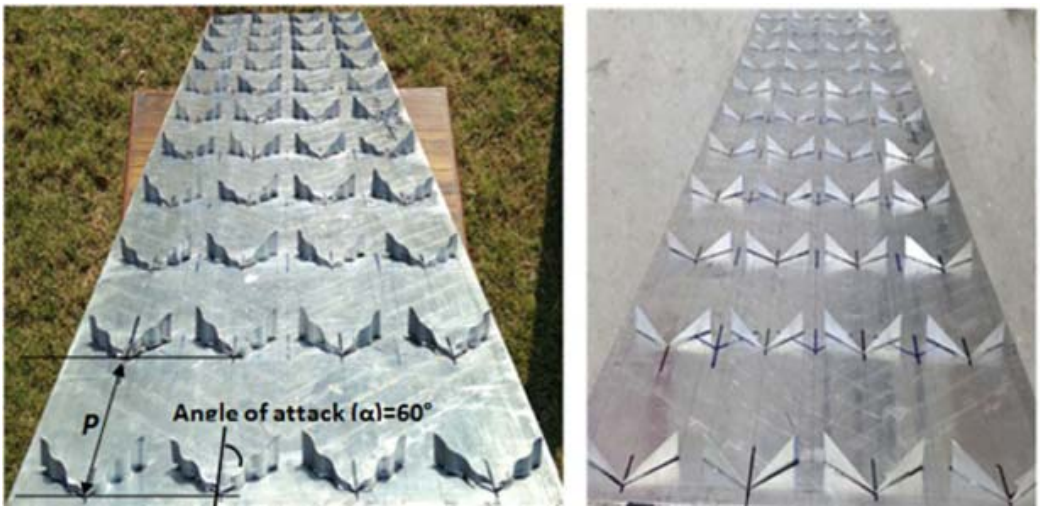

Figure 2.65. Wavy delta winglets Sawhney *et al*. [110].

2.3.7 Effect of arc-shaped wires/ribs/ baffle

Sahu and Prasad [111] investigated the thermal performance of a channel with a fitted roughened arc-shaped wire (Fig. 2.66). It was discovered that a pitch ratio of 10, blockage ratio of 0.0422, and relative

attack angle of 0.3333 produced the greatest flow reattachment and separation regions. In comparison to a conventional channel, the thermal efficiency increased by up to 56%. Hans *et al.* [112] examined a solar heater fitted with broken arc-ribs (Fig. 2.67). Heat transfer rates and pressure drop associated with the use of the ribs reached that were 1.19 and 1.14 times of a plain channel, respectively. Secondary flow brought on by broken arcs was the most important factor. Saravanakumar *et al.* [113] used analytical modeling to investigate the effects on the thermal performance of a channel with arc-shaped ribs installed. They discovered that arc-shaped ribs (Fig. 2.68) installed at width of the baffle and length of the baffle of 0.015 m and 0.2 m performed the greatest enhancement in thermal performance, to 82%, an increase of 28%. The influences of arc-shaped baffles (Fig. 2.69) on thermal performance were investigated by Promvonge *et al.* [114]. They revealed that the heat transfer at an attack angle of 90° was greater than those at 20°, 40°, 60°, and 80° by 5.8%, 3.9%, 2.3%, and 2.5%, respectively. The highest thermal performance factor of 1.43 was found by using the arc-shaped baffles with an angle of 90° and a pitch ratio of 8.0. Sureandhar *et al.* [115] evaluated the thermal performance, effectiveness of a channel fitted with arc-ribbed wire. As the volumetric airflow grew, the overall loss coefficient was reduced while the efficiency rose.

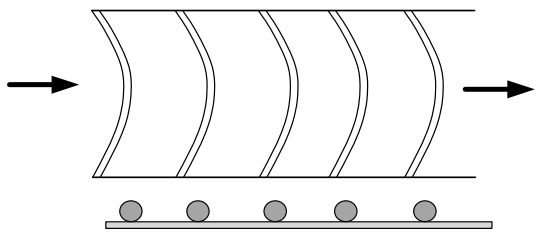

Figure 2.66. Arc shape wire roughness [111].

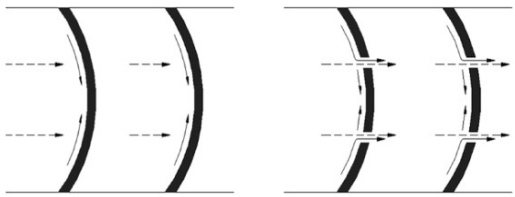

Figure 2.67. Broken arc rib [112].

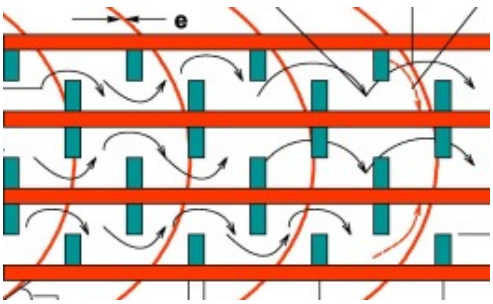

Figure 2.68. Arc shaped rib [113].

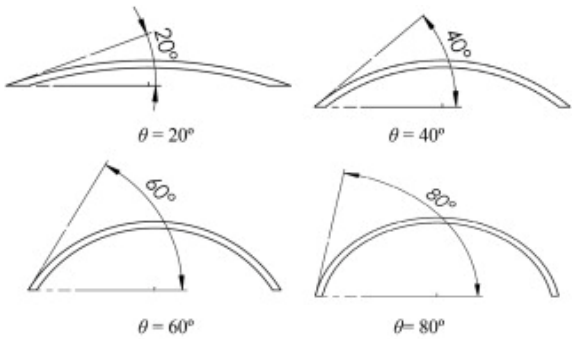

Figure 2.69. Arc-shaped baffle [114].

2.3.8 Summary of Baffle Applications

Baffles are promising in improving the thermal performance of heat exchangers and solar air heaters. Numerous researchers have investigated the effect of baffles on heat transfer rate and pressure loss

characteristics in air ducts. Perforations in baffles, V-shaped baffles, and twisted baffles have the potential to enhance thermal performance and reduce pressure losses, as discussed in the preceding sections.

2.4 Combined enhancement device

Recently, combined enhancement devices with roughened surfaces were used as vortex generators in a solar air heater duct. In a channel, Promvonge *et al.* [116] examined the influences of ribs and winglet-type on heat transfer and pressure loss characteristics. To create longitudinal vortex flows in the test duct, two sets of winglet-type devices with different attack angles were mounted at the channel's inlet, isosceles triangular-shaped ribs were installed inside duct walls to create a reverse flow. Their results demonstrated that combined enhancement devices, ribs and winglet-type, produced increased heat transfer over that of individual enhancement devices (rib). Furthermore, it was found that WVGs with higher attack angles were better at transferring heat. Promvonge *et al.* [117] additionally examined the influence of delta-winglets (DWs) on improving heat transfer in a solar air heater. Experimental results indicated that the DW pointed up (PU-DW) is more effective in transferring heat than a DW pointed down (PD-DW). The DW with the smallest attack angle and pointing down provided the greatest thermal performance.

As novel liquids, nanofluids are finding new applications in heat exchangers [118-120]. Nanoparticles are particles with sizes less than 100 nanometers (nm). Poor thermal conductivity of a basic fluid necessitates the utilize of nanoparticles to improve heat transfer efficiency. The concept is to enhance the heat transfer capacity of a material by increasing its thermal conductivity. This is made by including solid particles with higher heat conductivity than the original fluid. Compared to the thermal conductivity of the base fluid, a metal-specific solid is significantly better. Nonetheless, advancements in nanofluids technology are still required. The limitations of current technology mean that the nanofluids and nanoparticles used in their synthesis are expensive, and that only a small amount can be produced at a time. Additionally, most nanofluids become unstable after prolonged use, a problem that is addressed by adding other chemicals to the working fluid.

2.5 Observation

This literature review shows that numerous works have been performed to investigate the influence of artificial roughness of geometries shapes and conditions on flow structure, heat transfer rate and pressure loss characteristics. The important issues can be summarized as follows.

- The thermal performance of solar air heaters is often worse that of solar water heaters due to the absorber plate's naturally poorer heat transfer capabilities with the air passing through a duct. Heat transfer coefficient improvements are needed to make commercialization of solar air heaters possible. Improving the air-to-absorber plate convective heat transfer coefficient (h)

may be made by two major techniques. The first technique involves increasing the area of heat transfer by employing corrugated surfaces or enlarged surfaces known as fins. The second way is boosting convective heat transfer by generating surface disturbances. That can be implemented using ribs/baffles on the bottom of the absorber surface.

- Modified ribs/baffles have been invented to improve the coefficient of convective heat transfer. Well-designed ribs/baffles efficiently augment heat transfer while keeping pressure loss as low as possible to maximize the thermal performance factor. A thermal performance factor above unity indicates that an enhanced system is promising for energy saving.
- According to a review of baffles, perforations are an excellent way to minimizing pressure loss without significantly reducing the heat transfer rate. Perforated baffles offer higher thermal performance compared to solid baffles.
- Development of ribs and baffles focuses on varying their shape, geometry and arrangement. Flows through the ribs and baffles are extremely complex. Numerical investigation allows a deeper understanding of flow and heat transfer mechanisms associated with enhanced systems. The advantages of numerical methods are that they allow researchers to examine issues that cannot be practically studied by experimentation especially with two or more variables are related. Understanding flow and thermal behaviors is essential for the continued development of ribs and baffles for heat transfer augmentation.

2.6 Nomenclature

A	surface area, m^2
AR	aspect ratio of channel
BR	ratio of rib height to channel height
B_R	blockage ratio
C_p	specific heat at constant pressure, J kg^{-1} K^{-1}
CR	clearance ratio
d	inside or empty tube diameter, m
D	diameter, m
e	rib height/roughness element height, m
f	friction factor
f_s	friction factor in smooth channels/pipes
g	gap width, m
h	heat transfer coefficient, W m^{-2} K^{-1}
h_s	convection coefficient in smooth channels/pipes, W m^{-2} K^{-1}
H	height of duct/channel height, m
k	fluid thermal conductivity, W m^{-1} K^{-1}
L	axial tube length, m

$\dot{m}$	mass flow rate, kg s^{-1}
N	number of tubes in a shell-and-tube exchanger /number of rippled surfaces
Nu	Nusselt number
Nu_s	Nusselt number in smooth channels/pipes
p	pitch length/distance between ribs, m
P	pumping power, W
Pr	Prandtl number
P_R	pitch ratio
ΔP	pressure drop, Pa
Q	heat load or heat rate/quantify the additional heat load, W
Q_{st}	heat transfer rate for a plain or unaugmented tube, W
Q_{tt}	heat transfer rate for a plain tube with an insert, W
Re	Reynolds number
T	temperature, K
T_i	approach temperature difference, K
ΔT_m	true-mean temperature difference in a heat exchanger, K
TPF	thermal performance factor
U	overall heat transfer coefficient in a heat exchanger, W m^{-2} K^{-1}
V	velocity of air in the duct, m s^{-1}
w	width of twisted-baffle/rib width, m
W	width of duct, m
y	twist length (axial length of cycle, 180°), m

Greek Symbols

α	angle of flow attack/angle of attack, °
ε	heat exchanger thermal effectiveness
ρ	fluid density, kg m^{-3}
μ	fluid dynamic viscosity, kg s^{-1} m^{-1}
θ	rib inclination angle/arc-shaped baffle, °
δ	twisted tape thickness, m

Subscripts

b	bulk fluid temperature
h	hydraulic
i	inlet
o	outlet

pp pumping power

s smooth tube or channel

w wall

Abbreviations

DW delta-winglet

PEC performance evaluation criteria

PR rib spacing ratio

PU-DW pointing upstream delta-winglet

TLC thermochromic liquid crystal

WVG ribs and winglet-type vortex generator

References in chapter 2

1 Han JC, Chandra PR, Lau SC. Local heat/mass transfer distributions around sharp 180 deg turns in two-pass smooth and rib-roughened channels. Journal of Heat Transfer - Transactions of ASME. 1988;110:91-98.

2 Nikuradse J. Laws of flow in rough pipes. NACA. Technical Memorandum 1292. Nov 1950.

3 Varun, Saini RP, Singal SK. A review on roughness geometry used in solar air heaters. Solar Energy. 2007;81:1340-1350.

4 Webb RL, Haman LL, Hui TS. Enhanced channels in electric utility stream condensers. Heat transfer in Heat Rejection Systems - ASME Symposium. 1984;37:17-26.

5 Bergles AE. Techniques to enhance heat transfer. In: Rohsenow WM, Hartnett JP, Cho YI, editors. Handbook of Heat Transfer. 3rd ed. New York: McGraw-Hill; 1998. Ch. 11.

6 Manglik RM. Heat transfer enhancement. In: Bejan A, Kraus AD, editors. Heat Transfer Handbook. New Jersey: Wiley; 2003. Ch. 14.

7 Webb RL, Kim NK. Principles of Enhanced Heat Transfer. Florida: Taylor & Francis; 2005.

8 Bergles AE, Blumenkrantz AR, Tabore, J. Performance evaluation criteria for enhanced heat transfer surfaces. Heat Transfer-The Japan Society of Mechanical Engineers. 1974;2:234-238.

9 Webb RL, Bergles AE. Performance evaluation criteria for selection of heat transfer surface geometries used in low Reynolds number heat exchangers. In: Kakaç S, Shah RK, Bergles AE, editors. Low Reynolds number flow heat exchangers. Washington DC: Hemisphere; 1983. p. 735-752.

10 Wang L, Sundén B. Performance comparison of some tube inserts. International Communications in Heat and Mass Transfer. 2002;29:45-56.

11 Webb RL, Kim NH. Principle of Enhanced Heat Transfer. New York: Taylor & Francis; 1994.

12 Zhang G, Sundén B, Xie G. Combined experimental and numerical investigations on heat transfer augmentation in truncated ribbed channels designed by adopting fractal theory. International Communications in Heat and Mass Transfer. 2021;121:105080.

13 Ke Z, Zhang Y. Heat transfer enhancement in a rectangular channel with flow-induced pitching, heaving or surging of an airfoil. International Communications in Heat and Mass Transfer. 2023;142:106657.

14 Zhao Z, Luo L, Du W, Wang S, Zhou X, Sundén B. Experimental study on the augmented Nusselt number of the endwall through a square-sectioned sharp-turn channel using novel heat exchanger. International Journal of Heat and Mass Transfer. 2022;192:122920.

15 Eiamsa-ard S, Sripattanapipat S, Promvonge P. An experimental study of a channel flow over two obstacles hydrogen bubble technique. 7th Asian Symposium on Visualization (7ASV); 2003 Nov 3-7; Singapore: National University of Singapore; 2003. paper number 3A-1.

16 Eiamsa-ard S, Changcharoe, W. Analysis of turbulent heat transfer and fluid flow in channels with various ribbed internal surfaces. Journal of Thermal Science. 2011;20:260-267.

17 Eiamsa-ard S, Chuwattanakul V. Visualization of heat transfer characteristics using thermochromic liquid crystal temperature measurements in channels with inclined and transverse twisted-baffles. International Journal of Thermal Sciences. 2020;153:106358.

18 Yongsiri K, Eiamsa-ard P, Wongcharee K, Eiamsa-ard S. Augmented heat transfer in a turbulent channel flow with inclined detached-ribs. Case Studies in Thermal Engineering. 2014;3:1-10.

19 Sripattanapipat S, Eiamsa-ard S, Kongkaitpaiboon V, Promvonge P. Forced convection heat transfer and flow characteristics in rectangular channel with 90° baffles. Proceedings of 12th Asian Symposium on Visualization; 2013 May 19-23; Tainan: Taiwan; 2013.

20 Nuntadusit C, Wae-hayee M, Bunyajitradulya A, Eiamsa-ard S. Thermal visualization on surface with a transverse perforated rib. International Communications in Heat and Mass Transfer. 2012;39:634-639.

21 Changcharoen W, Eiamsa-ard S. Numerical investigation of turbulent heat transfer in channels with detached rib-arrays. Heat Transfer - Asian Research. 2011;40:431-447.

22 Jiang G, Gao J. Flow and heat transfer performance of the channel with different shaped ribs cooled by mist/steam two-phase flow. Case Studies in Thermal Engineering. 2022;38:102365.

23 Eiamsa-ard S, Promvonge P. Thermal characteristics of turbulent rib-grooved channel flows. International Communications in Heat and Mass Transfer. 2009;36:705-711.

24 Eiamsa-ard S, Promvonge P. Numerical study on heat transfer of turbulent channel flow over periodic grooves. International Communications in Heat and Mass Transfer. 2008;35:844-852.

25 Eiamsa-ard S, Sripattanapipat S, Promvonge P. Influence of triangular wavy baffles on heat and fluid flow characteristics in a channel. Journal of Mechanical Science and Technology. 2013;27:2199-2208.

26 Wang L, Sundén B. Experimental investigation of local heat transfer in a square duct with various-shaped ribs. Heat and Mass Transfer/Waerme - und Stoffuebertragung. 2007;43:759-766.

27 Xie G, Liu J, Ligrani PM, Sunden B. Flow structure and heat transfer in a square passage with offset mid-truncated ribs. International Journal of Heat and Mass Transfer. 2014;71:44-56.

28 Iacovides H, Kelemenis G, Raisee M. Flow and heat transfer in straight cooling passages with inclined ribs on opposite walls: an experimental and computational study. Experimental Thermal and Fluid Science. 2003;27:283-294.

29 Mahanand Y, Senapati JR. Thermo-hydraulic performance analysis of a solar air heater (SAH) with quarter-circular ribs on the absorber plate: A comparative study. International Journal of Thermal Sciences. 2021;161:106747.

30 Ekiciler R, Çetinkaya MSA. A comparative heat transfer study between monotype and hybrid nanofluid in a duct with various shapes of ribs. Thermal Science and Engineering Progress. 2021;23:100913.

31 Liu J, Hussain S, Wang J, Wang L, Xie G, Sunden B. Heat transfer enhancement and turbulent flow in a high aspect ratio channel (4:1) with ribs of various truncation types and arrangements. International Journal of Thermal Sciences. 2018;123:99-116.

32 Liu J, Hussain S, Wang W, Xie G, Sunden B. Experimental and numerical investigations of heat transfer and fluid flow in a rectangular channel with perforated ribs. International Communications in Heat and Mass Transfer. 2021;121:105083.

33 Prasad BN, Saini JS. Effect of artificial roughness on heat transfer and friction factor in a solar air heater. Solar Energy. 1988;41:555-560.

34 Prasad BN, Saini JS. Optimal thermohydraulic performance of artificial roughened solar air heater. Solar Energy. 1991;47:91-96.

35 Eiamsa-ard S, Sripattanapipat S, Promvonge P. Simulation of turbulent channel flow over two blocks in tandem arrangement. Proceedings of the Tenth Asian Congress of Fluid Mechanics (ACFMX); 2004 May 17-21; Sri Lanka: University of Peradeniya; 2004 paper number C-17.

36 Promvonge P, Changcharoen W, Kwankaomeng S, Thianpong C. Numerical heat transfer study of turbulent square-duct flow through inline V-shaped discrete ribs. International Communications in Heat and Mass Transfer. 2011;38:1392-1399.

37 Bahiraei M, Mazaheri N, Hosseini Y, Moayedi H. A two-phase simulation for analyzing thermohydraulic performance of Cu–water nanofluid within a square channel enhanced with 90° V-shaped ribs. International Communications in Heat and Mass Transfer. 2019;145:118612.

38 Layek A, Saini JS, Solanki SC. Effect of chamfering on heat transfer and friction characteristics of solar air heater having absorber plate roughened with compound turbulators. Renewable Energy. 2009;34:1292-1298.

39 Momin AME, Saini JS, Solanki SC. Heat transfer and friction in solar air heater duct with V-shaped rib roughness on absorber plate. International Journal of Heat and Mass Transfer. 2002;45:3383-3396.

40 Saini SK, Saini RP. Development of correlations for Nusselt number and friction factor for solar air heater with roughened duct having arc-shaped wire as artificial roughness. Solar Energy. 2008;82:1118-1130.

41 Karwa R, Solanki SC, Saini JS. Heat transfer coefficient and friction factor correlations for the transitional flow regime in rib-roughened rectangular ducts. International Journal of Heat and Mass Transfer. 1999:42;1597-1615.

42 Bhagoria JL, Saini JS, Solanki SC. Heat transfer coefficient and friction factor correlations for rectangular solar air heater duct having transverse wedge shaped rib roughness on the absorber plate. Renewable Energy. 2002;25:341-369.

43 Jaurker AR, Saini JS, Gandhi BK. Heat transfer and friction characteristics of rectangular solar air heater duct using rib-grooved artificial roughness. Solar Energy. 2006;80:895-907.

44 Karmare SV, Tikekar AN. Heat transfer and friction factor correlation for artificially roughened duct with metal grit ribs. International Journal of Heat and Mass Transfer. 2007;50:4342-4351.

45 Saini RP, Verma J. Heat transfer and friction factor correlations for a duct having dimple-shape artificial roughness for solar air heaters. Energy 2008;33:1277-1287.

46 Yadav AS, Bhagoria JL. A CFD (computational fluid dynamics) based heat transfer and fluid flow analysis of a solar air heater provided with circular transverse wire rib roughness on the absorber plate. Energy 2013;55:1127-1142.

47 Yadav AS, Bhagoria JL. A numerical investigation of square sectioned transverse rib roughened solar air heater. International Journal of Thermal Sciences. 2014;79:111-131.

48 Yadav AS, Bhagoria JL. A CFD based thermo-hydraulic performance analysis of an artificially roughened solar air heater having equilateral triangular sectioned rib roughness on the absorber plate. International Journal of Heat and Mass Transfer. 2014;70:1016-1039.

49 Aharwal KR, Gandhi BK, Saini JS. Experimental investigation on heat-transfer enhancement due to a gap in an inclined continuous rib arrangement in a rectangular duct of solar air heater. Renewable Energy. 2008;33:585-596.

50 Aharwal KR, Gandhi BK, Saini JS. Heat transfer and friction characteristics of solar air heater ducts having integral inclined discrete ribs on absorber plate. International Communications in Heat and Mass Transfer. 2009;52:5970-5977.

51 Sahu MM, Bhagoria JL. Augmentation of heat transfer coefficient by using 90° broken transverse ribs on absorber plate of solar air heater. Renewable Energy. 2005;30:2057-2063.

52 Varun Saini RP, Singal SK. Investigation of thermal performance of solar air heater having roughness elements as a combination of inclined and transverse ribs on the absorber plate. Renewable Energy. 2008;33:1398-1405.

53 Boonloi A, Jedsadaratanachai W. CFD analysis on heat transfer characteristics and fluid flow structure in a square duct with modified wavy baffles. Case Studies in Thermal Engineering. 2022;29:101660.

54 Boonloi A, Jedsadaratanachai W. Numerical investigation on turbulent forced convection and heat transfer characteristic in a square channel with discrete combined V-baffle and V-orifice. Case Studies in Thermal Engineering. 2016;8:226-235.

55 Chaube A, Gupta S, Verma P. Heat transfer and friction factor enhancement in a square channel having integral inclined discrete ribs on two opposite walls. Journal of Mechanical Science and Technology. 2014;28:1927-1937.

56 Kaewchoothong N, Maliwan K, Takeishi K, Nuntadusit C. Effect of inclined ribs on heat transfer coefficient in stationary square channel. Theoretical and Applied Mechanics Letters. 2007;7:344-350.

57 Han JC, Zhang YM, Lee CP. Augmented heat transfer in square channels with parallel, crossed and V-shaped angled ribs. Journal of Heat Transfer - Transactions of ASME. 1991;113:590-596.

58 Han JC, Zhang YM, Lee CP. Influence of surface heat flux ratio on heat transfer augmentation in square channels with parallel, crossed, and V-shaped angled ribs. Journal of Turbomachinery - ASME. 1992;114:872-880.

59 Xie G, Zheng S, Zhang W, Sundén B. A numerical study of flow structure and heat transfer in a square channel with ribs combined downstream half-size or same-size ribs. Applied Thermal Engineering. 2013;61:289-300.

60 Kumar A, HoeKim M. Heat transfer and fluid flow characteristics in air duct with various V-pattern rib roughness on the heated plate: A comparative study. Energy 2016;103:75-85.

61 Abraham S, Vedula RP. Heat transfer and pressure drop measurements in a square cross-section converging channel with V and W rib turbulators. Experimental Thermal and Fluid Science. 2016;70:208-219.

62 Han JC, Zhang YM. High performance heat transfer ducts with parallel broken and V-shaped broken ribs. International Journal of Heat and Mass Transfer. 1992;35:513-523.

63 Karwa R. Experimental studies of augmented heat transfer and friction in asymmetrically heated rectangular ducts with ribs on the heated wall in transverse, inclined, V-continuous and V discrete pattern. International Communications in Heat and Mass Transfer. 2003;30:241-250.

64 Tanda G, Abram R. Forced convection heat transfer in channels with rib turbulators inclined at 45 deg. Journal of Turbomachinery - ASME. 2009;131:021012.

65 Bazdid-Tehrani F, Naderi-Abadi M. Numerical analysis of laminar heat transfer in entrance region of a horizontal channel with transverse fins. International Communications in Heat and Mass Transfer. 2004;31:211-220.

66 Mousavi SS, Hooman K. Heat and fluid flow in entrance region of a channel with staggered baffles. Energy Conversion and Management. 2006;47:2011-2019.

67 Chang SW, Chen TW, Chen YW. Detailed heat transfer and friction factor measurements for square channel enhanced by plate insert with inclined baffles and perforated slots. Applied Thermal Engineering. 2019;159:113856.

68 Mashaei PR, Taheri-Ghazvini M, Moghadam RS, Madani S. Smart role of Al_2O_3-water suspension on laminar heat transfer in entrance region of a channel with transverse in-line baffles. Applied Thermal Engineering. 2017;112:450-463.

69 Promvonge P, Sripattanapipat S, Kwankaomeng S. Laminar periodic flow and heat transfer in square channel with 45° inline baffles on two opposite walls. International Journal of Thermal Sciences. 2010;49:963-975.

70 Promvonge P, Sripattanapipat S, Tamna S, Kwankaomeng S, Thianpong C. Numerical investigation of laminar heat transfer in a square channel with 45° inclined baffles. International Communications in Heat and Mass Transfer. 2010;37:170-177.

71 Kwankaomeng S, Promvonge P. Numerical prediction on laminar heat transfer in square duct with 30° angled baffle on one wall. International Communications in Heat and Mass Transfer. 2010;37:857-866.

72 Promvonge P, Jedsadaratanachai W, Kwankaomeng S. Numerical study of laminar flow and heat transfer in square channel with 30° inline angled baffle turbulators. Applied Thermal Engineering. 2010;30:1292-1303.

73 Dutta S, Dutta P, Jones RE, Khan JA. Heat transfer coefficient enhancement with perforated baffles. Journal of Heat Transfer. 1998;120:795-797.

74 Dutta P, Dutta S. Effect of baffle size, perforation, and orientation on internal heat transfer enhancement. International Journal of Heat and Mass Transfer. 1998;41:3005-30134.

75 Sahel D, Ameur H, Benzeguir R, Kamla Y. Enhancement of heat transfer in a rectangular channel with perforated baffles. Applied Thermal Engineering. 2016;101:156-164.

76 El Habet MA, Ahmed SA, Saleh MA. The effect of using staggered and partially tilted perforated baffles on heat transfer and flow characteristics in a rectangular channel. International Journal of Thermal Sciences. 2022;174:107422.

77 Alam T, Saini RP, Saini JS. Experimental investigation on heat transfer enhancement due to V-shaped perforated blocks in a rectangular duct of solar air heater. Energy Conversion and Management. 2014;81:374-383.

68 Chamoli S. A Taguchi approach for optimization of flow and geometrical parameters in a rectangular channel roughened with V down perforated baffles. Case Studies in Thermal Engineering. 2015:5:59-69.

79 Chamoli S, Thakur NS. Heat transfer enhancement in solar air heater with V-shaped perforated baffles. Journal of Renewable and Sustainable Energy. 2013;5:023122.

80 Chamoli S, Thakur NS. Correlations for solar air heater duct with V-shaped perforated baffles as roughness elements on absorber plate. International Journal of Sustainable Energy. 2016;35:1-20.

81 Promvonge P, Skullong S. Thermal characteristics in solar air duct with V-shaped flapped-baffles and chamfered-grooves. International Journal of Heat and Mass Transfer. 2021;172:121220.

82 Eiamsa-ard S, Sripattanapipat S, Promvonge P. Numerical heat transfer analysis in turbulent channel flow over a side-by-side triangular prism pair. Journal of Engineering Thermophysics. 2012;21:95-110.

83 Thakur DS, Khan MK, Pathak M. Solar air heater with hyperbolic ribs: 3D simulation with experimental validation. Renewable Energy. 2017;113:357-368.

84 Li Y, Rao Y, Wang D, Zhang P, Wub X. Heat transfer and pressure loss of turbulent flow in channels with miniature structured ribs on one wall. International Journal of Heat and Mass Transfer. 2019;131:584-593.

85 Jiang W, Zhao J, Rao Z. Heat transfer performance enhancement of liquid cold plate based on mini V-shaped rib for battery thermal management. Applied Thermal Engineering. 2021;189:116729.

86 Tanda G, Satta F. Heat transfer and friction in a high aspect ratio rectangular channel with angled and intersecting ribs. International Journal of Heat and Mass Transfer. 2021;169:120906.

87 Jin D, Zhang M, Wang P, Xu S. Numerical investigation of heat transfer and fluid flow in a solar air heater duct with multi V-shaped ribs on the absorber plate. Energy 2015;89:178-190.

88 Jin D, Quan S, Zuo J, Xu S. Numerical investigation of heat transfer enhancement in a solar air heater roughened by multiple V-shaped ribs. Renewable Energy. 2019;134:78-88.

89 Li J-L, Tang HW, Yang Y-T. Numerical simulation and thermal performance optimization of turbulent flow in a channel with multi V-shaped baffles. International Communications in Heat and Mass Transfer. 2018;92:39-50.

90 Fawaz HE, Badawy MTS, Abd Rabbo MF, Elfeky A. Numerical investigation of fully developed periodic turbulent flow in a square channel fitted with 45° in-line V-baffle turbulators pointing upstream. Alexandria Engineering Journal. 2018;57:633-642.

91 Dong Z, Liu P, Xiao H, Liu Z, Liu W. A study on heat transfer enhancement for solar air heaters with ripple surface. Renewable Energy. 2021;172:477-487.

92 Singh AP, Varun, Siddhartha. Heat transfer and friction factor correlations for multiple arc shape roughness elements on the absorber plate used in solar air heaters. Experimental Thermal and Fluid Science. 2014;54:117-126.

93 Singh S, Chande S, Saini JS. Investigations on thermo-hydraulic performance due to flow-attack-angle in V-down rib with gap in a rectangular duct of solar air heater. Applied Energy. 2012;97:907-912.

94 Singh S, Chander S, Saini JS. Thermo-hydraulic performance due to relative roughness pitch in V-down rib with gap in solar air heater duct - Comparison with similar rib roughness geometries. Renewable and Sustainable Energy Reviews. 2015;43:1159-1166.

95 Kumar A, Saini RP, Saini JS. Development of correlations for Nusselt number and friction factor for solar air heater with roughened duct having multi v-shaped with gap rib as artificial roughness. Renewable Energy. 2013;58:151-163.

96 Maithani R, Saini JS. Heat transfer and friction factor correlations for a solar air heater duct roughened artificially with V-ribs with symmetrical gaps. Experimental Thermal and Fluid Science. 2016;70:220-227.

97 Kumar R, Kumar A, Chauhan R, Sethi M. Heat transfer enhancement in solar air channel with broken multiple V-type baffle. Case Studies in Thermal Engineering. 2016;8:187-197.

98 Jedsadaratanachai W, Boonloi A. Effects of blockage ratio and pitch ratio on thermal performance in a square channel with 30° double V-baffles. Case Studies in Thermal Engineering. 2014;4:118-128.

99 Jedsadaratanachai W, Boonloi A. Numerical investigation on turbulent forced convection and heat transfer characteristic in a square channel with discrete combined V-baffle and V-orifice. Case Studies in Thermal Engineering. 2016;8:226-235.

100 Kumar R, Chauhan R, Sethi M, Kumar A. Experimental study and correlation development for Nusselt number and friction factor for discretized broken V-pattern baffle solar air channel. Experimental Thermal and Fluid Science. 2017;81:56-75

101 Kumar R, Sethi M, Chauhan R, Kumar A. Experimental study of enhancement of heat transfer and pressure drop in a solar air channel with discretized broken V-pattern baffle. Renewable Energy. 2017;101:856-872.

102 Promvonge P, Skullong S. Augmented heat transfer in tubular heat exchanger fitted with V-baffled tapes. International Journal of Thermal Sciences. 2020;155:106429.

103 Promvonge P, Skullong S. Enhanced thermal performance in tubular heat exchanger contained with V-shaped baffles. Applied Thermal Engineering. 2021;185:116307.

104 Phila A, Thianpong C, Eiamsa-ard S. Influence of geometric parameters of alternate axis twisted baffles on the local heat transfer distribution and pressure drop in a rectangular channel using a transient liquid crystal technique. Energies. 2019;12:2341.

105 Eiamsa-ard S. Study on thermal and fluid flow characteristics in turbulent channel flows with multiple twisted tape vortex generators. International Communications in Heat and Mass Transfer. 2010;37:644-651.

106 Kumar A, Layek A. Thermo-hydraulic performance of solar air heater having twisted rib over the absorber plate. International Journal of Thermal Sciences. 2018;133:181-195.

107 Kumar A, Layek A. Nusselt number and friction factor correlation of solar air heater having twisted-rib roughness on absorber plate. Renewable Energy. 2019;130:687-699.

108 Rashidi S, Akbarzadeh M, Karimi N, Masoodi R. Combined effects of nanofluid and transverse twisted-baffles on the flow structures, heat transfer and irreversibilities inside a square duct - A numerical study. Applied Thermal Engineering. 2018;130:135-148.

109 Zhang Q, Feng Z, Li Z, Chen Z, Huang S, Zhang J, Guo F. Numerical investigation on hydraulic and thermal performances of a mini-channel heat sink with twisted ribs. International Journal of Thermal Sciences. 2022;179:107718.

110 Sawhney JS, Maithani R, Chamoli S. Experimental investigation of heat transfer and friction factor characteristics of solar air heater using wavy delta winglets. Applied Thermal Engineering. 2017;117:740-751.

111 Sahu MK, Prasad RK. Exergy based performance evaluation of solar air heater with arc- shaped wire roughened absorber plate. Renewable and Sustainable Energy Reviews. 2016;96:233-243.

112 Hans VS, Gill RS, Singh S. Heat transfer and friction factor correlations for a solar air heater duct roughened artificially with broken arc ribs. Experimental Thermal and Fluid Science. 2017;80:77-89.

113 Saravanakumar PT, Somasundaram D, Matheswaran MM. Thermal and thermo-hydraulic analysis of arc shaped rib roughened solar air heater integrated with fins and baffles. Solar Energy. 2019;180:360-371.

114 Promvonge P, Eiamsaard S, Wongcharee K, Chuwattanakul V, Samruaisin P, Chokphoemphun S, Nanan K, Eiamsa-ard P. Characterization of heat transfer and artificial neural networks prediction on overall performance index of a channel installed with arc-shaped baffle turbulators. Case Studies in Thermal Engineering. 2021;26:101067.

115 Sureandhar G, Srinivasan G, Muthukumar P, Senthilmurugan S. Investigation of thermal performance in a solar air heater having variable arc ribbed fin configuration. Sustainable Energy Technologies and Assessments. 2022;52:102069.

116 Promvonge P, Chompookham T, Kwankaomeng S, Thianpong C. Enhanced heat transfer in a triangular ribbed channel with longitudinal vortex generators. Energy Conversion and Management. 2010;51:1242-1249.

117 Promvonge P, Khanoknaiyakarn C, Kwankaomeng S, Thianpong C. Thermal behavior in solar air heater channel fitted with combined rib and delta-winglet. International Communications in Heat and Mass Transfer. 2011;38:749-756.

118 Nazir U, Sohail M, Hafeez MB, Krawczuk M, Askar S, Wasif S. An inclination in thermal energy using nanoparticles with casson liquid past an expanding porous surface. *Energies*. 2021;*14*:7328.

119 Ahmed Z, Saleem S, Nadeem S, Khan AU. Squeezing flow of carbon nanotubes-based nanofluid in channel considering temperature-dependent viscosity: a numerical approach. Arabian Journal for Science and Engineering. 2021;46:2047-2053

120 Saleem S, Gopal D, Shah NA, Feroz N, Kishan N, Chung JD, Safdar S. Modelling entropy in magnetized flow of Eyring–Powell nanofluid through nonlinear stretching surface with chemical reaction: a finite element method approach. *Nanomaterials*. 2022;*12*:1811.

CHAPTER 3

Heat transfer enhancement in channel: Numerical investigation

---

3.1 Introduction

The present work offers a challenging ribs/ baffle design to promote heat transfer while diminish pressure drop as compared to those given by typical baffles/ribs. A main idea of reducing pressure drop is that of introducing semi-circular holes on V-shaped baffles. In addition, an idea of changing flow direction by busing the wing at different attack angles ($\theta = 5^o$, 10° and 15°) was applied to improve the heat transfer rate and thermal performance factor (TPF). This approach is inspired by the principle of impinging jets flow on the channel wall, in which the semi-circular wings leave air flows through holes as impinging jets behind V-shaped baffles [1-5]. The impinging jets were designed to be multi impinging jets to increase the heat transfer [3, 6]. The impinging jets directly hit the channel wall in different directions depending on the attack angle (θ). The impingement can inhibit the formation of multi-spots cooling-temperature zones and diminish pressure loss. Moreover, the impinging jets also strengthen the thermal disruption and fluid mixing behind the V-shaped baffle. It is expected that the combination of effect of impinging jets and local longitudinal vortexes generated by the V-shaped baffle should result in greater heat transfer enhancement than that given by a V-shaped baffle without semi-circular wings. In the current work, a numerical prediction is performed to understand the flow-topology/ structure and heat transfer mechanism. The important parameters of baffle design are pitch ratios (PR = 0.5, 1.0, 1.5 and 2.0) and blockage ratios (BR = 0.1, 0.15 and 0.2), attack angles ($\theta = 5^o$, 10° and 15°). The prediction was performed for Reynolds number (Re) ranging from 3,000 to 19,000. The results of typical V-shaped baffles without holes are also given along for comparative assessment.

3.2 Mathematical model

In this paper, the governing equations used to resolve the fluid flow and heat transfer in the rectangular channel contained with semi-circular wing perforated V-type baffles (SCW-PVBs) problems were the continuity, momentum, and energy equations. In order to reasonably simplify the simulations, the governing equations were based on the following assumptions:

1) The flow was three-dimensional, steady state, turbulent and incompressible.
2) The effect of the gravity, viscous dissipation, body forces, natural convection and radiation heat transfer were ignorable.
3) Heat transferred by force convection only.

4) The fluid properties were constant.

The governing equations can be expressed as

Continuity equation:

$$\frac{\partial(\rho u_i)}{\partial x_i} = 0 \tag{3.1}$$

Momentum equation:

$$\frac{\partial(\rho u_i u_j)}{\partial x_j} = -\frac{\partial p}{\partial x_i} + \frac{\partial}{\partial x_j}\left[\mu\left(\frac{\partial u_i}{\partial x_j} - \rho\overline{u_i' u_j'}\right)\right] \tag{3.2}$$

Energy equation:

$$\frac{\partial(\rho u_i T)}{\partial x_i} = \frac{\partial}{\partial x_j}\left((\Gamma + \Gamma_t)\frac{\partial T}{\partial x_j}\right) \tag{3.3}$$

where

$$\Gamma = \frac{\mu}{\Pr} \text{ and } \Gamma_t = \frac{\mu_t}{\Pr_t} \tag{3.4}$$

where

$$-\rho\overline{u_i' u_j'} = \mu_t\left(\frac{\partial u_i}{\partial x_j} + \frac{\partial u_j}{\partial x_i}\right) - \frac{2}{3}\left(\rho k + \mu_t\frac{\partial u_i}{\partial x_i}\right)\delta_{ij} \tag{3.5}$$

where

$$\mu_t = \rho c_\mu k^2 / \varepsilon$$

and

$$k = 0.5\overline{u_i' u_j'}$$

For the effect of the high strain rate and large streamline curvature, the RNG k-ε turbulent model was used to resolve this problem. The turbulent transport equations for k (turbulent kinetic energy) and ε (turbulent dissipation rate) are

$$\frac{\partial(\rho k u_i)}{\partial x_i} = \frac{\partial}{\partial x_j}\left(\sigma_k(\mu + \mu_t)\frac{\partial k}{\partial x_j}\right) + G_k + \rho\varepsilon \tag{3.6}$$

and

$$\frac{\partial(\rho\varepsilon u_i)}{\partial x_i} = \frac{\partial}{\partial x_j}\left(\sigma_\varepsilon(\mu+\mu_t)\frac{\partial\varepsilon}{\partial x_j}\right) + C'_{1\varepsilon}\frac{\varepsilon}{k}G_k - C_{2\varepsilon}\rho \tag{3.7}$$

where the $C'_{1\varepsilon}$ can be expressed as

$$C'_{1\varepsilon} = C_{1\varepsilon} - \frac{\eta(1-\eta/\eta_0)}{1+\lambda\eta^3} \tag{3.8}$$

where

$$\eta = (2E_{ij}\cdot E_{ij})^{1/2}\frac{k}{\varepsilon} \tag{3.9}$$

and

$$E_{ij} = \frac{1}{2}\left(\frac{\partial u_i}{\partial x_j} + \frac{\partial u_j}{\partial x_i}\right) \tag{3.10}$$

The constant values are

$$C_\mu = 0.09\ ,\ \sigma_k = 1.0\ \sigma_\varepsilon = 1.3\ ,\ C_{1\varepsilon} = 1.42\ ,\ C_{2\varepsilon} = 1.68\ ,\ \eta_0 = 4.377\ ,\ \lambda = 0.012 \tag{3.11}$$

The pressure and velocity were coupled by using the SIMPLE algorithm. For the convection terms, the QUICK scheme was used to discretize for the energy, momentum, turbulent kinetic energy (TKE), and specific dissipation equations. For the energy equation, the scaled convergence criterion was 10^{-9} while the other equations were 10^{-5}.

The parameters of interest are as follow:

The Reynolds number:

$$\mathrm{Re} = \rho\bar{u}D_h/\mu \tag{3.12}$$

The friction factor:

$$f = ((-dP/dx)\times D_h)\Big/\left(\frac{1}{2}\rho\bar{u}^2\right) \tag{3.13}$$

The local Nusselt number:

$$Nu_x = h_x D_h/k_a \tag{3.14}$$

The average Nusselt number:

$$Nu = \frac{1}{A}\int Nu_x dA \tag{3.15}$$

The overall thermal performance in term of a thermal performance factor (*TPF*) was evaluated by determining both heat transfer and friction loss. The concept the evaluation was previously described by Promvonge and Skullong [7]. The evaluation based on the same pumping power of both smooth channel and the one with inserts.

$$\left(\dot{V}\Delta P\right)_s = \left(\dot{V}\Delta P\right) \tag{3.16}$$

Rewrite the Eq. (3.16) to be in the Reynolds numbers (*Re*) and friction factor forms as below.

$$\left(f\,\mathrm{Re}^3\right)_s = \left(f\,\mathrm{Re}^3\right) \tag{3.17}$$

For both sides of the Eq. (3.17), multiplying by $\left(1/f_{s,\mathrm{Re}}\right)$, and rearranging as below.

$$\mathrm{Re}_s^3 \times \frac{f_s}{f_{s,\mathrm{Re}}} = \mathrm{Re}^3 \times \frac{f}{f_{s,\mathrm{Re}}} \tag{3.18}$$

Considering the ratio of heat transfer coefficients between the smooth and installed channels at equal pumping power, the thermal performance factor (*TPF*) can be written as

$$\mathrm{TPF} = \left.\frac{h}{h_s}\right|_{\mathrm{pp}} = \left.\frac{Nu}{Nu_s}\right|_{\mathrm{pp}} \tag{3.19}$$

$$\mathrm{TPF} = \left(\frac{Nu}{Nu_s}\right)_{\mathrm{Re}} \Bigg/ \left(\frac{f}{f_s}\right)_{\mathrm{Re}}^{\frac{1}{3}} \tag{3.20}$$

where Nu_s and f_s are the Nusselt number and friction factor of a smooth rectangular channel, respectively.

3.3 Computational domain and Semi-circular wing perforated V-type baffles (SCW-PVBs)

The rectangular channel with V-baffles installed on the lower channel wall employed in the present study is illustrated in Fig. 3.1. The cross-section area of the rectangular channel was 20 mm high and 200 mm wide ($AR = 10$). For the full-length model, the test section was divided into three sections; entry section, test section and exit section with the fixed lengths of $10H$ (to maintain the inlet velocity uniformity), $12H$ (to ensure a fully developed periodic velocity and heat transfer) and $2H$ (to prevent the reverse flow), respectively, as shown in Fig. 3.1(a). To investigate the heat transfer enhancement, the solid V-type baffles (VBs) with blockage ratios, BR = b/H = 0.10, 0.15 and 0.20 and pitch ratios, PR = p/H = 0.5, 1.0, 1.5 and 2.0, were investigated at constant angle of attack, $\alpha = 45^{o}$. To save energy usage due to higher pumping power caused by the increased pressure drop and to increase the heat transfer, the solid V-type baffles (VBs) was modified to be a semi-circular wing perforated V-type baffles (SCW-PVBs). Three semi-circular holes were punched to reduce the flow blockage and pressure drop. The wing was expected to create impinging jets when the fluid moved through the semi-circular holes, for enhancing heat transfer. As mentioned earlier, the solid V-type baffles (VBs) generated the main vortex flow, while the perforated/discrete/broken V-type baffles (VBs) created the secondary flow. The fluid flow through perforated/discrete/broken section affected the main flow velocity reduction, the main-vortex strength decreased, high heat transfer area caused by the main vortex flow reduced. Thus, in order to reduce the main vortex strength disruption together with the impinging jets flow creation at the heat transfer area (especially, at behind the solid V-type baffles (VBs) area that is the dead zone), the semi-circular holes were punched from the middle of the baffles toward the near channel wall with fixed parameter, $c = 0.5b$. The distance between the channel wall and the edge of the semi-circular holes (h) was fixed at $0.02H$. The parameter d was the diameter of the semi-circular holes and the parameter e was the distance between the semi-circular holes. The effect of attack angles ($\theta = 5^{o}$, 10° and 15°) was investigated. All parameters are summarized in Table 3.1.

The hexahedron element was applied for all the computational domain, high density element was generated at the near wall region ($y^{+} \approx 1$) because of the velocity and temperature were significantly changed due to the viscous sublayer. Thus, the near-wall modeling significantly impacts the accuracy of numerical solutions. In the present study, the modeling method for the near-wall region was applied with the Enhanced Wall Treatment (EWT). As mentioned earlier, the first near-wall cell next to the wall is determined by the dimensionless parameter, y^{+} which is defined as

$$y^{+} = \frac{u^{*} y \rho}{\mu} \tag{3.21}$$

where u^{*} and y are the friction velocity and height of the wall-to-wall adjacent cell, respectively, and u^{*} is defined as

$$u^{*} = \sqrt{\tau_0 / \rho} \tag{3.22}$$

where τ_0 is the shear stress of the wall.

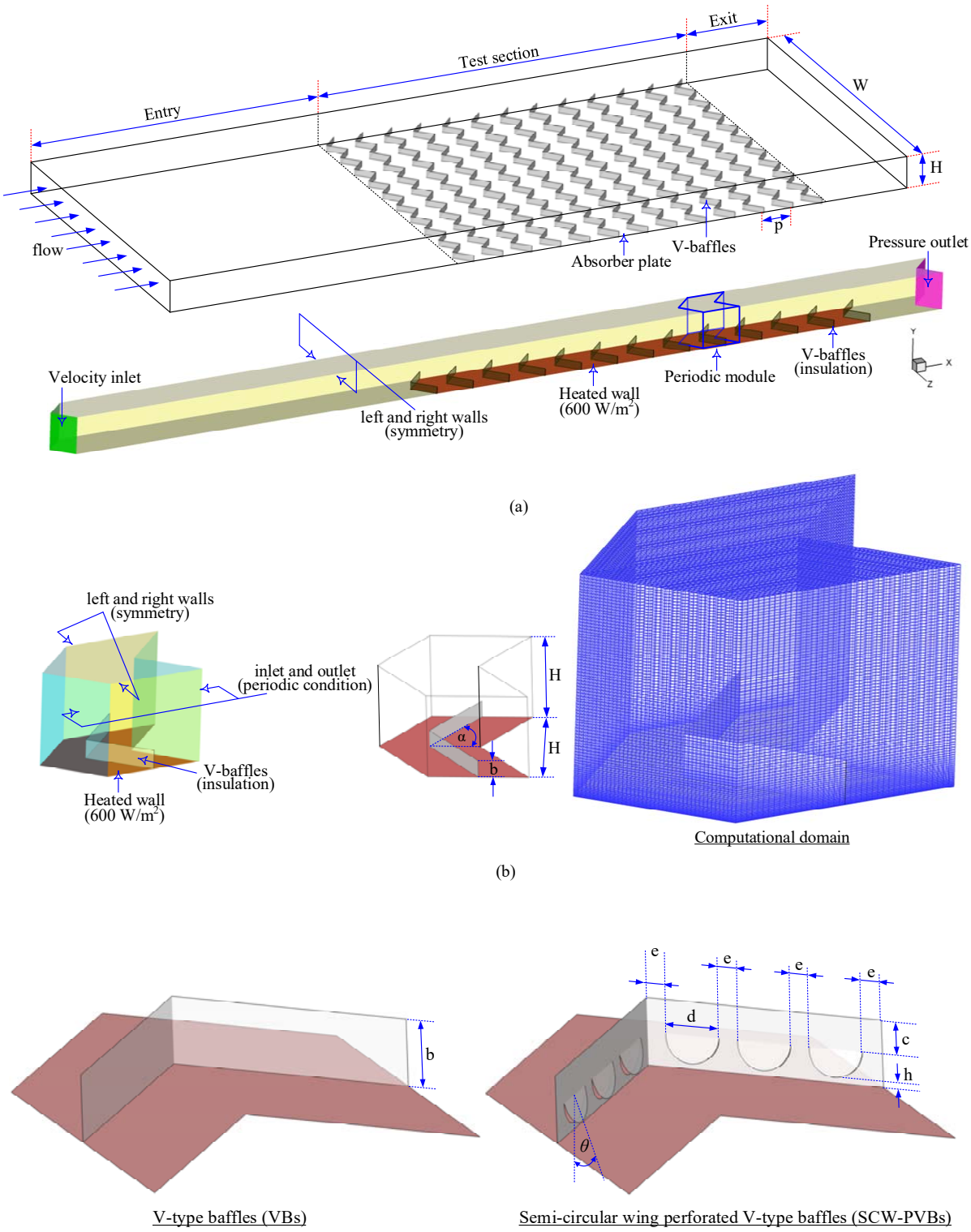

Figure 3.1. Details of channel for (a) full-length model (b) periodic module and (c) details VBs and SCW-PVBs.

The boundary conditions for the full length and the periodic module in the present work can be summarized as follows. For full length tubes, the inlet and outlet were applied with the constant air mass-flow rate and pressure outlet (P_{gage} = 0 Pa), respectively. For periodic modules, periodic condition was applied with the inlet and outlet. For all tubes, uniform heat flux of 600 W/m^2 was applied for the heated wall, no-slip condition was applied for all of the walls and the baffles were set to be insulation.

Table 3.1: Parameters investigated in the present work.

Baffles	*b/H*	*p/H*	*θ*	*α*	*c/b*	*d/H*	*e/H*	*h/H*
SCW-PVBs	0.10	0.5, 1.0, 1.5, 2.0	5°, 10°, 15°	45°	0.5	0.06	0.13	0.02
	0.15	0.5, 1.0, 1.5, 2.0	5°, 10°, 15°	45°	0.5	0.11	0.09	0.02
	0.20	0.5, 1.0, 1.5, 2.0	5°, 10°, 15°	45°	0.5	0.16	0.05	0.02
VBs	0.10, 0.15 0.20	0.5, 1.0, 1.5, 2.0	-	45°	-	-	-	-

Where parameters, $d = 2[(0.5b)-(h/H)]$ and $e = [[(H/2)/\sin\alpha]-3d]/4$

3.4 Results and discussion

3.4.1 Validation test

The validation test was performed by comparing the present numerical results obtained from five turbulent models; Standard *k-ε*, Realizable *k-ε*, RNG *k-ε*, Standard *k-ω*, and SST *k-ω* with those from other sources. For the smooth rectangular channel, the present results were compared with the data from Dittus-Boelter and Blasius correlations [8] and the experimental results by Promvonge and Skullong [7] and Tamna *et al.* [9] as presented in Fig. 3.2. For the channel installed with V-shaped baffles, the present results were compared with the experimental results by Tamna *et al.* [9] as shown in Fig. 3.3.

The Nusselt number correlation of Dittus-Boelter is defined as

$$Nu_s = 0.023\mathrm{Re}^{0.8}\mathrm{Pr}^{0.4} \quad \text{for heating} \tag{3.23}$$

The Blasius correlation is defined as

$$f_s = 0.316\mathrm{Re}^{-0.25} \tag{3.24}$$

The numerical results of the smooth rectangular channel showed similar trends with those of Dittus-Boelter and Blasius correlations [8] and the experimental results by Promvonge and Skullong [7] and Tamna *et al.* [9]. Among the models applied, considered both the Nusselt number and friction factor, the RNG *k-ε* predicted the most accurate data with deviations within ±10% (Fig. 3.2). Moreover, the

RNG k-ε turbulent model also showed good precision in predicting data for the rectangular channel installed with V-shaped baffles, with the mean deviations less than 10% as compared to those reported by Tamna *et al.* [9] (Fig. 3.3).

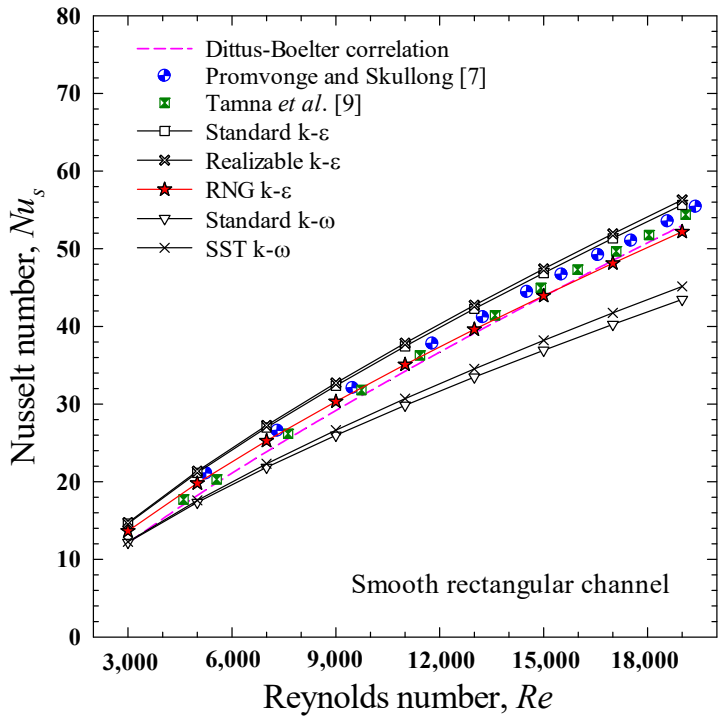

(a)

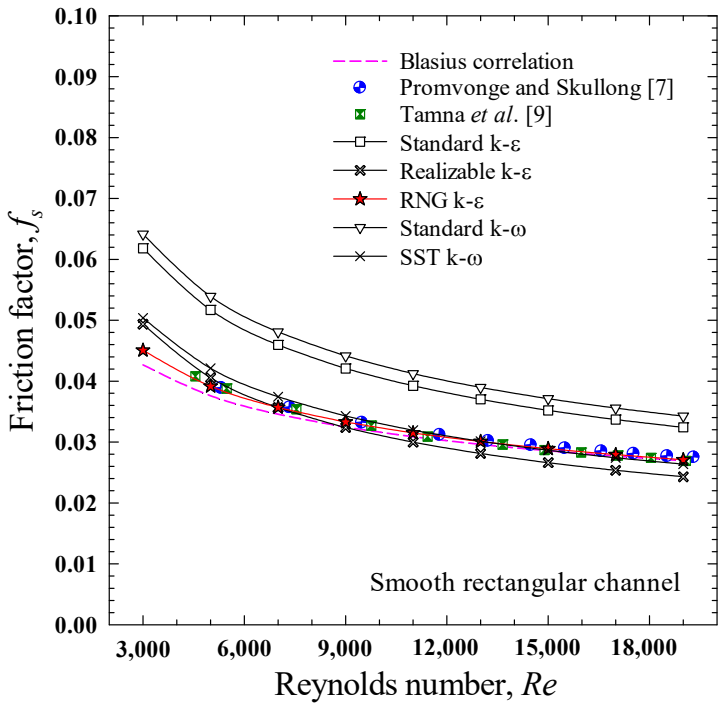

(b)

Figure 3.2. Comparison of (a) Nu_s and (b) f_s for smooth rectangular channel

The grid independence test was investigated by using Richardson extrapolation technique. Five different grid numbers of 51525, 210321, 355005, 500250 and 702540 were tested with the solid V-type baffles (VBs) at BR = 1.0, PR = 1.0 and α = 45°. Increasing the grid number from 500250 to 702540 resulted in insignificant deviations of the Nusselt number and friction factor (less than 0.45%). Therefore, a grid number around 500250 cells was adopted for further study, considered both convergent time and solution precision.

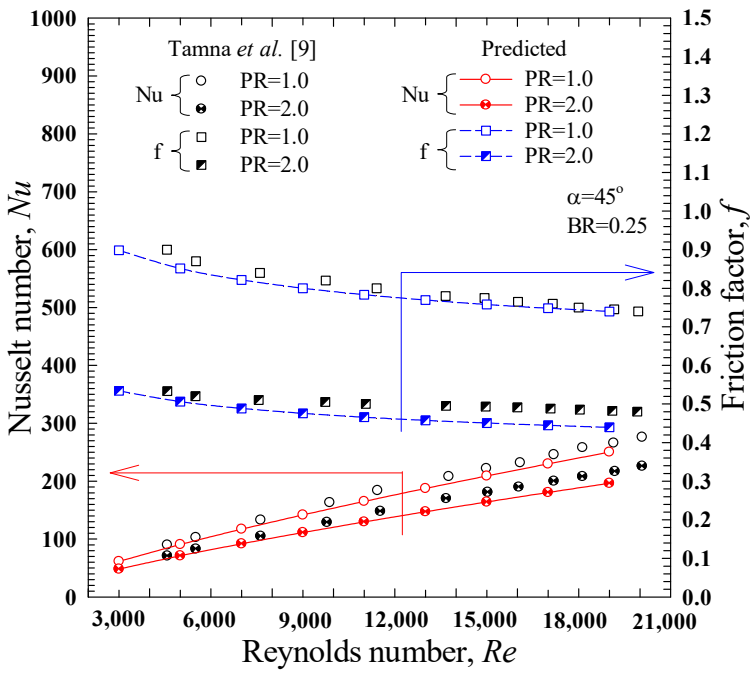

Figure 3.3. Nusselt number (*Nu*) and Friction factor (*f*) for rectangular channel with solid V-type baffles (VBs) inserts.

3.4.2 Fully developed periodic velocity and heat transfer conditions

Both the full-length model and periodic model were applied for the channel with solid V-type baffles (VBs) having BR = 0.20 and PR = 1.0 at Reynolds numbers (*Re*) of 10,000. The velocity (u/u_0) profile, heat transfer (Nu/Nu_s) profile, flow structure, TKE field and local wall Nusselt number are shown in Figs. 3.4-3.6.

Figure 3.4(a) displays the axial velocity (u/u_0) profiles from the full-length model at y/H = 0.2, 0.4, 0.6 and 0.8 with constant z/H = 0.25. Evidently, velocity (u/u_0) profiles became periodic at x/H = 2.0 and tended to decrease or increase from x/H = 2.0 to x/H = 6.0, depend on the location y/H. Then, the u/u_0 profiles became fully developed periodic at $x/H \geq 6.0$. In this region, the magnitudes of velocity (u/u_0) profiles were constant. In Fig. 3.4(b), Nu/Nu_s profile appeared to be periodic in the range of $0.0 \leq x/H$

≤ 6.0 which conformed to velocity profile. Therefore, the fully developed periodic velocity and heat transfer concepts were valid because of the constant u/u_0 and Nu/Nu_s periodic profiles.

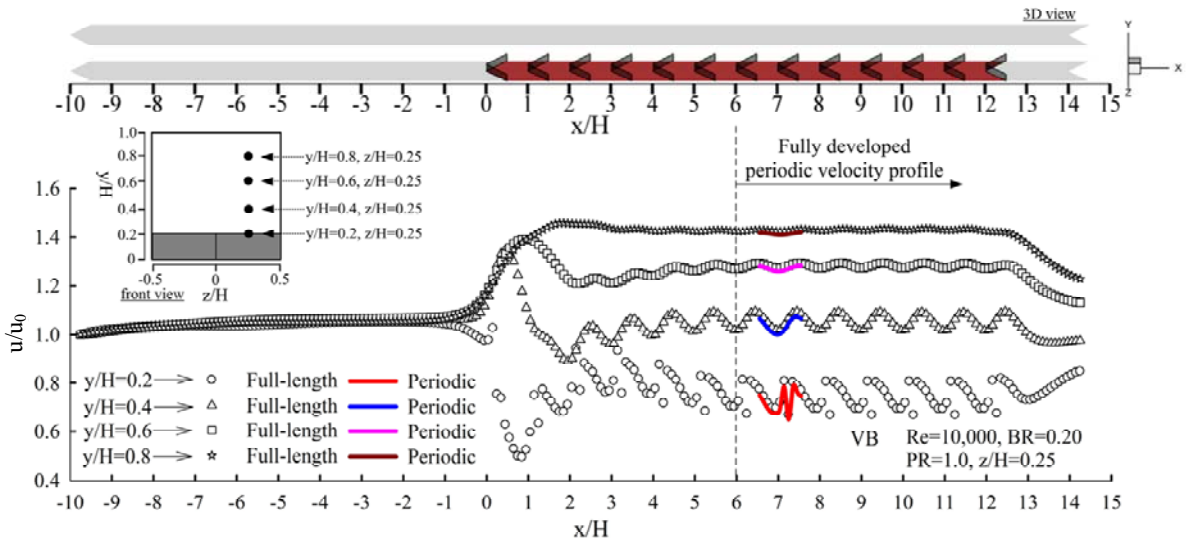

(a)

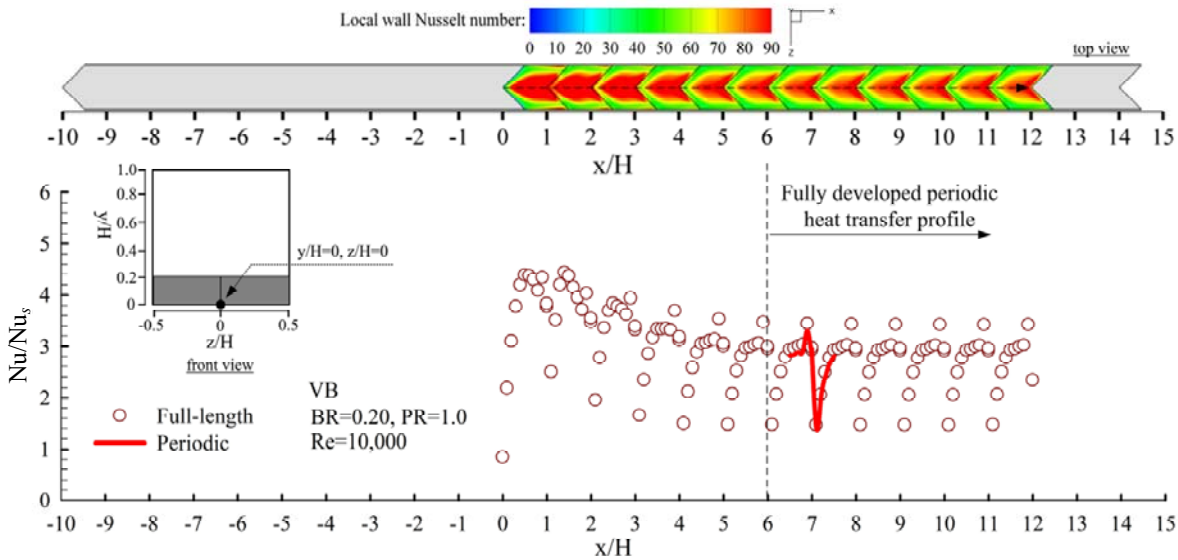

(b)

Figure 3.4. Profiles of (a) u/u_0 and (b) Nu/Nu_s in the axial flow.

Figures 3.5-3.6 show that the solid V-type baffles (VBs) generated vortex flows on the transverse plane and high TKE appeared near the channel wall. In addition, the flow structure, TKE field and local wall Nusselt number for the full-length model showed similar patterns in the fully developed periodic region. Besides, the results were similar to those achieved from the periodic model. Therefore, if the test rectangular channel with baffles inserted is sufficiently long, the fully developed periodic velocity and

heat transfer concepts can be applied efficiently in the turbulent flow. When considered both convergent time and solution precision, the periodic model was chosen for the rest of the computation.

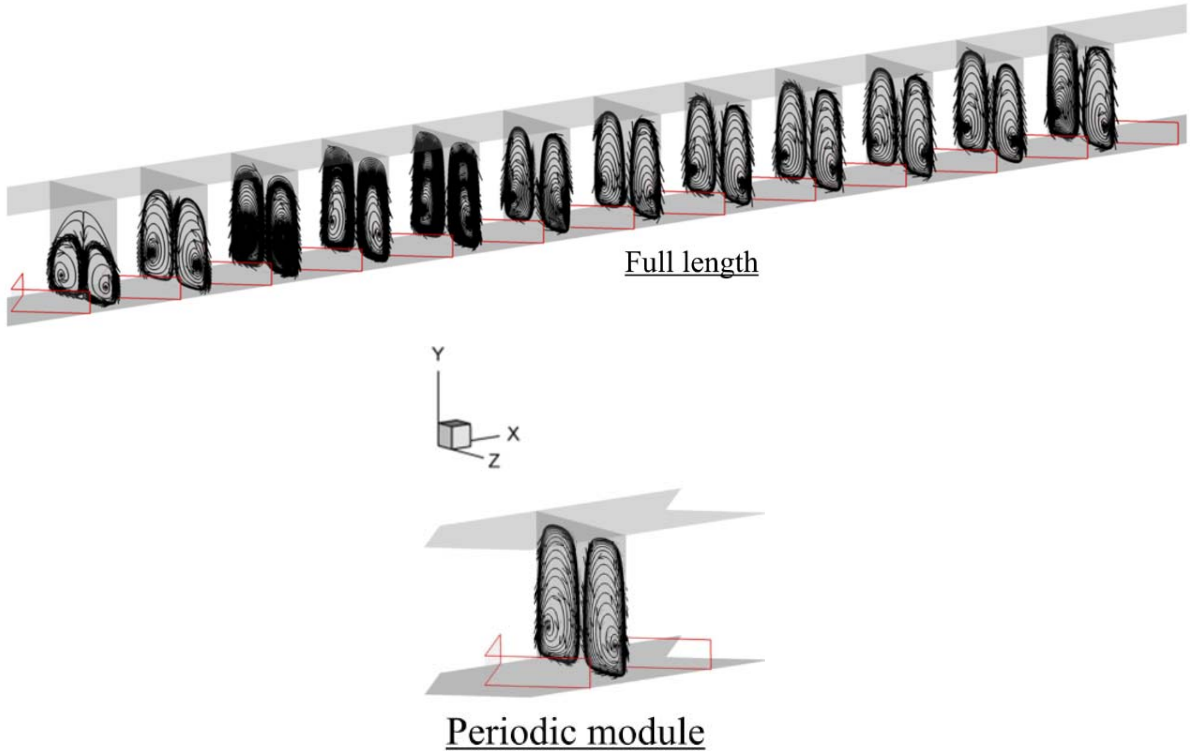

(a)

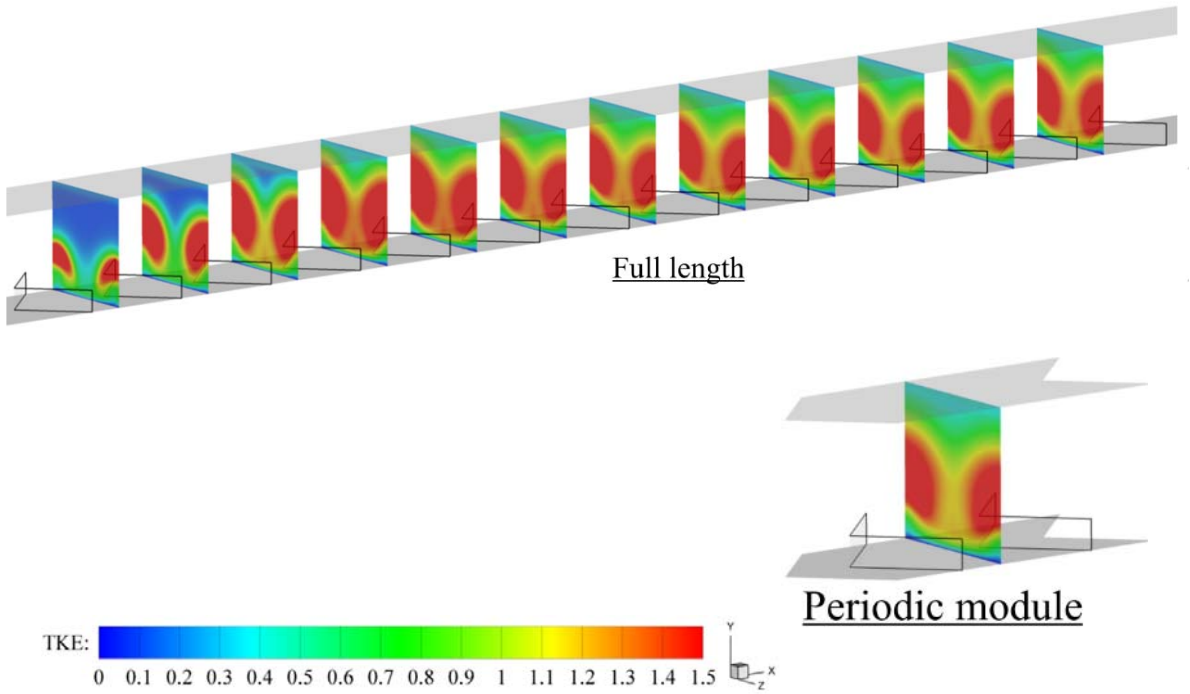

(b)

Figure 3.5. Comparison for (a) flow structure and (b) TKE field on the transverse plane between the full-length and the periodic module at BR = 0.20, PR = 1.0 and *Re* = 10,000.

3.4.3 Heat transfer mechanism and flow topology

4.3.3.1 Comparison between VBs and SCW-PVBs

Figure 3.7 presents a comparison between the solid V-type baffles (VBs) and semi-circular wing perforated V-type baffles (SCW-PVBs) at BR = 0.20, PR = 1.5, $\theta = 15^{o}$ and Re = 3,000. The 3D flow structure and local wall temperature, 2D flow structure on flow direction plane and local wall temperature, TKE field on transverse plane and local wall Nusselt number are displayed. In general, the solid V-type baffles (VBs) created only a vortex flow (called a main vortex flow). The attack of the main vortex resulted in a significant decrease of wall temperature due to the severe disruption of a thermal boundary layer leading to the efficient heat transfer through the channel wall. However, large dead zones (high wall temperature and high fluid temperature) appeared behind the baffles because the vortex flow cannot access those areas. Therefore, the heat transfer behind baffles was inefficient.

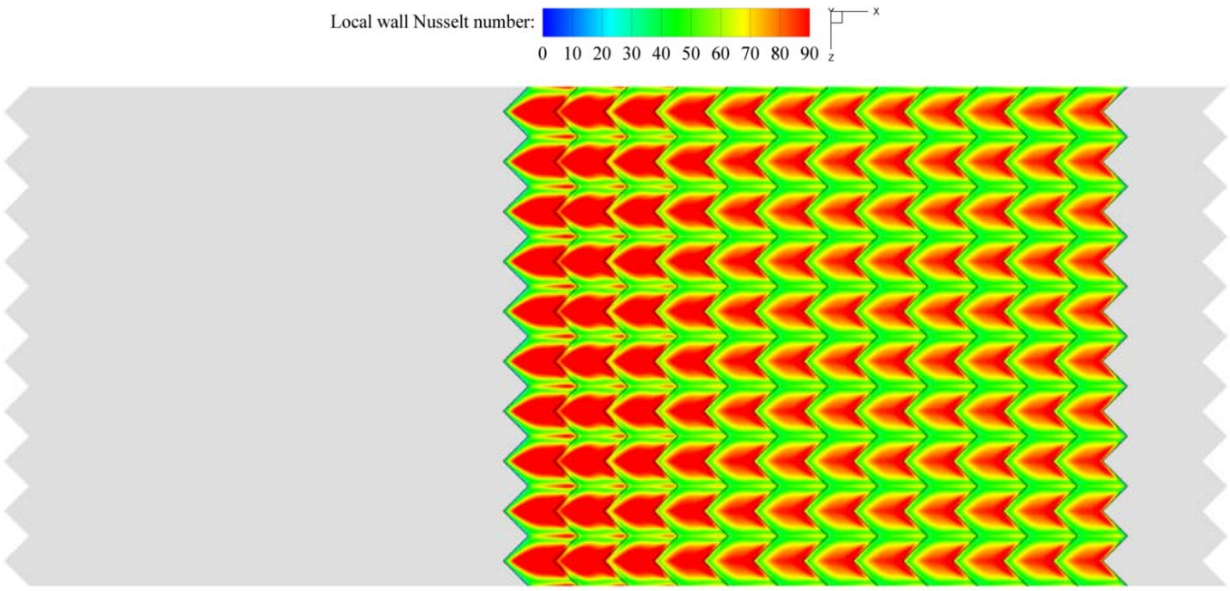

(a)

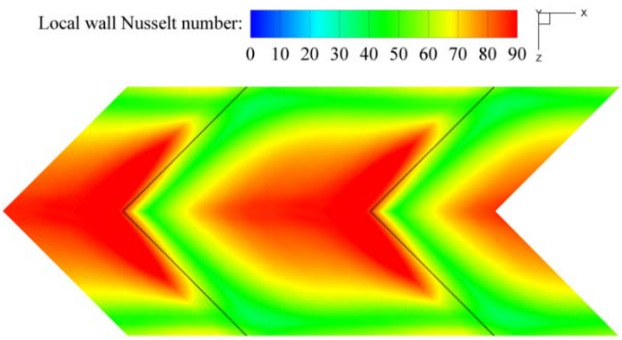

(b)

Figure 3.6. Local wall Nusselt number of the VBs for (a) full-length and (b) periodic module at BR = 0.20, PR = 1.0 and Re = 10,000

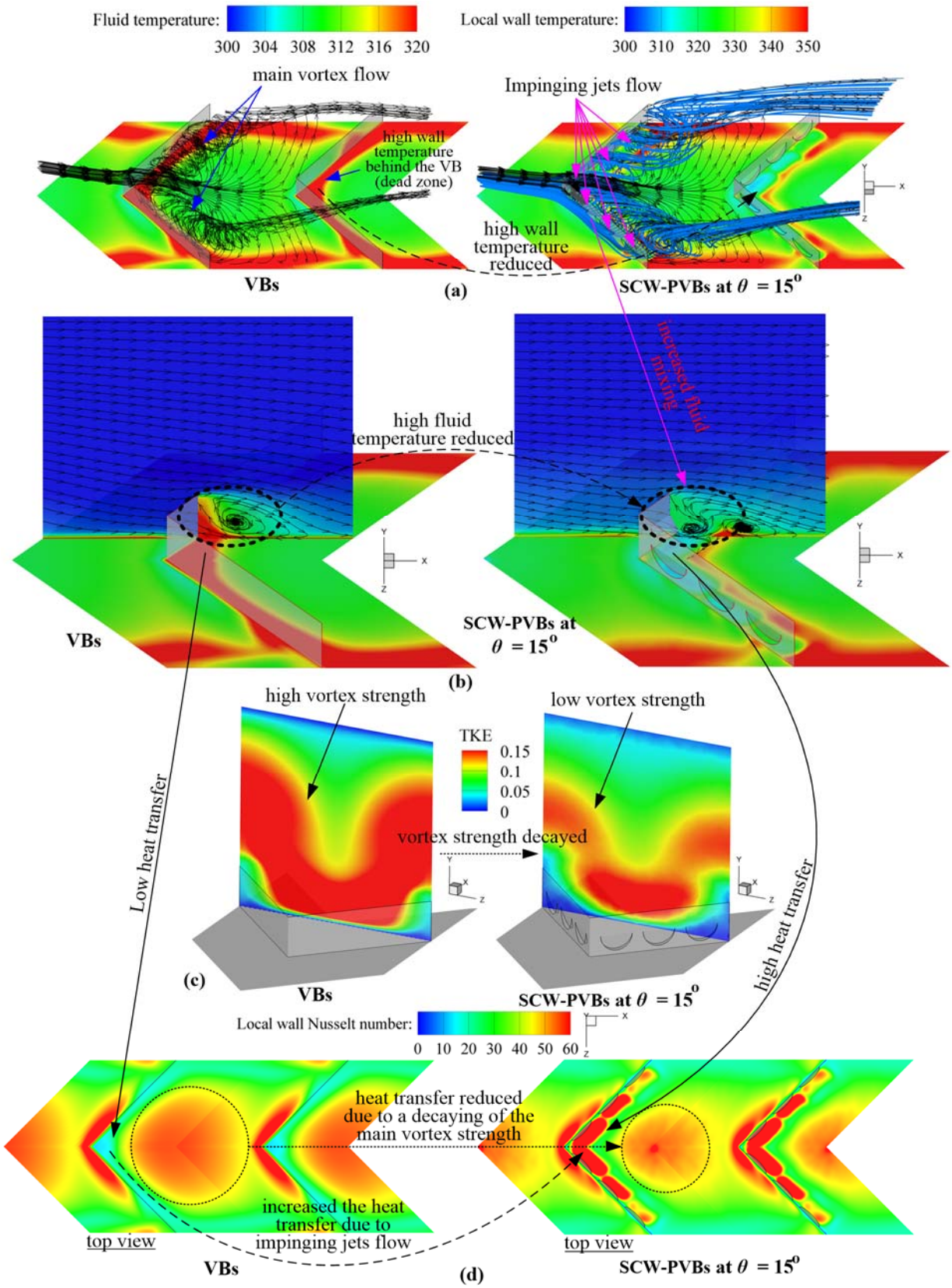

Figure 3.7. Comparison between VBs and SCW-PVBs at $\theta = 15^{o}$ on (a) 3D flow structure and local wall temperature, (b) 2D flow structure on flow direction plane and local wall temperature, (c) TKE field on transverse plane, and (d) local wall Nusselt number at BR = 0.20, PR = 1.0 and *Re* = 3,000.

In the case of semi-circular wing perforated V-type baffles (SCW-PVBs), there were two effects: (1) the impinging jet generated by the fluid flowed through the semi-circular holes of the wing and (2) the main vortex flow. The two effects showed better performance in promoting fluid mixing and thus heat transfer than the one effect (only the main vortex flow) offered by solid V-type baffles (VBs). The dead zones were diminished by using semi-circular wing perforated V-type baffles (SCW-PVBs) instead of solid V-type baffles (VBs). However, the semi-circular wing perforated V-type baffles (SCW-PVBs) gave weaker TKE than solid V-type baffles (VBs) because the main vortex strength reduced caused by the fluid flow through the semi-circular holes. The details of the local wall Nusselt number values for the solid V-type baffles (VBs) and semi-circular wing perforated V-type baffles (SCW-PVBs) are depicted in Fig. 3.8.

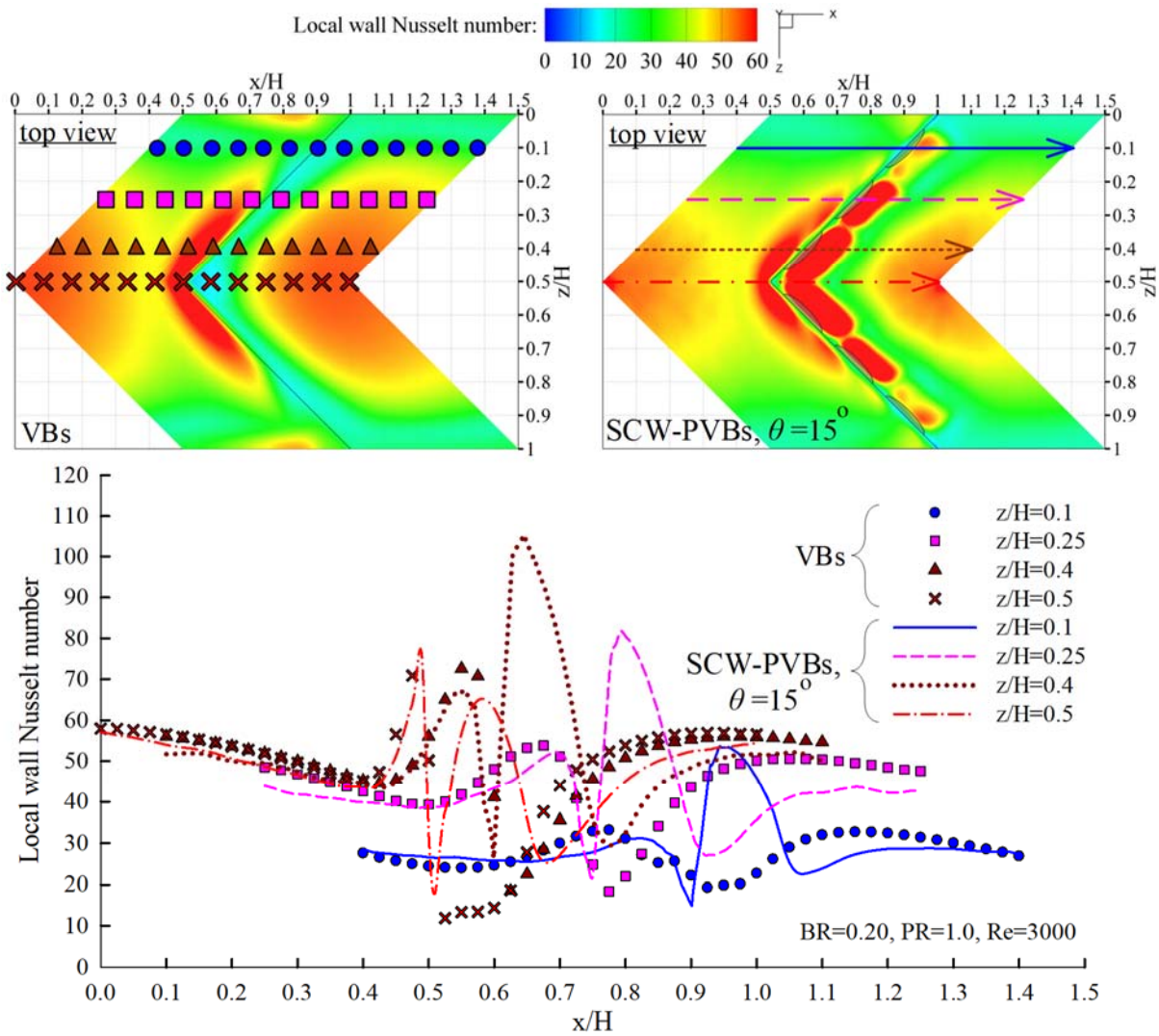

Figure 3.8. Local wall Nusselt numbers associated with VBs and SCW-PVBs at $\theta = 15^{o}$ at BR = 0.20, PR = 1.0 and *Re* = 3,000.

3.4.3.2 Effect of blockage ratio

Figure 3.9 displays the effect of blockage ratio (BR) of semi-circular wing perforated V-type baffles (SCW-PVBs) on the 3D flow structure and local wall temperature, 2D flow structure on flow direction plane and local wall temperature, TKE field on transverse plane and local wall Nusselt number. The controlled parameters were $\theta = 15^{o}$, PR = 1.0 and Re = 3,000. The numerical results showed that semi-circular wing perforated V-type baffles (SCW-PVBs) with larger BR gave smaller dead zones because the fluid flow through semi-circular holes and fluid mixing were facilitated. Therefore, the fluid temperature and wall temperature behind the baffles were considerably reduced. Moreover, the main vortex strength increased with increasing BR, the thermal boundary layer was more severely disrupted and thus, there was more efficient heat transfer through the channel wall.

3.4.3.3 Effect of pitch ratio

The effect of pitch ratio (PR) on the 3D flow structure and local wall temperature, 2D flow structure on flow direction plane and local wall temperature, TKE field on transverse plane and local wall Nusselt number are depicted in Fig. 3.10. The fixed parameters were $\theta = 15^{o}$, BR = 0.20 and Re = 3,000. In general, the semi-circular wing perforated V-type baffles (SCW-PVBs) generated the main vortex flow combined with the impinging jets flow for all PR. At the PR = 0.5, the main vortex flow and the impinging jets flow could access the whole area of the channel wall for every module. The boundary layer was drastically disturbed, the wall temperature was low and the heat transfer through the channel wall was high. The channel-wall area which was attacked by the main vortex flow showed high heat transfer behavior. As the PR increased, wall temperature increased because there was a large area which the main vortex flow could not access, especially, at the PR = 2.0. Moreover, decreasing of vortex strength led to a weaker disruption of a thermal boundary-layer. Therefore, heat transfer became less efficient.

3.4.3.4 Effect of attack angle

The Effect of attack angle (θ) on the semi-circular wing perforated V-type baffles (SCW-PVBs) is presented in Fig. 3.11. The 3D flow structure and local wall temperature, 2D flow structure on flow direction plane and local wall temperature, TKE field on transverse plane and local wall Nusselt number are reported at the same parameters: BR = 0.20, PR = 1.0 and Re = 3,000. As attack angle (θ) increased from 5° to 10°, the fluid flow through the semi-circular holes was promoted resulting in better fluid mixing and a smaller dead zone (high wall temperature behind the baffles reduced). Consequently, the heat transfer behind the baffles was enhanced. However, the strength of the main vortex flow was simultaneously diminished. Thus, the heat transfer of the area that was attacked by the main vortex flow was decreased. The effect of changing attack angle (θ) from 10° to 15° on heat transfer behavior

was similar to that from attack angle (θ) 5° to 10°. However, it is noteworthy that the heat transfer behind the baffles was only slightly improved.

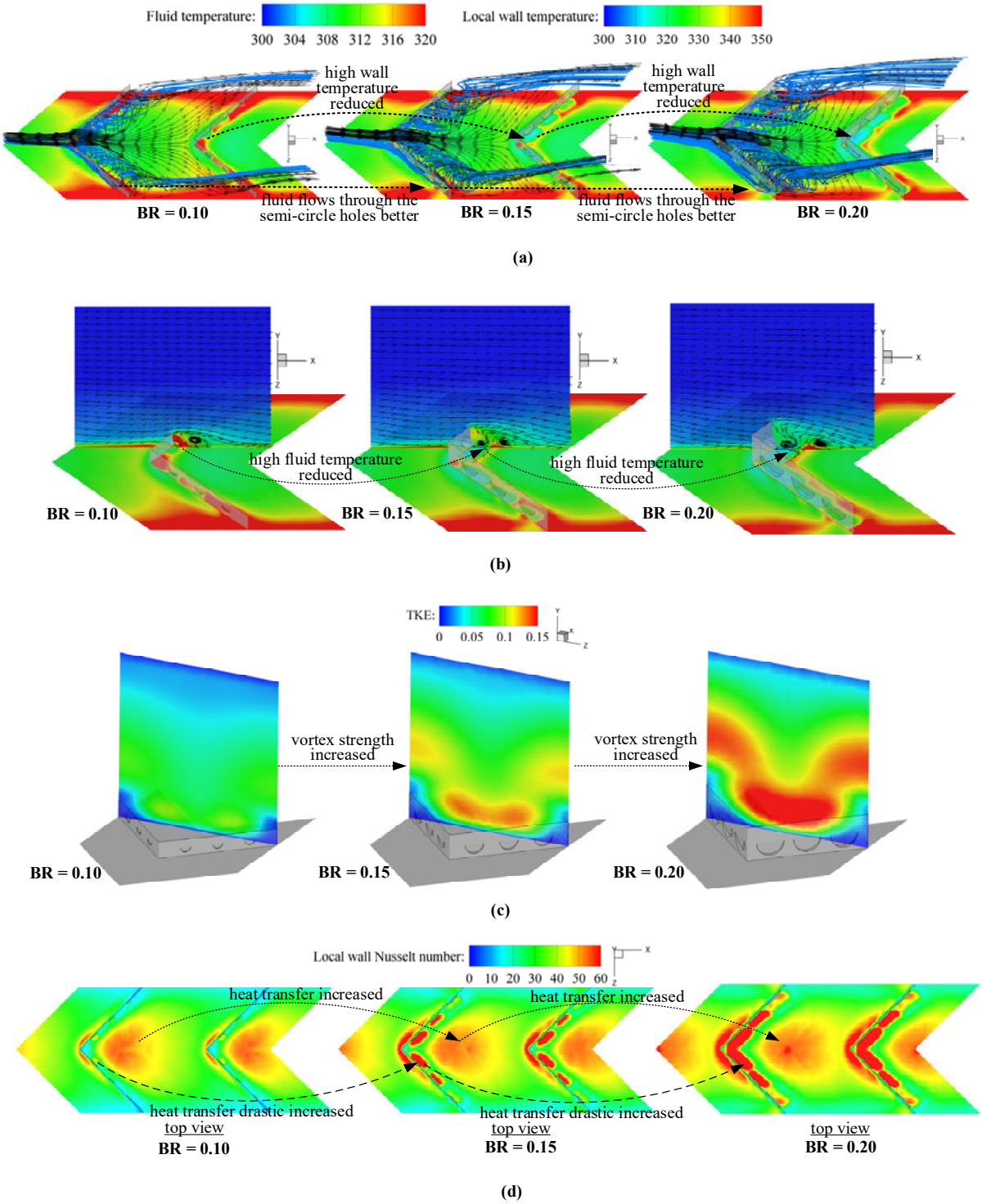

Figure 3.9. Effect of BR on (a) 3D flow structure and local wall temperature, (b) 2D flow structure on flow direction plane and local wall temperature, (c) TKE field on transverse plane, and (d) local wall Nusselt number for the SCW-PVBs at θ = 15°, PR = 1.0 and Re = 3,000.

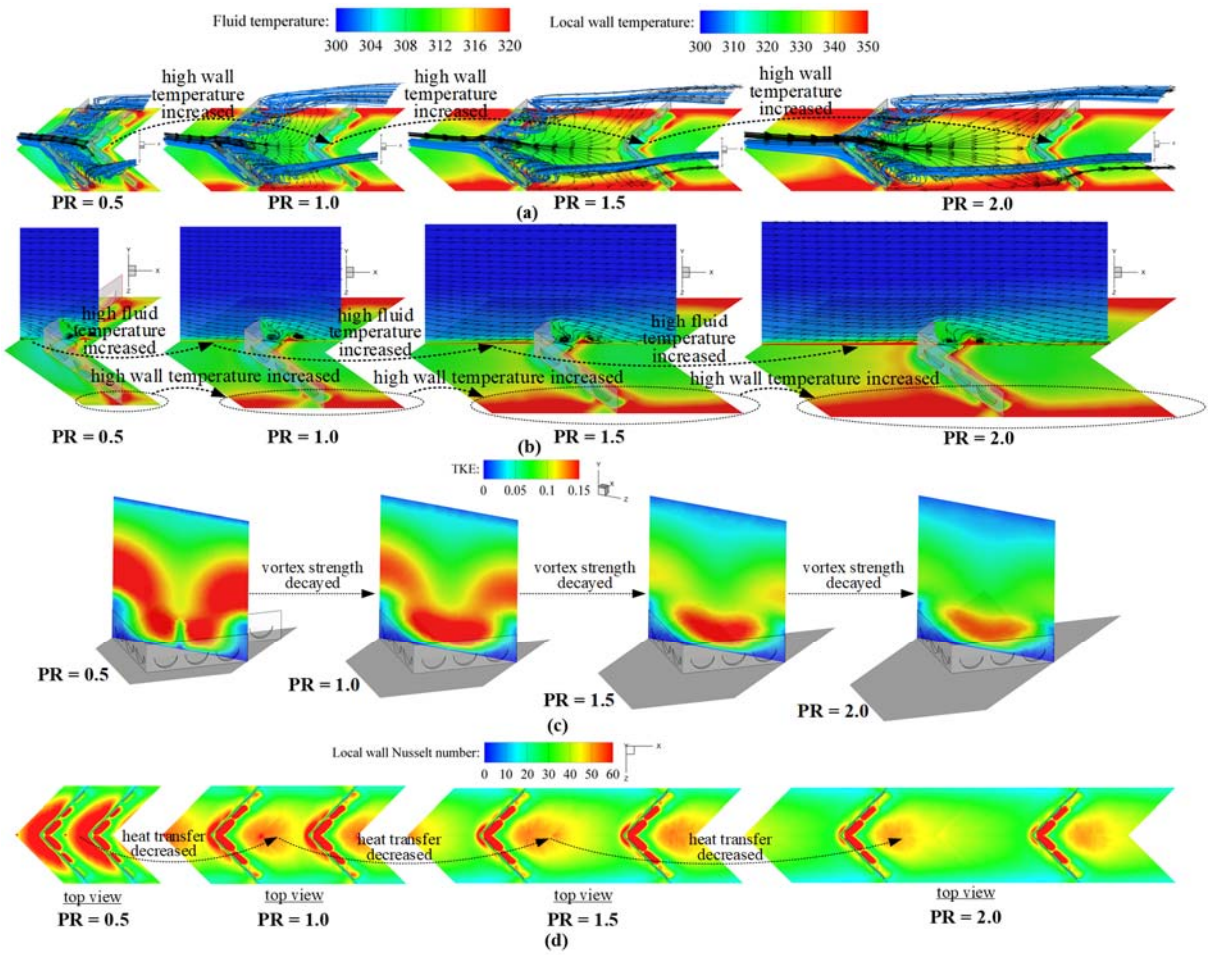

Figure 3.10. Effect of PR on (a) 3D flow structure and local wall temperature, (b) 2D flow structure on flow direction plane and local wall temperature, (c) TKE field on transverse plane, and (d) local wall Nusselt number for the SCW-PVBs at $\theta = 15^{o}$, BR = 0.20 and Re = 3,000.

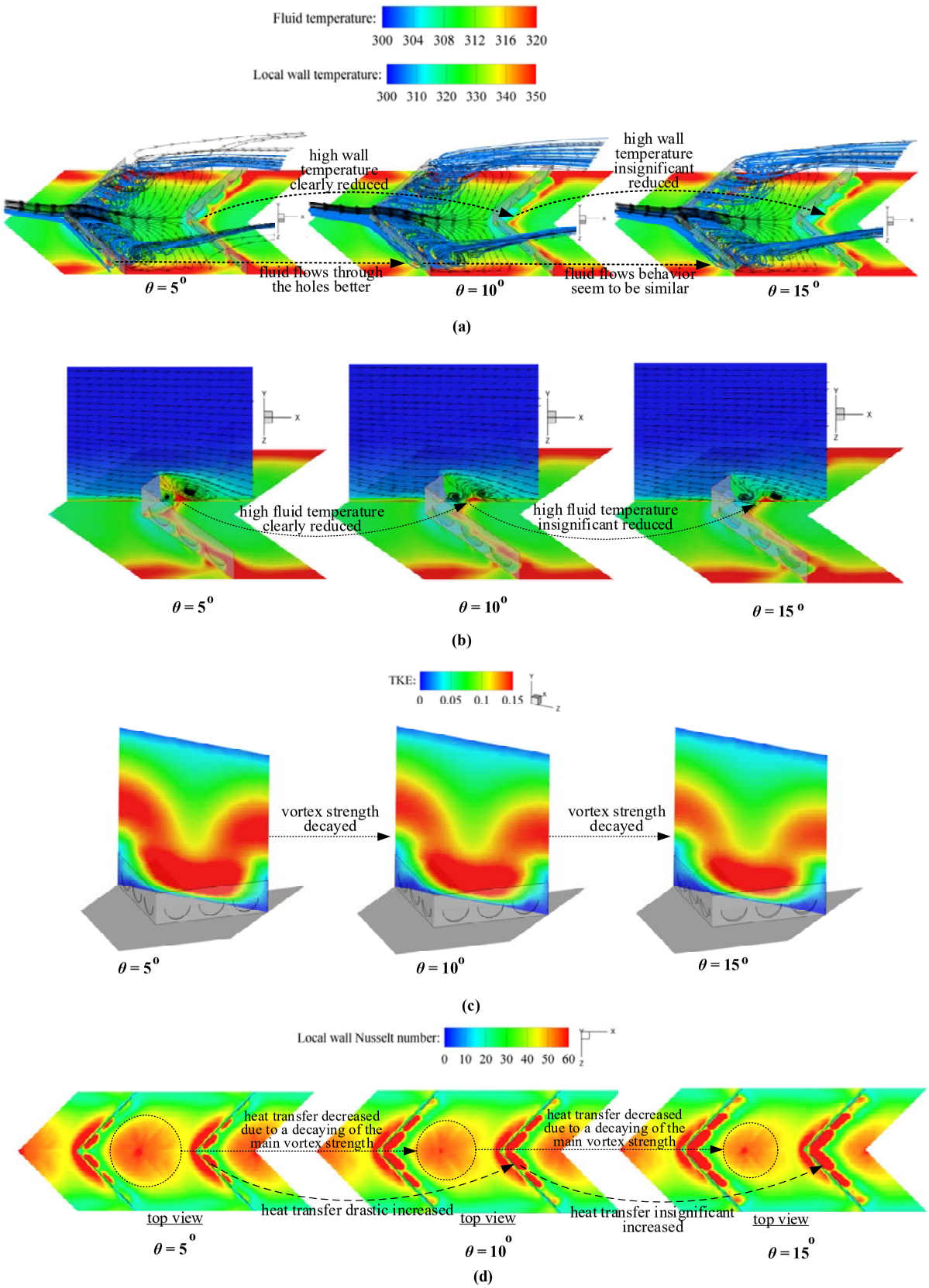

Figure 3.11. Effect of attack angle (θ) on (a) 3D flow structure and local wall temperature, (b) 2D flow structure on flow direction plane and local wall temperature, (c) TKE field on transverse plane, and (d) local wall Nusselt number for the SCW-PVBs at BR = 0.20, PR = 1.0 and Re = 3,000.

3.4.4 Performance evaluation

In this section, the heat transfer and pressure drop are presented in term of the ratio of Nusselt number, Nu/Nu_s, and the ratio of friction factor, f/f_s, respectively. The overall thermal performance is presented in term of TPF. For all cases, the data were obtained from the periodic model.

3.4.4.1 Heat transfer

The relationships of the Nusselt number ratio (Nu/Nu_s) with Re, Nusselt number ratio (Nu/Nu_s) with PR and Nusselt number ratio (Nu/Nu_s) with attack angle (θ) and PR are reported in Figs. 3.12-3.13. In general, Nusselt number ratio (Nu/Nu_s) tended to decrease with the rise of Reynolds numbers (Re) for all cases. At similar operating conditions, semi-circular wing perforated V-type baffles (SCW-PVBs) provided higher Nusselt number ratio (Nu/Nu_s) than the solid V-type baffles (VBs) for all cases because of the reduction of dead zone caused by the impinging jets flowing through the semi-circular holes. The rise of BR improved Nusselt number ratio (Nu/Nu_s) which related to the increased main vortex strength and promoted fluid flow through the semi-circular holes. On the other hand, the increasing PR led to decrease the Nusselt number ratio (Nu/Nu_s) due to the decaying main vortex strength, thicker thermal boundary layer and more blocked the heat transfer. Among the determined, attack angle of $\theta = 10^{o}$ gave the highest Nusselt number ratio (Nu/Nu_s). Because the baffles with $\theta = 10^{o}$ resulted in both moderate heat transfer behind the baffles and also in the area attacked by main vortex flow. However, baffles with $\theta = 5°$ and 15° provide too low heat transfer behind the baffles and in the area attacked by main vortex flow, respectively. Thus, the average heat transfer rates at $\theta = 5°$ and 15° were lower than that obtained at $\theta = 10°$. Because of the fluid moving through the semi-circular holes was better than $\theta = 5^{o}$ leading to drastically increased heat transfer at the region behind the baffles, while $\theta = 15^{o}$ gave a slight increase in the heat transfer at the region behind the baffles, but the heat transfer at the area where be attacked by the main vortex flow is reduced. Hence, the average heat transfer on the channel wall for $\theta = 15^{o}$ was lower than $\theta = 10^{o}$ for all cases. In the range of PR = 0.5-2.0, the Nusselt number ratio (Nu/Nu_s) for the solid V-type baffles (VBs) with BR = 0.10, 0.15 and 0.20 were in the range of 1.93-4.23, 2.11-4.79 and 2.23-5.14, respectively. For the semi-circular wing perforated V-type baffles (SCW-PVBs) at PR = 0.5-2.0, the Nusselt number ratio (Nu/Nu_s) with BR = 0.10, 0.15 and 0.20 were, respectively, in the range of 1.96-4.33, 2.07-4.6 and 1.99-4.46; 2.18-4.99, 2.23-5.22 and 2.21-5.09; and 2.33-5.37, 2.43-5.57 and 2.37-5.47 at $\theta = 5^{o}$, 10° and 15°, respectively. In the range of PR = 0.5-2.0, the semi-circular wing perforated V-type baffles (SCW-PVBs) with BR = 0.10, 0.15 and 0.20 provided higher Nusselt number ratio (Nu/Nu_s) than that the corresponding solid V-type baffles (VBs) by around 1.73-2.5%, 3.04-3.54% and 3.63-4.45%, respectively for $\theta = 5^{o}$; 7.3-8.75%, 7.66-8.98% and 7.78-8.48%, respectively, and for $\theta = 10^{o}$; and 3.02-5.58%, 4.29-6.31% and 5.92-6.47% respectively for $\theta =$

15°. The semi-circular wing perforated V-type baffles (SCW-PVBs) at BR = 0.20, PR = 0.5 and θ = 10° provided the maximum Nusselt number ratio (Nu/Nu_s) at 5.57 at the lowest Reynolds numbers (Re).

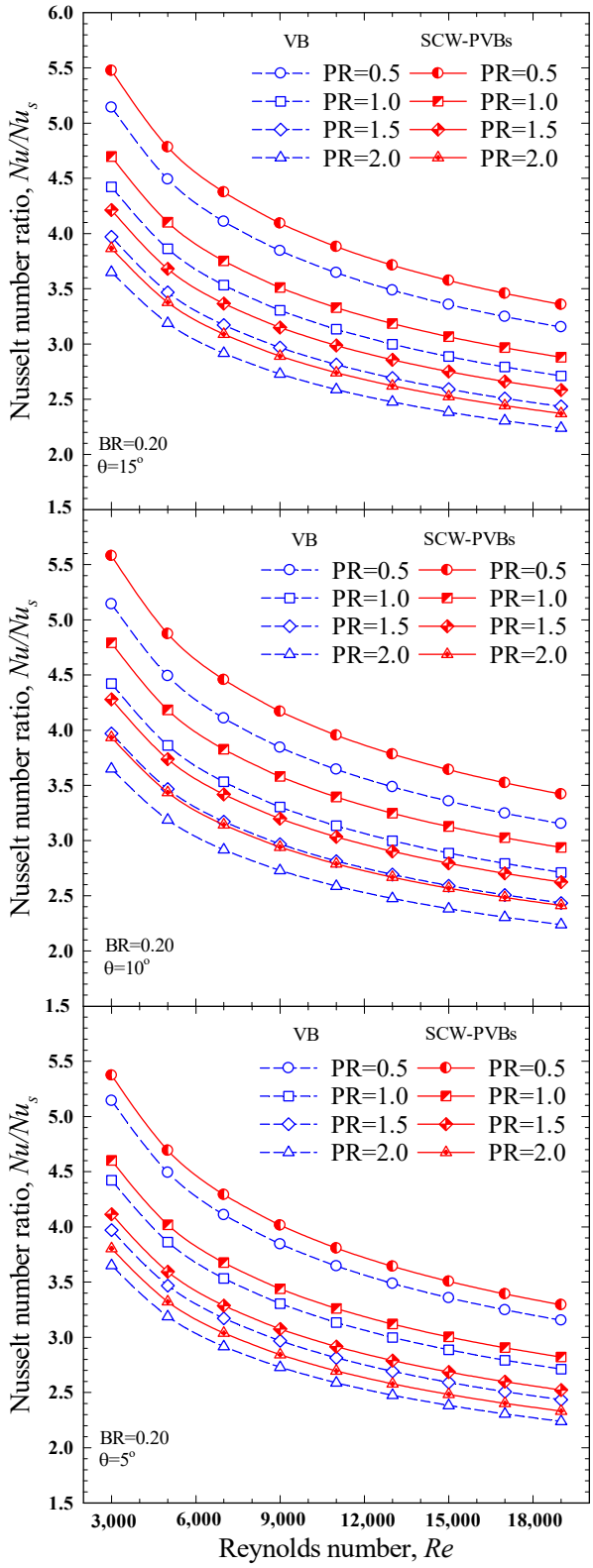

(a) BR = 0.2

Figure 3.12. Relationships of (a) Nusselt number ratio (Nu/Nu_s) with Reynolds number and (b) Nusselt number ratio (Nu/Nu_s) with PR.

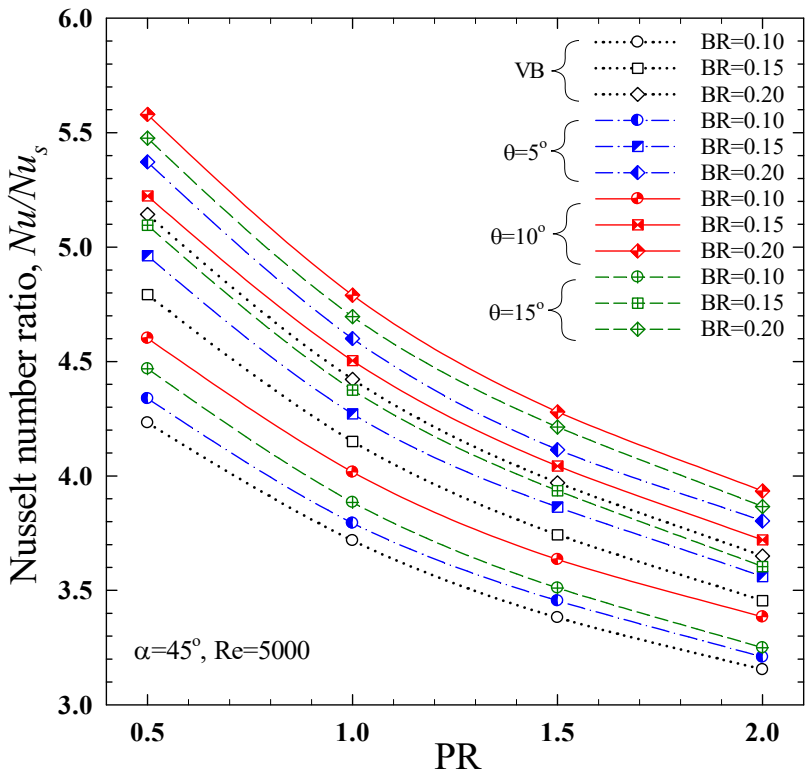

(b) BR = 0.1-0.2

Figure 3.12. Relationships of (a) Nusselt number ratio (Nu/Nu_s) with Reynolds number and (b) Nusselt number ratio (Nu/Nu_s) with PR. (*continued*)

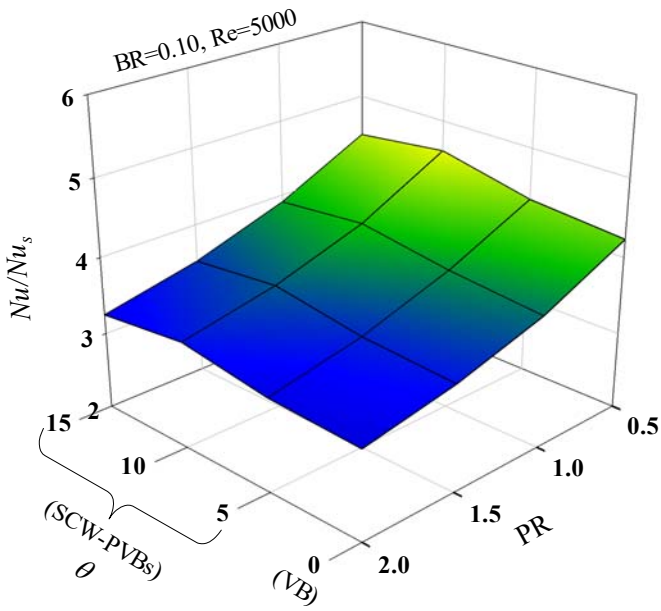

(a)

Figure 3.13. Relationships of Nusselt number ratio (Nu/Nu_s) with attack angle (θ) and PR for (a) BR = 0.10, (b) BR = 0.15 and (c) BR = 0.20 at *Re* =5,000.

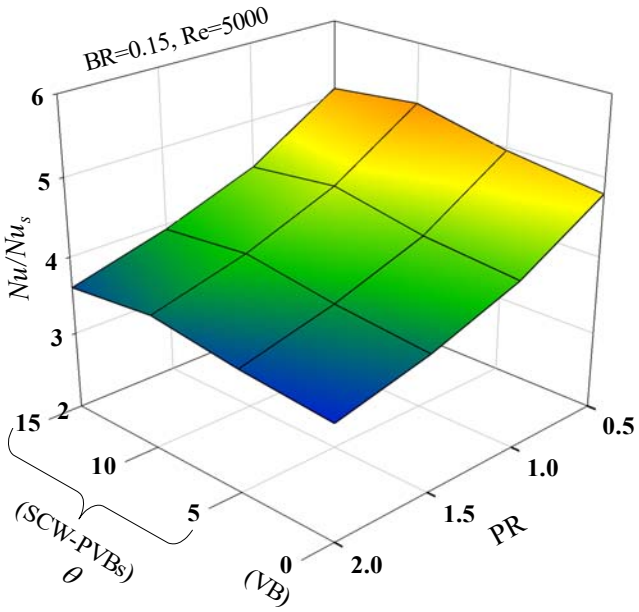

(b)

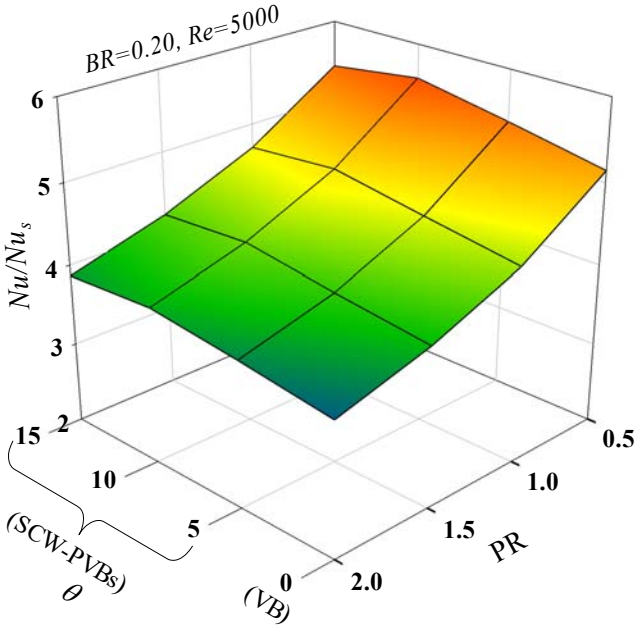

(c)

Figure 3.13. Relationships of Nusselt number ratio (Nu/Nu_s) with attack angle (θ) and PR for (a) BR = 0.10, (b) BR = 0.15 and (c) BR = 0.20 at *Re* =5,000. (*continued*)

3.4.4.2 Friction factor

The relationships of the friction factor ratio (f/f_s) with Reynolds numbers (*Re*), friction factor ratio (f/f_s) with PR and friction factor ratio (f/f_s) with attack angle (θ) and PR are reported in Figs. 3.14-3.15. In general, friction factor ratio (f/f_s) tended to increase with the rise of Reynolds numbers (*Re*) for all cases. At a given Re, the semi-circular wing perforated V-type baffles (SCW-PVBs) provided lower friction factor ratio (f/f_s) than the solid V-type baffles (VBs). Because of the flow blockage was reduced caused

by presence of the semi-circular holes. The reduction of friction loss helps in saving energy or pumping power. Increasing BR led to increased friction factor ratio (f/f_s) for both the solid V-type baffles (VBs) and semi-circular wing perforated V-type baffles (SCW-PVBs), due to more flow blockage. On the other hand, the rises of PR and θ resulted in lower friction factor ratio (f/f_s) due to less flow blockage. In the range of PR = 0.5-2.0, the friction factor ratio (f/f_s) for the solid V-type baffles (VBs) with BR = 0.10, 0.15 and 0.20 were in the range of 4.87-12.34, 7.38-21.64 and 10-31.59, respectively. For the semi-circular wing perforated V-type baffles (SCW-PVBs) at PR = 0.5-2.0, the friction factor ratio (f/f_s) with BR = 0.10, 0.15 and 0.20 were, respectively, in the range of 4.42-11, 6.98-19.65 and 9.17-28.18; 3.92-10.39, 6.38-18.62 and 8.49-25.81; and 3.56-9.76, 5.9-17.85 and 7.77-23.72 at $\theta = 5^o$, 10° and 15°, respectively. In the range of PR = 0.5-2.0, the semi-circular wing perforated V-type baffles (SCW-PVBs) with BR = 0.10, 0.15 and 0.20 provided lower friction factor ratio (f/f_s) than that the corresponding solid V-type baffles (VBs) by around 9.31-11.52%, 5.41-9.2% and 8.25-10.77%, respectively for $\theta = 5^o$; 15.8-19.5%, 13.18-13.95% and 15.07-18.28%, respectively for $\theta = 10^o$; and 20.89-26.84%, 17.5-20.04% and 22.13-24.9% respectively for $\theta = 15^o$.

3.4.4.3 Thermal enhancement factor

The relationships of the thermal performance factor (*TPF*) with Reynolds numbers (*Re*), thermal performance factor (*TPF*) with PR and thermal performance factor (*TPF*) with attack angle (θ) and PR are reported in Figs. 3.16-3.17. Generally, thermal performance factor (*TPF*) tended to decrease with the rise of Reynolds number. At similar conditions, the semi-circular wing perforated V-type baffles (SCW-PVBs) consistently provided higher thermal performance factor (*TPF*) than solid V-type baffles (VBs). This is because of the increasing heat transfer together with the decreasing pressure drop of the semi-circular wing perforated V-type baffles (SCW-PVBs). In the range of PR = 0.5-2.0, the thermal performance factor (*TPF*) for the solid V-type baffles (VBs) with BR = 0.10, 0.15 and 0.20 was found in the range of 1.18-2.27, 1.15-2.2 and 1.12-2.13, respectively. For the semi-circular wing perforated V-type baffles (SCW-PVBs) at PR = 0.5-2.0, the thermal performance factor (*TPF*) with BR = 0.10, 0.15 and 0.20 were, respectively, in the range of 1.21-2.41, 1.18-2.35 and 1.17-2.3; 1.32-2.59, 1.27-2.51 and 1.24-2.45; and 1.3-2.56, 1.25-2.50 and 1.23-2.45 at $\theta = 5^o$, 10° and 15°, respectively. In the range of PR = 0.5-2.0, the semi-circular wing perforated V-type baffles (SCW-PVBs) with BR = 0.10, 0.15 and 0.20 provided lower thermal performance factor (*TPF*) than that the corresponding solid V-type baffles (VBs) by around 4.51-5.79%, 4.63-6.33% and 6.7-7.78%, respectively for $\theta = 5^o$; 13.92-14.28%, 12.05-13.59% and 12.74-14.69%, respectively for $\theta = 10^o$; and 12.29-12.92%, 10.93-12.11% and 13.53-15.22% respectively for $\theta = 15^o$. The maximum thermal performance factor (*TPF*) of 2.6 was achieved by using the semi-circular wing perforated V-type baffles (SCW-PVBs) having BR = 0.10, PR = 0.5, $\theta = 10^o$ at *Re* of 3,000.

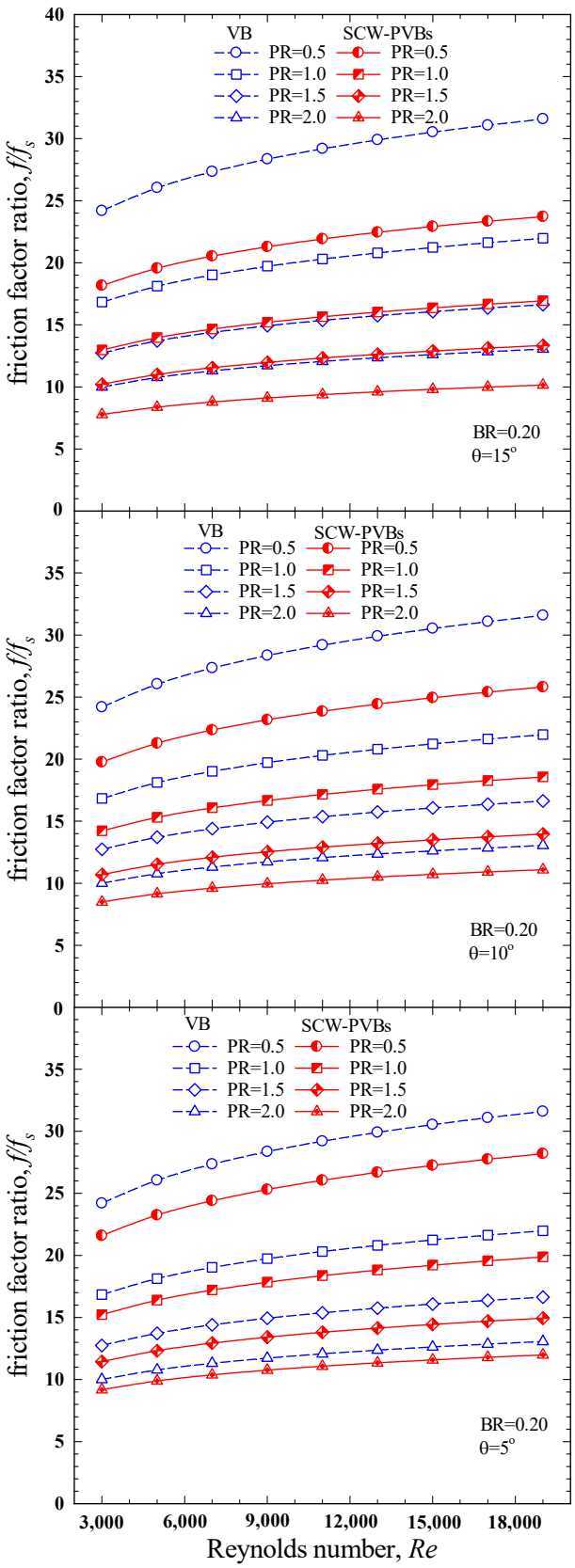

(a) BR = 0.2

Figure 3.14. Relationships of (a) friction factor ratio (f/f_s) with Reynolds number and (b) friction factor ratio (f/f_s) with PR.

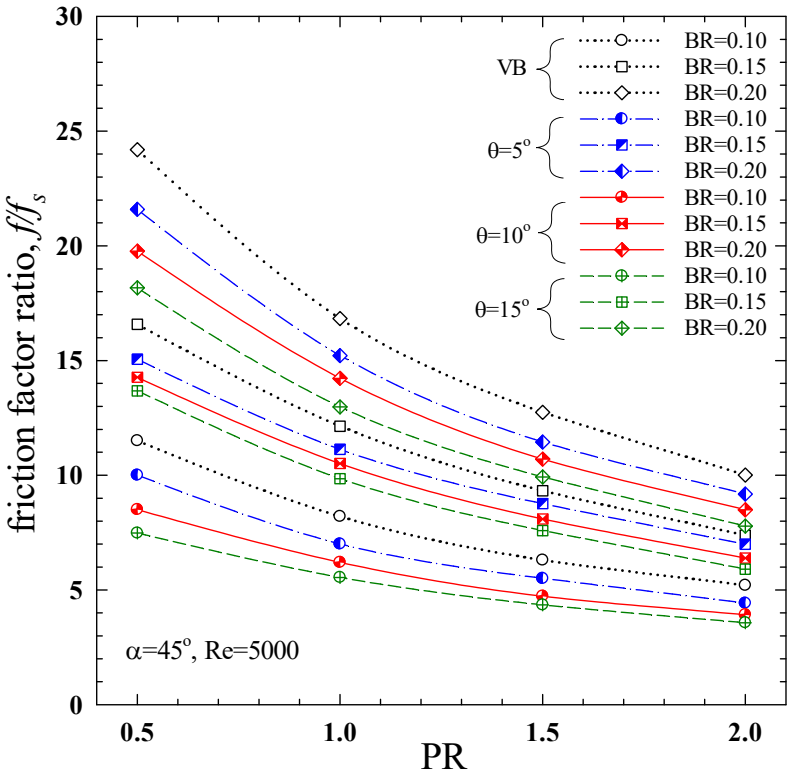

(b) BR = 0.1-0.2

Figure 3.14. Relationships of (a) friction factor ratio (f/f_s) with Reynolds number and (b) friction factor ratio (f/f_s) with PR. (*continued*)

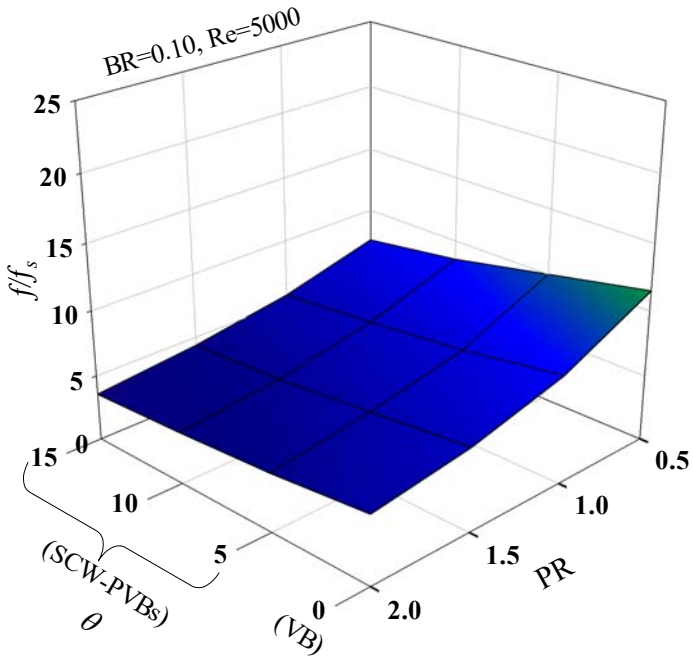

(a)

Figure 3.15. Relationships of friction factor ratio (f/f_s) with attack angle (θ) and PR for (a) BR = 0.10, (b) BR = 0.15, and (c) BR = 0.20 at *Re* =5,000.

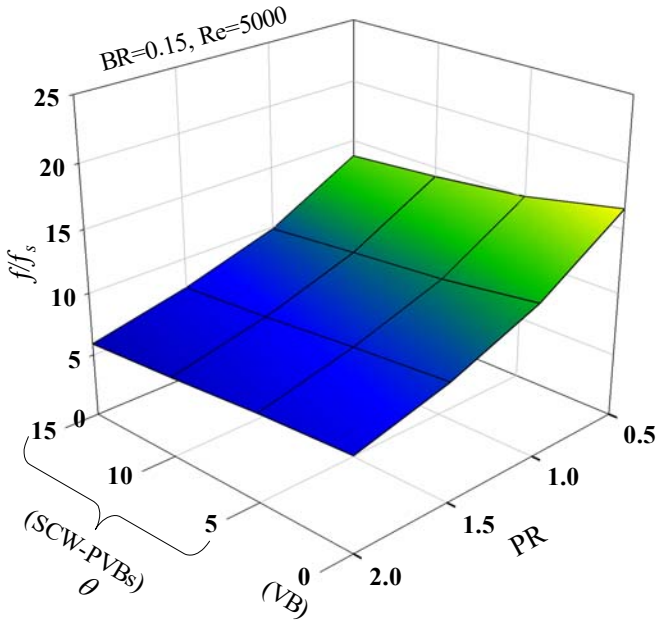

(b)

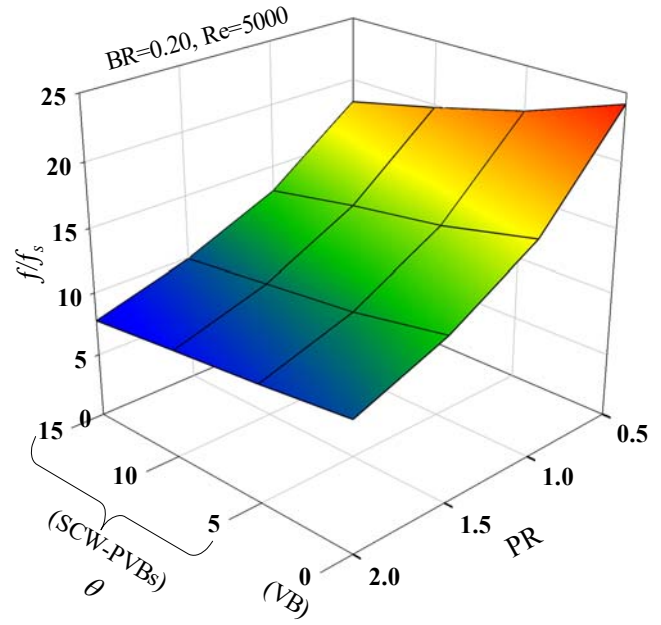

(c)

Figure 3.15. Relationships of friction factor ratio (f/f_s) with attack angle (θ) and PR for (a) BR = 0.10, (b) BR = 0.15, and (c) BR = 0.20 at *Re* =5,000. (*continued*)

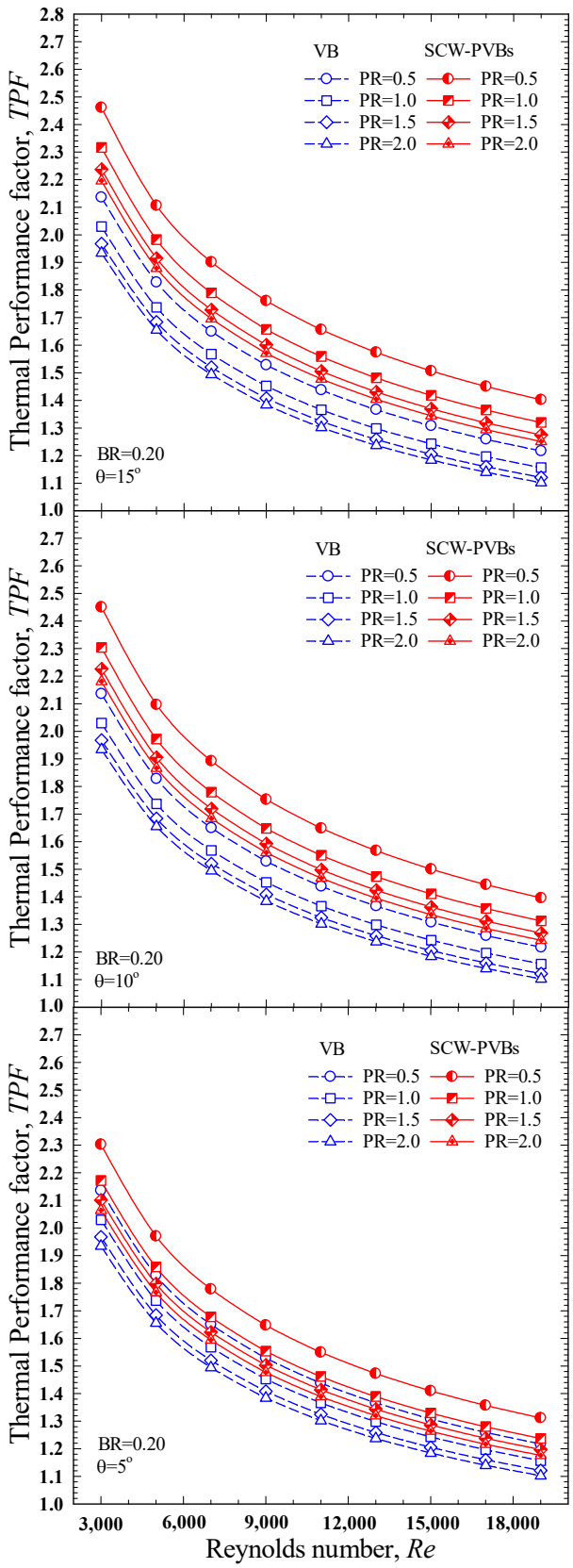

(a) BR = 0.2

Figure 3.16. Relationships of (a) thermal performance factor (*TPF*) with Reynolds number and (b) thermal performance factor (*TPF*) with PR.

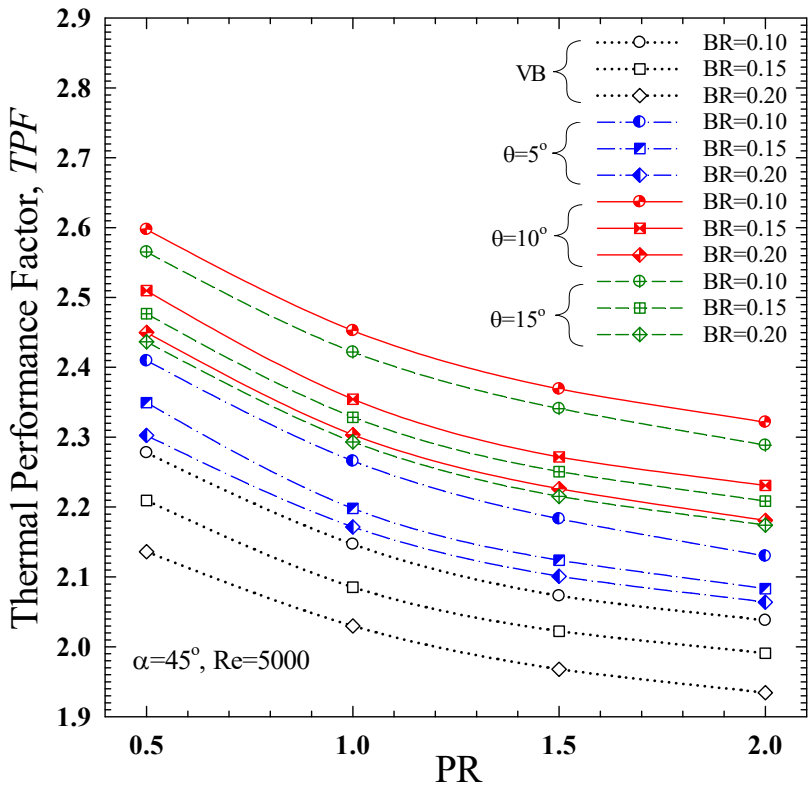

(b) BR = 0.1-0.2

Figure 3.16. Relationships of (a) thermal performance factor (*TPF*) with Reynolds number and (b) thermal performance factor (*TPF*) with PR. (*continued*)

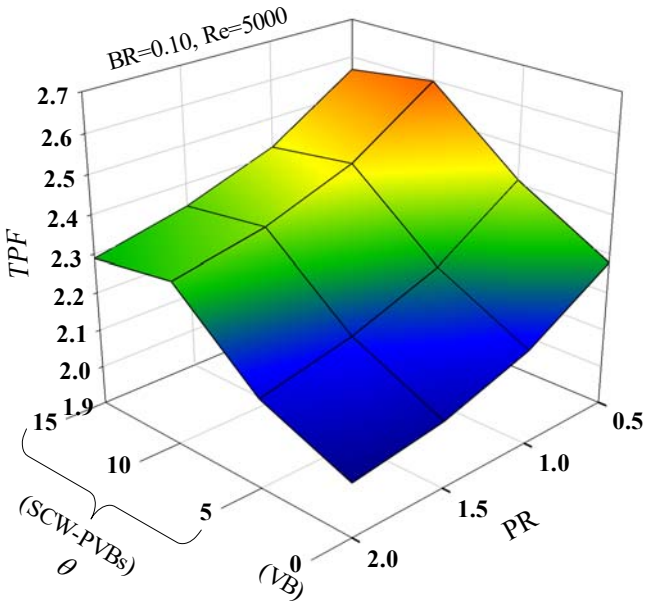

(a)

Figure 3.17. Relationships of thermal performance factor (*TPF*) with attack angle (θ) and PR for (a) BR = 0.10, (b) BR = 0.15, and (c) BR = 0.20 at *Re* =5,000.

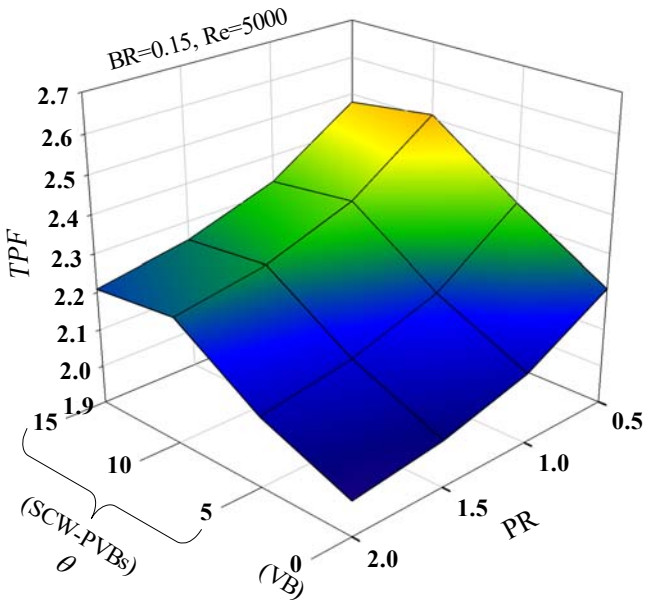

(b)

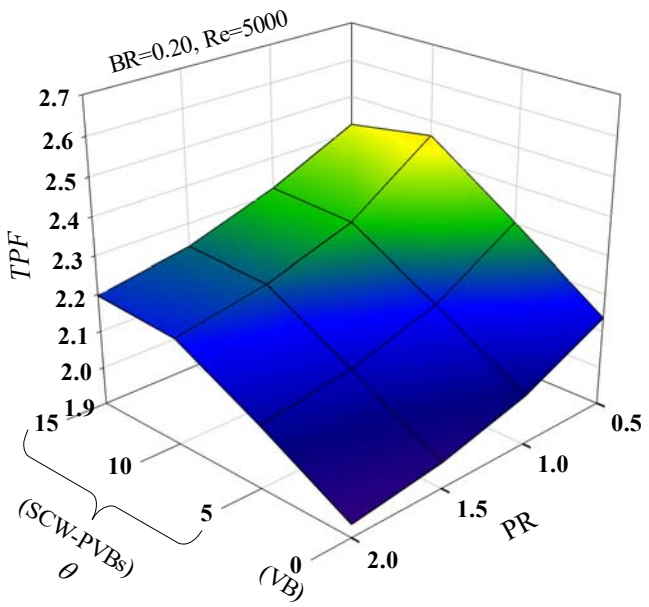

(c)

Figure 3.17. Relationships of thermal performance factor (*TPF*) with attack angle (θ) and PR for (a) BR = 0.10, (b) BR = 0.15, and (c) BR = 0.20 at *Re* =5,000. (*continued*)

3.5 Nomenclature

A	heat transfer area, m^2
BR	blockage ratio, dimensionless
$C_{1\varepsilon}$	turbulent model coefficient, dimensionless
$C_{2\varepsilon}$	turbulent model constant, dimensionless
C_{μ}	function of the mean strain and rotation rate, dimensionless
D_h	hydraulic diameter, m

e	distance between the semi-circular hole, mm
f	friction factor, dimensionless
G_k	production of turbulence kinetic energy due to the mean velocity gradients, kg s^{-3} m^{-1}
H	channel height, mm
h_x	local convective heat transfer coefficient, W m^{-2} K^{-1}
k	turbulent kinetic energy, m^2 s^{-2}
k_a	thermal conductivity of air, W m^{-1} K^{-1}
Nu	average Nusselt number, dimensionless
Nu_x	local Nusselt number, dimensionless
P	static pressure, Pa
Pr	Prandtl number, dimensionless
p	distance between the baffles, mm
Re	Reynolds number, dimensionless
u	velocity, m s^{-1}
$\bar{u}$	mean velocity, m s^{-1}
u_i	velocity component in x_i-direction, m s^{-1}
u_i'	fluctuation velocity in x_i-direction, m s^{-1}
u_j	velocity component in x_j-direction, m s^{-1}
u_j'	fluctuation velocity in x_j-direction, m s^{-1}
W	channel wide, mm
x_i, x_j	coordinate direction, m
x	x-position, m
y	y-position, m
z	z-position, m

Greek letters

μ	dynamic viscosity, kg s^{-1} m^{-1}
Γ	thermal diffusivity, kg s^{-1} m^{-1}
Γ_t	turbulent thermal diffusivity, kg s^{-1} m^{-1}
σ_k	turbulent Prandtl numbers for k, dimensionless
σ_ε	turbulent Prandtl numbers for ε, dimensionless
δ_{ij}	Kronecker delta, m
ε	turbulent dissipation rate, m^2 s^{-3}
ρ	density, kg m^{-3}
θ	attack angle, degree

Subscripts

s	smooth channel

t turbulent

s surface

a air

Superscripts

— average

References in chapter 3

1 Nuntadusit C, Wae-hayee M, Bunyajitradulya A, Eiamsa-ard S. Thermal visualization on surface with transverse perforated ribs. International Communications in Heat and Mass Transfer. 2012;39:634-639.

2 Promvonge P, Skullong S. Thermal characteristics in solar air duct with V-shaped flapped-baffles and chamfered-grooves. International Journal of Heat and Mass Transfer. 2021;172:121220.

3 Kumar R, Kumar A, Chauhan R, Sethi M. Heat transfer enhancement in solar air channel with broken multiple V-type baffle. Case Studies in Thermal Engineering. 2016;8:187-197.

4 Kumar R, Sethi M, Chauhan R, Kumar A. Experimental study of enhancement of heat transfer and pressure drop in a solar air channel with discretized broken V-pattern baffle. Renewable Energy. 2017;101:856-872.

5 Kumar R, Chauhan R, Sethi M, Kumar A. Experimental study and correlation development for Nusselt number and friction factor for discretized broken V-pattern baffle solar air channel. Experimental Thermal and Fluid Science. 2017;81:56-75

6 Maithani R, Saini JS, Heat transfer and friction factor correlations for a solar air heater duct roughened artificially with V-ribs with symmetrical gaps. Experimental Thermal and Fluid Science. 2016;70:220-227.

7 Promvonge P, Skullong S, Heat transfer in solar receiver heat exchanger with combined punched-V-ribs and chamfer-V-grooves. International Journal of Heat and Mass Transfer. 2019;143:118486.

8 Incropera F, Dewitt PD. Introduction to Heat Transfer. 3rd edition, John Wiley & Sons Inc, New York, 2006.

9 Tamna S, Skullong S, Thianpong C, Promvonge P. Heat transfer behaviors in a solar air heater channel with multiple V-baffle vortex generators. Solar Energy. 2014;110:720-735.

Publication list

1) S. Eiamsa-ard, A. Suksangpanomrung, P. Promthaisong, Enhanced heat transfer mechanism and flow topology of a channel contained with semi-circular hinged V-shaped baffles, *International Journal of Thermal Sciences*, Vol. 177, Article no. 107577, July 2022, 23 pages, DOI: 10.1016/j.ijthermalsci.2022.107577.

CHAPTER 4

Heat transfer enhancement in channel: Experimental investigation

4.1 Experimental design details

4.1.1 Experimental setup

Figure 4.1 represents a schematic diagram of the heat transfer enhancement apparatus. Air was drawn by a 3 hp blower through the flow meter and then a setting chamber with a 1.0 kW heater. A high-pressure blower, heating section and settling chamber, were connected in series for the experiments. A three-phase high pressure blower was used to supply test air to the apparatus through a calming section. The volumetric air flow rate was controlled by an inverter and the bypass valves located behind the blower exit. The Reynolds numbers of air through the orifice flow meter were set at 6,000, 9,000, 12,000, 15,000, 18,000, 21,000, and 24,000. A circular tube with an orifice plate flow meter positioned between the air blower and the settling chamber allowed for the measurement of the pressure loss across an orifice plate using a digital pressure gauge. A rectangular channel with a 40 mm height (H) and 150 mm width (W) had 3 sections—an inflow section, a heating section, and an exit flow section, located in line with a settling chamber. A 2,000 mm long inflow or calming section was used to obtain fully developed flow in the test channel. The lengths of the heating and outlet flow sections were 900 mm and 600 mm, respectively. The bottom surface of the test channel was made of an acrylic bar to which a heat flux was applied and a thermochromic liquid crystal sheet (TLC) was performed to indicate the temperature response. To mitigate heat losses from the heater, the channel is insulated with glass wool on the backside of the plate heater and covered with polyethylene foam and thick wood. At the interfaces of the entry and outlet ends of the channel, low thermal conductivity acrylic bars were positioned to act as a thermal barrier. With a channel aspect ratio of AR = 3.75, a constant wall temperature in the transverse direction can be assumed. In the experimental tests, the speed of a 3-hp air blower was controlled using a three-phase inverter to achieve the desired volumetric air flow rates. The tested Reynolds numbers (Re) ranged from 6,000 to 24,000, with air velocities ranging between 1.509 and 6.039 m/s. An orifice plate flow meter was built in accordance with ASME standards which calibrated with a vane anemometer. A pair static pressure gauges were set up on the top of the channel wall in order to measure the axial pressure losses across the test section, which were then utilized for calculating the friction factor. These were positioned on the channel's centerline. One of these taps is positioned 40 mm ahead of the entrance to the testing section, while another is placed 20 mm downstream of the exit from the test section. Using calibrated resistance temperature detectors (RTDs) the entry and exit air temperatures were identified. Twenty thermocouples of the T type were affixed

to the top channel wall to monitor the surface temperatures at selected locations along the test section. Temperatures and pressure drops were collected at steady state conditions utilizing a data logger. An AC power supply was used in conjunction with a clamp meter (Fluke 376 FC) to measure the power input needed to heat the channel bottom and keep the heat flux at a constant 600 W m^{-2}. A thin heater sheet with a thickness of 50.8 μm was utilized on the heat transfer surface. The thin heater sheet was stretched across two copper bus bars. A heat transfer surface or thin heater sheet was heated by an alternating current power supply capable of supplying current (I) up to 0.8 Amps. A power controller circuit modulated the electrical input to the plate heater in order to maintain a constant wall heat flux condition. Calculation of the overall electrical power provided to the heater was based on electrical current and voltage measured using the calibrated power meter. Electrical input to the plate heater was modulated using a power controller circuit to achieve uniform wall heat flux.

A 2.2-kW blower and an inverter-adjustable working speed was employed to initiate and control the flow of 26 °C indoor air into the apparatus. The required mass flow rate (modulated with an orifice flow meter) was estimated using an ASME standard [1] that was carefully calibrated utilizing hot-wire anemometers (Testo 480). The test part was made of clear, see-through acrylic so that images could be taken. As shown in Fig. 4.1, TLCs were mounted on the inside bottom wall to measure how the temperature of the channel walls changed. A TLC sheet covered the thin heating sheet to indicate the wall temperature distribution. Then, a high-resolution camera was used to record the changes in color of the TLCs, and an image processing tool was utilized to figure out the temperature of the channel walls. A thermochromic liquid crystal (TLC) sheet was placed on the heated test surface to collect data on the surface temperature distribution. A temperature range of 30-35 ºC was appropriate for the TLCs utilized in the present investigation. After that, an image processing program was used to perform an analysis of the obtained images to provide the local Nusselt number. Three RTDs (Pt-100) were installed downstream and upstream of the testing channel to evaluate the fluid temperature. A data logger (Fluke 2680A) was used to collect all thermocouple outflow temperature data and continually log the information to a computer. The mean friction factor was calculated using two static pressure taps positioned on top of the testing channel. A digital pressure gauge (Dwyer Mark III) was utilized to monitor the longitudinally recorded pressure decreases over the testing section. Experiments on pressure drop and heat transfer were performed independently. The heat transfer experiment was carried out under a uniform wall heat flux. The bottom wall was used as the heat transfer area and was kept at a constant steady heat flux condition. The isothermal pressure drop across the test section was measured isothermally without heat supplied through a heating sheet. All of the equipment used in the current measurement was calibrated using benchmarked calibrators. The instruments utilized in the current investigation had an estimated precision of 0.12 m/s for the vane-type anemometer, 0.5 mm for the manometer, and 0.1°C for the thermocouples.

(a) Image of a rectangular channel heat transfer setup

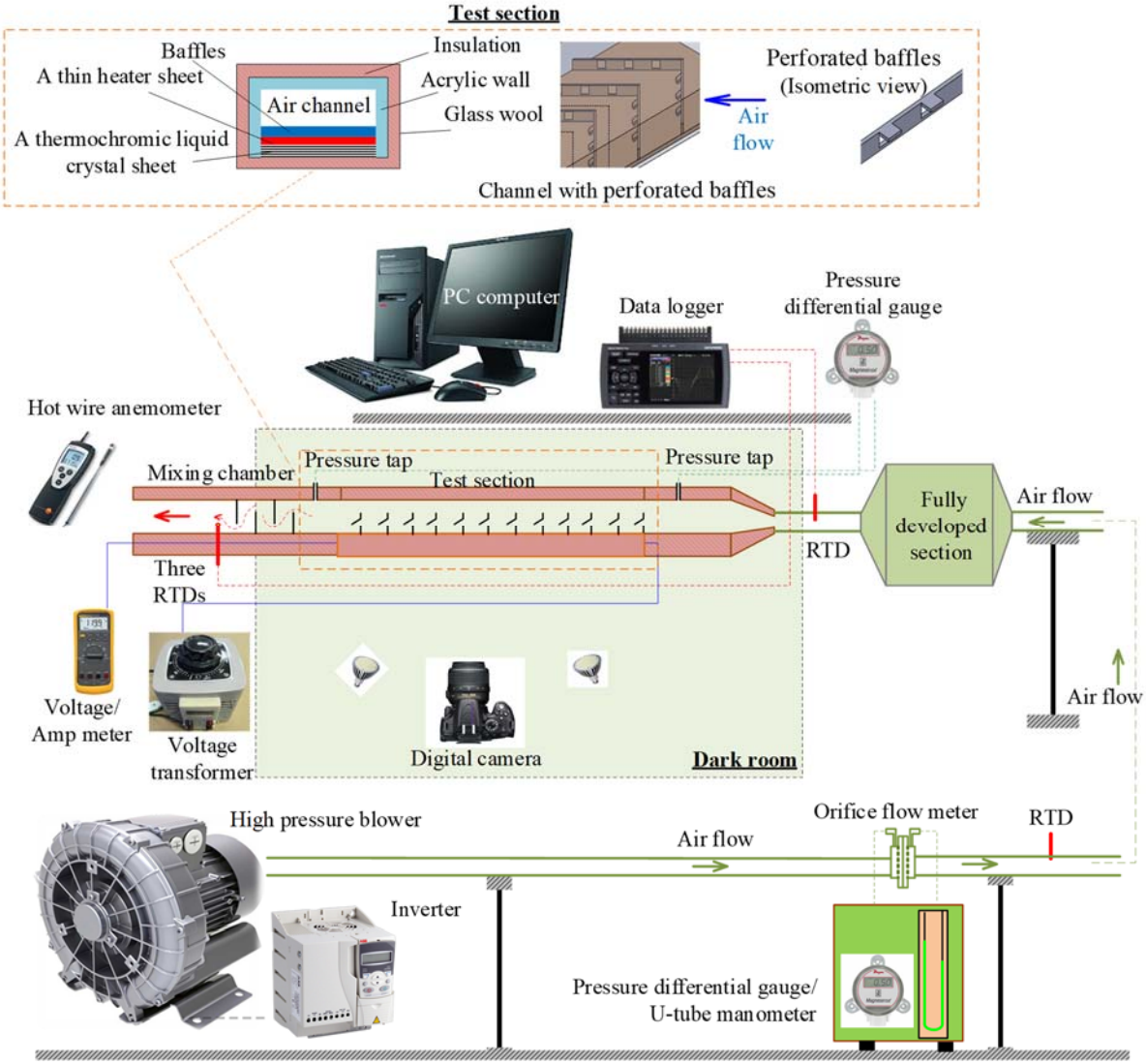

(b) Schematic diagram of heat transfer setup

Figure 4.1. Image and schematic diagram of channel mounted with various perforated baffles.

4.1.2 Thermochromic liquid crystals

Thermochromic liquid crystals (TLCs) are materials that indicate temperature without making physical touch. Temperature causes TLCs to change color. This approach is both affordable and practical. It does not need any special equipment or precise measurements. The hue of thermochromic surfaces is used to determine temperature change. Thermochromic data may be captured in high-resolution using digital cameras. Image processing and analysis are simply made using software [2]. In general, commercial TLCs are divided into two categories based on their bandwidths: narrowband and wideband. The wideband TLCs can measure temperature distributions in the range of 5-20 °C, while narrowband TLCs can only measure temperature distributions in the range of 0.5-2 °C. Most heat transfer research focuses on temperature differences greater than 5°C. As a result, wideband TLCs have been used in a number of investigations [3]. The wideband thermochromic liquid crystal sheets are also applied in the present work. Prior to the measurement, TLCs are calibrated.

4.1.2.1 Molecular structure of TLCs

Thermochromic liquid crystal materials are organic compounds that change their state (solid or liquid) as a function of temperature. When exposed to white light, they take on the appearance of a translucent solid. Their chemical structure changes when the temperature rises to a particular degree. Subsequently, they reflect light at wavelengths that vary with temperature. When a material hits its red start point (T_{rs}), its hue shifts from translucent to grey, then red, orange, yellow, and green as the temperature rises. The material achieves its blue start point at higher temperatures (T_{bs}). The hue shifts from purple to dark purple as the temperature rises, before reverting to its original condition of transparency. There are several forms of thermochromic liquid crystals. Oil, powder, tiny capsules, liquid sprayed to surfaces, or polymer sheets which are capable to measure temperature on complex surfaces, such as those applied in the current work [4].

4.1.2.2 TLC Calibration

Grassi *et al.* [5] proposed a thermochromic liquid crystal calibration approach that is important for reliable temperature measurement. Either isothermal calibration or temperature gradient calibration is capable of performing the procedure. The former method is selected for the present work. The temperature of a thermochromic liquid crystal surface is kept steady using this approach. The colors were collected using a Nikon D5100 digital camera. Despite the fact that the equipment and calibration method are simple, an accurate calibration takes time for collecting enough data. In addition, picture parameters such as exposure, camera settings, lighting angles, and image angles in the calibration process must be comparable to those applied in experiments.

The equipment used in the calibration procedure is shown in Fig. 4.2(a). The 304 stainless steel bucket dimension was 400×400×400 mm^3 with a 0.8 mm thickness. To raise the water temperature, a 2.0-kW

heater was employed, which was regulated by an adjustable AC power supply. Water in the bucket was stirred for uniform temperature distribution. Insulation was placed in the regions surrounding the test sample to limit heat losses to the environment. A rectangular 200-mm-wide and 200-mm-long piece at the bottom of the test stand was opened for the installation of a 0.05-mm-thick stainless-steel sheet. The stainless-steel sheet was covered with a thermochromic liquid crystal layer. To collect color pictures, a high-resolution digital camera was mounted in front of the TLCs. The temperature was monitored with an RTD Pt100, and the surface temperatures of the stainless-steel sheet were measured using three RTD Pt100s. The temperature ranged from 25- 40 °C in each color calibration, from the point where the thermochromic liquid crystals no longer turned black color to the point where the TLCs turn dark blue color or dark purple color. The TLCs were temperature calibrated by comparing measured temperatures to photos acquired when the temperatures of the stainless-steel sheet were held constant for at least 10 seconds. To check for hysteresis (details in section 2.3), color calibration was performed during both heating (25-40 °C) and cooling (40-25 °C). During calibration, the temperature was raised in 0.1°C increments. Triplicate calibration measurements were taken.

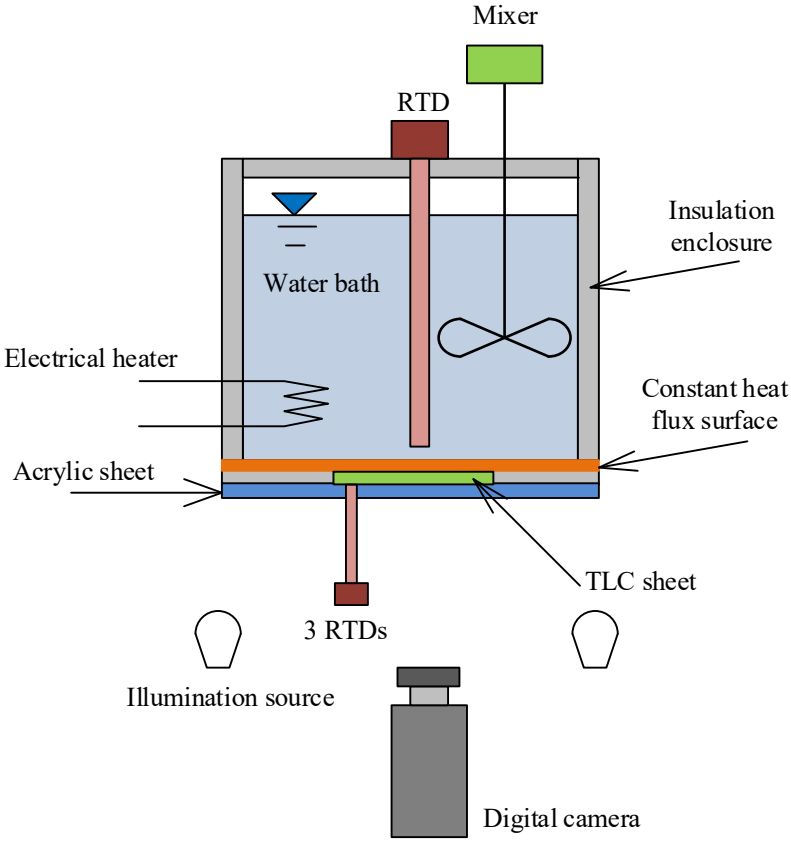

(a) TLC calibration flowchart

Figure 4.2. The thermochromic liquid crystals calibration equipment: (a) calibration test equipment, and (b) uniform surface temperature pictures by color.

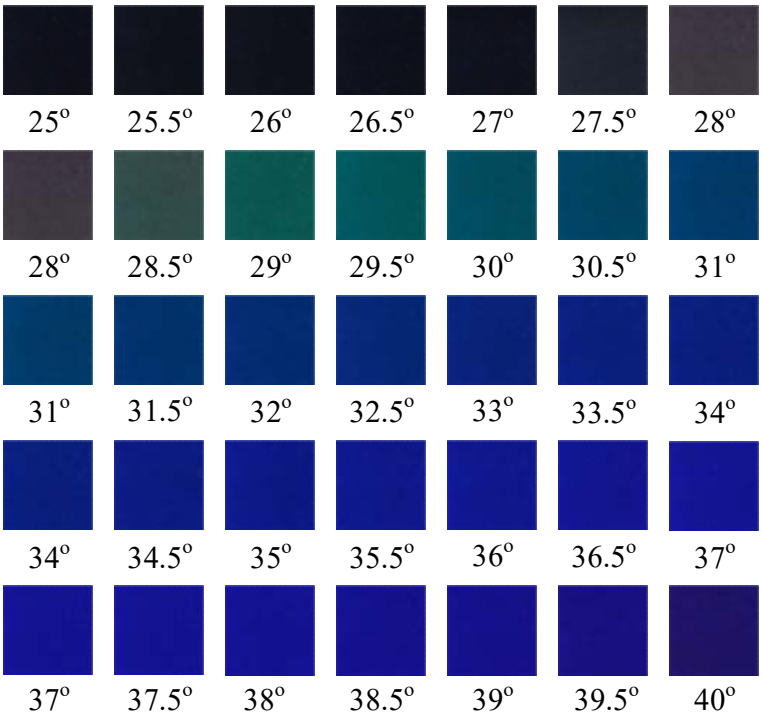

(b) A color-playing image with a constant surface temperature

Figure 4.2. The thermochromic liquid crystals calibration equipment: (a) calibration test equipment, and (b) uniform surface temperature pictures by color. (*continued*)

4.1.2.3 Imaging system

Figure 4.2(b) displays a calibration using a thermochromic liquid crystal sheet at various temperatures. Prior to being converted to an HSI color system, the color calibration photographs were initially assessed in an RGB color system. The software performed image processing using the following equations:

$$H = \begin{Bmatrix} \theta \\ 360-\theta \end{Bmatrix} \begin{Bmatrix} if\ B \le G \\ if\ B > G \end{Bmatrix} \tag{4.1}$$

where

$$\theta = \cos^{-1}\left\{ \frac{0.5\left[(R-G)+(R-B)\right]}{\left[(R-G)+(R-B)+(G-B)\right]^{0.5}} \right\} \tag{4.2}$$

$$S = 1 - \frac{3}{(R+G+B)}\left[\min(R,G,B)\right] \tag{4.3}$$

$$I = \frac{1}{3}(R+G+B) \tag{4.4}$$

H (hue) is a value that represents a real, original color derived from primary colors (red, green, and dark blue). In such instances, an angle in the range of 0-360° is created around the vertical axis. Each angle is turned to form a hexagon and has a color value of 60 degrees. *S* (saturation) is a characteristic that runs from 0 to 1.0 and is used to assess the rate at which pure color is diluted with white. Finally, *I* (intensity) is a characteristic that denotes color depth (crispness) or brightness.

Using the MATLAB program, the average hue value at various temperatures was calculated using Eqs. (4.1)–(4.4). As a result, as illustrated in Fig. 4.3, a graphical link between temperature and color was constructed. TLC hysteresis is a phenomenon in which the color of TLCs changes depending on whether they are chilled or heated. Hysteresis is a phenomenon that happens when TLCs are heated to or cooled from temperatures over their clearing point, as found by a number of studies [6, 7]. In common, TLC calibrations are repeatable, duplicable, and reversible (or free of hysteresis). During calibration, no hysteresis errors or output signal discrepancies were noticed, as shown in Fig. 4.3.

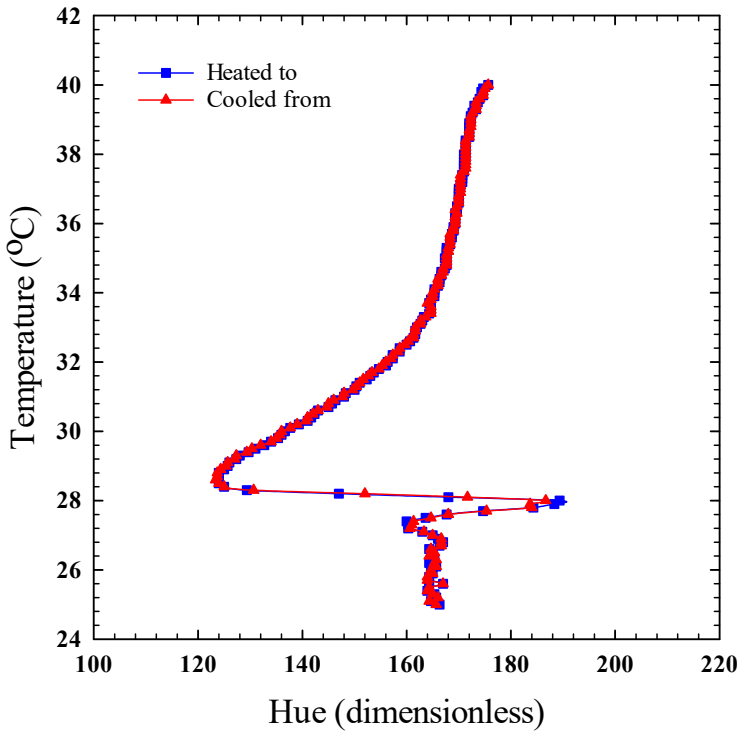

Figure 4.3. TLC sheet hue-temperature calibrations.

The averaged color and temperature values were fitted to a third-order polynomial form with an R-square value of 0.9884, and the resultant equation is

$$T_w = 0.000262H^3 - 0.112715H^2 + 16.167973H - 744.041481 \quad (4.5)$$

Over the temperature range of 29-38 °C, Eq. (4.5) can only be utilized to find the wall temperature (T_w) of each picture pixel.

4.1.3 Baffle vortex generator

4.1.3.1 Transverse baffle

Although transverse solid baffle turbulators enhance heat transfer rate, the enhancement is always accompanied by significantly increased pressure loss. This inspires the present work to modified baffles in form of perforated baffles in order to reduce pressure loss. Moreover, the perforated baffles were created to induce jet flow against the hot rear surfaces of the baffles.

4.1.3.1.1 Transverse perforated baffle

Typical/conventional transverse baffle (TB) is used to generate recirculation flow adjacent to baffle rear, followed by reattachment which helps to increase the heat transfer rate. However, the recirculation inefficiently transfers heat between the fluid flow and the local wall. The current work seeks ways to minimize the recirculation by forming a square wing to induce an impinging jet flow, attacking on the wall next to the rear, in order to improve heat transfer in the region. Several researchers attempted to modify baffles to enhance the heat transfer rate and reduce pressure losses. According to earlier researches, holes and perforations in baffles (Fig. 4.4) significantly helped reduce pressure losses. This idea has been adopted for newly designed baffles, namely transverse baffles with square-wing (SW-PB). The square-wing perforated transverse baffle (SW-PB) was utilized to form (a) recirculation flow, which creates flow reattachment between the baffles, as well as (2) multiple impinging flows behind the baffles to diminish dead zone. The combination is expected to enhance the fluid-wall contact and thus, heat transfer rate. In addition, the presence of gaps on the baffles is also helps in reducing friction loss.

Figure 4.4 demonstrates the structure of the rectangular channel mounted with modified baffle turbulators at the bottom wall. Baffle turbulators with three different forms: transverse solid baffle (TB), perforated-baffle (PB) and perforated-baffle with square wing (SW-PB) were tested. Their geometry details are shown in the figure. All baffles were made of Polylactic Acid (PLA) plastic having a height (e) of 12 mm and 1.5 mm thick (t). Baffle turbulators were mounted on the bottom wall to promote fluid mixing and increase fluid disturbance and, thus enhance the synergy of temperature and velocity fields. Each set of the baffle turbulators were mounted at pitch ratio of p/H = 1.5.

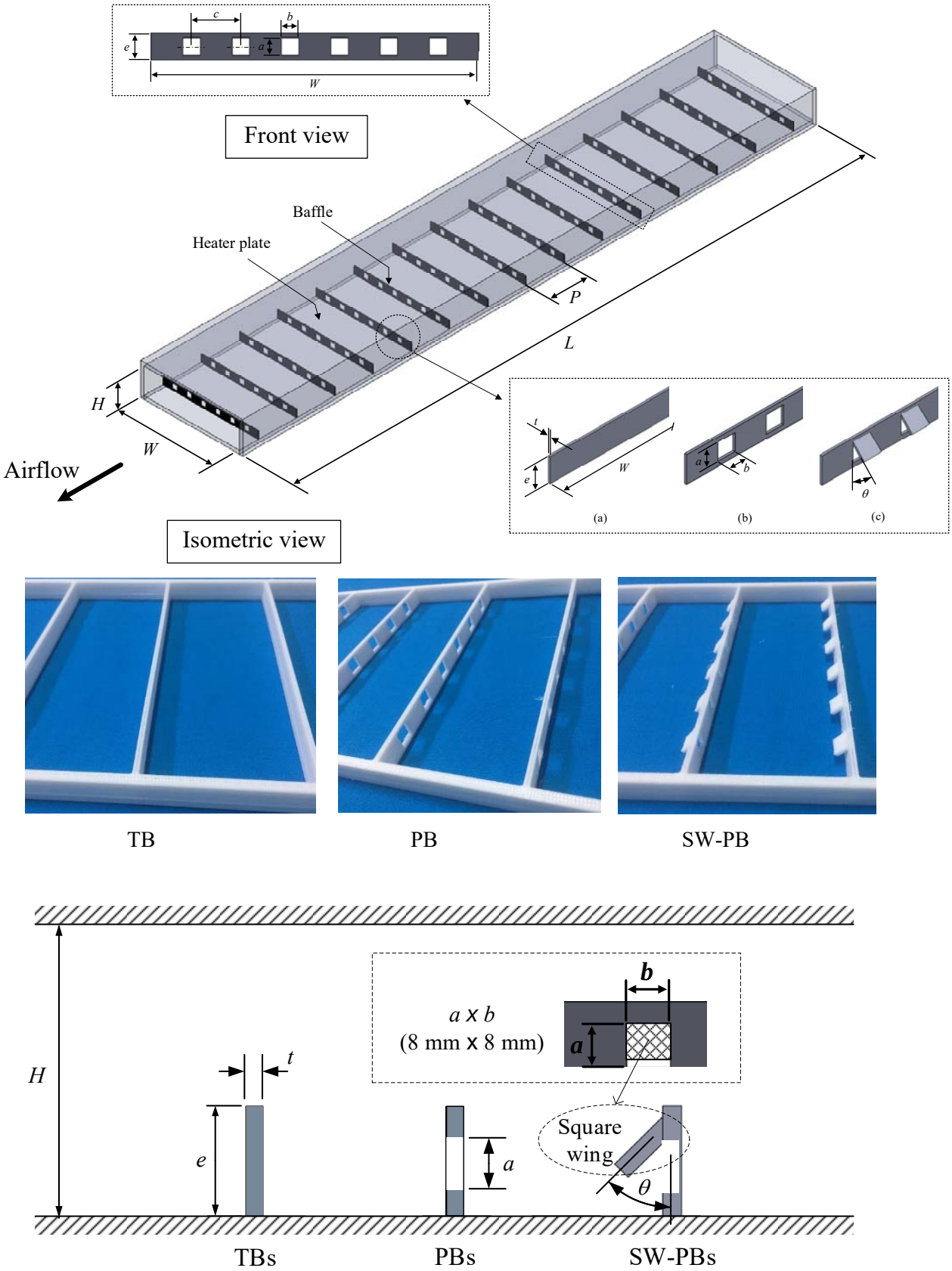

Figure 4.4. The structure of a rectangular channel mounted with various baffles: transverse solid baffle (TB), perforated-baffle (PB), and perforated-baffle with square wing (SW-PB).

4.1.3.1.2 Square-wing perforated transverse baffle

The current work offers a newly designed square-wing perforated transverse baffle (SW-PB) for heat transfer augmentation. The presence of opening areas of the square-wings is expected to help in reducing pressure loss and thus promote thermal performance of channel. In the ongoing investigation, square-winged aircraft are also used to generate multiple jet flows which facilitates the contact between the working fluid and heat transfer surfaces. It is also expected that the different positions of the wings will result in different flows behind the baffle and thus heat transfer behaviors. Therefore, it is extremely important to optimize the location of the wing in order to achieve optimal heat transfer, reduced pressure losses, and thermal performance in a rectangular channel. The purpose of the current work is to investigate the influence of combined reverse and multiple impinging jet flows on the heat transfer rate and pressure drop characteristics in a channel utilizing square-wing perforated transverse baffle (SW-PB). Figure 4.5 depicts the channel heat exchanger equipped with square-wing perforated transverse baffle (SW-PB) employed in this experiment. The polylactic acid (PLA) plastic square-wing perforated transverse baffle (SW-PB) with 0.8×0.8 cm^2 wing cross-sectional area ($\theta = 45^o$) were formed by 3D printing. Each baffle had a length (w), of 15 cm and a height (e) of 12 mm as declared in Fig. 4.5. The square-wing locations of SW-PB were set to $h/e = 0.92$ (the highest wing location $h = 1.1$ cm), 0.83 ($h = 1.0$ cm), 0.75 ($h = 0.9$ cm), and 0.67 (the lowest wing location, $h = 0.8$ cm). Transverse baffles with square-wings (SW-PBs) were also fabricated with wing attack angles (θ) of 0° (solid transverse-baffle), 22.5^o, 45°, 67.5^o and 90°. The SW-PBs were installed with a constant pitch length (p) of 60 mm or a pitch ratio (p/H) of 1.5 (60 mm).

Table 4.1: The geometric parameters and conditions of the experiments.

No.	*Parameter*	*Value*
1	Blockage ratio (e/H)	0.3
2	Pitch ratio (p/H)	1.5
3	Square-wing attack angles (θ)	0°, 22.5^o, 45°, 67.5^o and 90°
4	Area ratio of the perforation holes	0.21
5	Aspect ratio ($W:H$)	3.75
6	Reynolds number (Re)	6,000-24,000
7	Heat flux condition	600 W/m^2

The opening area ratio (β) of the perforated baffles with wing was determined in this study as the area ratio of the perforation holes to the SW-PB frontal area as:

$$\beta = n(a \times b)/(W \times e) \tag{4.6}$$

where n is the number of perforation holes, a is perforation width (8 mm), b is perforation height (8 mm), W is a baffle width (150 mm), and e is a baffle height (12 mm). The opening area ratio (β) was kept constant at 0.21. The test conditions for the experiment are fully described in Table 4.1.

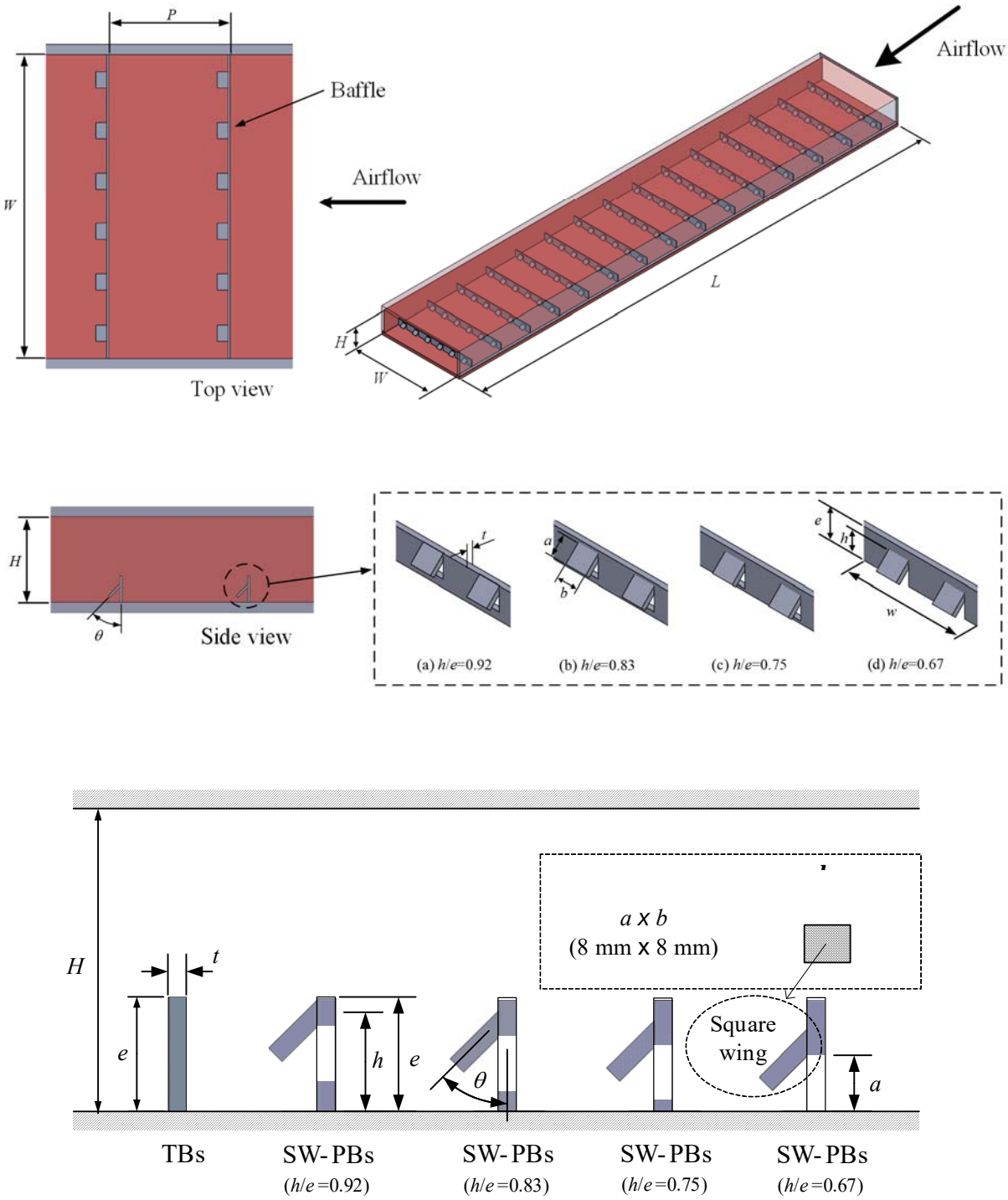

Figure 4.5. Channel heat exchanger equipped with square-wing perforated transverse baffle (SW-PB) at $\theta = 45^{o}$ and square-wing locations of h/e = 0.92, 0.83, 0.75, and 0.67.

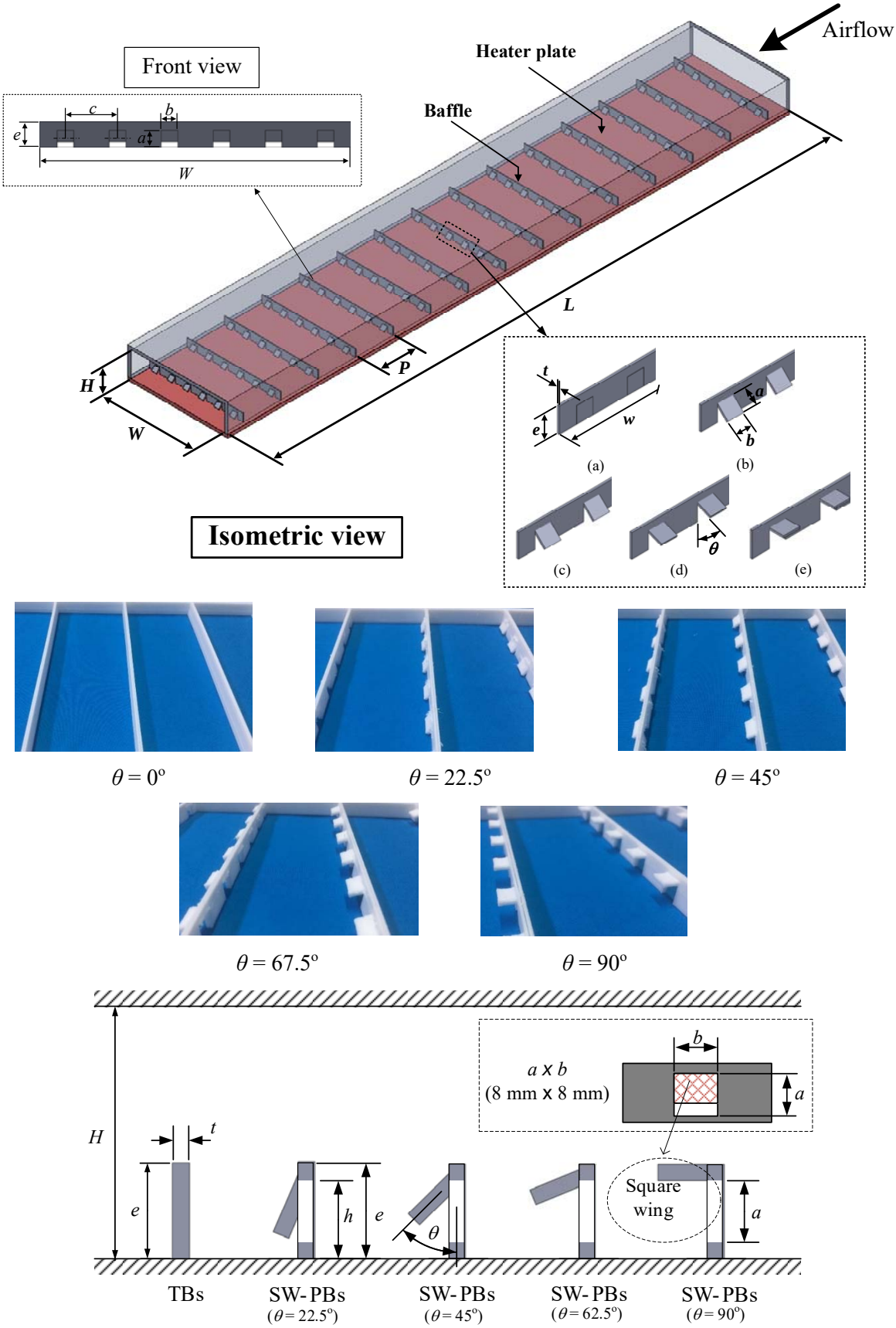

Figure 4.6. Channel heat exchanger equipped with square-wing perforated transverse baffle (SW-PB) at square-wing attack angles $\theta = 0^{o}$ (solid transverse-baffle), 22.5°, 45°, 67.5° and 90°.

4.1.3.2 V-type baffle

Many types of vortex flow generators can be utilized to enhance traditional heat exchangers employing various techniques for intensification or augmentation. Numerous heating and cooling systems have made full use of techniques for augmented heat transfer rate in tubes and channels employing vortex flow generators to disrupt the thermal boundary layers and increase turbulence levels. Vortex flow devices are utilized to enhance heat transfer, resulting in smaller heat exchanger systems and improved efficiency. These devices, including twisted tapes, baffles, ribs, dimples, grooves, are frequently used in heating/cooling systems. They are often used in heat exchangers to improve the degree of cooling or heating by supplying cooling or heating air to the ducts into which many baffles are installed. In these cases, the local heat transfer distribution may be completely altered by baffles in the flow-structure.

The primary goal of the present effort is to augment heat transfer rate and aerothermal performance by arranging delta/semi-oval/square-wing perforated V-type baffle in response to generated vortices. There has been much research on various channel inserts, however, there has been no study of the aerothermal performance of channels with delta/semi-oval/square-wing perforated V-type baffle periodically installed in a channel. In this work, the delta/semi-oval/square-wing perforated V-type baffle created counter vortex-flows and multiple impinging jets that boosted the heat transfer rate while causing minimal pressure losses. Since this delta/semi-oval/square-wing perforated V-type baffle lessen the influence of obstructed flow, it is expected to have a lower pressure drop than a solid V-type baffle. Additionally, to enhance the heat transfer rate and thermal performance, an innovation was put into effect altering the flow direction by busing the delta-wing at various wing attack angles (θ). This method is based on the concept of impinging jet flows on the channel wall, which describes a situation in which air flows past perforations as impinging jets behind V-shaped baffles [8, 9]. This technique is motivated by this basic concept. The flow of the impinging jets incorporates several impinging jets to effectively maximize the level of heat transfer [10, 11]. The wing's attack angle (θ) affects the direction in which the impinging jets directly interact with the channel wall. These jets can strike the wall in a variety of ways. Impingement can prevent establishment of many regions with different temperature gradients and can additionally decrease the pressure drop. In furtherance of this, the impinging jets enhance disturbance of the thermal boundary layer and mixing of the fluids behind the V-shaped baffle. It is expected that the combined influence of impinging jets and local longitudinal vortices formed by the delta/semi-oval/square-wing perforated V-type baffle can provide an enhanced heat transfer over that achieved by a V-shaped baffle that was not equipped with delta-wings. According to earlier studies, relative baffle blockage and pitch ratios of $h/H = 0.3$ and $p/H = 1.5$ were deemed appropriate to provide the best performance for thermal systems. The current research attempts to optimize thermal performance. This novel heat exchanger system design using a newly created delta/semi-oval/square-wing perforated V-type baffle vortex generator appears to be highly beneficial. The effects of wing

attack angles (θ = 0°) on the flow structure, pressure losses, and thermal performance are done in the current study utilizing air as the test fluid at Reynolds number (*Re*) values between 6,000 and 24,000.

4.1.3.2.1 Delta-wing perforated V-type baffle

Delta-wing perforated V-type baffle (DW-PVB) were fabricated using 3D printing. Each baffle had six equal wings that are 8 mm in height (*a*) and 16 mm in base width (*b*). A perforated cross-sectional area of 64 mm^2. Five delta-wing attack angles θ = 0° (solid V-shaped baffle/no holes), 22.5°, 45°, 67.5°, and 90° with respect to the vertical plane, were used in the investigation (see Fig. 4.7). It was anticipated that the various delta-wing attack angles (θ) would generate impinging jets that were either directed toward on the channel's bottom wall or minimize head losses. In the present report, both the baffle blockage, e/H = 0.3, and the pitch ratio, p/H = 1.5, were held constant.

4.1.3.2.2 Semi-oval wing perforated V-type baffle

Figure 4.8 shows the feature and construction of the test section with the semi-oval wing perforated V-type baffle (SOW-PVB). Figures 4.8(a-b) show a simplified diagram of the focused structure of the test section. In order to augment the heat transfer and thermal performance of a channel, a 900 mm long, 150 mm wide, and 40 mm high test/heating section is employed. Also, a 600 mm long unheated exit section was employed to avoid backflow, and a 2,000 mm long unheated entry section was included to ensure that the incoming flow is hydrodynamically completely developed. In the experiment, the heated bottom wall of the channel was installed with semi-oval wing perforated V-type baffle (SOW-PVB) vortex generators. The test portion was manufactured of 10-mm thick acrylic with a cross-sectional size of 150 mm (*W*) and 40 mm (*H*). Polylactic Acid was utilized for fabricating the semi-oval wing perforated V-type baffle (SOW-PVB). A perforated cross-sectional area of 64 mm^2. Each baffle had a height (*e*) of 12 mm and a thickness (*t)* of 1.5 mm. The distance between the baffles (*p*) or pitch was 60 mm, corresponding to a relative pitch ratio (*P/H*) of 1.5. Semi-oval wing attack angle was varied from 0° to 90°. The baffles assisted in the separation of flow layers within the channels [11].

4.1.3.2.3 Square-wing perforated V-type baffle

The square-wing perforated V-type baffle (SW-PVB) used in the current test are depicted in Fig. 4.9. The square-wing perforated V-type baffle (SW-PVB) was fabricated from 2.0 mm thick PVC sheets using 3D printing. They were then attached to the lower channel walls with five different square-wing attack angles of θ = 0° (VB, solid V-type baffle), 22.5°, 45°, 67.5° and 90°. Relative baffle pitch was set to 1.5 (*P/H*). A perforated cross-sectional area of 64 mm^2. Baffles were connected to the channel walls with a nut lock that can be removed to create new baffle shapes.

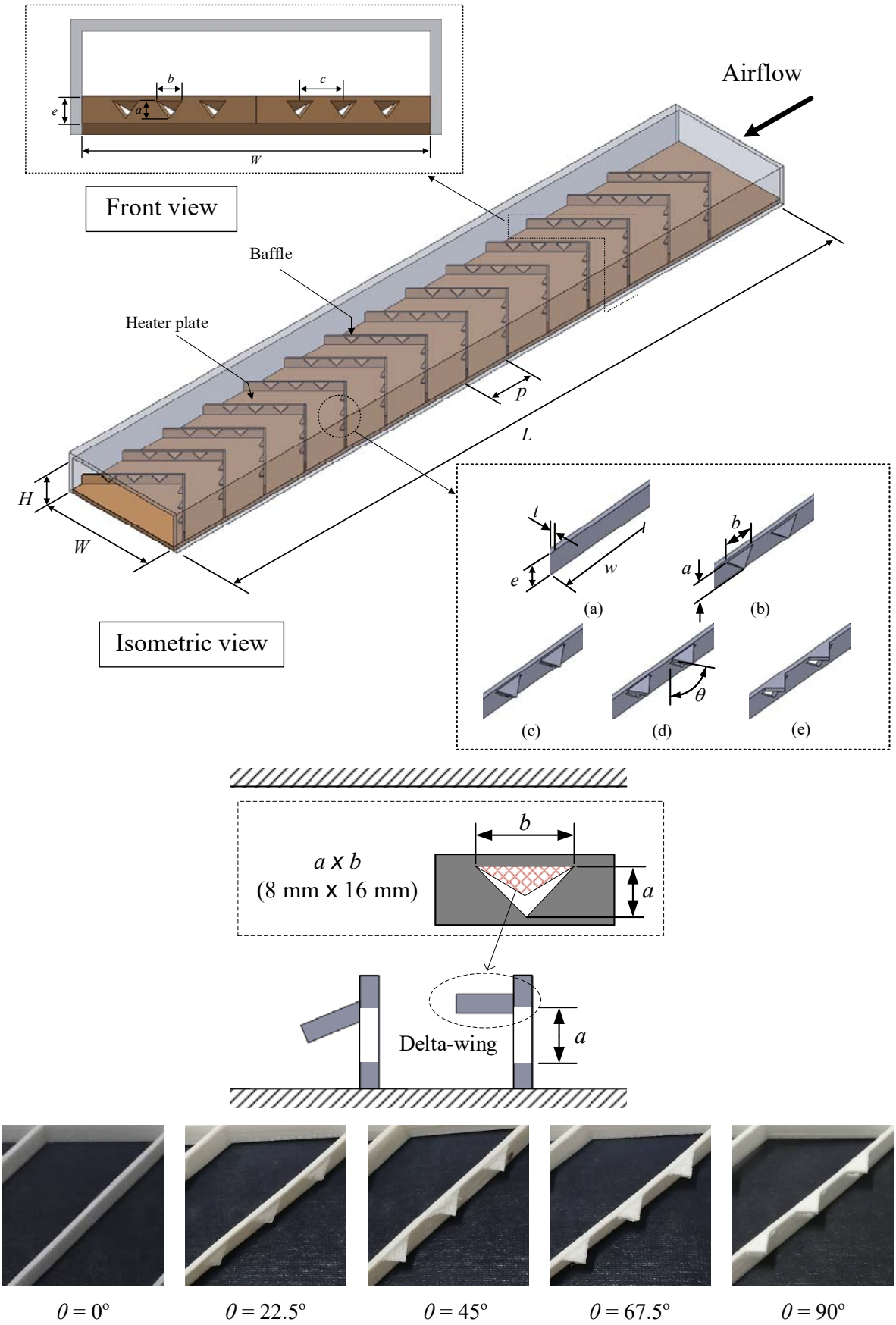

Figure 4.7. Channel heat exchanger equipped with delta-wing perforated V-type baffle (DW-PVB) at square-wing attack angles of $\theta = 0^{o}$ (solid transverse-baffle), 22.5°, 45°, 67.5° and 90°.

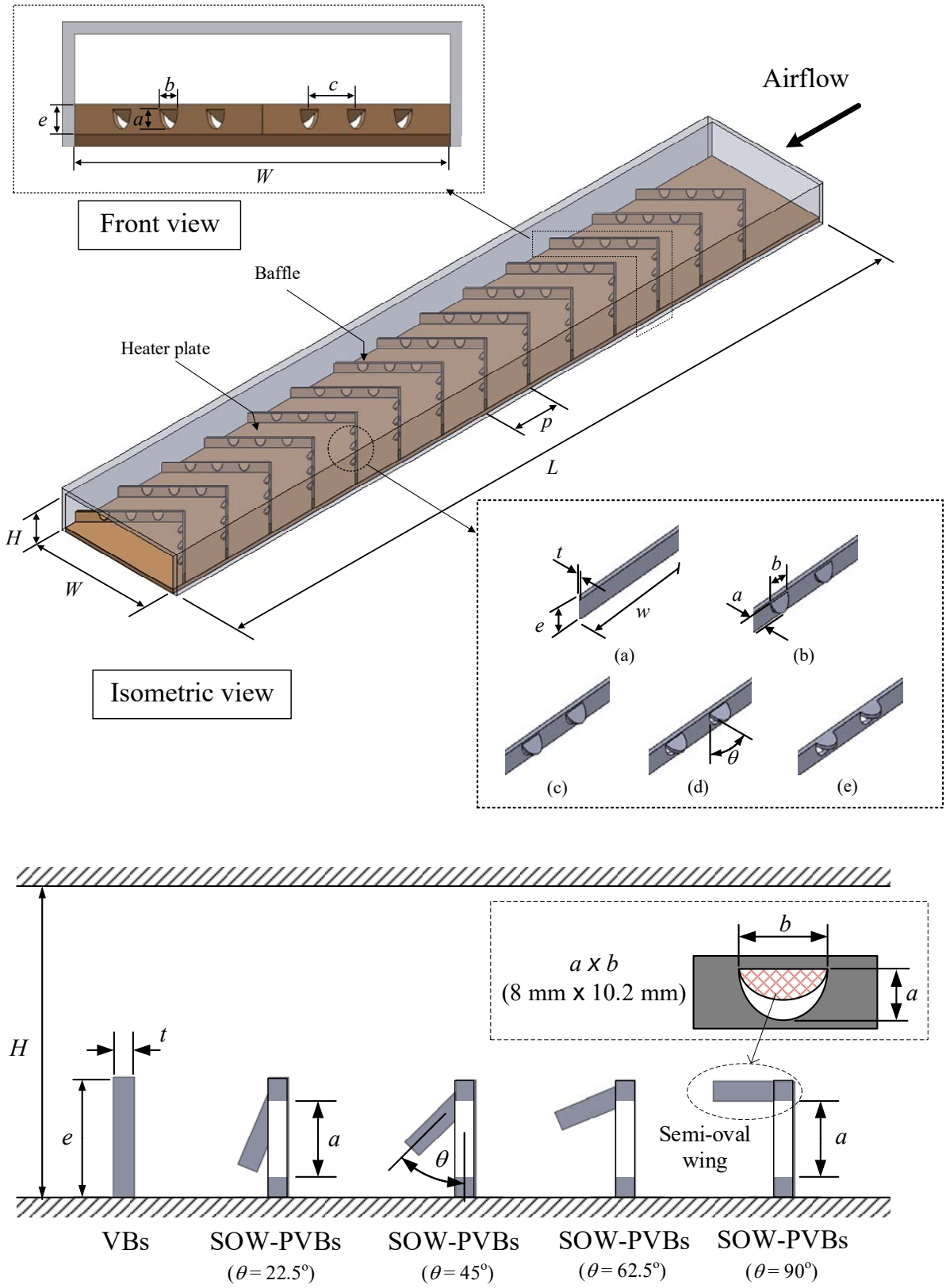

Figure 4.8. Channel heat exchanger equipped with semi-oval wing perforated V-type baffle (SOW-PVB) at square-wing attack angles of $\theta = 0^{o}$ (solid transverse-baffle), 22.5°, 45°, 67.5° and 90°.

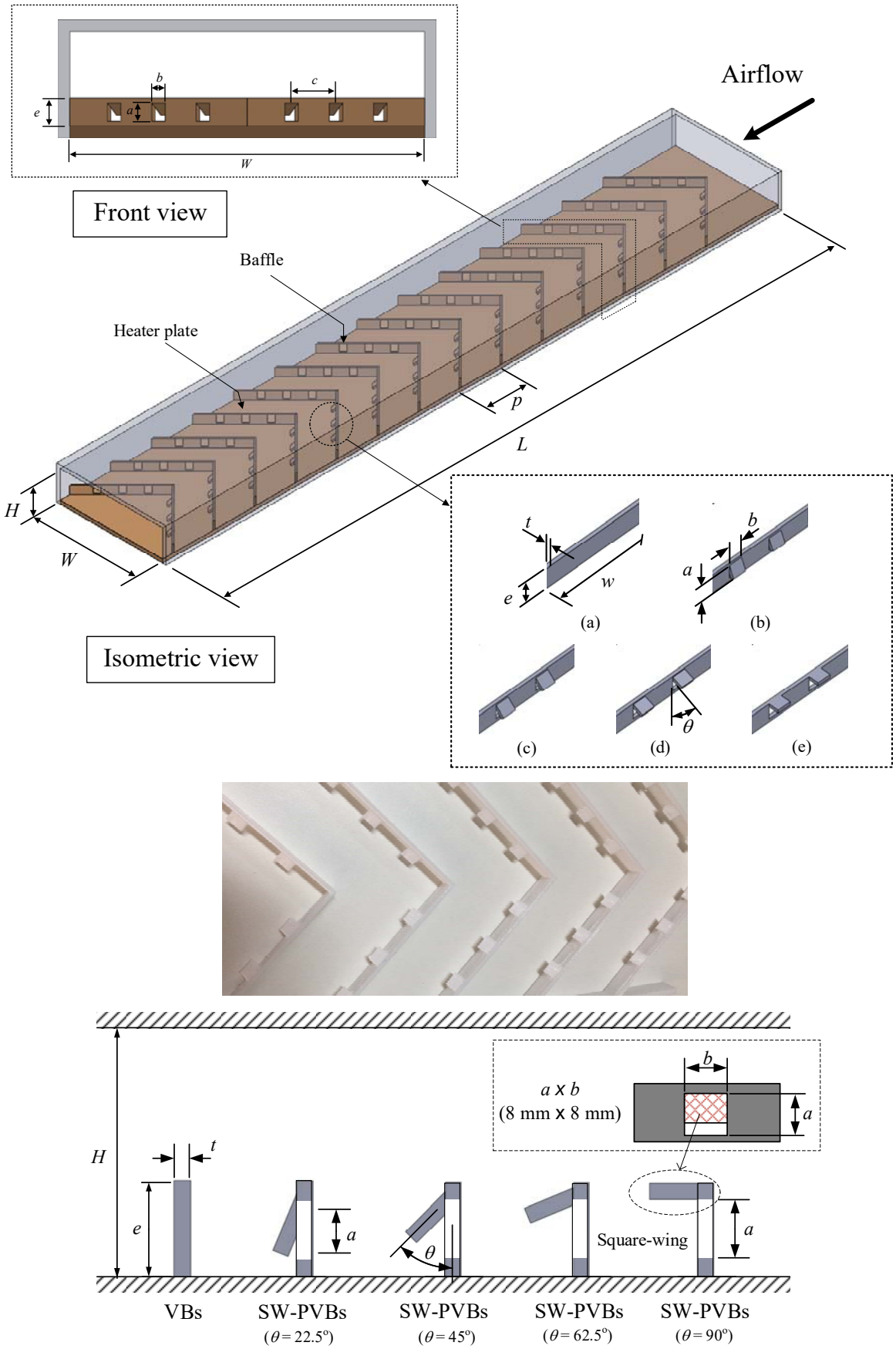

Figure 4.9. Channel heat exchanger equipped with square-wing perforated V-type baffle (SW-PVB) at square-wing attack angles of $\theta = 0^{o}$ (solid transverse-baffle), 22.5°, 45°, 67.5° and 90°.

4.1.4 Background and calculation in theory

Under a constant heat flux, the experimental data for both the channel wall and air temperature at various locations were recorded. The Nusselt numbers and friction factors within the rectangular channel are calculated using experimental data. The mass flow rate can be calculated using the pressure difference (ΔP) across an orifice plate via the following formula [12]:

$$\dot{m} = C_d A_o \left[\frac{2\rho \Delta P_o}{1-\left(d_2/d_1\right)^4} \right]^{0.5} \tag{4.7}$$

The orifice meter coefficient of discharge (C_d) was 0.624, as established by the orifice meter calibration using a hot-wire anemometer. The air velocity (V) is estimated from

$$V = \frac{\dot{m}}{\rho W H} \tag{4.8}$$

Reynolds number (Re) of the air flow can be expressed as

$$\mathrm{Re} = \frac{V D_h}{\nu} \tag{4.9}$$

The hydraulic diameter is determined from

$$D_h = \frac{4A_c}{P} = \frac{4\left(WH\right)}{2\left(W+H\right)} \tag{4.10}$$

The Duffie and Beckman [13] relationships are used to evaluate the thermo-physical characteristics of gas at atmospheric pressure:

$$\rho = 1.204\left(\frac{293}{T}\right) \tag{4.11}$$

$$\mu = 181\times 10^{-5}\left(\frac{T}{293}\right)^{0.735} \tag{4.12}$$

$$c_p = 1,006\left(\frac{T}{293}\right)^{0.0155} \tag{4.13}$$

$$k = 0.0275\left(\frac{T}{293}\right)^{0.86} \tag{4.14}$$

The heat transfer rate (Q_{abs}) is calculated the mass flow rate and the fluid temperature difference as

$$Q_{abs} = \dot{m}c_p\left(T_o - T_i\right) \tag{4.15}$$

where T_i and T_o can be found in the following formulas:

$$T_i = \frac{T_{i,1} + T_{i,2} + T_{i,3}}{3} \tag{4.16}$$

$$T_o = \frac{T_{o,1} + T_{o,2} + T_{o,3} + \ldots + T_{i,8}}{8} \tag{4.17}$$

The local heat transfer coefficient (h_x) is calculated using the heat flux (q), average wall temperature along the y-axis at any x-position (T_{wx}), and local fluid temperature (T_{bx}) as shown in Eq. (4.18). Note that the local fluid temperature was calculated using a linear interpolation approach between the inlet and outlet air temperatures.

$$h_x = \frac{q}{\left(T_{wx} - T_{bx}\right)} \tag{4.18}$$

The average inner wall temperature of the plate ($T_{w,avg}$) which was converted from the surface image of TLCs and computed by Eq. (4.16), and the average fluid temperature ($T_b = (T_i+T_o)/2$) were used to determine the average heat transfer coefficient (h).

$$h = \frac{Q_{abs}}{A_{hs}\left(T_{w,avg} - T_b\right)} \tag{4.19}$$

Nusselt number (Nu) was evaluated from the heat transfer coefficient (h), hydraulic diameter (D_h), and thermal conductivity (k) as

$$Nu = \frac{hD_h}{k} \tag{4.20}$$

Using the fundamental equation established by Darcy-Wiesbash, the friction factor (f) was calculated from the pressure drop within the test section and the velocity (V) of air moving through the test section:

$$f = \frac{\Delta P_t}{\left(\frac{L}{D_h}\right)\left(\rho \frac{V^2}{2}\right)} \tag{4.21}$$

Webb and Kim [14] introduces the concept of heat transfer augmentation or thermal performance factor (*TPF*), which is defined as the ratio of the heat transfer coefficient (h) of an enhanced channel to that of a smooth channel (h_s) at constant pumping power.

A similar pumping power (*pp*) condition is utilized to evaluate the heat transfer performance values of the channel with delta/semi-oval/square-wing perforated V-type baffle installed and for a smooth channel. This is done to assess the thermal performance. It is assumed that the fluid pumping power in a plain/smooth channel is same to that in a channel installed with baffles. Using the criterion of a constant pumping power evaluation [14]:

$$\left(\dot{V}\Delta P\right)_s = \left(\dot{V}\Delta P\right) \tag{4.22}$$

where "s" is a subscript designating a smooth channel. The parameters in Eq. (4.22) are then converted into the friction factor and *Re* as

$$\left(f\,\mathrm{Re}^3\right)_s = \left(f\,\mathrm{Re}^3\right) \tag{4.23}$$

$$\mathrm{Re}_s = \mathrm{Re}\left(f/f_s\right)^{1/3} \tag{4.24}$$

Under the same pumping (*pp*) condition, thermal performance factor (*TPF*) is evaluated by simultaneous determination of enhanced heat transfer and friction loss in terms Nusselt number ratio and friction factor ratio, respectively. The equation of *TPF* can be written as [14].

$$\mathrm{TPF} = \left.\frac{h}{h_s}\right|_{pp} = \left.\frac{Nu}{Nu_s}\right|_{pp} = \left(\frac{Nu}{Nu_s}\right)\left(\frac{f_s}{f}\right)^{1/3} \tag{4.25}$$

where Nu_s and f_s are, respectively, the Nusselt number and the friction factor for a smooth channel.

In the current study, the uncertainties of key parameters were evaluated using Eqs. (4.26-4.30). Equations (4.26-4.30) were utilized in this investigation to calculate the percentages of uncertainty associated with important parameters. Kline and McClintock [15] developed these equations to determine the uncertainties of a prediction parameter (X). The equations are based on the errors of the individually observed parameters ($x_1, x_2, \ldots x_n$), and they are used to calculate uncertainty.

$$\frac{\delta X}{X} = \sqrt{\left(\frac{\delta x_1}{x_1}\right)^2 + \left(\frac{\delta x_2}{x_2}\right)^2 + \ldots + \left(\frac{\delta x_n}{x_n}\right)^2} \tag{4.26}$$

$$\frac{\Delta \mathrm{Re}}{\mathrm{Re}} = \sqrt{\left(\frac{\Delta u}{u}\right)^2 + \left(\frac{\Delta \mu}{\mu}\right)^2 + \left(\frac{\Delta \rho}{\rho}\right)^2} \tag{4.27}$$

$$\frac{\Delta Nu}{Nu} = \sqrt{\left(\frac{\Delta h}{h}\right)^2 + \left(\frac{\Delta k}{k}\right)^2} \tag{4.28}$$

$$\frac{\Delta f}{f} = \sqrt{\left(\frac{\Delta(\Delta P)}{\Delta P}\right)^2 + \left(\frac{\Delta \rho}{\rho}\right)^2 + \left(\frac{2\Delta u}{u}\right)^2} \tag{4.29}$$

$$\frac{\Delta TPF}{TPF} = \frac{1}{3}\sqrt{\left(\frac{3\Delta Nu}{Nu}\right)^2 + \left(\frac{3\Delta Nu_{\mathrm{p}}}{Nu_{\mathrm{p}}}\right)^2 + \left(\frac{\Delta f}{f}\right)^2 + \left(\frac{\Delta f_{\mathrm{p}}}{f_{\mathrm{p}}}\right)^2} \tag{4.30}$$

The largest uncertainties of the non-dimensional important parameters were observed to be around ±3.63% for Nusselt numbers, ±2.79 % for Reynolds numbers, and ±3.2% for friction factors. The precision of the measurement equipment was determined to be ±0.5 Pascals for the digital pressure gauge, ±0.12 m/s for the hot wire anemometer, and ±0.1 °C for the RTD.

4.1.5 Numerical method

The 3D simulation of a turbulent channel flow model was carried out utilizing computational fluid dynamics (CFD) code, ANSYS FLUENT, to better understand the flow pattern in a channel containing delta-wing perforated V-type baffle (DW-PVB). The following delta-wing perforated V-type baffle (DW-PVB) configurations are employed for carrying out a three-dimensional numerical computation of the incompressible air periodic turbulent flow and heat transfer characteristics in uniform heat flux channels utilizing a finite volume approach. Based on periodically fully developed flow in the channel, just one periodic flow module, including the computational domain and its grid arrangement, was chosen as a

periodic flow model for the simulation. As suggested by Patankar *et al.* [16], the flow model achieves a periodic flow in which the velocity pattern repeats itself from one module to another. The delta-wing perforated V-type baffle (DW-PVB) was simulated at baffle blockage and pitch ratios of $b/H = 0.2$, $Re = 6{,}000$ and $P/H = 1.5$, and delta-wing attack angles of $\theta = 0°$ (solid V-shaped baffle), 22.5°, 45°, 67.5°, and 90° to analyze the flow mechanism. The flow field is governed by the three-dimensional Reynolds-averaged Navier-Stokes (RANS) equations which can be written as mentioned in chapter 3.

A finite volume approach was utilized to solve all the governing equations [17]. The equations were discretized using the QUICK (Quadratic upstream interpolation for convective kinetics differencing scheme) technique. The discretized equations were then solved using a finite volume approach using the SIMPLE (Semi Implicit Method for Pressure-Linked Equations) algorithm. The transport equations were solved using the Realizable k-ε turbulence model [18]. In the computations, the inlet and the outlet planes of the domain were set to periodic boundaries with a constant mass air flow rate at 300 K throughout. Both sides of the computational domain were specified as symmetrical boundaries as seen in Fig. 4.10. The physical characteristics of steady-state air were also used. The increase wall function was used while the channel wall and all delta-wing perforated V-type baffle (DW-PVB) surfaces were set to no-slip conditions with impermeable boundaries. While the adiabatic wall was set to the delta-wing perforated V-type baffle (DW-PVB), a channel-wall heat-flux of 600 W/m^2 was applied. The minimal convergence requirement was 10^{-6} for the continuity equation, velocity and turbulence quantities and 10^{-8} for the energy equation.

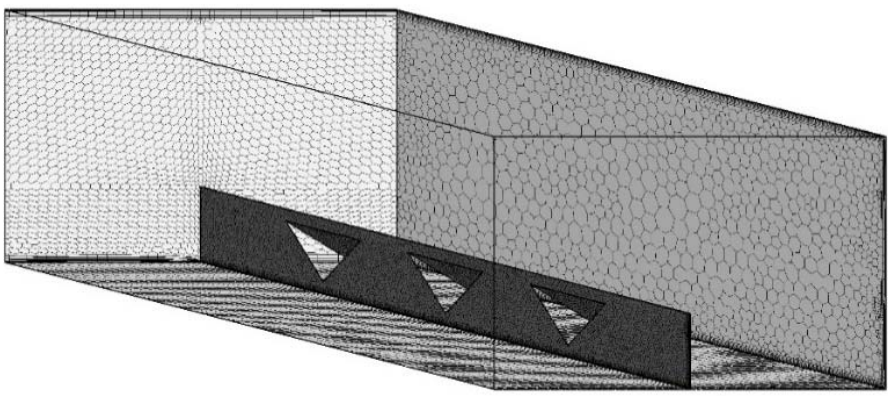

Figure 4.10. Computation domain of a channel equipped with delta-wing perforated V-type baffle (DW-PVB).

4.2 Experimental results and Discussion

The current section describes the validation test results and the influences of delta/semi-oval/square-wing perforated V-type baffle (DW-PVB/SOW-PVB/SW-PVB) with five different attack angles (θ) on the heat transfer, pressure losses and thermal performance factor behaviors.

4.2.1 Experiment verification

The Nusselt number *(Nu)* and friction factor (*f*) results of the current smooth channel are validated by comparing experimental data with the results obtained from standard correlations [19], as illustrated in Fig. 4.11. This analysis shows the reliability of the experimental system. Figures 4.11(a-b) show the results of experiments that measured heat transfer in terms of Nusselt number and friction factor for the smooth channel. These results are in good agreement with those obtained from Dittus-Boelter, Gnielinski, Blasius and Petukhov equations. Comparisons indicate that the deviations of Nusselt number *(Nu)* and friction factor (*f*) were ±3.17% and ±10.38%, respectively, which are acceptable. The current findings also demonstrated that Nusselt number *(Nu)* increased and friction factor (*f*) decreased with increasing *Re* values. The values and trends of Nusselt number *(Nu)* and friction factor (*f*) verification demonstrated that the experimental equipment was accurate and appropriate for practical use.

Nusselt number correlations for the smooth channel:

Correlation of Dittus-Boelter;

$$Nu = 0.023Re^{0.8}Pr^{0.4} \tag{4.31}$$

Validity: $Re > 10{,}000$

$0.7 \leq Pr \leq 160$

Friction factor correlations for the smooth channel:

Correlation of Petukhov;

$$f = (0.79\ln Re 1.64)^{-2} \tag{4.32}$$

Validity: $3000 < Re < 5 \times 10^6$

Correlation of Blasius;

$$f = 0.184Re^{-0.2} \tag{4.33}$$

Validity: $2 \times 10^4 < Re \leq 2 \times 10^6$

4.2.2 Transverse perforated baffle

In this section, the results obtained with the channel equipped typical transverse baffle (TB), perforated baffle (PB) and square-wing perforated transverse baffle (SW-PB) at various wing locations ($h/e = 0.92$, 0.83, 0.75, and 0.67) and wing attack angles ($\theta = 0^o$ (solid transverse-baffle), 22.5°, 45°, 67.5° and 90°) are depicted in the form of Nusselt number or friction factor versus Reynolds number (*Re*). The trends of Nusselt number ratio (Nu/Nu_s) or friction factor ratio (f/f_s) versus *Re* are also analyzed. The thermal

performance factor (*TPF*) is used to evaluate the comprehensive performance of the enhancement devices. The heat transfer, friction losses and thermal performance results of the channel containing transverse baffle (TB), perforated baffle (PB) and square-wing perforated transverse baffle (SW-PB) having Reynolds number varying from 6,000 to 24,000 are presented and discussed along with those of the smooth channel.

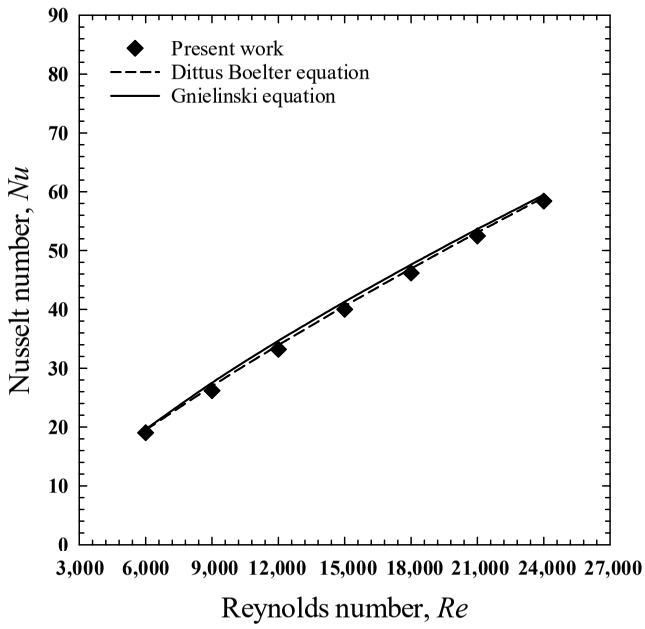

(a) *Nu*

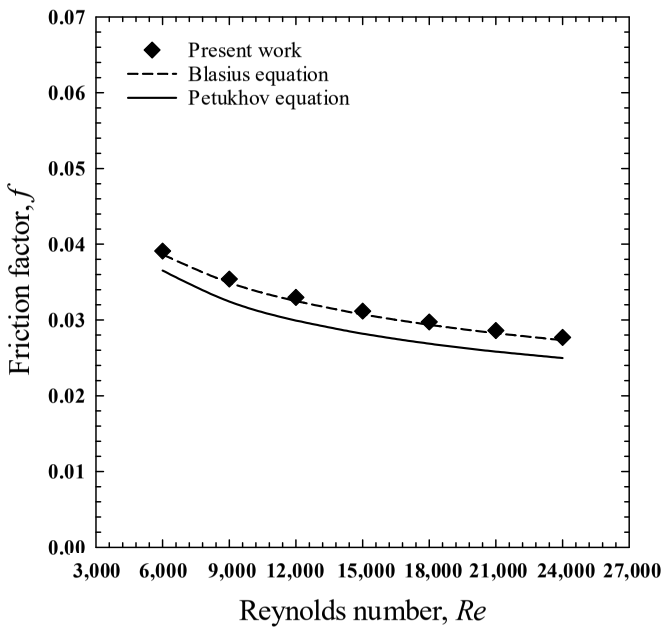

(b) *f*

Figure 4.11. Validation test of smooth channel: (a) Nusselt number as a function of Reynolds number, and (b) friction factor as a function of Reynolds number.

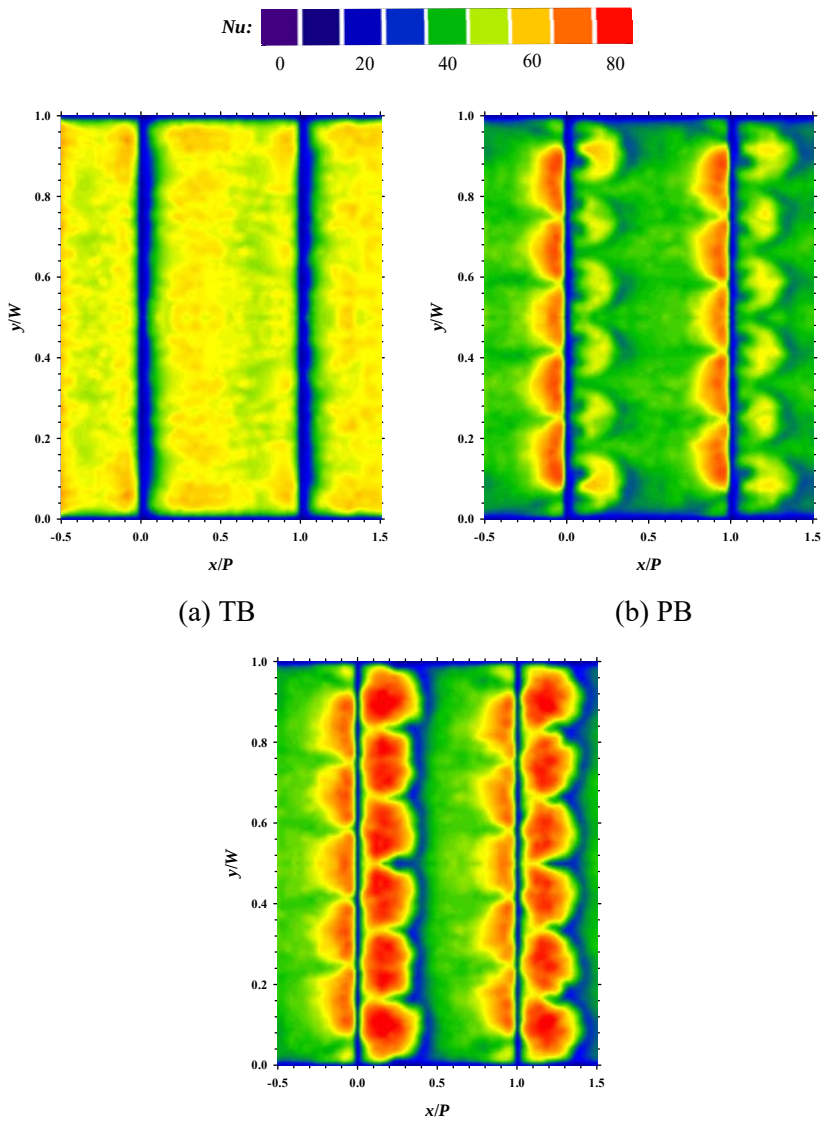

Figure 4.12. Local Nusselt numbers around transverse baffle (TB), perforated baffle (PB) and square-wing perforated transverse baffle (SW-PB) at Reynolds number (*Re*) of 6,000.

4.2.2.1 Perforated baffle

4.2.2.1.1 Heat transfer results

Figures 4.12 and 4.13 present local Nusselt number (Nu_x) around transverse baffle (TB), perforated baffle (PB) and square-wing perforated transverse baffle (SW-PB) at Reynolds number (*Re*) of 6,000. For transverse baffle (TB), a very low Nusselt number zone appeared adjacent to the transverse solid baffle rear ($0.0 < x/P < 0.1$). Then, Nusselt number became higher in $0.2 < x/P < 0.5$ region due to the effect of flow reattachment. The perforated baffle (PB) brought a wall-like flow near the front baffle. This helped in improving heat transfer rate at $x/P < -1.0$ and $0.1 < x/P < 0.3$. Then, low Nusselt number zone appeared in $0.3 < x/P < 0.9$ owing to flow recirculation. The thermal patterns of channel bottom wall installed with square-wing perforated transverse baffle (SW-PB) were similar to those found with

perforated baffle (PB). In addition, jet flow against the hot rear surfaces of the baffles caused the multiple high heat transfer areas. The upstream heat transfer ($0 < x/P < 0.4$) associated with square-wing perforated transverse baffle (SW-PB) was observed to be more effective than that found with the perforated baffle (PB) due to the presence of the multiple jets which helped in expanding high heat transfer area.

Figures 4.14(a-b) demonstrate mean Nusselt numbers (*Nu*) contributed by transverse baffle (TB), perforated baffle (PB) and square-wing perforated transverse baffle (SW-PB) at various Reynolds numbers. Obviously, Nusselt numbers (*Nu*) were significant affected by Reynolds numbers. At low Reynolds numbers, Nusselt numbers contributed by transverse baffle (TB), perforated baffle (PB) and square-wing perforated transverse baffle (SW-PB) were comparable. The influence of baffle geometry became more important at higher Reynolds number. The square-wing perforated transverse baffle (SW-PB) enhanced Nusselt numbers (*Nu*) by 71.1 to 157.3% over the smooth channel. At same Reynolds numbers, the square-wing perforated transverse baffle (SW-PB) showed superiority of heat transfer augmentation over the TB and PB by 1.01-1.03 and 1.13-1.16 times, respectively. The major key of the outstanding heat transfer enhancement of SW-PB was the presence of the multiple jets as mentioned above.

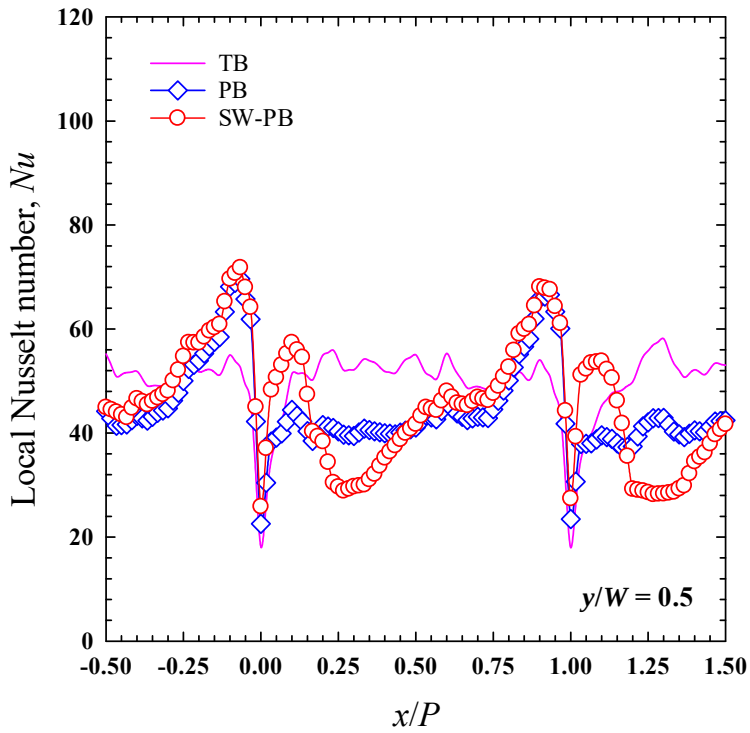

(a) $y/W = 0.5$

Figure 4.13. Normalized of Nusselt number at $y/W = 0.5$, $y/W = 0.57$ and $x/P = 0.15$ for transverse baffle (TB), perforated baffle (PB) and square-wing perforated transverse baffle (SW-PB) at Reynolds number (*Re*) of 6,000.

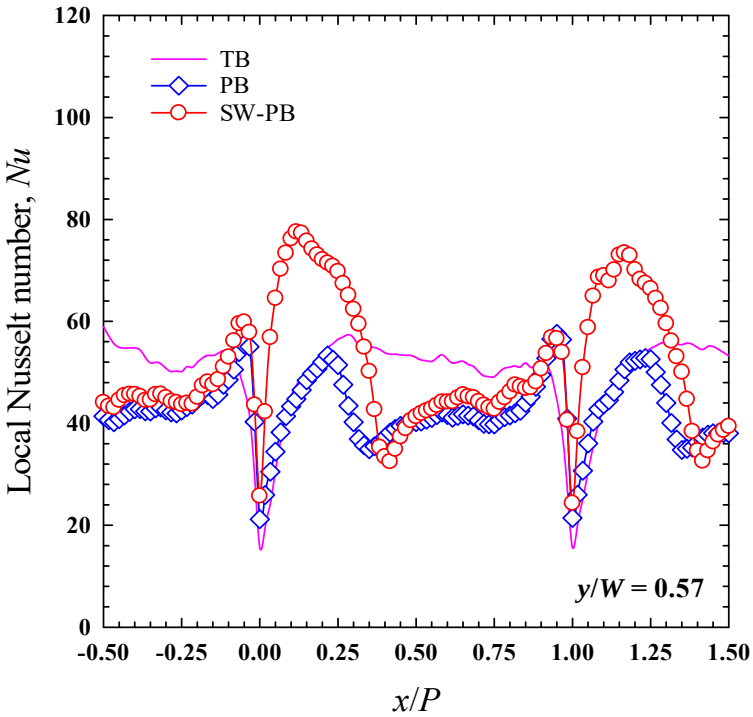

(b) $y/W = 0.57$

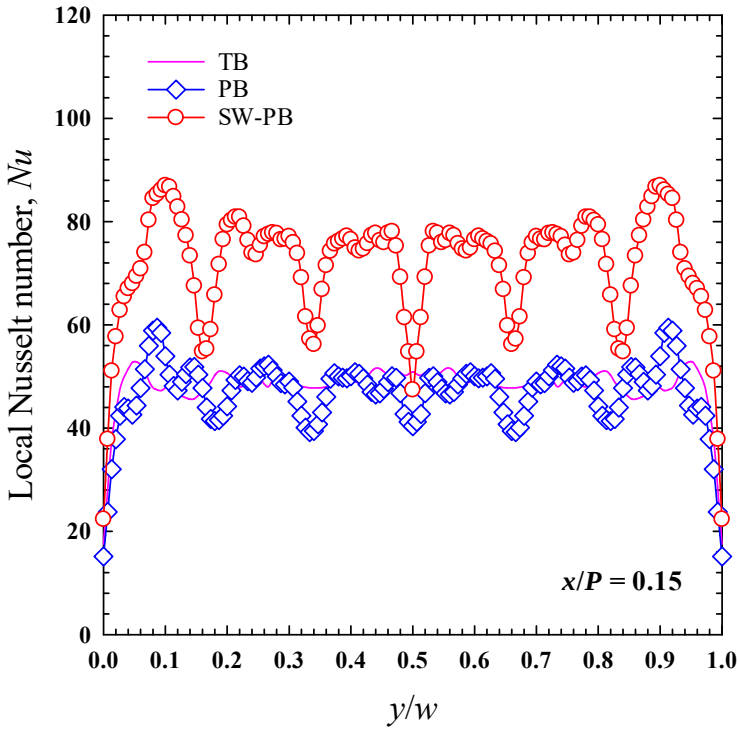

(c) $x/P = 0.15$

Figure 4.13. Normalized of Nusselt number at $y/W = 0.5$, $y/W = 0.57$ and $x/P = 0.15$ for transverse baffle (TB), perforated baffle (PB) and square-wing perforated transverse baffle (SW-PB) at Reynolds number (*Re*) of 6,000. (*continued*)

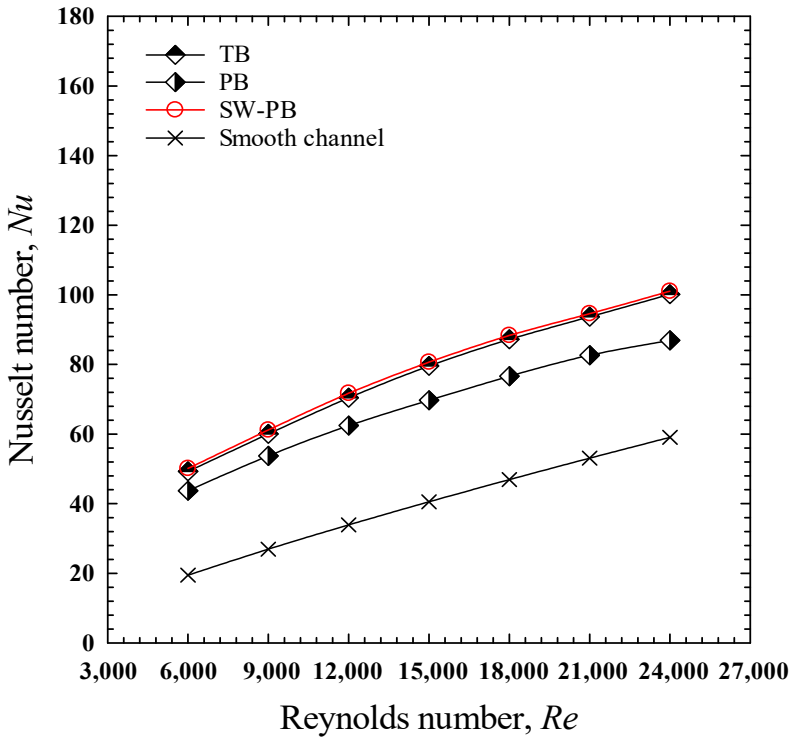

(a) *Nu*

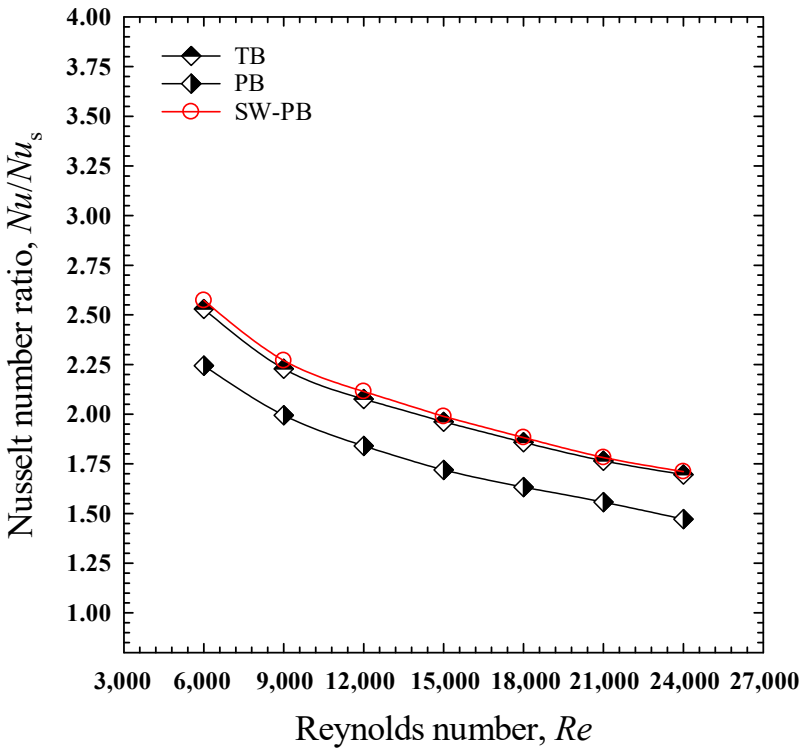

(b) Nu/Nu_s

Figure 4.14. Effect of transverse baffle (TB), perforated baffle (PB) and square-wing perforated transverse baffle (SW-PB) on Nusselt number.

4.2.2.1.2 Friction factor results

Friction factors (*f*) of the channel mounted with transverse baffle (TB), perforated baffle (PB) and square-wing perforated transverse baffle (SW-PB) at different Reynolds numbers (*Re*) is displayed in Figs. 4.15(b) and 4.15(b). In all baffles, friction factors significantly reduced with rising Reynolds numbers (*Re*). It can be indicated that the friction factor of the channels equipped with all types of the baffles were considerably greater than those of the smooth channel because baffles caused flow disturbance resulting in multiple impinging flows and strong turbulence. The pressure loss of the channels mounted with transverse baffle (TB), perforated baffle (PB) and square-wing perforated transverse baffle (SW-PB) were as high as 11.73, 9.33 and 10.1 times of the smooth channel. The square-wing perforated transverse baffle (SW-PB) caused lower friction losses by 7.54-8.69% and higher friction losses by 13.17-14.67% as compared to perforated baffle (PB) and transverse baffle (TB), respectively. The reduction of friction factor was greatly influenced by perforation. The friction factors caused by perforated baffle (PB) and square-wing perforated transverse baffle (SW-PB) dropped by 20.5% and 14% compared to those caused by transverse baffle (TB).

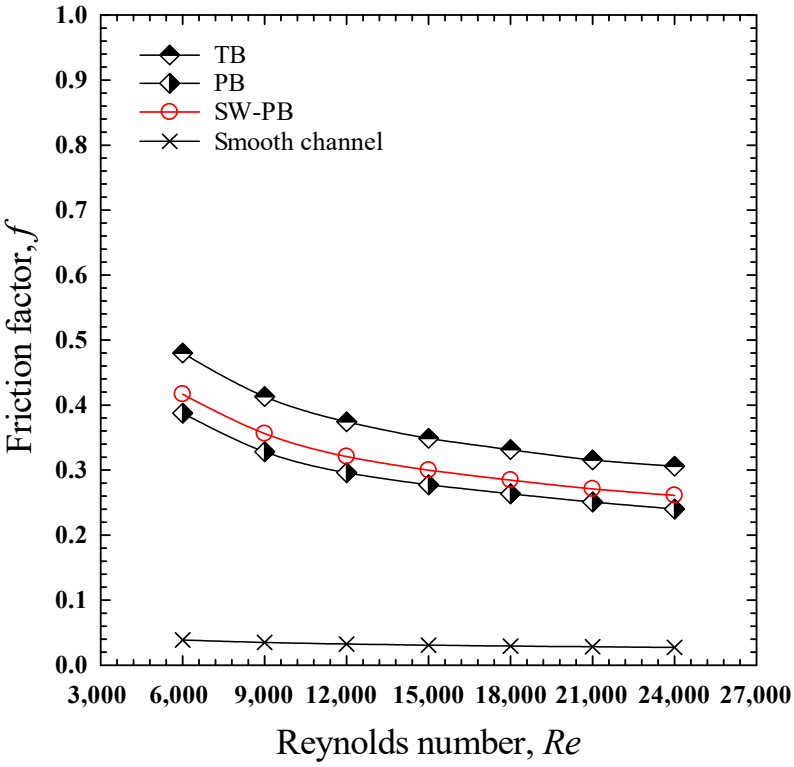

(a) *f*

Figure 4.15. Effect of transverse baffle (TB), perforated baffle (PB) and square-wing perforated transverse baffle (SW-PB) on friction factor.

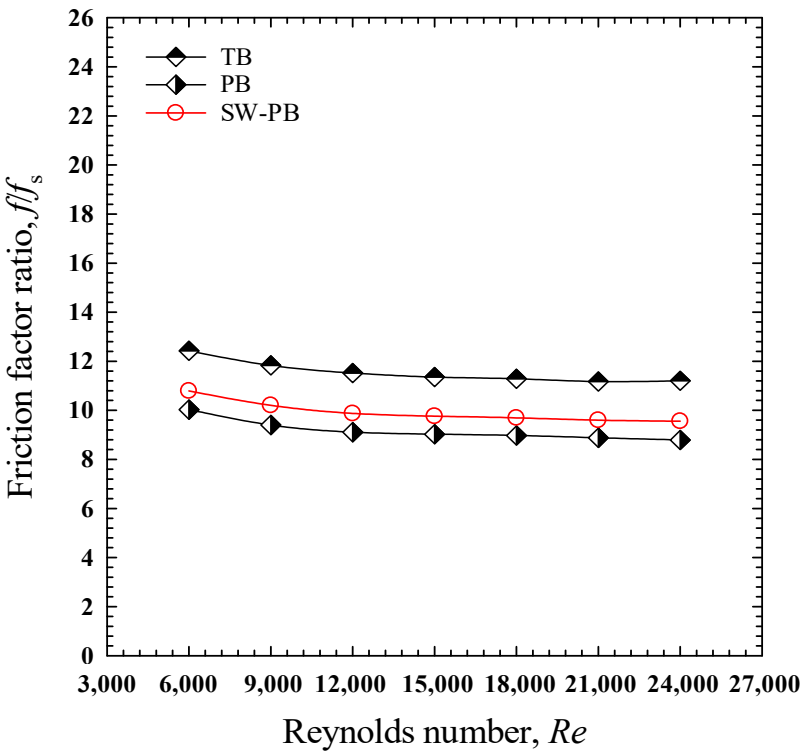

(b) f/f_s

Figure 4.15. Effect of transverse baffle (TB), perforated baffle (PB) and square-wing perforated transverse baffle (SW-PB) on friction factor. (*continued*)

4.2.2.1.3 Thermal performance factor results

The heat transfer intensification (Nu/Nu_s) of the channel mounted with various baffle turbulators (TBs, PBs and SW-PBs) always occurs together with the rise of pressure drop or flow resistance. The heat gain index or thermal performance factor (*TPF*) can qualitatively measure whether the rise of Nusselt number (*Nu*) is more dominant than that of friction loss under the constant pump power as depicted in Fig. 4.16(a-b). A channel with baffles has a higher thermal performance factor (*TPF*) than a non-baffle flow channel or a smooth channel. To put it another way, the transverse baffle (TB) and square-wing perforated transverse baffle (SW-PB) can improve the thermal performance factor (*TPF*) of perforated baffle (PB). The maximum thermal performance factor (*TPF*) values given by transverse baffle (TB), perforated baffle (PB) and square-wing perforated transverse baffle (SW-PB) were 1.06, 1.01, and 1.13, respectively. The thermal performance factor (*TPF*) of given by square-wing perforated transverse baffle (SW-PB) was 6.65% and 12% over than those given by transverse baffle (TB) and perforated baffle (PB).

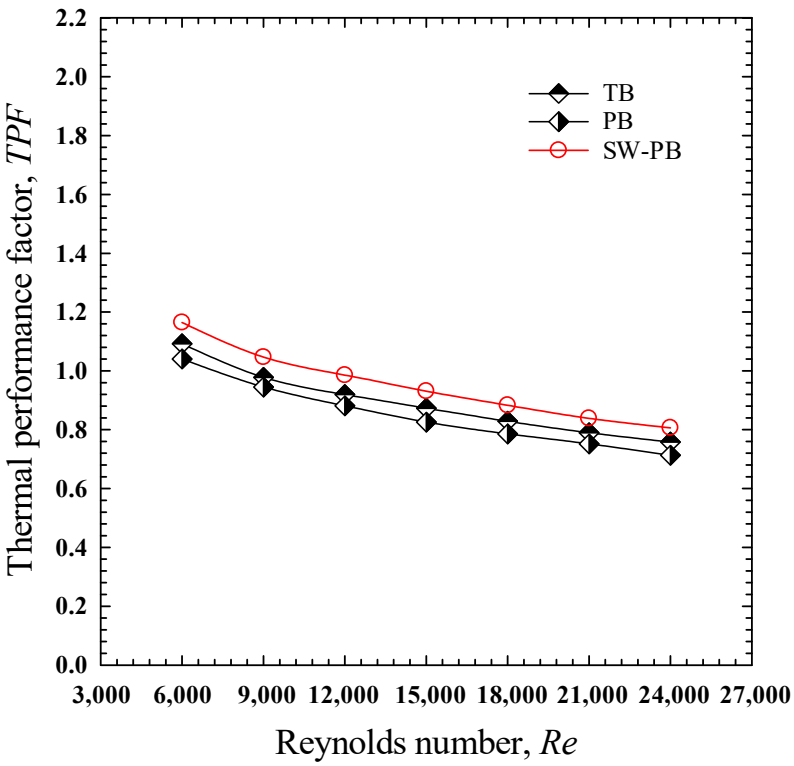

(a)

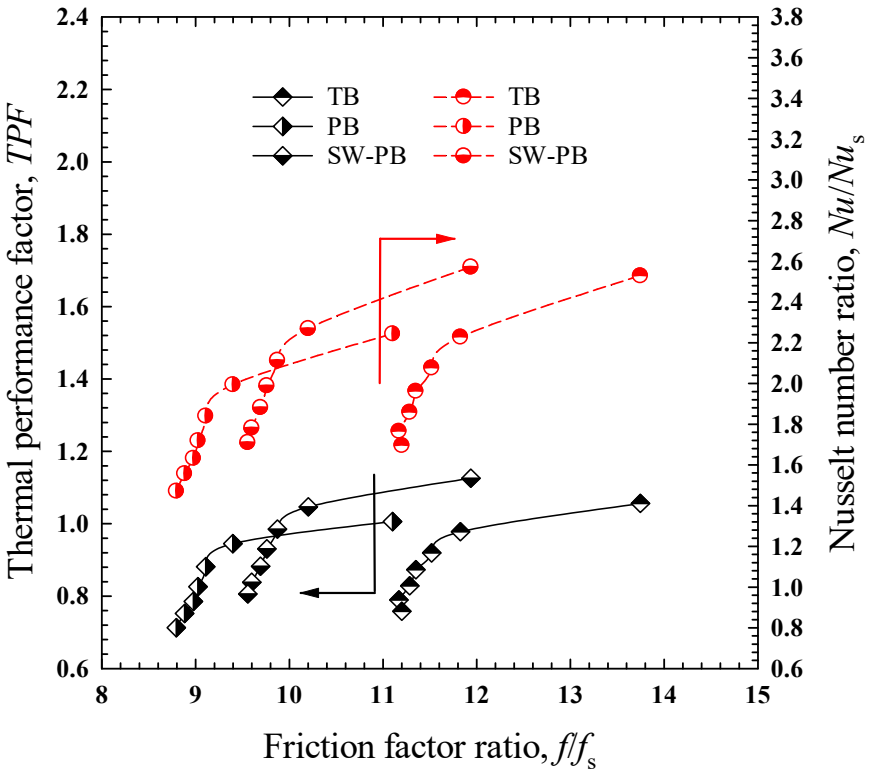

(b)

Figure 4.16. Effect of transverse baffle (TB), perforated baffle (PB) and square-wing perforated transverse baffle (SW-PB) on thermal performance factor.

4.2.2.2 Square-wing perforated transverse baffle: Effect of square-wing location

4.2.2.2.1 Heat transfer results

Figures 4.17 and 4.18 show the Nusselt number distributions on the lower wall of the channel fitted with square-wing perforated transverse baffle (SW-PB) at various square-wing locations (*h/e* = 0.92 (the highest wing location), 0.83, 0.75, and 0.67 (the lowest wing location)). In general, the application of baffle results in considerable enhancement as compared to the smooth channel. In the channel with the typical transverse baffles (TB), the wide bands of low Nusselt number areas exist according to the positions of the baffles. The result is caused by the flow separation over the baffles. Then, uniformly moderate Nusselt number area appears behind each baffle (for example, *x/P* = 0.2-0.9), reflecting the uniform flow reattachment. For the channel with square-wing perforated transverse baffles (SW-PB), there are high local Nusselt number areas due to the jet impingement through spaces of wings. The impingement intensity tends to increase as the wing location becomes lower. This can be explained by the fact that the lower wings bring the bulk fluid closer to bottom wall, leading to the stronger impingement and better contact between them, as emphasized in Fig. 4.17(c). Moreover, it is observed that high Nusselt number regions also appear at the front of each baffle. This is most likely caused by a reverse flow. These features aid in minimizing flow separation and thus enhancing heat transfer as compared to the transverse baffles (TB) case. Additionally, the Nusselt number increases with the increasing Reynolds number (*Re*), as shown in Figs. 4.19 and 4.20. When impingement takes place, jets with a higher Reynolds numbers (*Re*) have a greater velocity or momentum. As a result, disruption of the velocity/thermal boundary layer and heat transfer become more efficient.

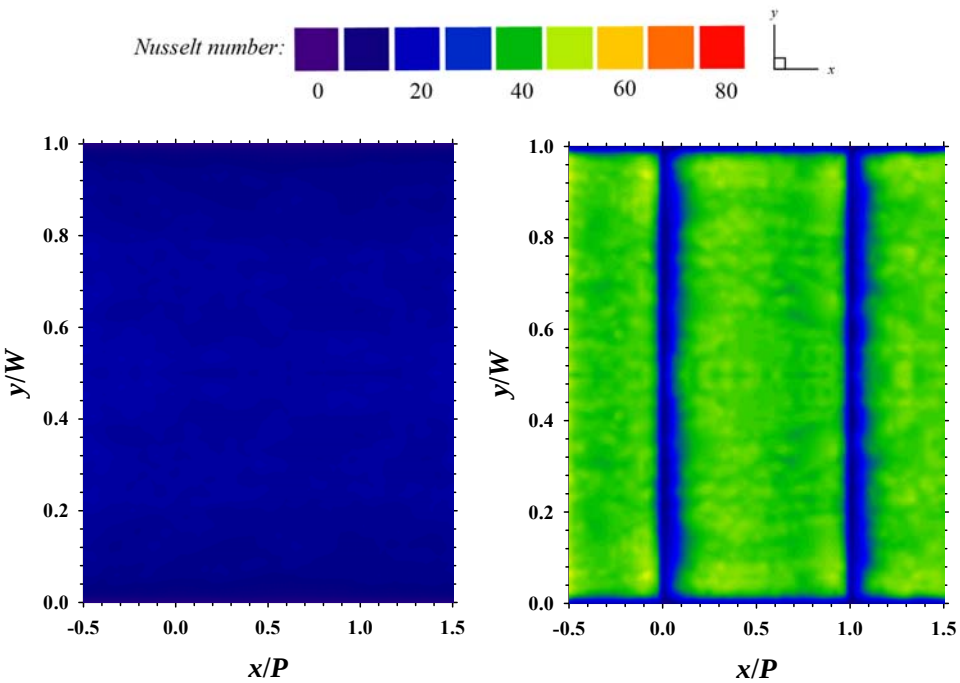

(a) smooth channel (b) TB

Figure 4.17. Influence of square-wing perforated transverse baffle (SW-PB) at *Re* = 6,000 with various square-wing locations (*h/e* = 0.92, 0.83, 0.75, and 0.67) on local heat transfer distribution.

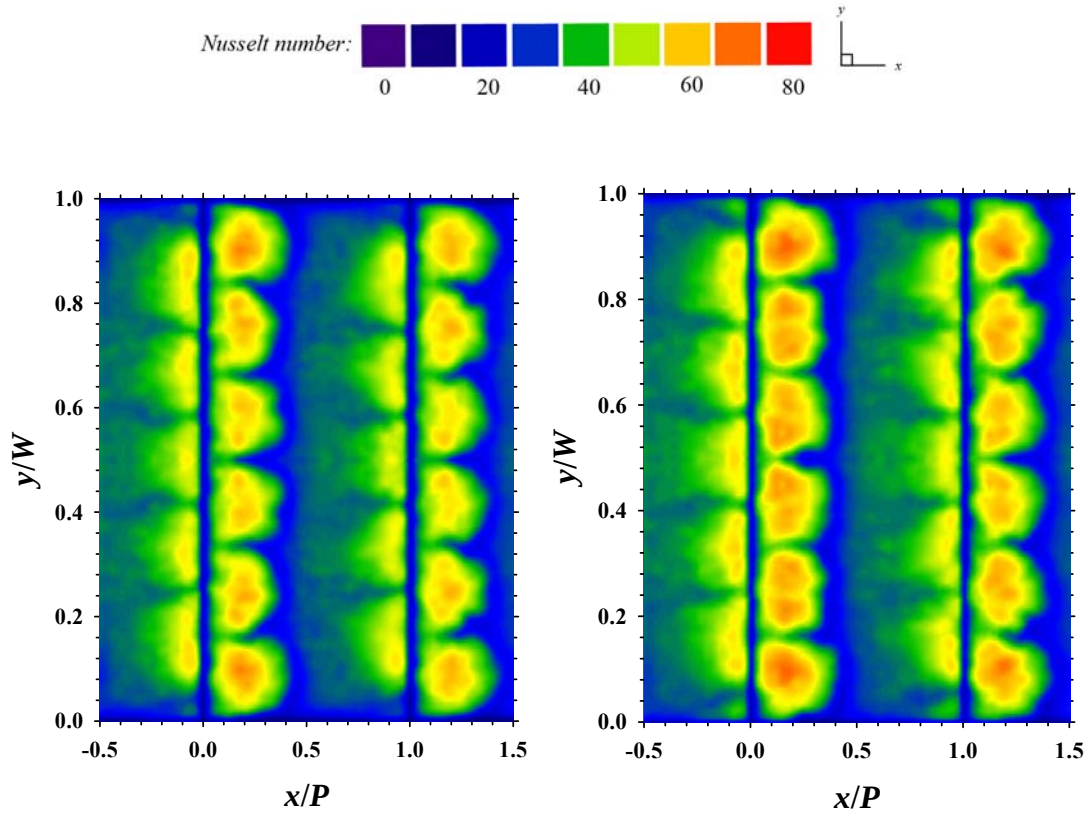

(c) SW-PBs, *h/e* = 0.92

(d) SW-PBs, *h/e* = 0.83

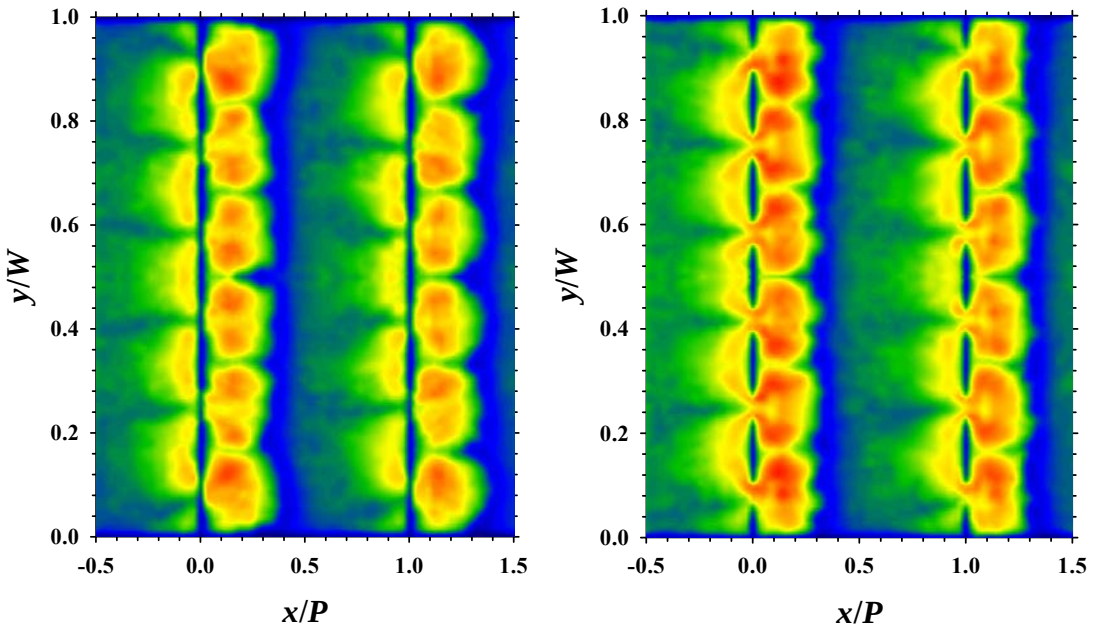

(e) SW-PBs, *h/e* = 0.75

(f) SW-PBs, *h/e* = 0.67

Figure 4.17. Influence of square-wing perforated transverse baffle (SW-PB) at *Re* = 6,000 with various square-wing locations (*h/e* = 0.92, 0.83, 0.75, and 0.67) on local heat transfer distribution. (*continued*)

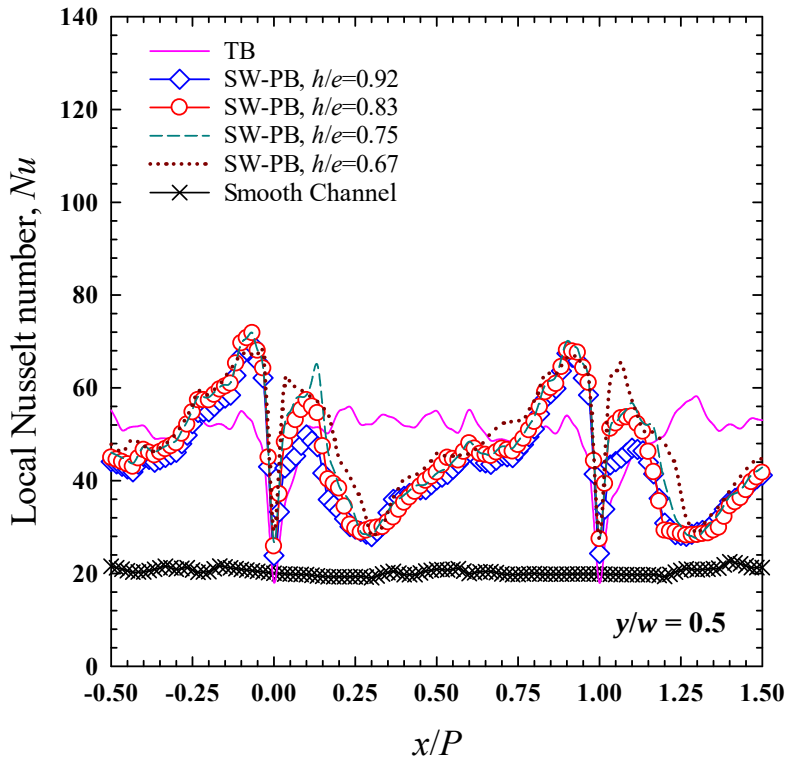

(a) $y/w = 0.5$

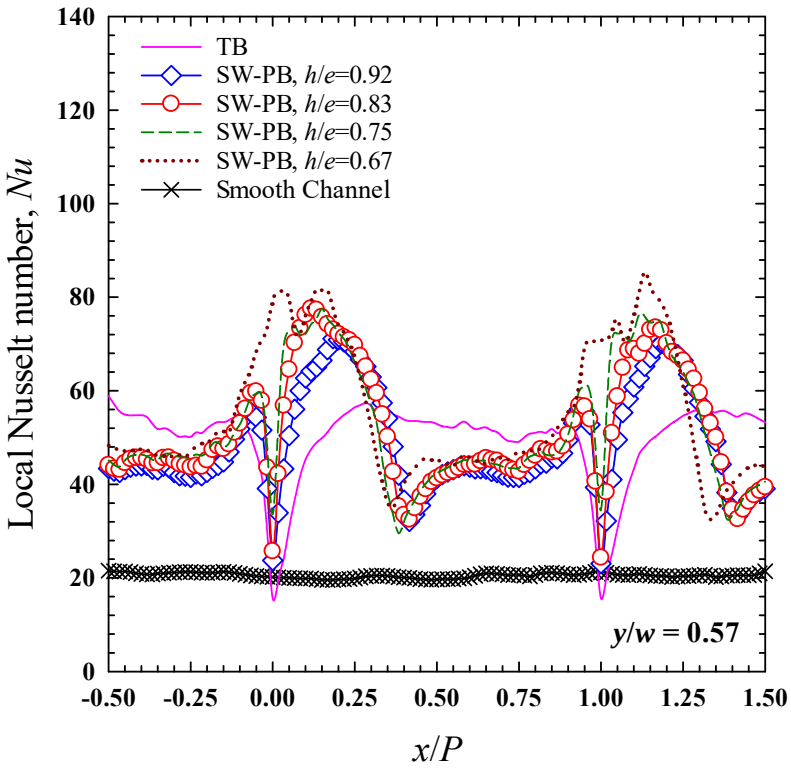

(b) $y/w = 0.57$

Figure 4.18. Normalized Nusselt number at $y/w = 0.5$, $y/w = 0.57$ and $x/P = 0.15$ for a Reynolds number of 6,000.

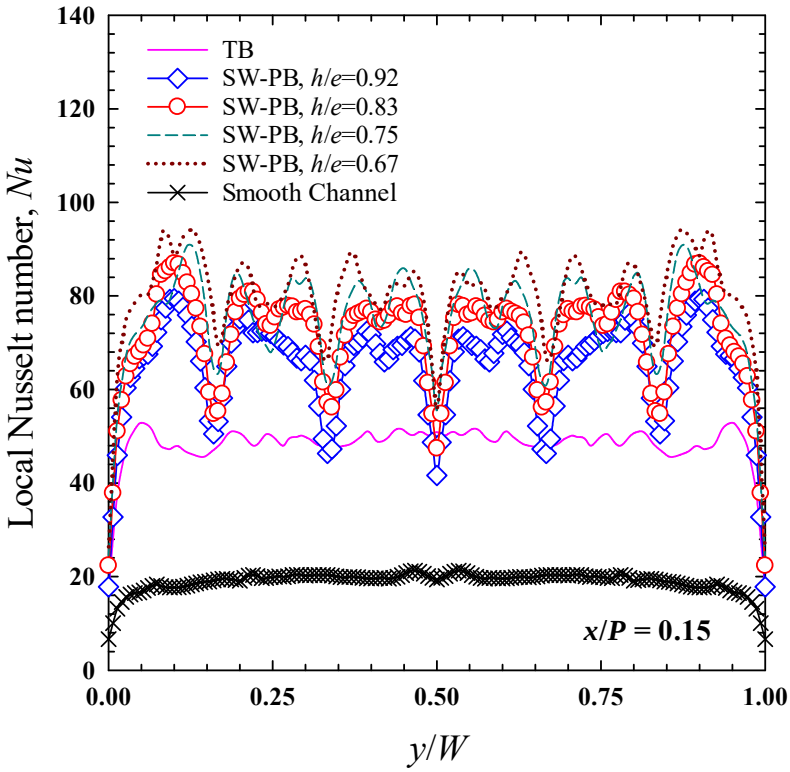

(c) $x/P = 0.15$

Figure 4.18. Normalized Nusselt number at $y/w = 0.5$, $y/w = 0.57$ and $x/P = 0.15$ for a Reynolds number of 6,000.

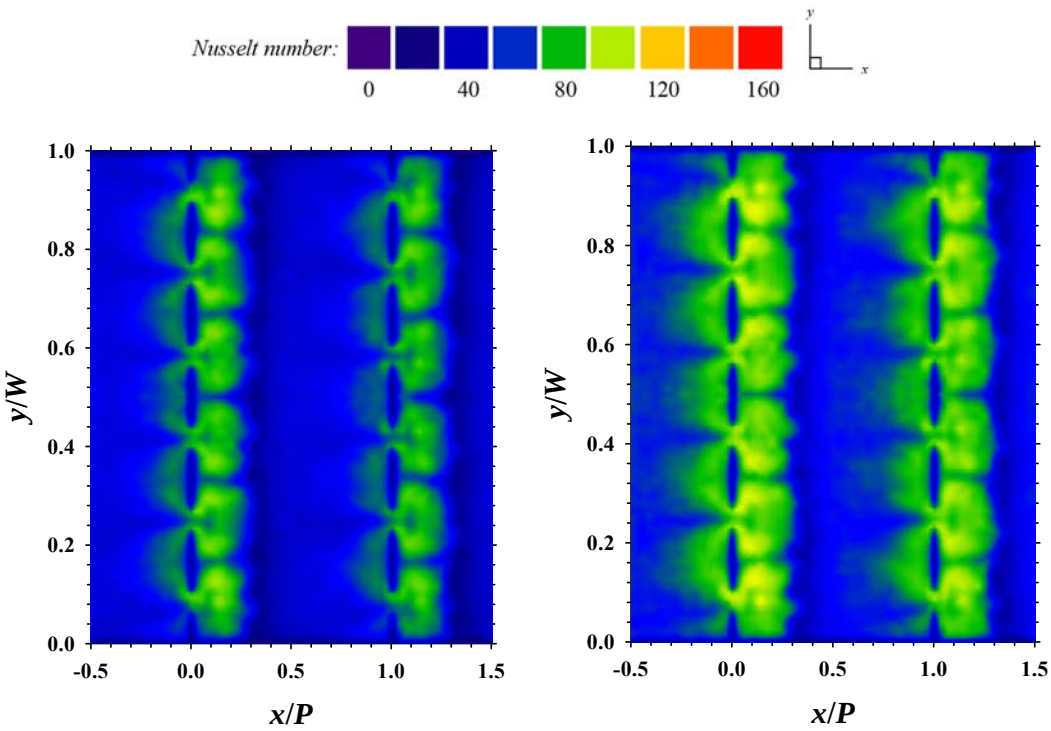

(a) $Re = 6{,}000$ (b) $Re = 9{,}000$

Figure 4.19. Influence of square-wing perforated transverse baffle (SW-PB) at square-wing locations of $h/e = 0.67$ with various Reynolds number on local heat transfer distribution.

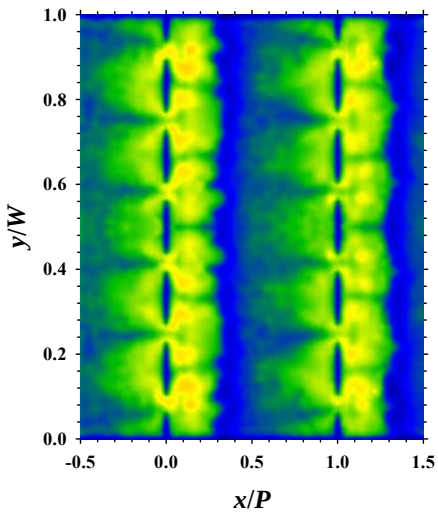

(c) *Re* = 12,000

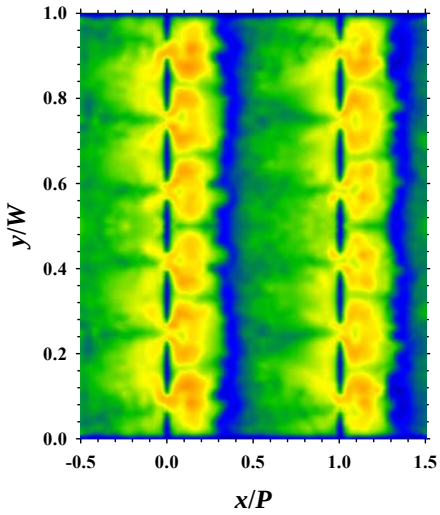

(d) *Re* = 15,000

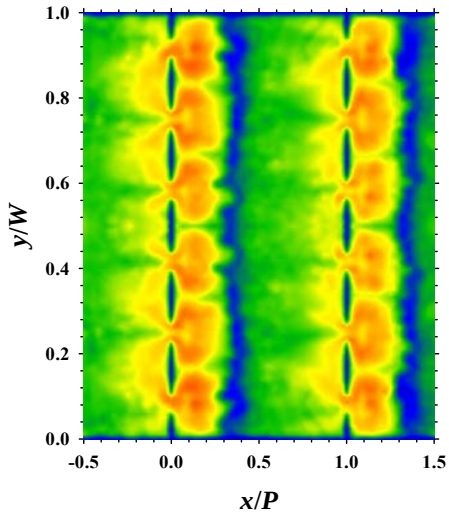

(e) *Re* = 18,000

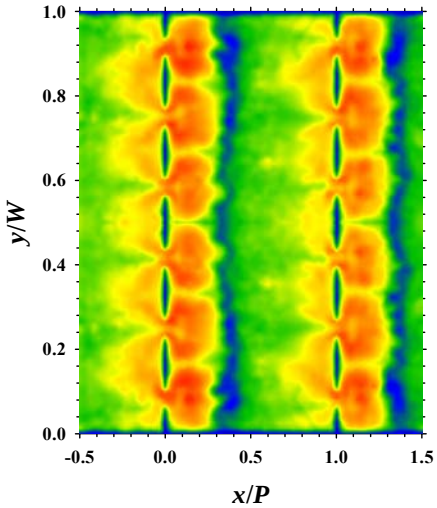

(f) *Re* = 21,000

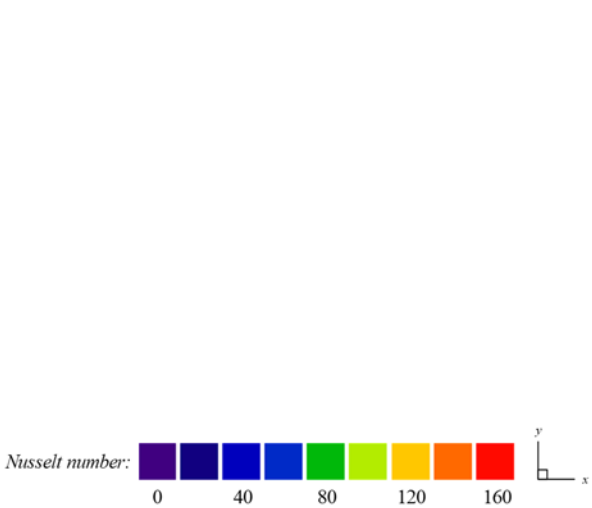

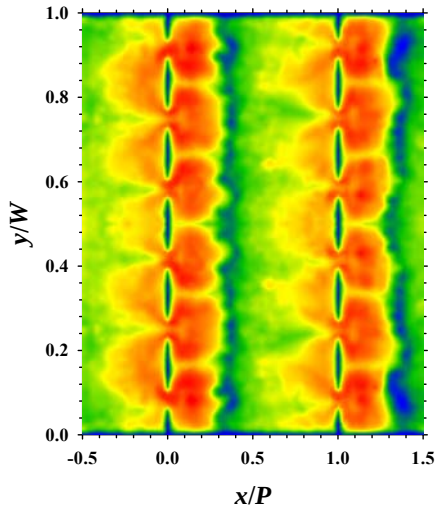

(g) *Re* = 24,000

Figure 4.19. Influence of square-wing perforated transverse baffle (SW-PB) at square-wing locations of *h/e* = 0.67 with various Reynolds number on local heat transfer distribution. (*continued*)

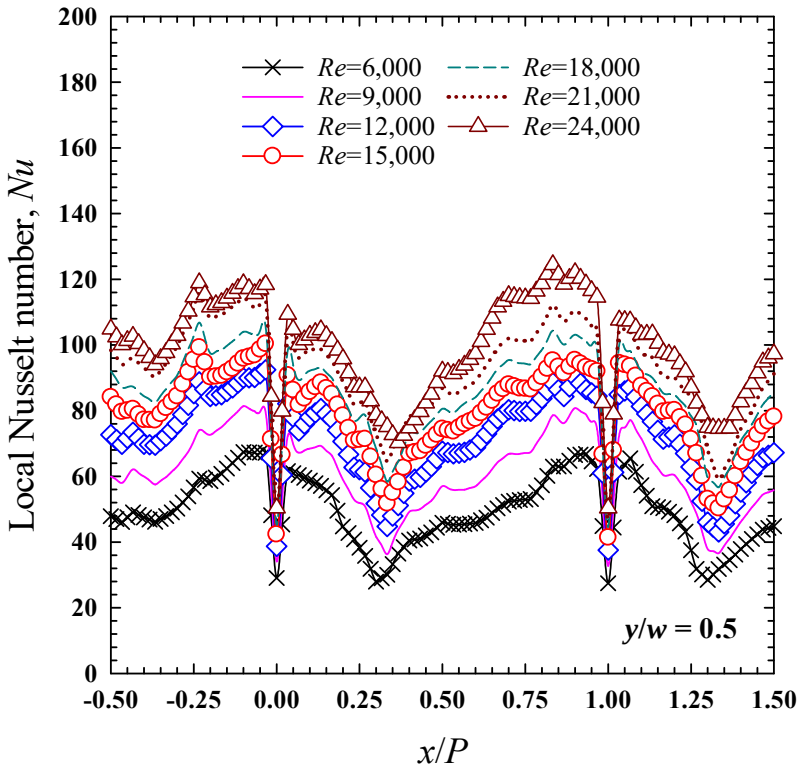

(a) y/w=0.5

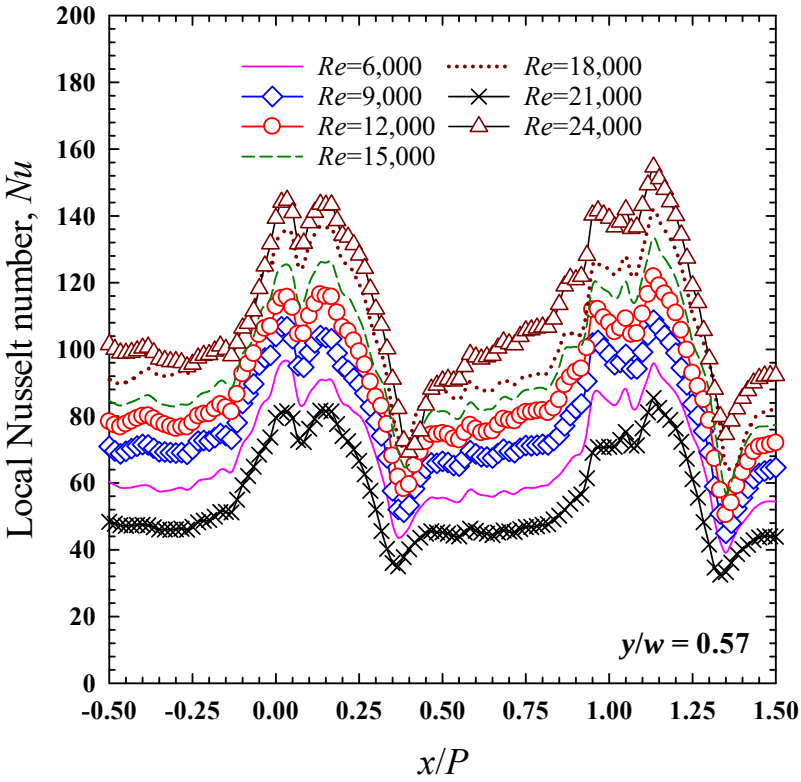

(b) y/w = 0.57

Figure 4.20. Normalized of Nusselt number at y/w = 0.5 and y/w = 0.57 for SW-PBs at square-wing locations of h/e = 0.67.

Figures 4.21(a-b) display average Nusselt number results of all cases. At each Reynolds number, the enhanced channels consistently yield higher the smooth one. Despite the fact that similar behaviors are observed for all square-wing perforated transverse baffles, the ones with lower locations offer superior average heat transfer. As compared to the smooth channel, the ones with square-wing perforated transverse baffles (SW-PBs) having square-wing locations, *h/e* = 0.92 (the highest wing location), 0.83, 0.75, and 0.67 (the lowest wing) show heat transfer enhancements by approximately 66-148%, 71-157%, 76-166%, and 83-180%, respectively. In other words, the square-wing perforated transverse baffles (SW-PB) with the lowest wing location, *h/e* = 0.67, which is most efficient for heat transfer augmentation give Nusselt numbers higher than those located at *h/e* = 0.92, 0.83, and 0.75 by 8.66-11.38%, 6.21-8.09%, and 0.89-1.74%, respectively.

The trend is principally due to the higher strength of impinging jet caused by the wings located nearer to the bottom wall. It is noteworthy that the transverse baffle (TB) gives comparable Nusselt number to the square-wing perforated transverse baffle (SW-PB) having square-wing locations, *h/e* = 0.92.

4.2.2.2.2 Friction factor results

Figures 4.22(a-b) present the variation of the friction factor as a function of the Reynolds number (*Re*). As the Reynolds number (*Re*) raises, the friction factor (*f*) is slightly reduced. The friction factors of the channels with baffles (TB and SW-PBs) are significantly greater than those of a smooth channel. This is due to the dissipation of fluid dynamic pressure as a result of secondary flow caused by the baffles. However, friction factors caused by square-wing perforated transverse baffle (SW-PB) are considerably lower than those caused by the typical transverse baffles (TBs). This can be explained that the friction loss is suppressed by the presence of the spaces on the square-wing perforated transverse baffle (SW-PB). The friction factor is slightly increased as the square-wing location (*h/e*) decreases.

Utilization of the square-wing perforated transverse baffles (SW-PBs) with the lowest wing location, *h/e* = 0.67, results in a greater friction factor of approximately 1.33-2.77%, 0.86-1.91%, and 0.42-1.21% than that with *h/e* = 0.92 (highest wing location), 0.83, and 0.75, respectively. As compared to the smooth channel, square-wing perforated transverse baffles (SW-PBs) having *h/e* = 0.92, 0.83, 0.75, and 0.67 caused higher friction factors by approximately 9.51-10.69, 9.56-10.79, 9.59-10.86, and 9.64-10.99 times, respectively.

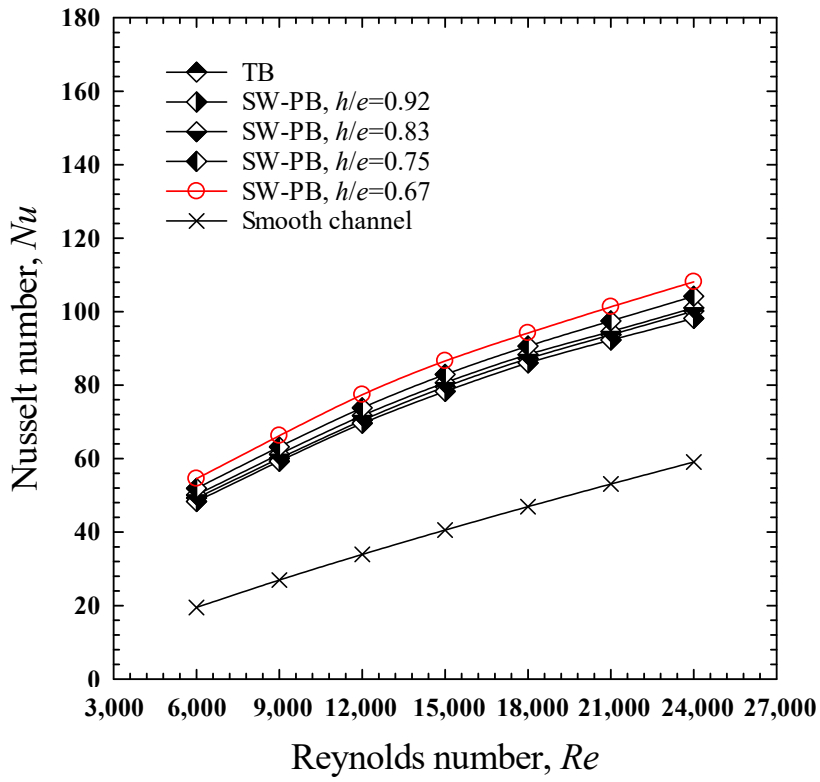

(a) *Nu*

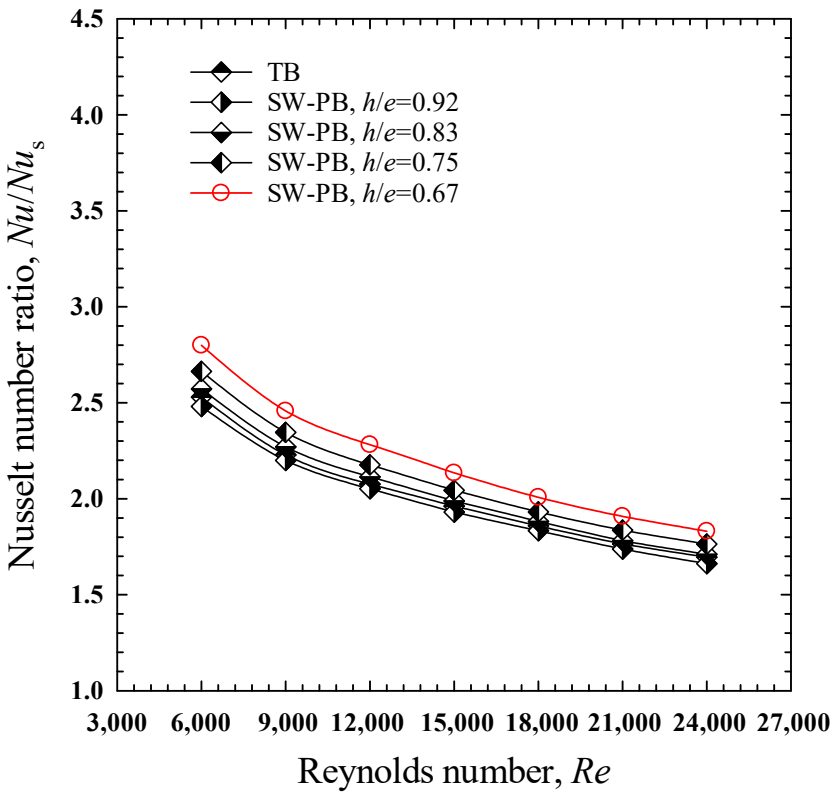

(b) Nu/Nu_s

Figure 4.21. Influence of square-wing perforated transverse baffle (SW-PB) at various wing locations (*h/e* = 0.92, 0.83, 0.75, and 0.67) on average Nusselt number.

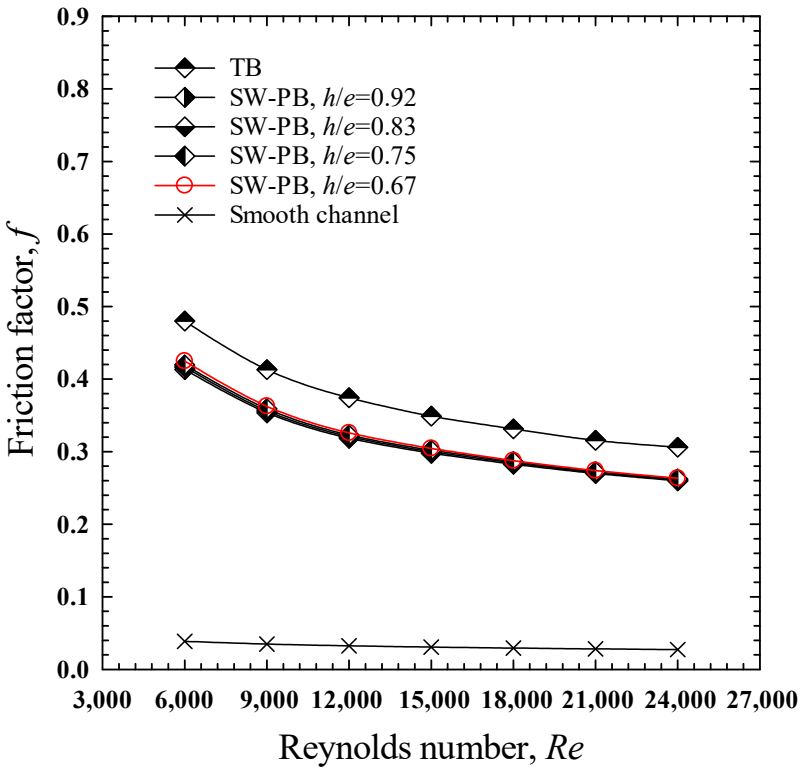

(a) f

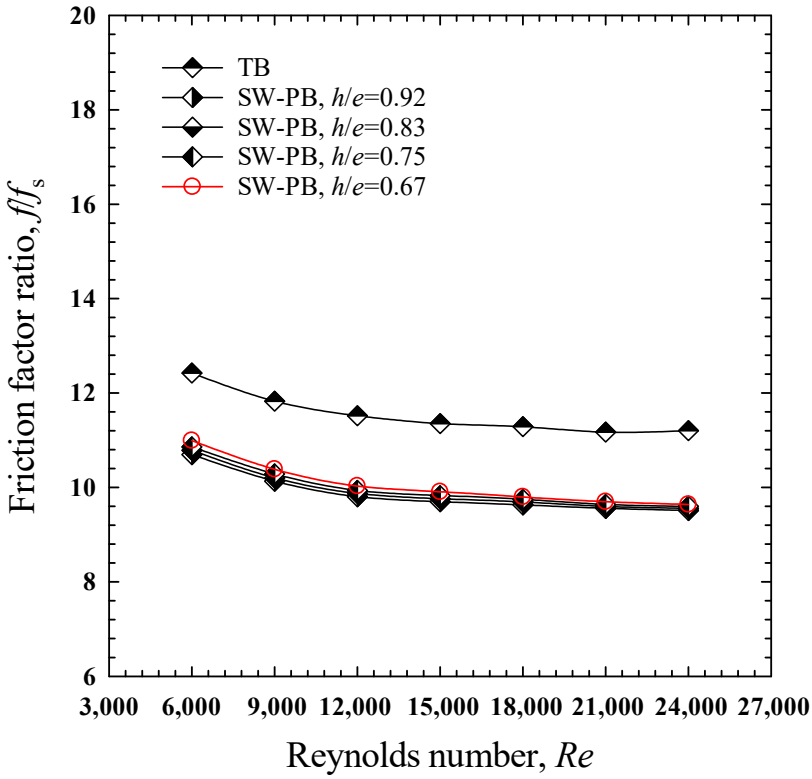

(b) f/f_s

Figure 4.22. Influence of square-wing perforated transverse baffle (SW-PB) at various wing locations (h/e = 0.92, 0.83, 0.75, and 0.67) on friction factor.

4.2.2.2.3 Thermal performance factor results

Figures 4.23(a-b) show variations of the thermal performance factor (*TPF*) as a function of the Reynolds numbers. At specific Reynolds number, all square-wing perforated transverse baffles (SW-PBs) show superior performances to the transverse baffle (TB). The greater performances of the square-wing perforated transverse baffle (SW-PB) is mainly attributed to the lower friction losses. Moreover, the square-wing perforated transverse baffle (SW-PB) gives thermal performance factor (*TPF*) over unity over the wider Reynolds number range than the transverse baffle (6,000 ≤ *Re* ≤ 9,000 compared to only at *Re* = 6,000). This suggests that the use of the channel with square-wing perforated transverse baffle (SW-PB) is preferable to the use of the channel with transverse baffle (TB) and also the smooth wall channel, particularly at low Reynolds numbers. Thermal performance factors (*TPF*) of the channels with square-wing perforated transverse baffle (SW-PB) having *h/e* = 0.92, 0.83, 0.75, and 0.67, are approximately 0.78-1.13, 0.81-1.16, 0.83-1.21, and 0.86-1.26 times, respectively. The employment of the square-wing perforated transverse baffle (SW-PB) with the lowest wing location, *h/e* = 0.67, results in a greater thermal performance factor *(TPF)* than those with *h/e* = 0.92 (highest wing location), 0.83, and 0.75, by around 8.86-11.82%, 6.23-8.12%, and 3.64-4.67%, respectively. Over the studied range, the maximum thermal performance factor *(TPF)* of 1.26 is attained by the square-wing perforated transverse baffle (SW-PB) having *h/e* =0.67 at *Re* = 6,000.

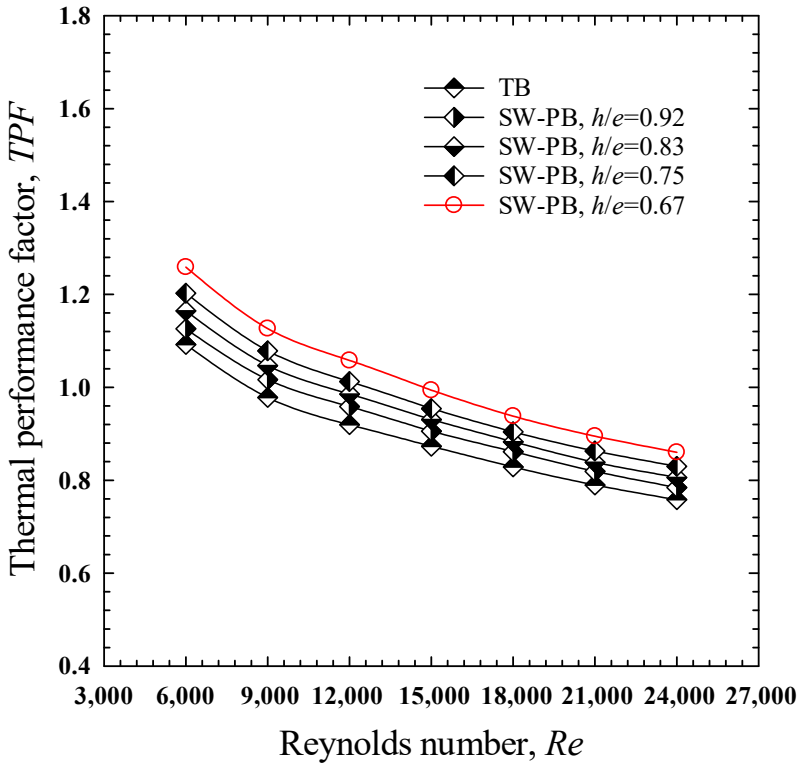

(a) *TPF* & *Re*

Figure 4.23. Influence of square-wing perforated transverse baffle (SW-PB) at various wing locations (*h/e* = 0.92, 0.83, 0.75, and 0.67) on thermal performance factor.

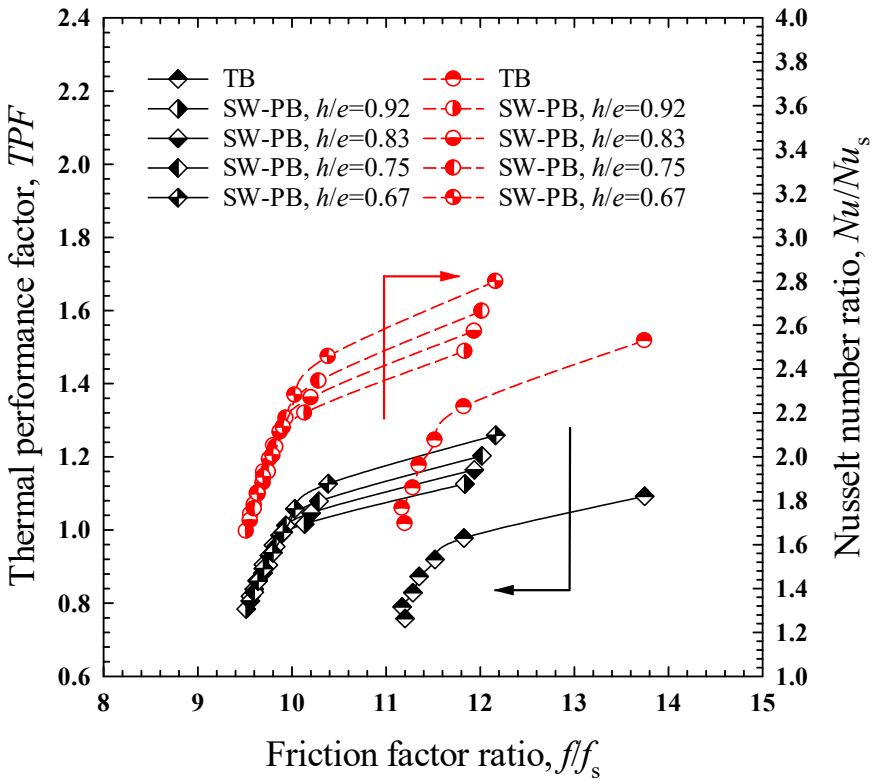

(b) f/f_s & $TPF/Nu/Nu_s$

Figure 4.23. Influence of square-wing perforated transverse baffle (SW-PB) at various wing locations (h/e = 0.92, 0.83, 0.75, and 0.67) on thermal performance factor. (*continued*)

4.2.2.2.4 Empirical correlations

The Nusselt number (Nu), friction facto (f) and thermal performance factor (TPF) results of the channels installed with square-wing perforated transverse baffle (SW-PB) having h/e = 0.92, 0.83, 0.75, and 0.67, are applied for the empirical correlation development. The experimental findings demonstrated that the geometries of square-wing perforated transverse baffle (SW-PB) had a significant impact on Nusselt number (Nu), friction facto (f) and thermal performance factor (TPF). The established correlations were a function of wing attack angle (θ), the flow characteristics (Re) and the fluid properties (Pr), as indicated by Eqs. (4.34), (4.35) and (4.36).

$$Nu = f_1(Re, Pr, \theta) \tag{4.34}$$

$$f = f_2(Re, \theta) \tag{4.35}$$

$$TPF = f_3(Re, \theta) \tag{4.36}$$

All correlations for the range of the present experimental setup and parameters were developed using multiple regression, including correlations for the Nusselt number (Nu), friction facto (f) and thermal

performance factor (*TPF*). Equations (4.34), (4.35) and (4.36) provide empirical correlations obtained from studies done in the range of 6,000 < *Re* < 24,000. The resultant correlations are shown below.

Empirical correlation of Nusselt number (*Nu*)

$$Nu = 0.663 Re^{0.5072} Pr^{0.4} (h/e)^{-0.3193} \tag{4.37}$$

Empirical correlation of friction factor (*f*)

$$f = 7.585 Re^{-0.3364} (h/e)^{-0.0627} \tag{4.38}$$

Empirical correlation of thermal performance factors (*TPF*)

$$TPF = 9.161 Re^{-0.2449} (h/e)^{-0.2983} \tag{4.39}$$

Figures 4.24(a-c) disclose the comparison between the experimental and predicted results. Evidently, the predicted Nusselt number (*Nu*), friction facto (*f*) and thermal performance factor (*TPF*) deviate from the experimental ones only within ±2.2%, ±3.5% and ±4.7%, respectively.

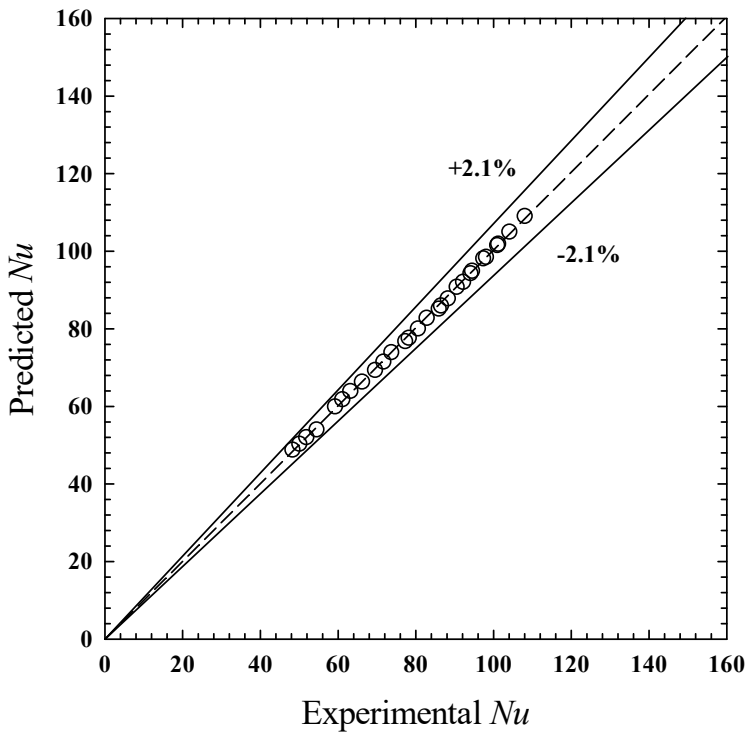

(a) *Nu*

Figure 4.24. Experimental results & predicted values of the empirical correlations.

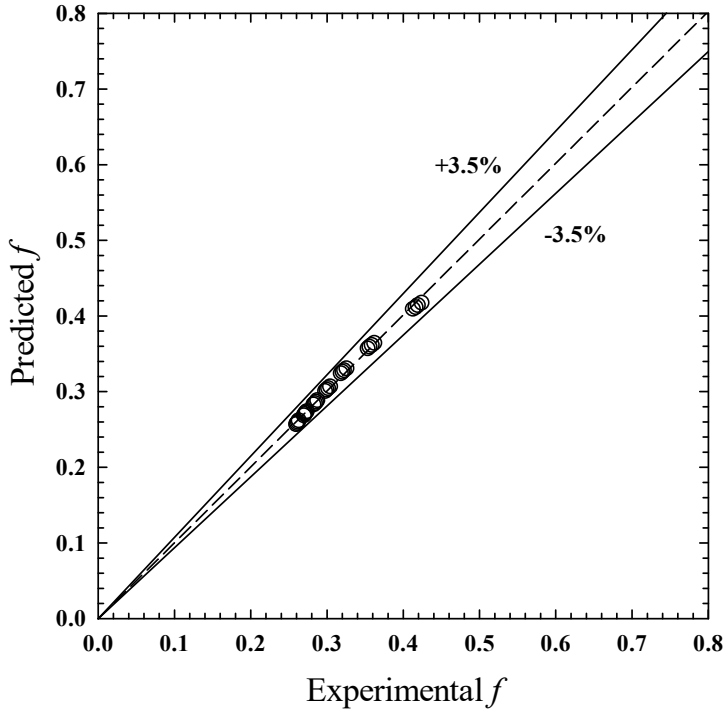

(b) *f*

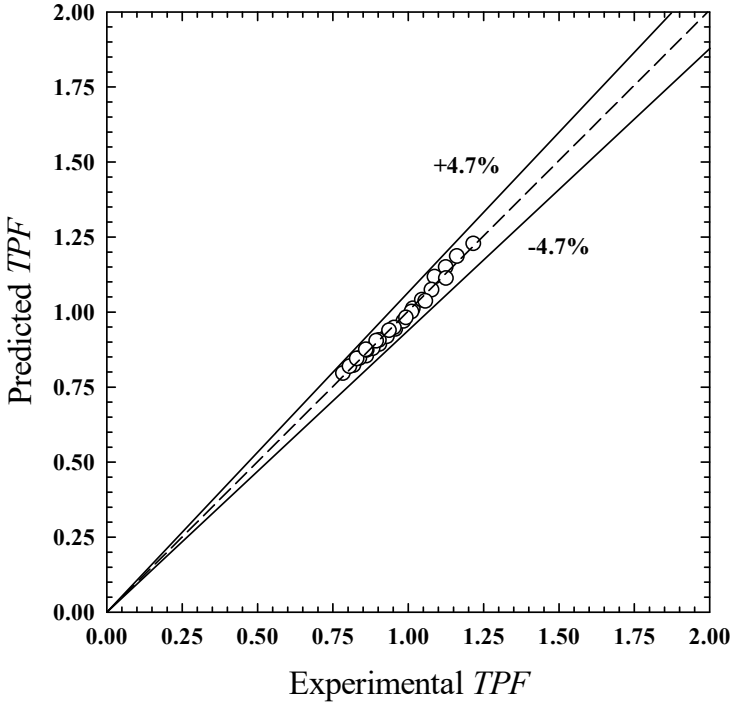

(c) *TPF*

Figure 4.24. Experimental results & predicted values of the empirical correlations. (*continued*)

4.2.2.3 Square-wing perforated transverse baffle: Effect of attack angle

4.2.2.3.1 Heat transfer results

Figures 4.25 and 4.26 display the local Nusselt number profiles on the bottom wall which was mounted with baffles having a blockage ratio *(e/H)* of 0.3 and a pitch ratio *(P/H)* of 1.5 at *Re* = 6,000. Clearly,

the presence of baffles resulted in greater heat transfer (*Nu*) than for the smooth channel. The channel equipped square-wing perforated transverse baffles can generate impinging jet flows and recirculation behind the baffles. Impinging jets and recirculation promote fluid mixing in the near-wall region and behind the rear baffles. Figure 4.25(b) shows that heat transfer in a channel fitted with square wing perforated transverse baffles is superior to that in a smooth channel.

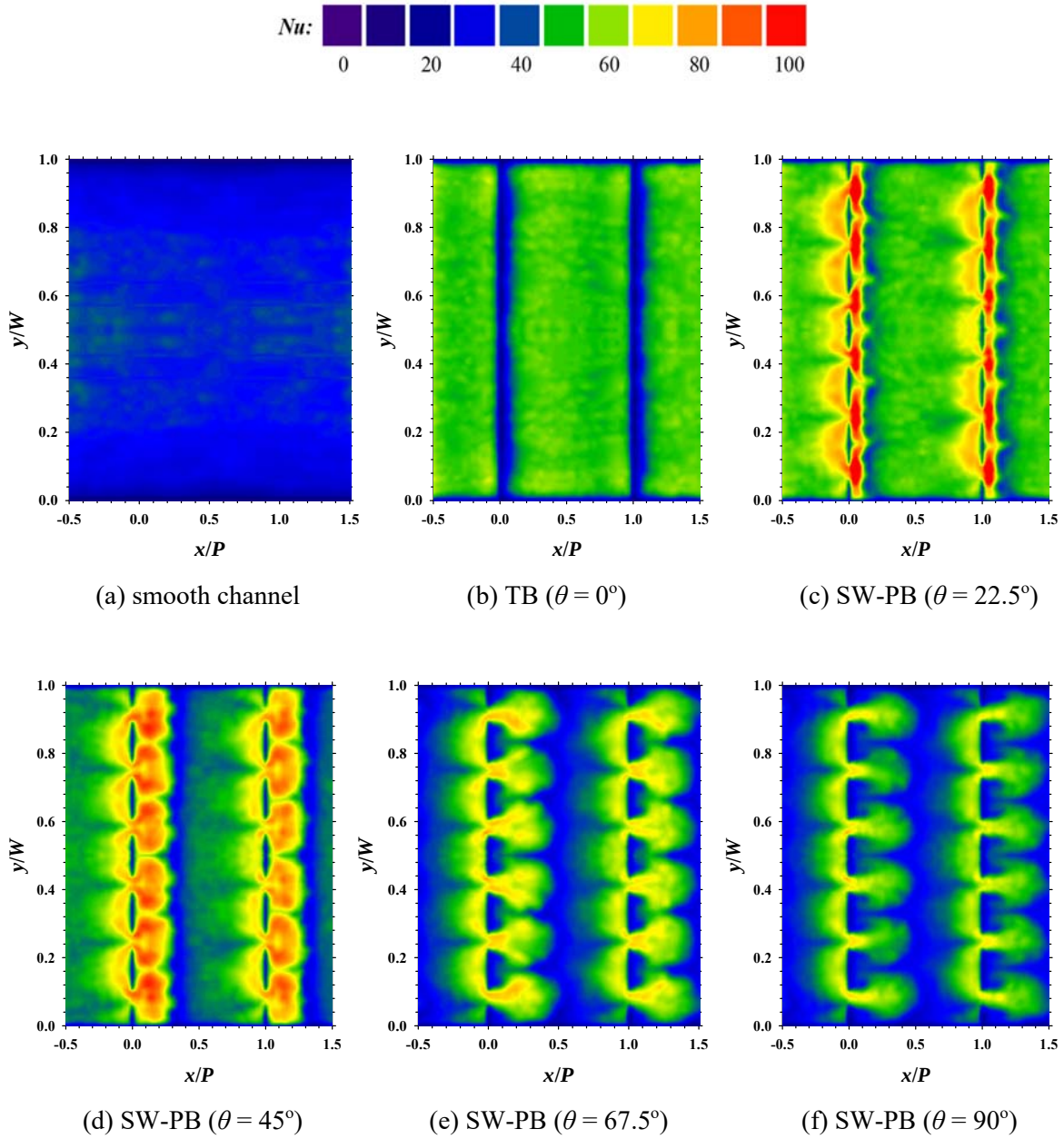

Figure 4.25. Influence of square-wing perforated transverse baffle (SW-PB) at *Re* = 6,000 with various wing attack angles (θ = 0°, 22.5°, 45°, 67.5° and 90°) on local heat transfer distribution.

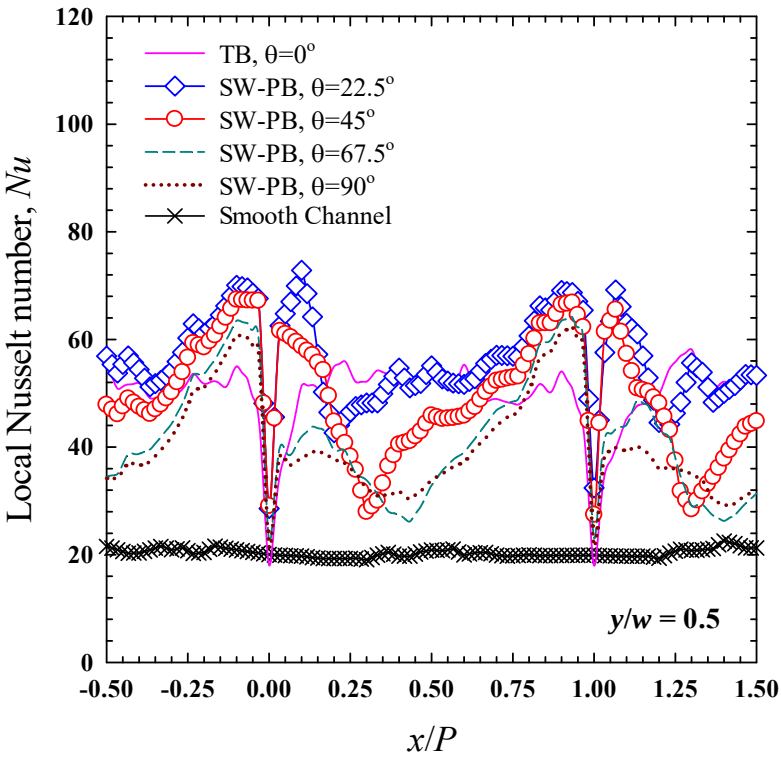

(a) $y/w = 0.5$

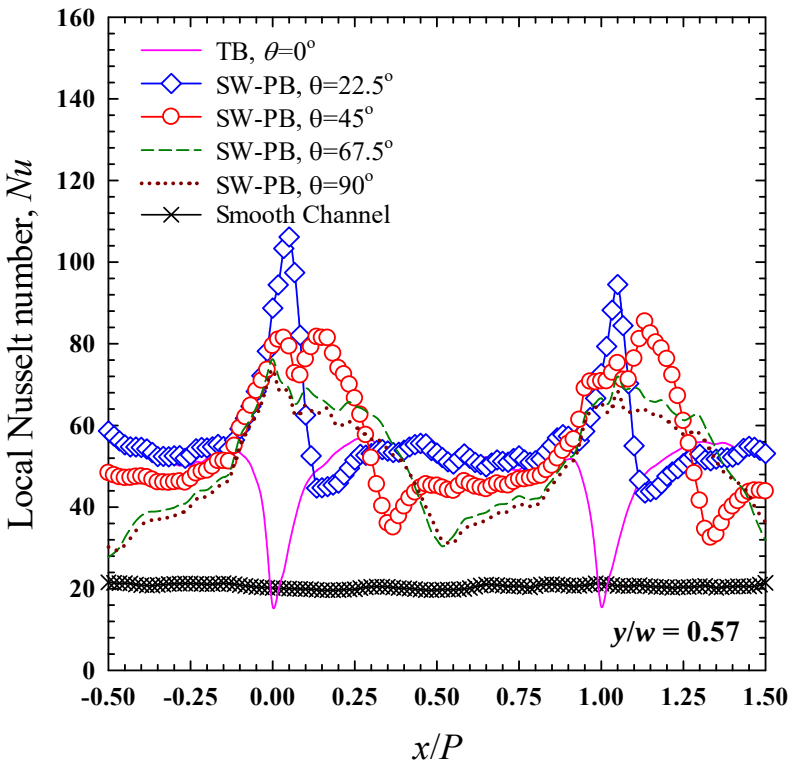

(b) $y/w = 0.57$

Figure 4.26. Normalized of Nusselt number at $y/w = 0.5$, $y/w = 0.57$ and $x/P = 0.05$ at $Re = 6{,}000$.

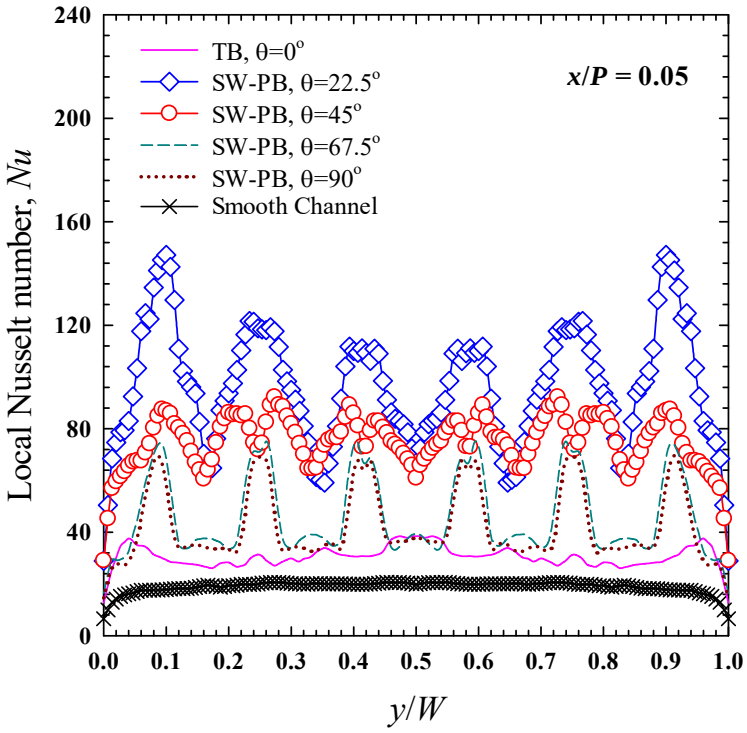

(c) $x/P = 0.05$

Figure 4.26. Normalized of Nusselt number at y/w = 0.5, y/w = 0.57 and x/P = 0.05 at Re = 6,000. (*continued*)

Solid transverse-baffles (TB, $\theta = 0^{o}$) gave moderate heat transfer rates between the baffles. However, the heat transfer rates were extremely low in vicinity of the baffles (x/P = 0.0 and 1.0). These results can be explained since the baffles inhibited flow reattachment around this area. Fluid flowed over the baffles and then reattached causing flow recirculation which helped enhance heat transfer. For perforated transverse baffles with square-wings (SW-PBs) and square-wing attack angles of 22.5°, 45°, 67.5° and 90°, high heat transfer rates appeared in vicinity of the baffles (x/P = 0.0 and 1.0) due to the shapes of multiple impingement flows. At larger square-wing attack angles, high heat transfer areas shifted further from the baffles due to changes of flow reattachment. Additionally, high heat transfer areas became larger reflecting a spreading of the reattachment and recirculation flow. However, at smaller square-wing attack angles, the intensities of high heat transfer were increased and the dead zone became narrower. This indicates that impingement at smaller square-wing attack angles was stronger. Among all square-winged transverse-baffles, the ones with the square-wing attack angles (θ) of 22.5° and 45° showed the optimal results signified by high intensity and large heat transfer area, especially at x/P = 0.0-0.1 and x/P = 1.0-1.1 as seen in Fig. 4.26(a-b). The results reflects that the baffles with the optimum square-wing attack angle (θ) introduce strong impingement that effectively washes dead zones, as seen in Fig. 4.26(c). This enlarged area for heat transfer allows the fluid in the core and near-wall regions to mix evenly under the influence of irregular disturbances and impinging jet flows and recirculation, thereby enhancing heat transfer. The influences of the two factors are amplified under

turbulent flow conditions. Thus, heat transfer capability increases with decreasing square wing attack angle.

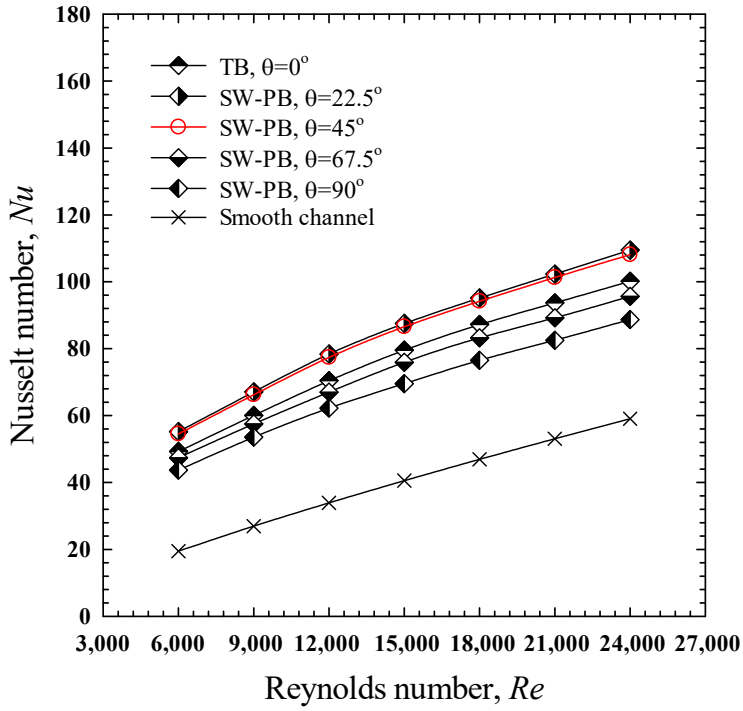

(a) *Nu*

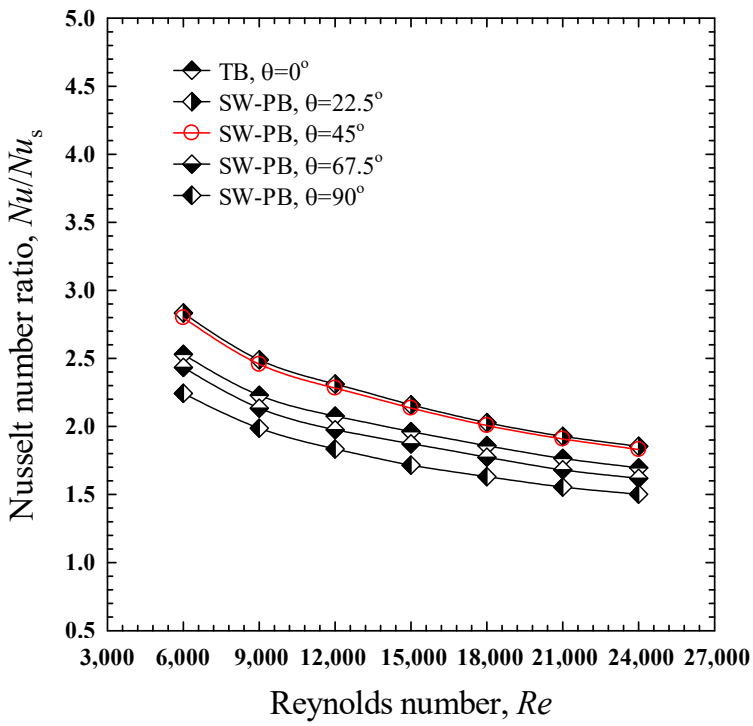

(b) Nu/Nu_s

Figure 4.27. Influence of square-wing perforated transverse baffle (SW-PB) at various wing attack angles (θ = 0°, 22.5°, 45°, 67.5° and 90°) on average Nusselt number (*Nu*).

Figure 4.27 shows the variation of the average heat transfer rate with Reynolds number for a channel containing square-wing perforated transverse baffle (SW-PB) with various square-wing attack angles (θ = 22.5°, 45°, 67.5° and 90°) as well as a smooth channel. The Nusselt number (*Nu*) from the smooth channel is also plotted for comparison. The heat transfer rate increased with decreased square wing attack angles (θ) and increased Reynolds number. Under all conditions, the heat transfer rate increased with the Reynolds number because of the higher intensity of fluid turbulence. At the same operating conditions, the channel fitted square-wing perforated transverse baffle (SW-PB) significantly outperformed the smooth channel in terms of their Nusselt numbers. The results are due to the secondary flows described in early section. The consequences were stronger fluid collision and greater fluid fluctuation caused by recirculation and longitudinal vortex flows that resulted greater heat transfer.

The square-wing perforated transverse baffle (SW-PB) with θ = 0° (solid transverse-baffle), 22.5°, 45°, 67.5° and 90° respectively enhanced the Nusselt number (*Nu*) by 69.6-152.9%, 85.4-183.4%, 83.05-179.9%, 61.9-143.3%, and 50.2-124.3% above those of the smooth channel. The highest heat transfer rate among the square wing attack angles (θ) is achieved for θ = 22.5°. Among the baffles, the square-wing perforated transverse baffle (SW-PB) with an attack angle of 45° yielded heat transfer rates that were superior to those with attack angles of 0°, 22.5°, 67.5° and 90°, by around 7.95-10.68%, 0.99-1.29%, 13.04-15.46%, and 21.88-24.8%, respectively. As illustrated in Fig. 4.27, the Nusselt number ratio (Nu/Nu_s) decreased as the Reynolds number (*Re*) increased. At $6{,}000 \leq Re \leq 24{,}000$, the Nusselt number ratio (Nu/Nu_s) increase by the square-wing perforated transverse baffle (SW-PB) with θ = 0° (solid transverse-baffle), 22.5°, 45°, 67.5° and 90° were 1.69-2.53, 1.85-2.83, 1.83-2.79, 1.62-2.43, and 1.51-2.24, respectively.

4.2.2.3.2 Friction factor results

The relationship between pressure loss in terms of friction factor (*f*) and Reynolds number (*Re*) for the channel fitted with square-wing perforated transverse baffle (SW-PB) at various attack angles (θ = 22.5°, 45°, 67.5° and 90°) and Reynolds numbers, is presented in Figs. 4.28(a-b) along with the results for a smooth channel. The influence of the square-wing perforated transverse baffle (SW-PB) on the friction factor (*f*) is shown in Fig. 4.28(a). These finding suggests that the channel fitted with square-wing perforated transverse baffle (SW-PB) caused an additional pressure drop, leading to higher friction factors as compared to a smooth channel. Contact between the large upwind area of the square-wing perforated transverse baffle (SW-PB) and air, long flow paths and strong turbulence at the boundary layer caused intensive turbulences and impinging jets were the main sources of the flow resistance change.

Experimental results also showed that square-wing perforated transverse baffle (SW-PB) caused a significant increase in the friction factor by 6.5 to 36 times above the smooth channel. This is ascribed

to flow obstruction, increased surface area, recirculation and impinging flows generated by the square-wing perforated transverse baffle (SW-PB). Generally, the recirculation/reverse flow induces a much greater increase in friction factor than axial flow does. Additionally, friction was also caused by increased contact area and dynamic pressure dissipation. Figure 4.28 reveals that an increase in the air velocity (Reynolds number) led to a drop in the friction factor (f) because the friction between the surface of square-wing perforated transverse baffle (SW-PB) and the air was reduced. For $6{,}000 \leq Re \leq 24{,}000$, the use of square-wing perforated transverse baffle (SW-PB) with $\theta = 0^{o}$ (solid transverse-baffle), 22.5°, 45°, 67.5° and 90°, respectively, yielded friction factor ratios (f/f_s) of 11.17-12.42, 10.25-11.69, 9.64-10.99, 9.24-10.59, and 8.89-10.23. In other word, the friction factors (f) caused by solid transverse-baffles were greater than that than those caused by square-wing perforated transverse baffle (SW-PB) with $\theta = 22.5^{o}$, 45°, 67.5° and 90° by up to 1.06-1.09, 1.13-1.16, 1.17-1.21, and 1.21-1.26 times, respectively. The results indicated that the presence of the gap on square-wing perforated transverse baffle (SW-PB) helped in reducing friction loss as compared to the solid one.

4.2.2.3.3 Thermal performance factor results

Figures 4.29(a-b) show the variation in thermal performance factor (*TPF*) with Reynolds number (*Re*) for channels with square-wing perforated transverse baffle (SW-PB) installed. Figures 4.29(a-b) depict the effect of square-wing perforated transverse baffles (SW-PB) on the thermal performance factor (*TPF*) at an equal pumping power. For all square-winged transverse-baffles, increased Reynolds number (*Re*) values reduced the thermal performance factor (*TPF*). Overall, thermal performance factor (*TPF*) varies from 0.76 to 1.26, which indicates that the channel with square-wing perforated transverse baffle (SW-PB) installed may not achieve the expected energy saving under turbulent flow. However, channels with square-wing perforated transverse baffle (SW-PB) inserts are advantageous in terms of energy saving at low Reynolds numbers (*Re*). The thermal performance factor (*TPF*) for square-wing perforated transverse baffle (SW-PB) with low wing attack angles ($\theta = 22.5^{o}$, 45° and 67.5°) was above unity and substantially higher than that produced by a solid baffle ($\theta = 0^{o}$) under similar flow conditions. This suggests that square-wing perforated transverse baffle (SW-PB) offer an advantage over using solid baffles.

For all square-wing perforated transverse baffles (SW-PBs) examined, the thermal performance factor (*TPF*) tended to increase as the attack angle (θ) decreased. For $6{,}000 \leq Re \leq 24{,}000$, the thermal performance factor (*TPF*) values for square-wing perforated transverse baffle (SW-PB) with $\theta = 0^{o}$, 22.5°, 45°, 67.5° and 90° were in the ranges of 0.76-1.09, 0.85-1.25, 0.86-1.26, 0.77-1.11 and 0.72-1.03, respectively.

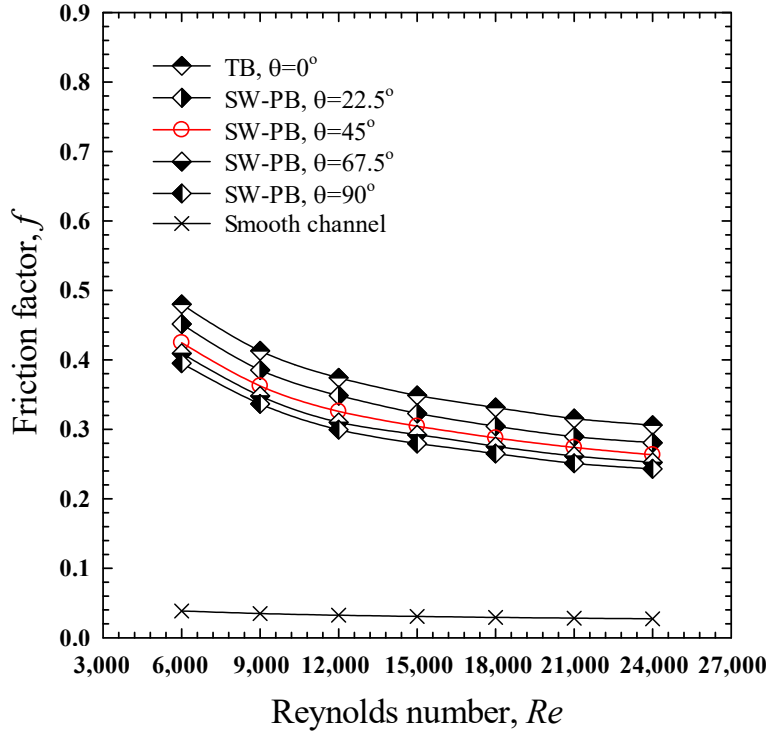

(a) f

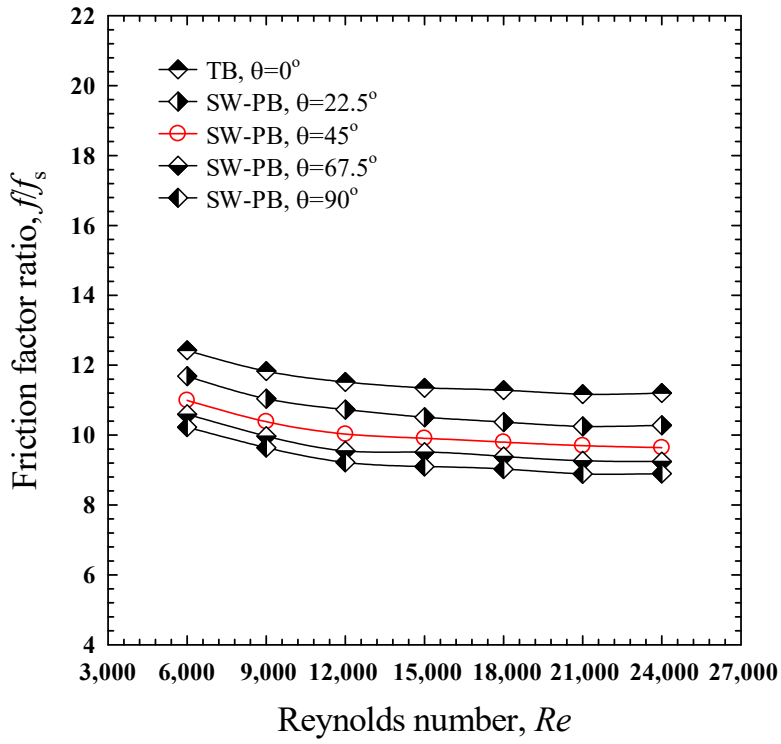

(b) f/f_s

Figure 4.28. Influence of square-wing perforated transverse baffle (SW-PB) at various wing attack angles (θ = 0°, 22.5°, 45°, 67.5° and 90°) on friction factor.

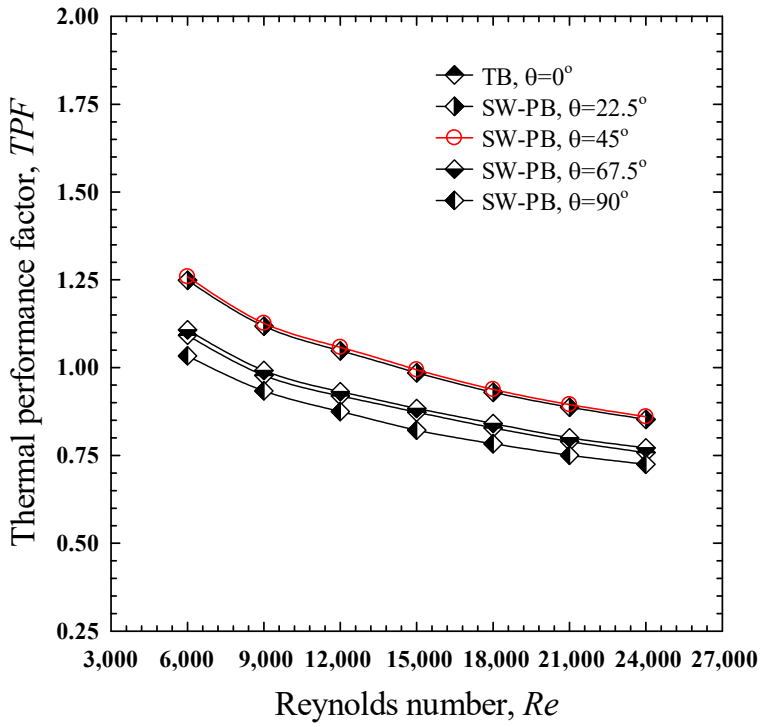

(a) *TPF* & *Re*

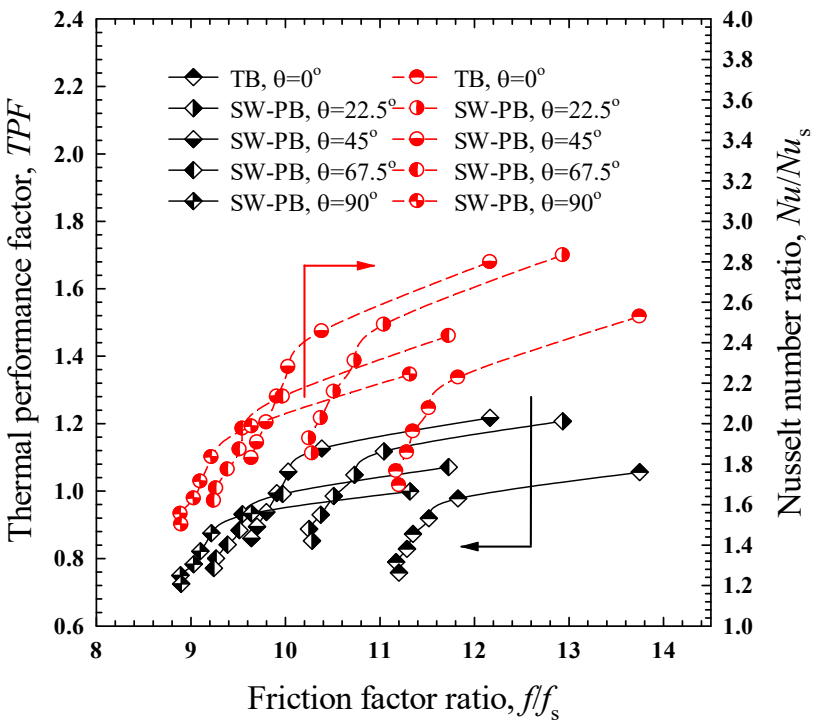

(b) f/f_s & $TPF/Nu/Nu_s$

Figure 4.29. Influence of square-wing perforated transverse baffle (SW-PB) at various wing attack angles (θ = 0°, 22.5°, 45°, 67.5° and 90°) on thermal performance factor.

The SW-PB with an attack angle of 45° presented a greater thermal performance factor (*TPF*) than other square-wing perforated transverse baffles (SW-PBs) owing to the resultant high heat transfer and moderate friction losses. The thermal performance factor (*TPF*) of the square-wing perforated transverse baffle (SW-PB) at an attack angle of 45° were found to be 13.21-15.28%, 0.75-0.95%, 11.47-13.64%, and 18.67-21.84% greater than those of channels with $\theta = 0°$, 22.5°, 67.5° and 90°, respectively.

4.2.2.3.4 *Empirical correlations*

All correlations for the range of the present experimental setup and parameters were developed using multiple regression, including correlations for the Nusselt number (*Nu*), friction factor (*f*), and thermal performance factor (*TPF*). In the present work, the predicted results from these equations were verified, and the outcomes are displayed in Figs. 4.30(a-c).

Empirical correlation of Nusselt number (*Nu*)

$$Nu = 1.878Re^{0.506}Pr^{0.4}(90 + \theta)^{-0.201} \tag{4.40}$$

Empirical correlation of friction factor (*f*)

$$f = 38.472Re^{-0.342}(90 + \theta)^{-0.314} \tag{4.41}$$

Empirical correlation of thermal performance factors (*TPF*)

$$TPF = 15.1Re^{-0.244}(90 + \theta)^{-0.097} \tag{4.42}$$

Equations (4.22), (4.23) and (4.24) provide empirical correlations obtained from studies done in the range of $6{,}000 < Re < 24{,}000$ and $Pr = 0.71$.

The comparison of experimental data and correlations for Nusselt number (*Nu*), friction factor (*f*), and thermal performance factor (*TPF*) is shown in Figs. 4.30(a-c). The predicted data Nusselt number (*Nu*), friction factor (*f*), and thermal performance factor (*TPF*) deviate from experimental data within ±9.7%, ±2.7% and ±10%, respectively. The deviations are mainly due to the experimental inconsistencies including, the turbulent fluctuation, axial heat loss and textured surface of square-wing perforated transverse baffle (SW-PB).

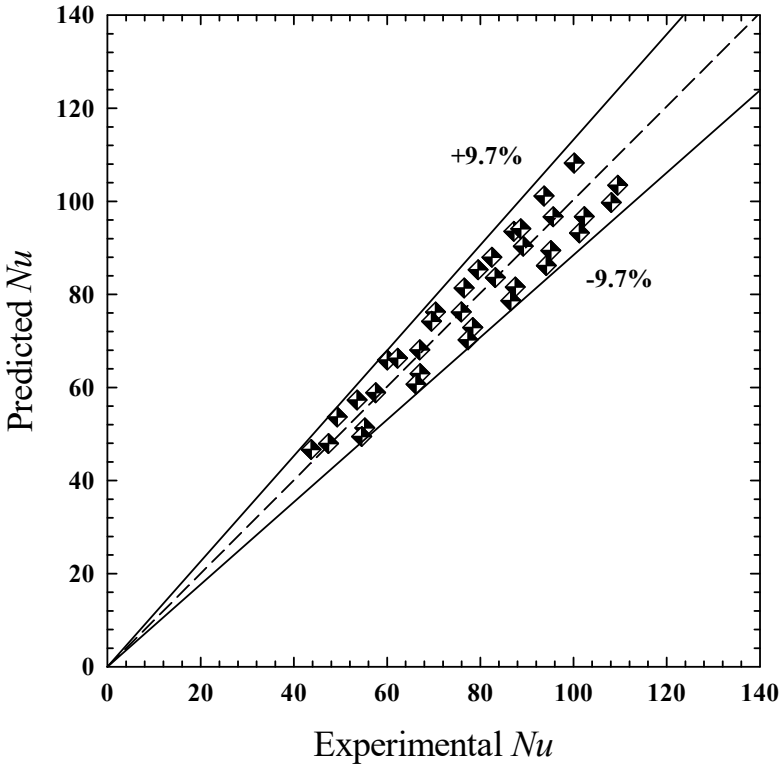

(a) *Nu*

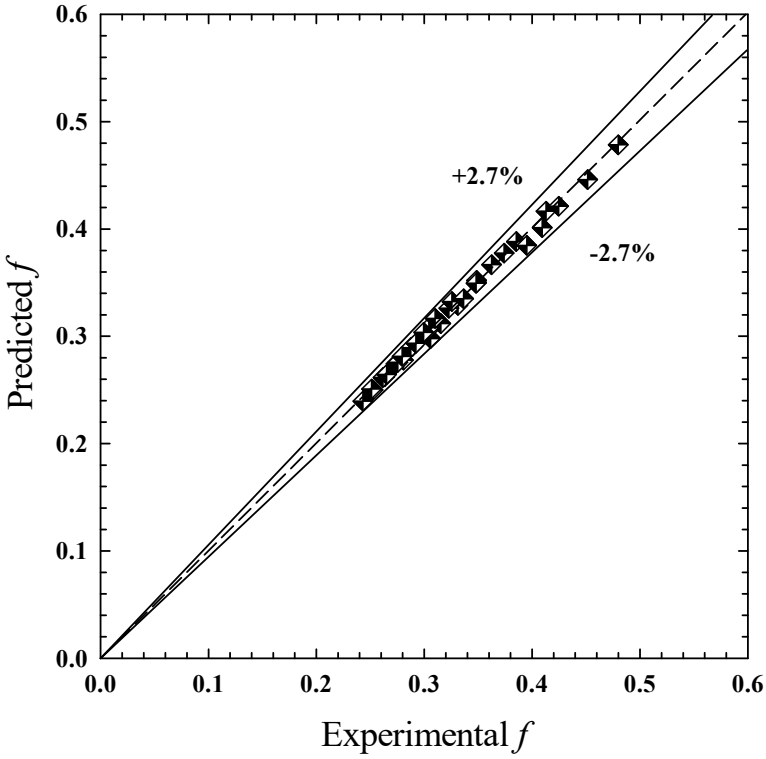

(b) *f*

Figure 4.30. Experimental results & predicted values of the empirical correlations.

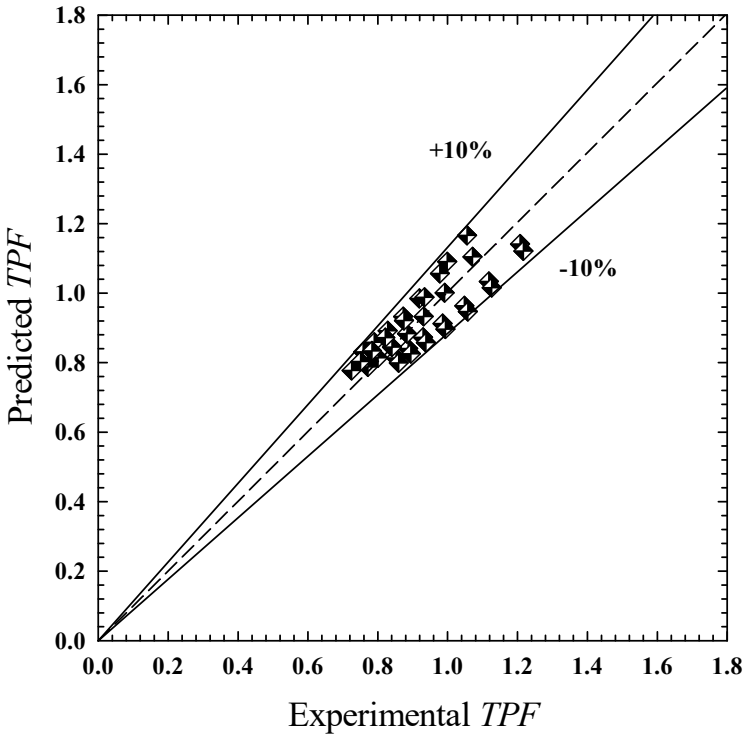

(c) *TPF*

Figure 4.30. Experimental results & predicted values of the empirical correlations. (*continued*)

4.2.3 Delta/Semi-oval/Square-wing perforated V-type baffle

In this section, the results obtained with the channel equipped with delta-wing perforated V-type baffle (DW-PVB), semi-oval wing perforated V-type baffle (SOW-PVB) and square-wing perforated V-type baffle (SW-PVB) are depicted in the form of Nusselt number (*Nu*) or friction factor (*f*) versus Reynolds number (*Re*). The trends of Nusselt number ratio (Nu/Nu_s) or friction factor ratio (f/f_s) versus Reynolds number (*Re*) are also analysed. The thermal performance factor (*TPF*) is used to evaluate the comprehensive performance of the enhancement devices. The heat transfer, friction losses and thermal performance results of the channel containing transverse baffles with delta/semi-oval/square-wing perforated V-type baffle having attack angles of 22.5°, 45°, 67.5°, and 90° and Reynolds number varying from 6,000 to 24,000 are presented and discussed along with those of the smooth channel.

4.2.3.1 Delta wing perforated V-type baffles

4.2.3.1.1 Heat transfer results

As depict in Fig. 4.31, the flow pattern and coherent vortex in the channel containing delta-wing perforated V-type baffles (DW-PVBs) are displayed as streamlines and iso-surfaces along with various delta-wing attack angles at *Re* = 9,000. As can be observed, the bottom channel section, where a solid V-shaped baffle (θ = 0°) is located, has two pairs of counter-rotating vortices. Due to greater fluid transport from the core to the near-wall areas, which is evident in the increased local Nusselt number seen in Figs. 4.31-4.33, the streamwise vortex-pairs aids in accelerating the heat transfer rate. Behind

the baffle, where the common flow-up vortices are visible, a greater Nusselt number (red zone) may be seen. Concurrently, the channel wall regions, where the common-flow-down vortices appear, have lower Nusselt numbers. The impinging jets behind the baffles are clearly visible for $\theta = 22.5^{o}$ and 45°, whereas only a very small area of impinging jets can be observed for the higher delta-wing attack angles of $\theta = 67.5^{o}$ and 90°. It is noteworthy that the area of lower Nusselt numbers using the higher delta-wing attack angles, $\theta = 67.5^{o}$ and 90°, is caused by multiple delta-wing jets that were flown over the low channel, acting as a barrier to prevent the vortex pairs from impinging on the channel wall. A lower Nusselt number area is seen behind the baffles when the Nusselt number contours are considered. Additionally, at low delta-wing attack angles of $\theta = 22.5^{o}$ and 45°, multiple jets from the delta-wing flow directly attacked the channel wall almost the rear baffle then it is not like flow barrier then the vortex-pairs can attack the channel wall lead to still higher heat transfer rates as in the case of $\theta = 0^{o}$, while it may reduce pressure losses in a channel. This indicates that the increased heat transfer behind the baffles is caused by delta-wing generated multiple impinging flows.

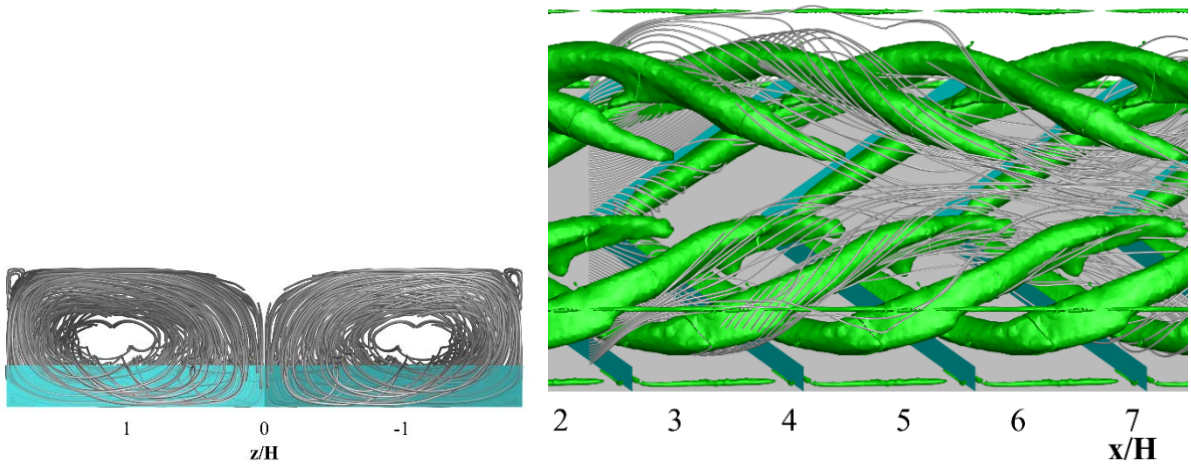

(a) $\theta = 0^{o}$ (solid V-shaped baffle)

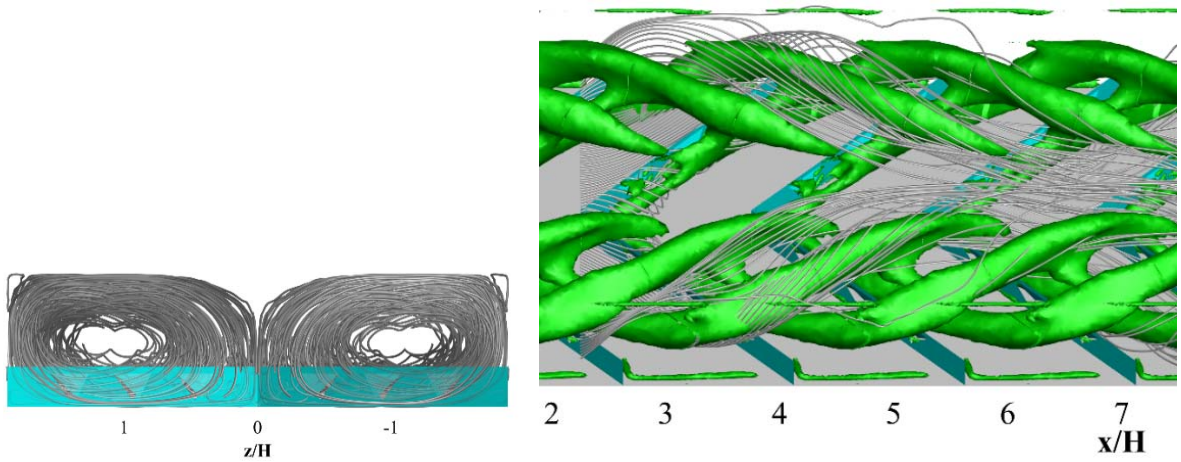

(b) $\theta = 22.5^{o}$

Figure 4.31. Streamline and iso-surface in channel containing delta-wing perforated V-type baffles (DW-PVB).

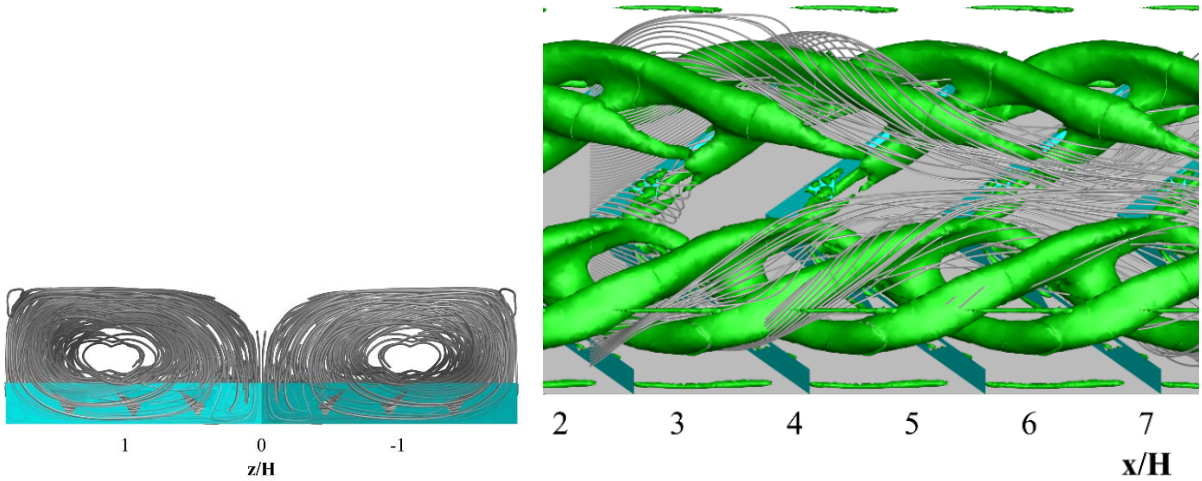

(c) $\theta = 45^{o}$

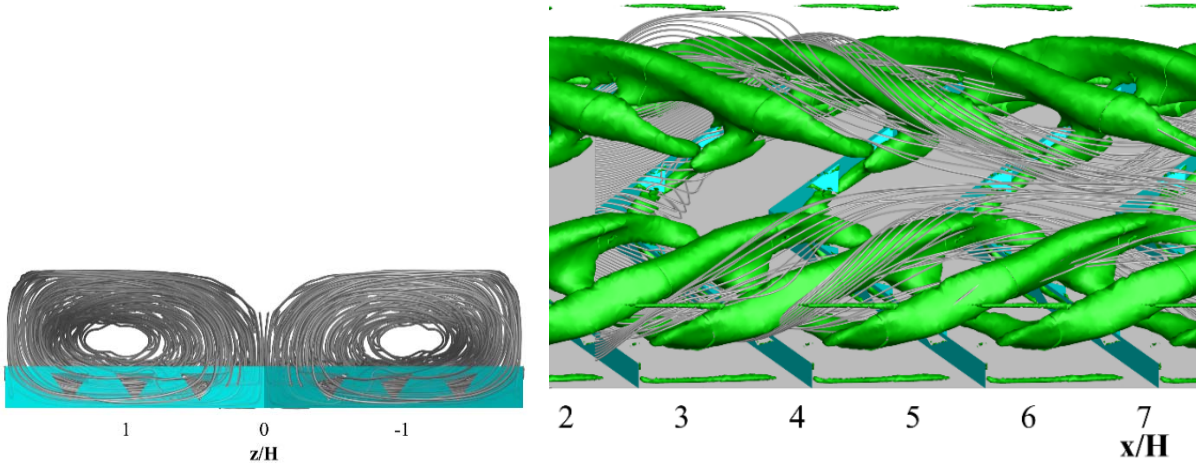

(d) $\theta = 67.5^{o}$

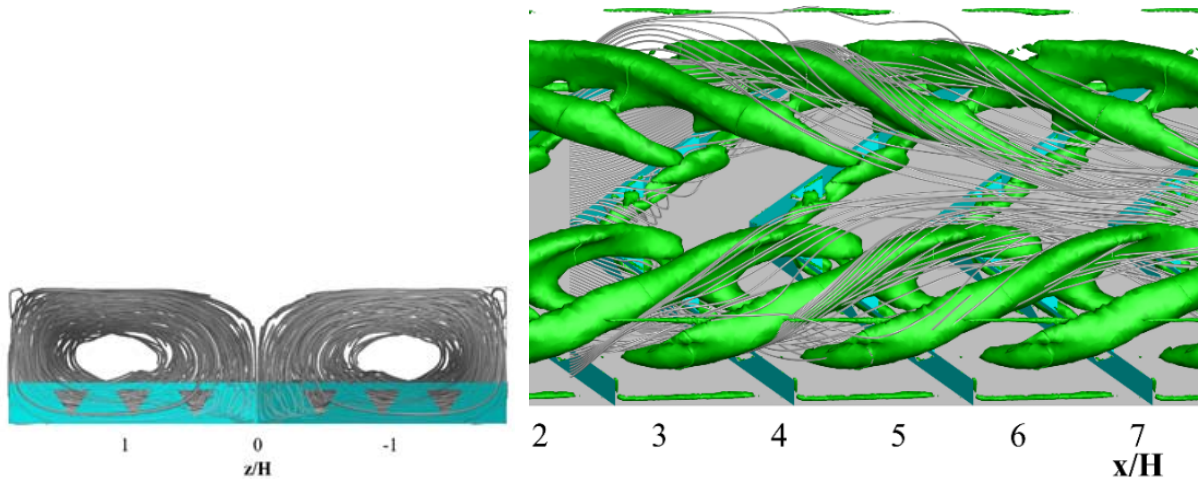

(e) $\theta = 90^{o}$

Figure 4.31. Streamline and iso-surface in channel containing delta-wing perforated V-type baffles (DW-PVB). (*continued*)

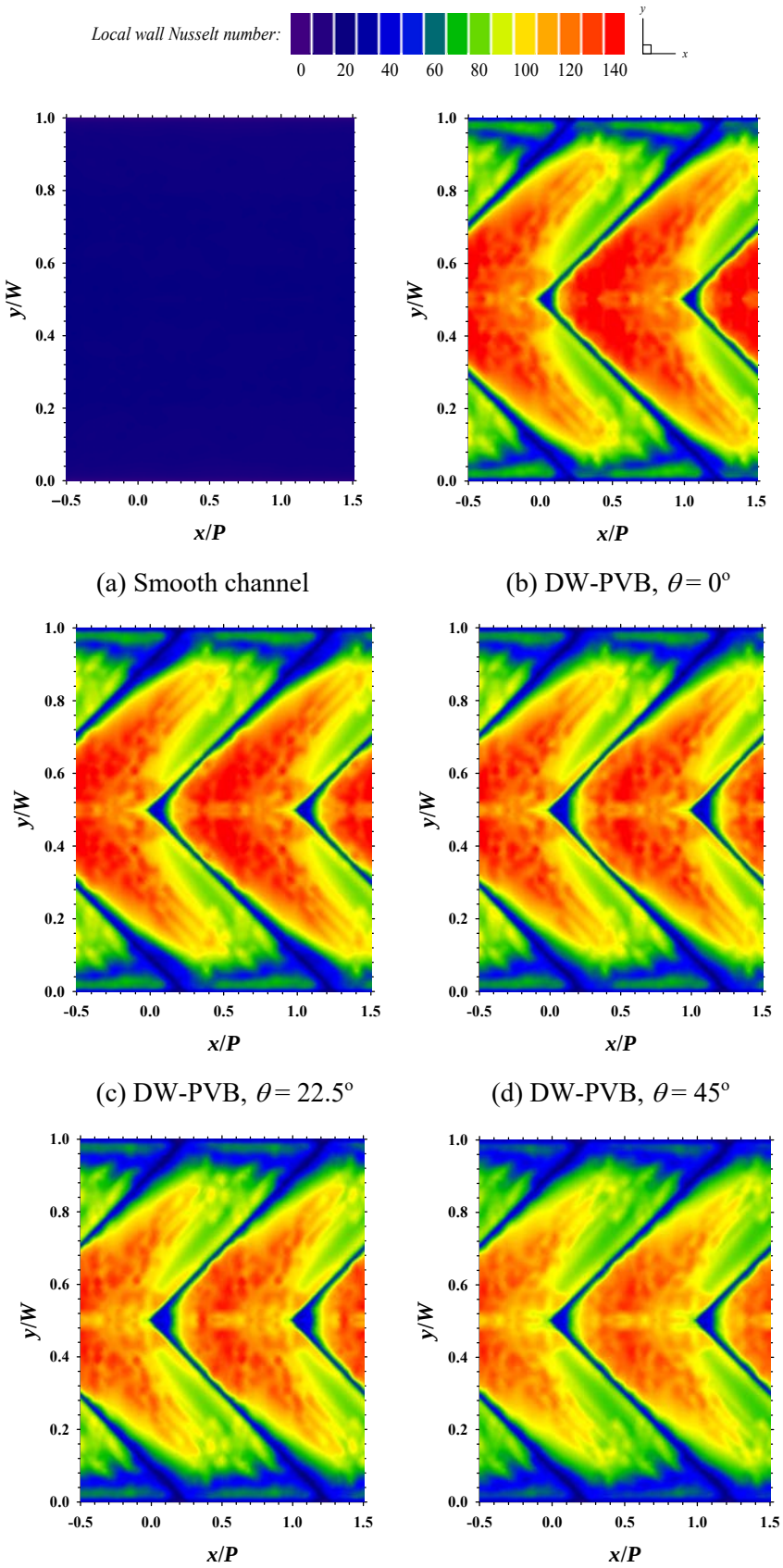

(a) Smooth channel

(b) DW-PVB, $\theta = 0^{o}$

(c) DW-PVB, $\theta = 22.5^{o}$

(d) DW-PVB, $\theta = 45^{o}$

(e) DW-PVB, $\theta = 67.5^{o}$

(f) DW-PVB, $\theta = 90^{o}$

Figure 4.32. Influence of delta-wing perforated V-type baffle (DW-PVB) at various wing attack angles ($\theta = 0^{o}$, 22.5^{o}, 45°, 67.5^{o} and 90°) on local heat transfer distribution.

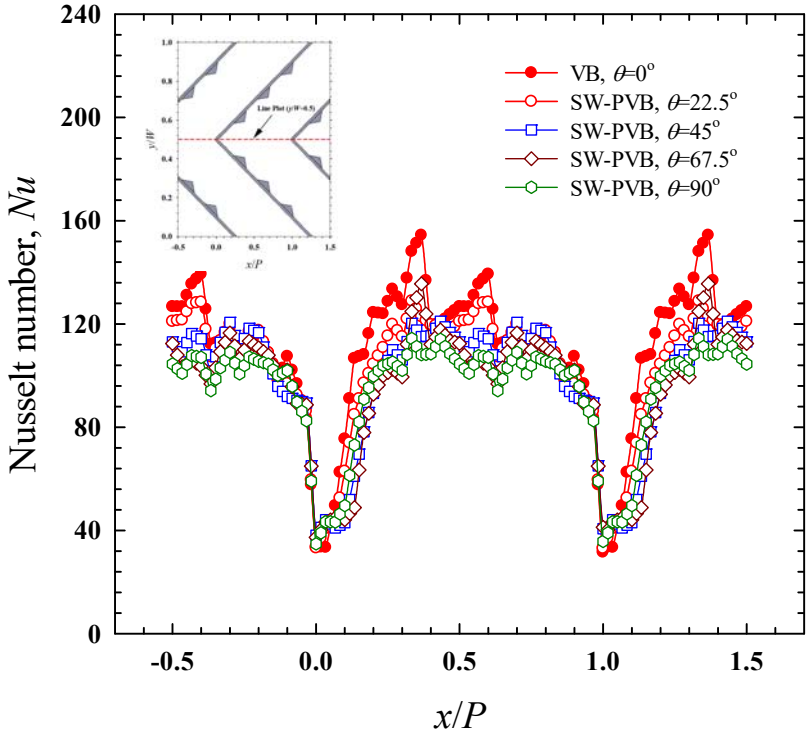

(a) $y/W = 0.5$

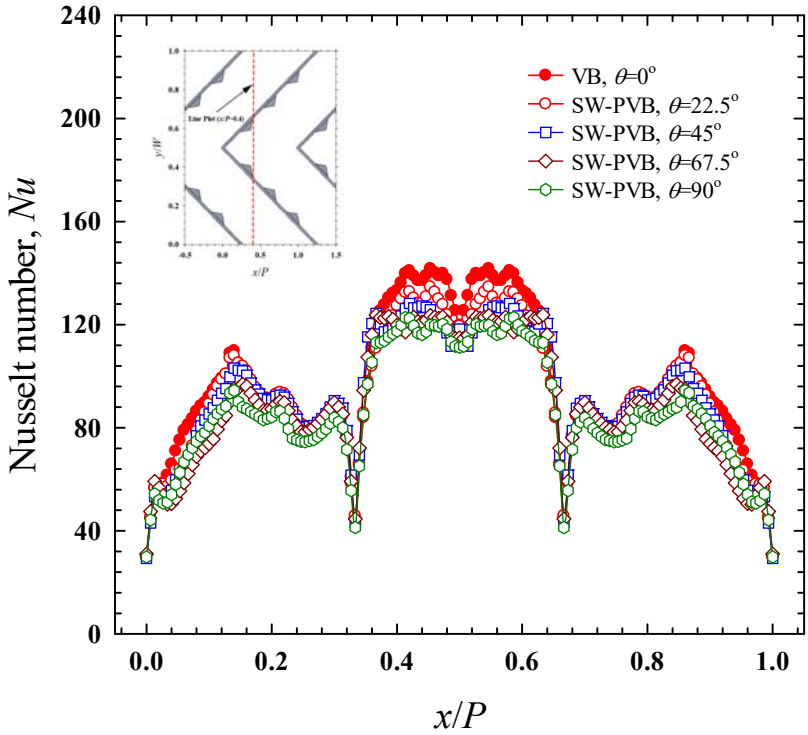

(b) $x/P = 0.5$

Figure 4.33. Normalized of Nusselt number of delta-wing perforated V-type baffles (DW-PVB) at various wing attack angles (θ = 0°, 22.5°, 45°, 67.5° and 90°).

For delta-wing perforated V-type baffles (DW-PVBs) with various delta-wing attack angles (θ), variation in Nusselt number (Nu) and Nusselt number ratio (Nu/Nu_s) with Reynolds number (Re) is seen in Figs. 4.34-4.35. This figure shows that Nusselt number ratio (Nu/Nu_s) tends to increase as the Reynolds number (Re) decreases. The Nusselt number is significantly higher in comparison to a smooth channel when a delta-wing perforated V-type baffle (DW-PVBs) is used. The major factor responsible for this may be that internal double counter-rotating vortices can be produced with the assistance of a delta-wing perforated V-type baffle (DW-PVB). Formation of two vortices, also known as common-flow-down vortices, can cause several impinging jets to form on the channel surface region behind the baffle.

It is noteworthy that the Nusselt number ratio (Nu/Nu_s) while utilizing small delta-wing perforated V-type baffle (DW-PVB) attack angles, $\theta = 22.5^o$ and 45°, is 2.68-4.89 times higher than when using a smooth channel alone. Apart from rapid fluid mixing, disrupting the formation of the thermal boundary layer and increased flow residence time are the causes of the stronger vortex strength. The great increase in heat transfer can result from these effects. In Fig. 4.34, it can be indicated that Nusselt number ratio (Nu/Nu_s) reduces with delta-wing attack angles of $\theta = 67.5°$ and 90°. The increase in heat transfer for the delta-wing perforated V-type baffle (DW-PVB) is much greater than for a smooth channel.

Additionally, the use of a solid V-shaped baffle creates greater thermal boundary layer disruption and rapid mixing between hot and cold fluid areas. The delta-wing perforated V-type baffle (DW-PVB) with $\theta = 22.5°$ and 45° respectively showed an approximate 2.06% and 3.45% lower Nusselt number ratio (Nu/Nu_s) than those with $\theta = 0°$, while DW-PVBs with $\theta = 67.5°$ and 90° presented significant lower Nusselt number ratios (Nu/Nu_s), of around 6.64% and 8.92%, respectively. This is because delta-wing perforated V-type baffle (DW-PVB) of $\theta = 22.5°$ and 45° provide multiple impinging jets behind the baffle that are typically close to the channel wall. This leads to greater mixing of the flow and interruption of the boundary layer, both of which contribute to flow turbulence.

The heat transfer rate is increased as a result of these changes while delta-wing perforated V-type baffle (DW-PVB) with $\theta = 67.5°$, and 90° had weaker multiple impinging jets behind the baffle with minimal attached jet zones on the walls. Nusselt number ratio (Nu/Nu_s) is highest at delta-wing attack angles of $\theta = 0°$ (solid V-shaped baffle), 22.5°, 45°, 67.5°, and 90° which are, respectively, about 2.76-5.01, 2.71-4.89, 2.68-4.81, 2.59-4.63, and 2.54-4.48, times higher than for a smooth channel.

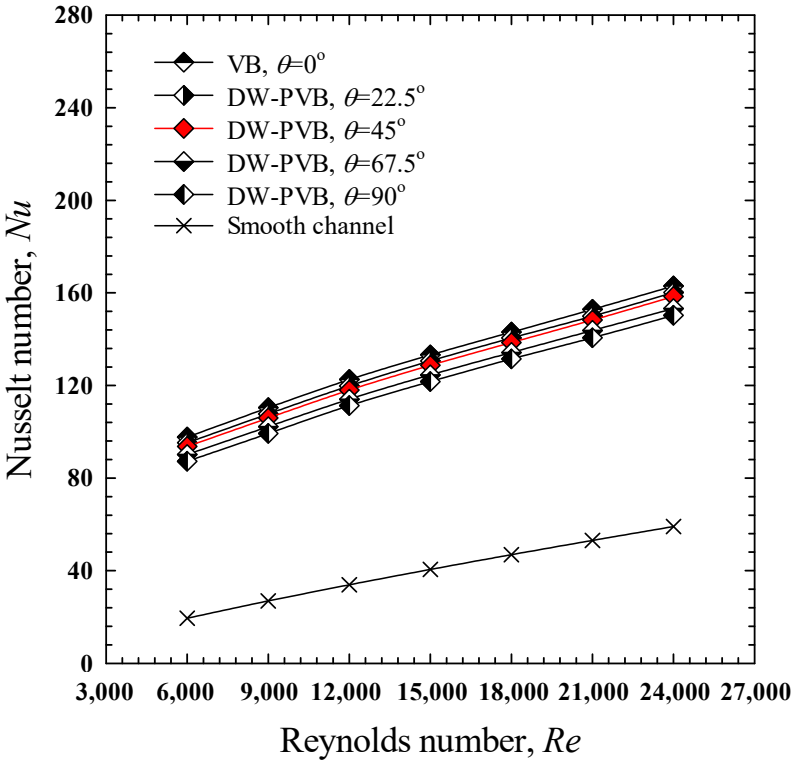

(a) *Nu*

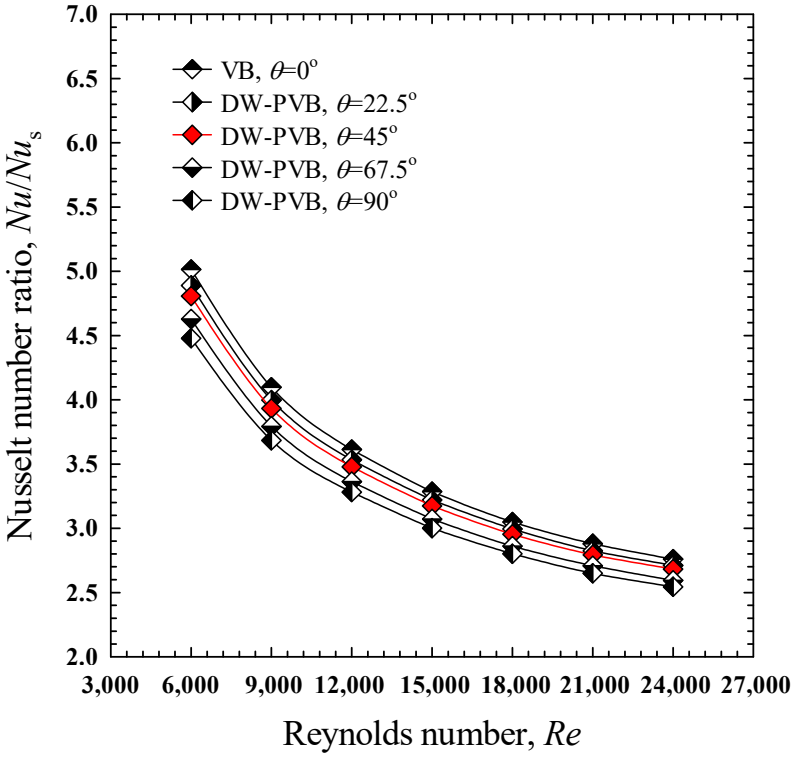

(b) Nu/Nu_s

Figure 4.34. Influence of delta-wing perforated V-type baffles (DW-PVB) at various wing attack angles (θ = 0°, 22.5°, 45°, 67.5° and 90°) on average Nusselt number.

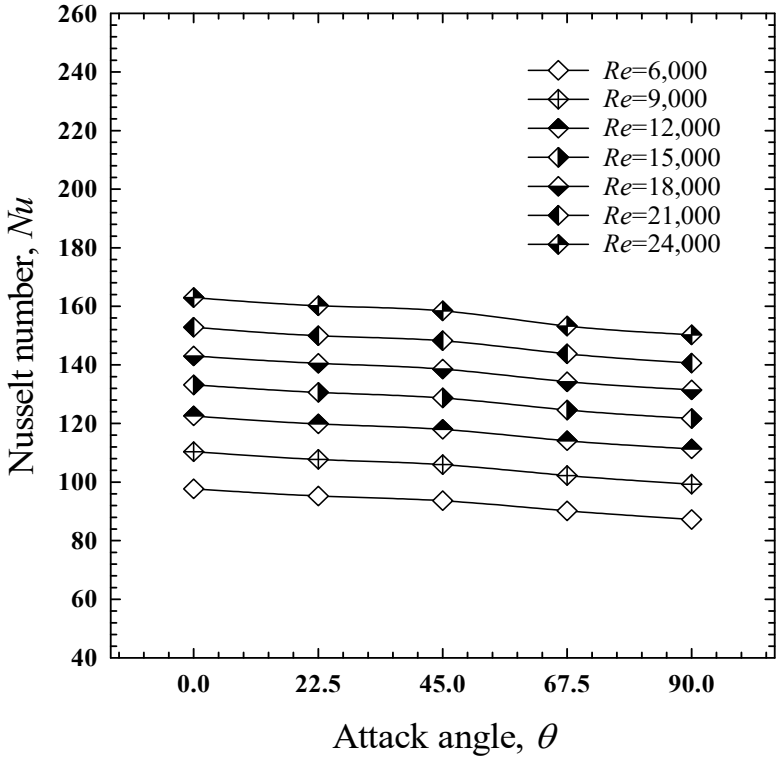

(a) *Nu*

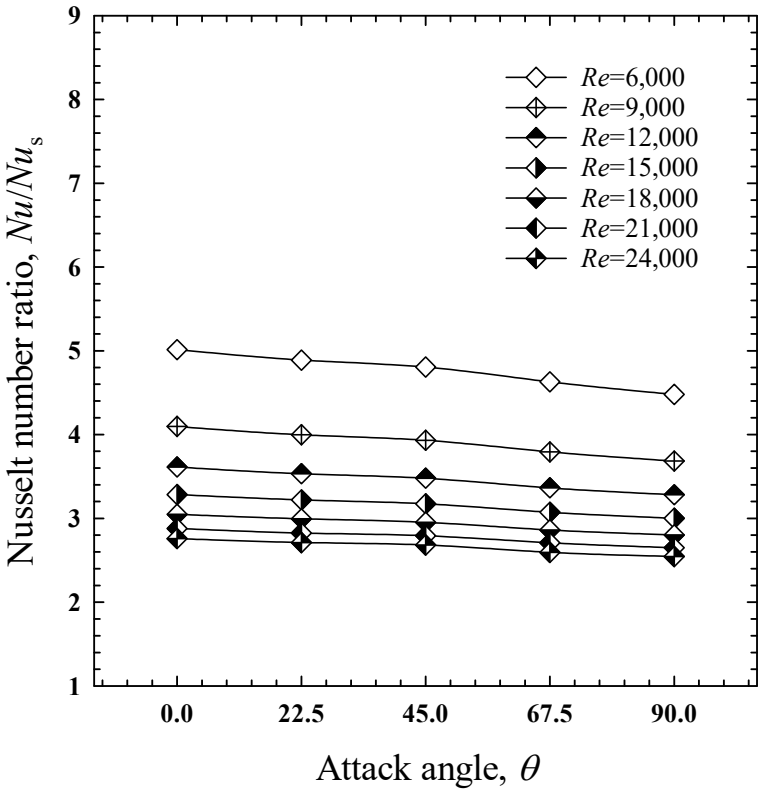

(b) Nu/Nu_s

Figure 4.35. Influence of delta-wing perforated V-type baffle (DW-PVB) at various wing attack angles (θ = 0°, 22.5°, 45°, 67.5° and 90°) on Nusselt number.

4.2.3.1.2 Friction factor results

The preceding section examined the effects through using delta-wing perforated V-type baffle (DW-PVB) with various delta-wing attack angles (θ) values on the Nusselt number ratio (Nu/Nu_s). It was determined that turbulence intensity, strong fluid contact with the channel-wall, and quick mixing of fluid greatly enhance heat transfer for delta-wing perforated V-type baffle (DW-PVB). Concurrently, the turbulence intensity creates increased flow friction, which results in a pressure loss penalty. Thus, the pressure loss influence of delta-wing perforated V-type baffle (DW-PVB) is investigated in terms of friction factor (f) and friction factor ratio (f/f_s) as seen in Figs. 4.36-4.37. Figs. 4.36-4.37 demonstrates the variation of the friction factor with Reynolds number (Re). For the range of interest, friction factor (f) decreases with raising Reynolds number while friction ratio (f/f_s) increases as Reynolds number increases. Eventually, the friction factors of the channels installed with delta-wing perforated V-type baffle (DW-PVB) are higher than smooth channel, under similar conditions. This is due to the augmented dissipation of dynamic pressure of the fluid due to an extra interaction of the pressure forces with inertial forces in the boundary layer caused by delta-wing perforated V-type baffle (DW-PVB).

Distributions of friction factor ratio (f/f_s) with Re for delta-wing perforated V-type baffle (DW-PVB) at various delta-wing attack angles (θ) values is presented in this section. Figures 36 and 37 depict the relationship of the friction factor ratio (f/f_s) with Re for delta-wing perforated V-type baffle (DW-PVB) as a function of delta-wing attack angles (θ) values. According to Figs. 4.36-4.37, the friction factor ratio (f/f_s) increases with the Re. However, utilizing delta-wing perforated V-type baffle (DW-PVB) boosts friction factor ratio (f/f_s) far more than for a smooth channel alone. This is due to dynamic pressure fluid dissipation, an increase in wall area, and creation of additional fluid interactions between the core and wall areas. It is also showed that when delta-wing attack angles (θ) increase, the friction factor ratio (f/f_s) decreases. Furthermore, delta-wing perforated V-type baffles (DW-PVBs) with a delta-wing attack angle $\theta = 0°$ (solid V-shaped baffle) had substantially greater friction than baffles with $\theta = 22.5°$, 45°, 67.5°, and 90°, respectively showing 8.42-10.99%, 15.79-20.86%, 21.04-28.08%, and 24.27-34.75% greater friction. This is due to the extra disturbance by the delta-wing as vortex generators inducing the change of wall shear as well as momentum flux. The highest friction factor ratio (f/f_s) is obtained at $\theta = 0°$ (solid V-shaped baffle). This is because delta-wing perforated V-type baffle (DW-PVB) result in greater flow obstruction. However, as predicted, adding a solid V-shaped baffle ($\theta = 45°$) in the channel can minimize the friction factor by approximately 5.84-17.26% when compared to both $\theta = 0°$ (solid V-shaped baffle) and 22.5°.

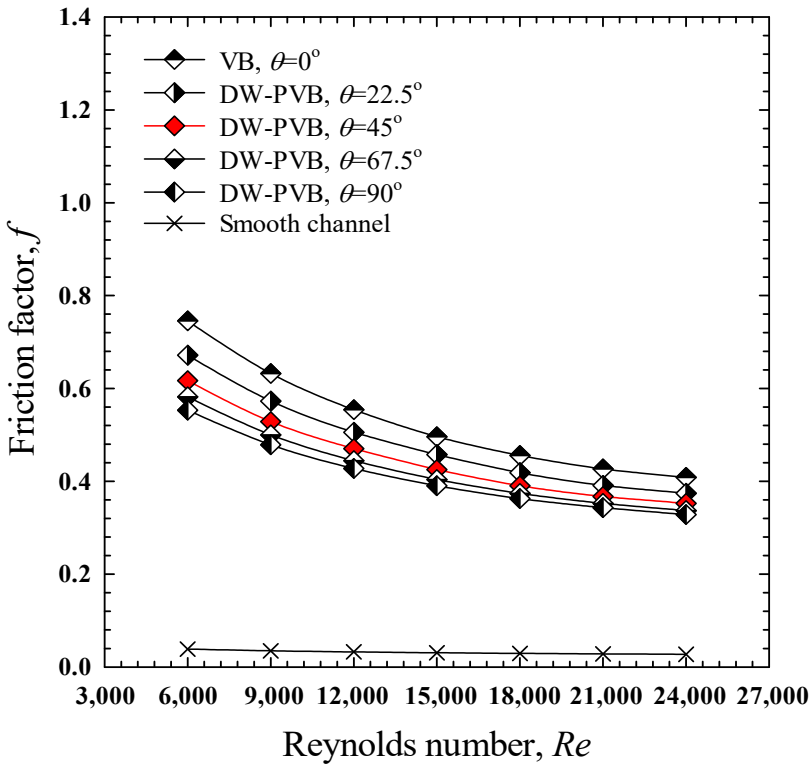

(a) f

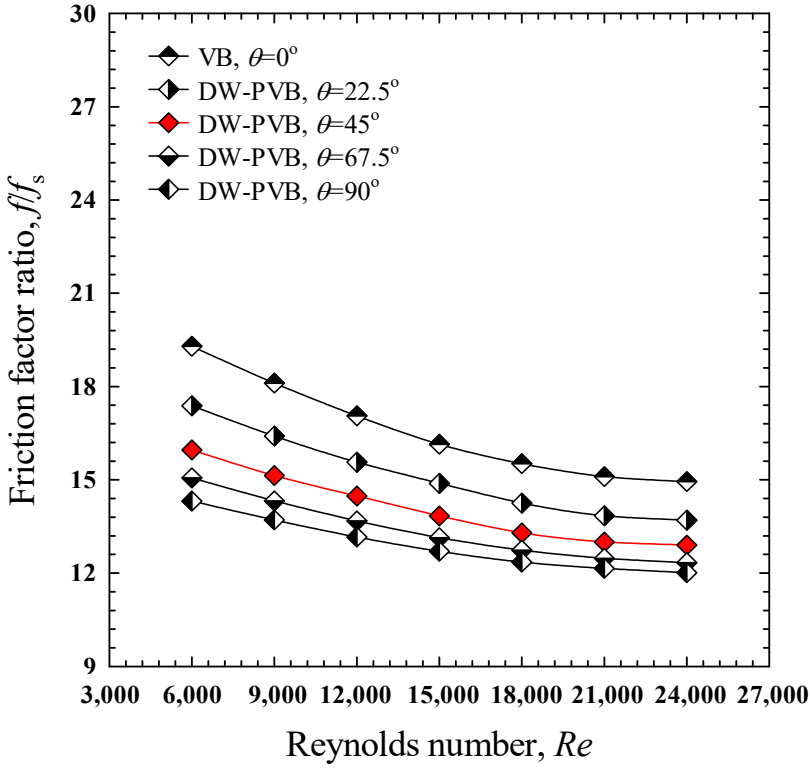

(b) f/f_s

Figure 4.36. Influence of delta-wing perforated V-type baffle (DW-PVB) at various wing attack angles (θ = 0°, 22.5°, 45°, 67.5° and 90°) on friction factor.

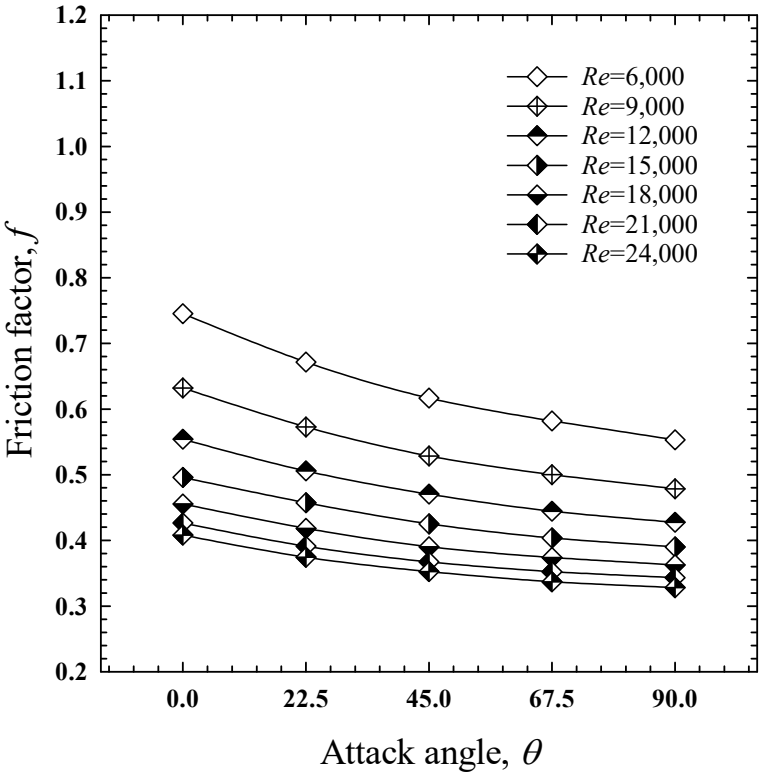

(a) f

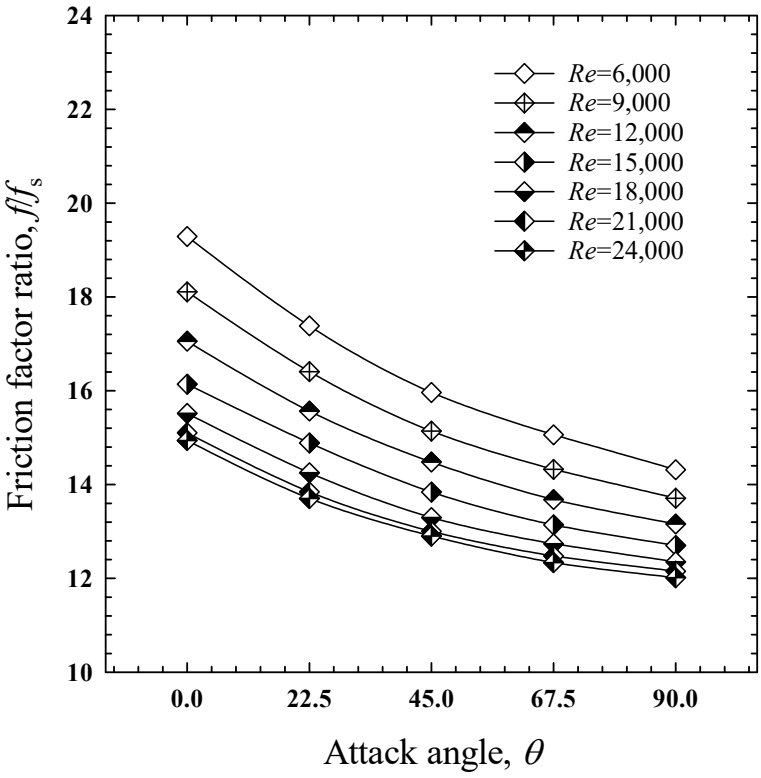

(b) f/f_s

Figure 4.37. Influence of delta-wing perforated V-type baffle (DW-PVB) at various wing attack angles (θ = 0°, 22.5°, 45°, 67.5° and 90°) on friction factor.

4.2.3.1.3 Thermal performance factor results

Comparing flows at identical pumping power, a parameter known as the thermal performance factor (*TPF*) is used to analyze heat transfer benefits over pressure losses. It is a dimensionless variable presented in terms of a Nusselt number ratio (Nu/Nu_s) and friction factor ratio (f/f_s). Any delta-wing perforated V-type baffle (DW-PVB), recirculation, or longitudinal vortex-flow device with physical baffles boosts heat transfer rate. The maximal Nusselt number ratio (Nu/Nu_s) at the lowest and highest Reynolds number is increased by roughly 2.76 times and 5.01 times, respectively, according to the current study. In heat exchanger design, optimizing heat transfer while reducing pressure drop is a design objective. As a result, a thermal performance factor (*TPF*) can represent the advantage of heat transfer as well as the cost of pressure losses. The greater thermal performance factor (*TPF*), the greater the advantages in terms of heat transfer versus pressure loss.

The thermal performance factor (*TPF*) indication, which is displayed against Reynolds number values in Fig. 38, may indicate the performance of delta-wing perforated V-type baffles (DW-PVBs) with various delta-wing attack angles (θ) values. Figure 4.38 also shows that the thermal performance factor (*TPF*) declines as the Reynolds number rises. The thermal performance factor (*TPF*) is found to be substantially more than unity for all delta-wing perforated V-type baffles (DW-PVBs), with a peak at 1.91 for θ = 45°. Thermal performance factor (*TPF*) values for delta-wing perforated V-type baffle (DW-PVB) are 1.12-1.87, 1.13-1.89, 1.14-1.91, 1.12-1.87, and 1.11-1.84 at θ = 0° (solid V-shaped baffle), 22.5°, 45°, 67.5°, and 90°, respectively. Concurrently, the greatest thermal performance factor (*TPF*) at θ = 45°, is obtained at Re = 6,000, demonstrating that modest delta-wing attack angles (θ) may be used due to a significant reduction in pressure drop, around 13.64-17.26%, compared to θ = 0° (solid V-shaped baffle).

4.2.3.14 Empirical correlations

The present data was used to generate Nusselt number (*Nu*), friction factor (*f*) and thermal performance factor (*TPF*) correlations for delta-wing perforated V-type baffle (DW-PVB) on a heated channel wall. Variations were produced by changing delta-wing attack angles from θ = 0° to 90° and Reynolds number from Re = 6,000 to 24,000. A least-square regression technique was employed to correlate the data, which is basic and appropriate for both commercial and academic purposes. Equations (4.43)-(4.45) demonstrate Nusselt number (*Nu*), friction factor (*f*) and thermal performance factor (*TPF*) relationships. The experimental data for Nusselt number (*Nu*), friction factor (*f*) and thermal performance factor (*TPF*) are displayed against predictions of the correlations, as depict in Figs. 39(a-c). Their variances are determined to be ±6.4% for Nusselt number (*Nu*), ±6.2% for friction factor (*f*) and ±7.4% for thermal performance factor (*TPF*).

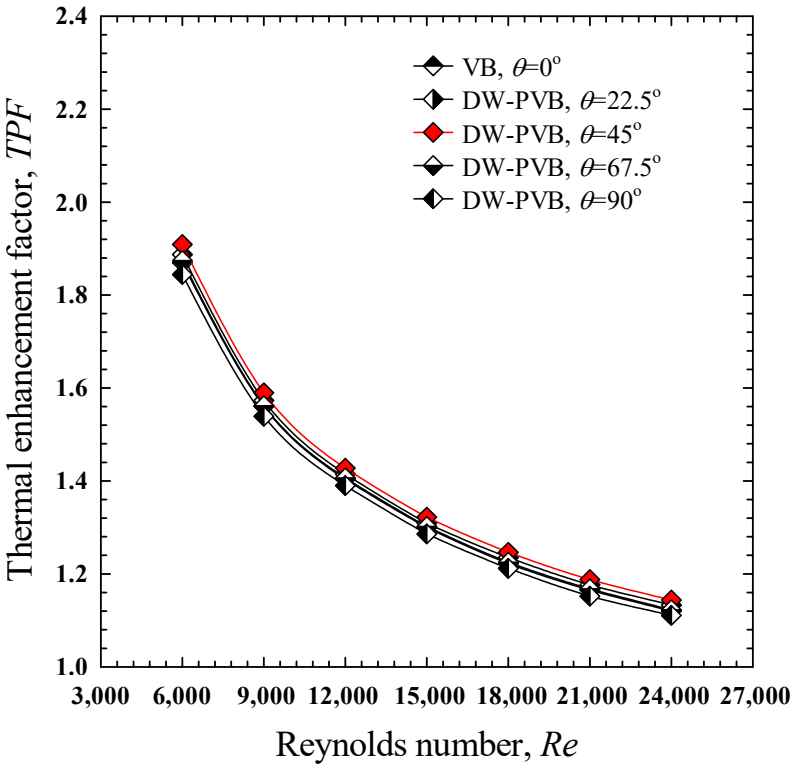

(a) *Re* & *TPF*

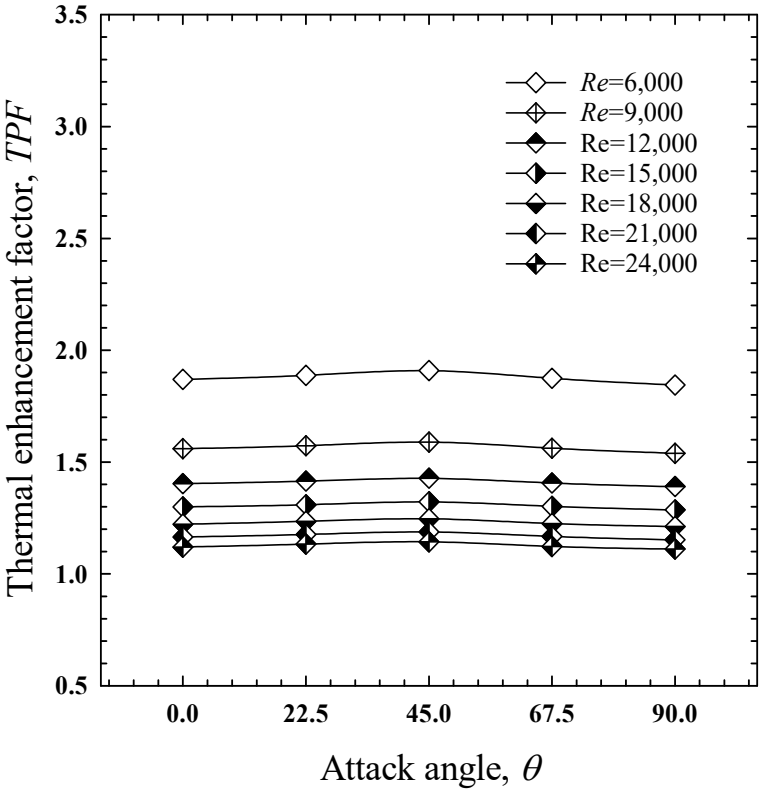

(b) *θ* & *TPF*

Figure 4.38. Influence of delta-wing perforated V-type baffle (DW-PVB) at various wing attack angles (θ = 0°, 22.5°, 45°, 67.5° and 90°) on thermal performance factor.

Empirical correlation of Nusselt number (Nu)

$$Nu = 7.388Pr^{0.4}Re^{0.381}(90 + \theta)^{-0.134} \tag{4.43}$$

Empirical correlation of friction factor (f)

$$f = 136.65Re^{-0.415}(90 + \theta)^{-0.362} \tag{4.44}$$

Empirical correlation of thermal performance factors (TPF)

$$TPF = 46.93Re^{-0.365}(90 + \theta)^{-0.013} \tag{4.45}$$

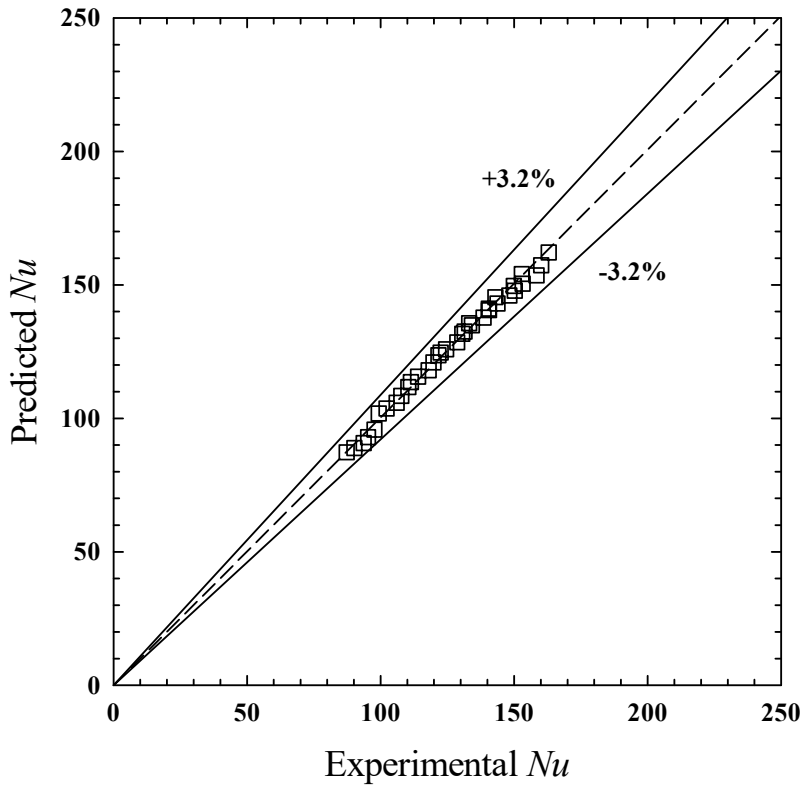

(a) Nu_{exp}, & Nu_{pred}

Figure 4.39. Experimental results & predicted values of the empirical correlations.

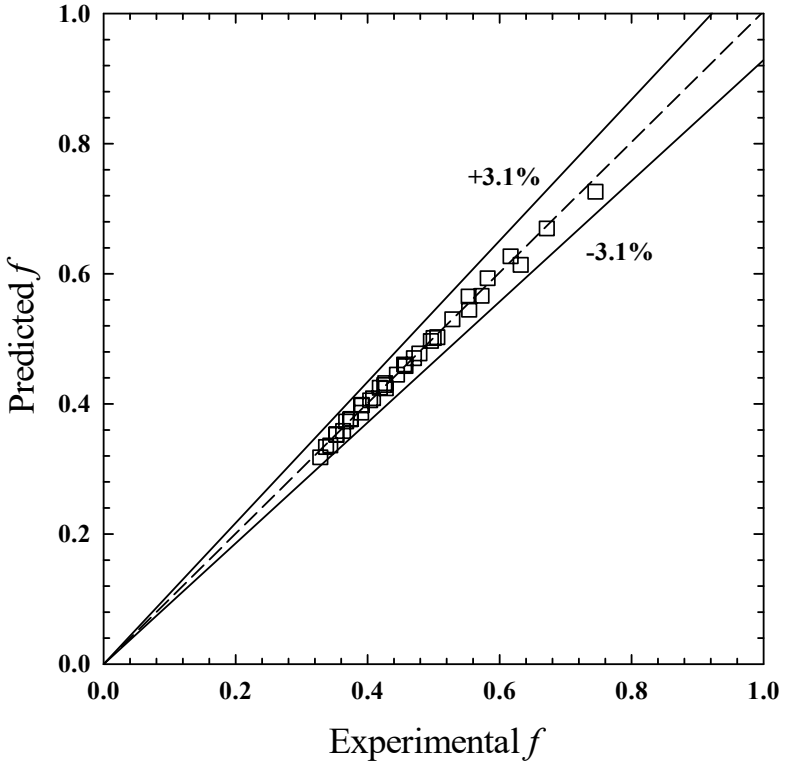

(b) f_{exp} & f_{pred}

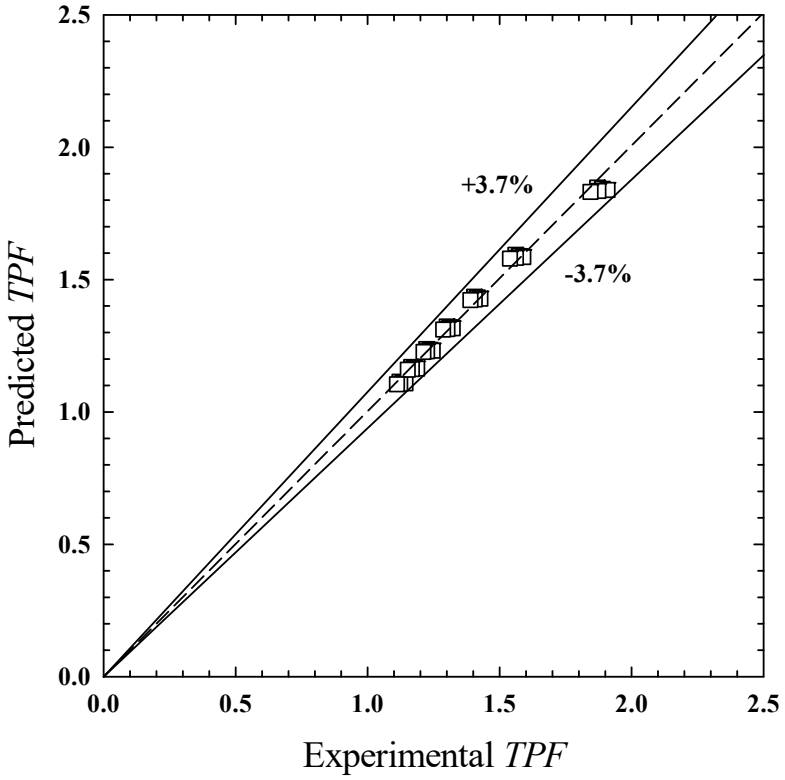

(c) TPF_{exp} & TPF_{pred}

Figure 4.39. Experimental results & predicted values of the empirical correlations. (continued)

4.2.3.2 Semi-oval wing perforated V-type baffle

4.2.3.2.1 Heat transfer results

Figures 4.40 and 4.41 also show the local Nusselt number (*Nu*) of the channel containing the semi-oval wing perforated V-type baffle (SOW-PVB) tended to increase with decreasing semi-oval wing attack angle. The higher Nusselt number (*Nu*) at a smaller attack angle is most likely attributed to the still remaining the stronger longitudinal vortex and high impingement on the bottom surface that can be seen near the main flow or moddle channle (Fig. 4.40). It was observable that the combined impinging jet and air passing through the semi-oval wings, helped in boosting fluid turbulence. For the range considered, the use of the semi-oval wing perforated V-type baffle (SOW-PVB) with wing attack angles of $\theta = 22.5^{o}$, 45°, 67.5^{o} and 90° improves mean Nusselt numbers by around 248.2%, 243%, 231% and 222.6%, respectively as compared to that of the smooth channel. The heat transfer rates of the channel with the semi-oval wing perforated V-type baffle (SOW-PVB) having semi-oval wing attack angles for $\theta = 22.5^{o}$, 45°, 67.5^{o} and 90° were respectively 0.97-1.64%, 2.04-3.45%, 5.63-7.65% and 7.99-11.09% lower than those in the tube with the typical transverse baffle (VB). The results indicated that the semi-oval wing perforated V-type baffle (SOW-PVB) with small semi-oval wing attack angles ($\theta = 22.5^{o}$ and 45°) gave comparable heat transfer rate to that given by the typical transverse baffle (VB).

For a rectangular channel with typical transverse baffle (VB) or the semi-oval wing perforated V-type baffle (SOW-PVB) at a Reynolds number of 6000, the local spanwise Nusselt number distribution and contour are shown in Figs. 4.40-4.41. Two longitudinal vortices took place on both sides of the V-type baffle turbulator. As a result, both friction loss and heat transfer were promoted. Due to the reattachment of the longitudinal vortices, the maximum heat transfer areas appeared corresponding to the reattachment commence positions. The strongest longitudinal vortex flow and resultantly higher heat transfer rate was achieved by the typical transverse baffle (VB, $\theta = 0^{o}$) as compared to the semi-oval wing perforated V-type baffle (SOW-PVB). This is because the semi-oval wing perforated V-type baffle (SOW-PVB) split the flow into two main types: the longitudinal vortex flow across the baffle, and the multiple impinging jets through the baffle. In the case of the semi-oval wing perforated V-type baffle (SOW-PVB) with smallest wing attack angles ($\theta = 22.5^{o}$), it did not significantly reduce heat transfer compared to the typical transverse baffle (VB) as seen in Fig. 4.41(b), which led to large impinging jets on the wall and even greater heat transfer near the V-type baffle. It can be observed that the presence of perforation (semi-oval holes) in the semi-oval wing perforated V-type baffle (SOW-PVB) resulted in decreased friction loss due to the fluids' reduced resistance. In conclude, the semi-oval wing perforated V-type baffle (SOW-PVB) are excellent options for enhancing thermal performance, as will be discussed in the next section.

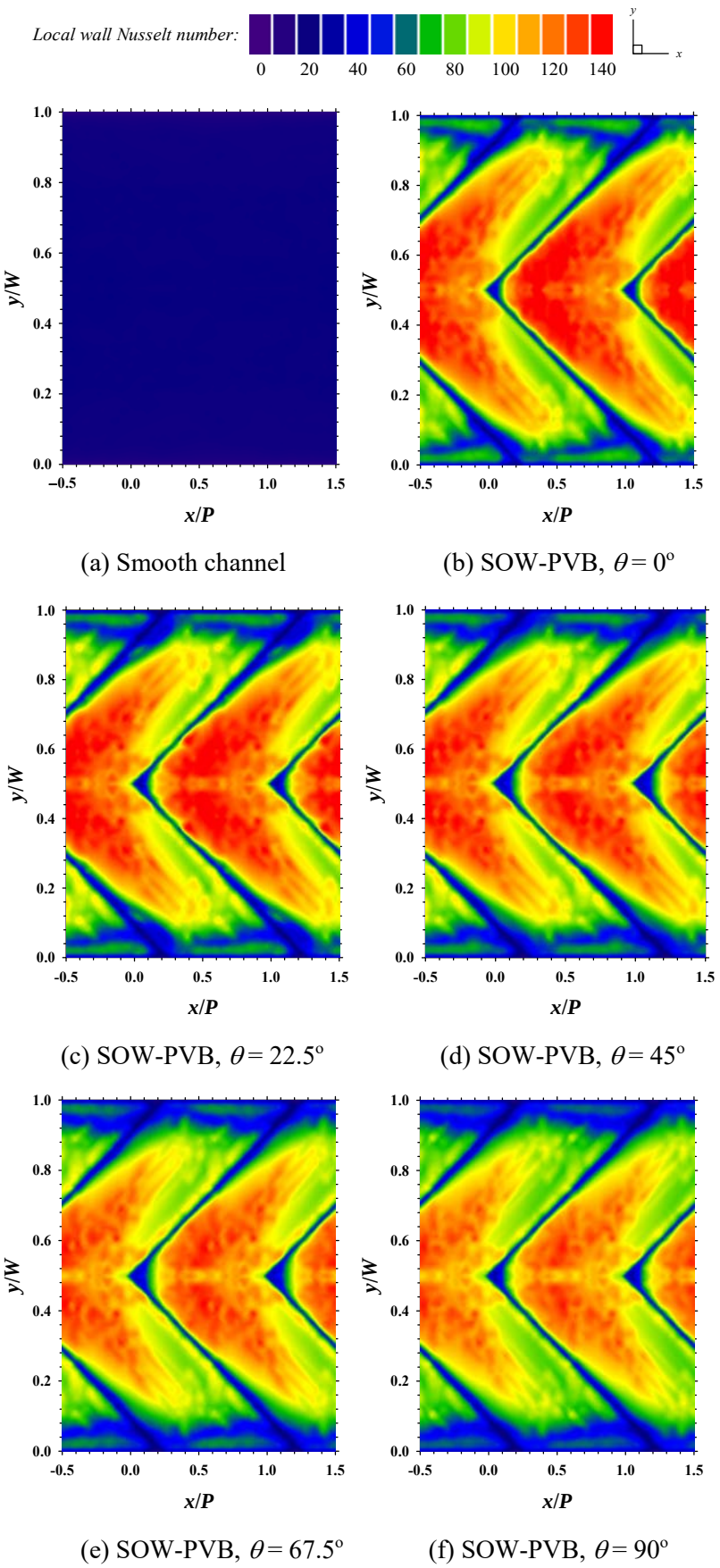

(a) Smooth channel

(b) SOW-PVB, $\theta = 0^{o}$

(c) SOW-PVB, $\theta = 22.5^{o}$

(d) SOW-PVB, $\theta = 45^{o}$

(e) SOW-PVB, $\theta = 67.5^{o}$

(f) SOW-PVB, $\theta = 90^{o}$

Figure 4.40. Influence of semi-oval wing perforated V-type baffle (SOW-PVB) at various wing attack angles ($\theta = 0^{o}$, 22.5^{o}, 45°, 67.5^{o} and 90°) on local heat transfer distribution.

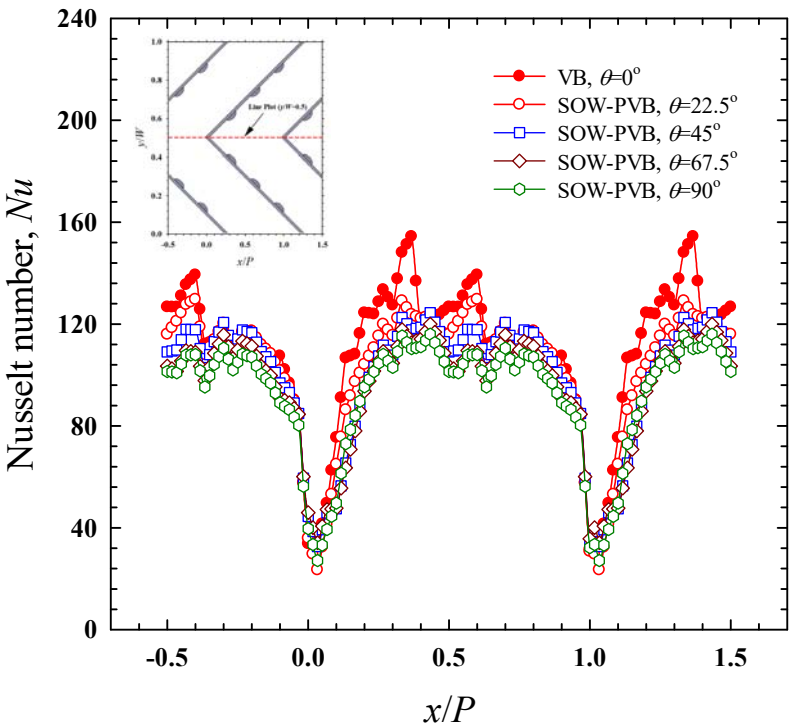

(a) $y/W = 0.5$

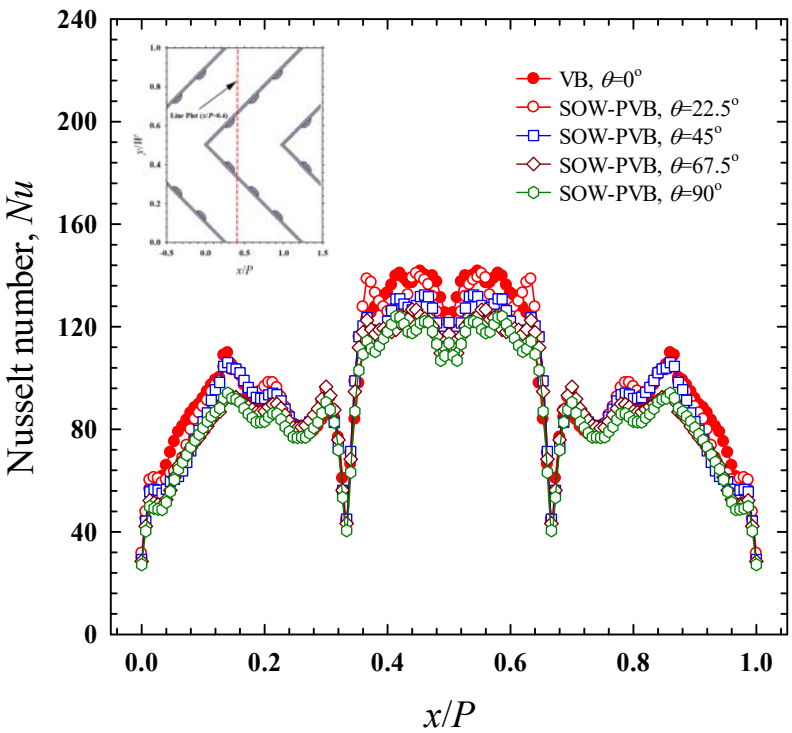

(b) $x/P = 0.5$

Figure 4.41. Normalized of Nusselt number of SOW-PVB at various wing attack angles (θ = 0°, 22.5°, 45°, 67.5° and 90°).

A uniform heat flux channel wall that is equipped with a semi-oval wing perforated V-type baffle (SOW-PVB) is depicted in Figs. 4.42-4.43. These illustrations highlight the relationship between the Nusselt number (*Nu*) and the Reynolds number (*Re*). As the Reynolds number (*Re*) grows, the Nusselt number (*Nu*) also increases. This is because the degree of fluid turbulence rises as the Reynolds number increases. The channel that is installed with a semi-oval wing perforated V-type baffle (SOW-PVB) continually produces a greater Nusselt number than the smooth channel does when the conditions are identical. Because their wings are shaped like a half-oval, the V-type baffle creates two longitudinal vortices in addition to the many flows that smash into it. Due to the three-dimensional spiraling motion of the fluid, the two longitudinal vortices, in general, contribute to a significant improvement in heat transfer abilities. Because of this, the semi-oval wing and the V-type baffle worked together better to transfer heat than the axial flow or the smooth channel without baffles.

In Figs. 4.42-4.43, for rectangular channels with the semi-oval wing perforated V-type baffle (SOW-PVB), the effects of the Reynolds number (*Re*) on the Nusselt number (*Nu*) and Nusselt number ratio (Nu/Nu_s) are also shown for the conditions of $e/H = 0.3$ and $p/H = 1.5$. Because the viscous sub layer was suppressed as the Reynolds number rose, the friction factor decreased. The ratio of convective to conduction heat flow resistance, which was also improved by a reduction in boundary layer thickness, causing the Nusselt number to rise with the Reynolds number. As a result, the Nusselt number increased as the convective resistance decreased. This can be explained by the fact that as the Reynolds number rises, turbulence increases, amplifying convective heat transfer. At identical Reynolds numbers, the channel with the semi-oval wing perforated V-type baffle (SOW-PVB) of all semi-oval wing attack angles ($\theta = 0^o$, 22.5^o, 45°, 67.5^o and 90°) consistently yielded higher heat transfer rates than the smooth channel.

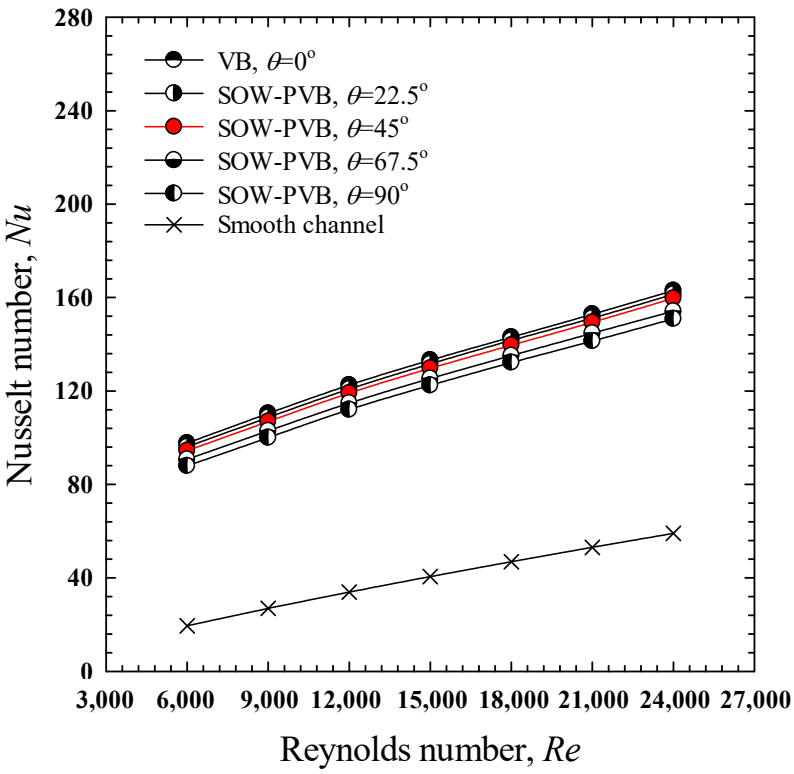

(a) *Nu*

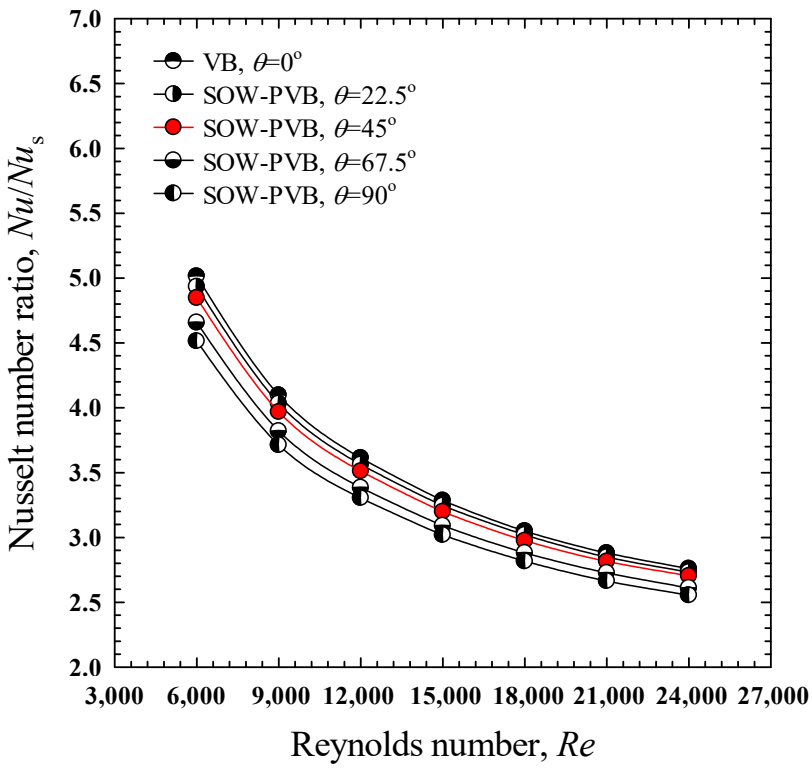

(b) Nu/Nu_s

Figure 4.42. Influence of semi-oval wing perforated V-type baffle (SOW-PVB) at various Reynolds number (*Re*) on average Nusselt number.

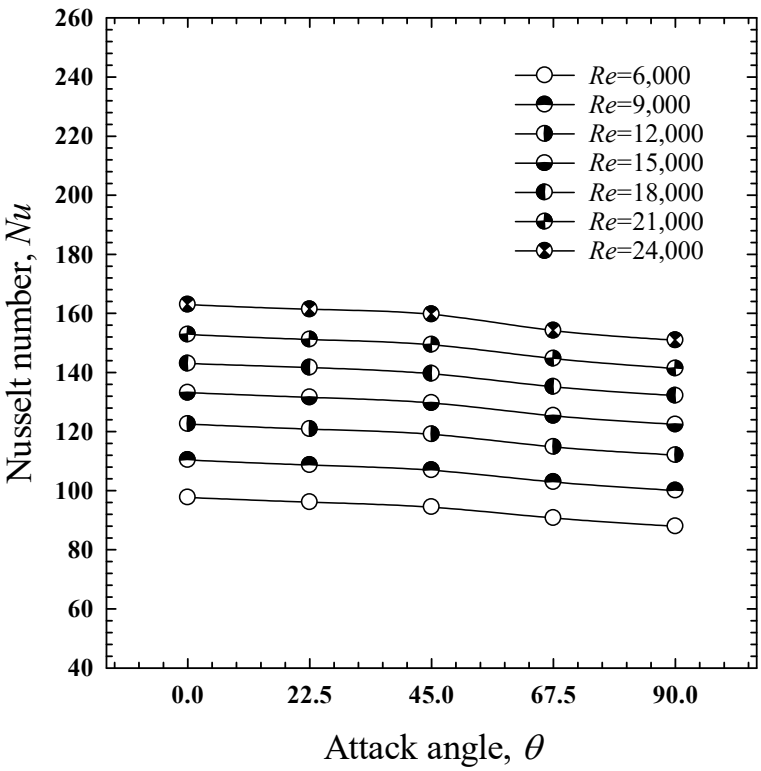

(a) *Nu*

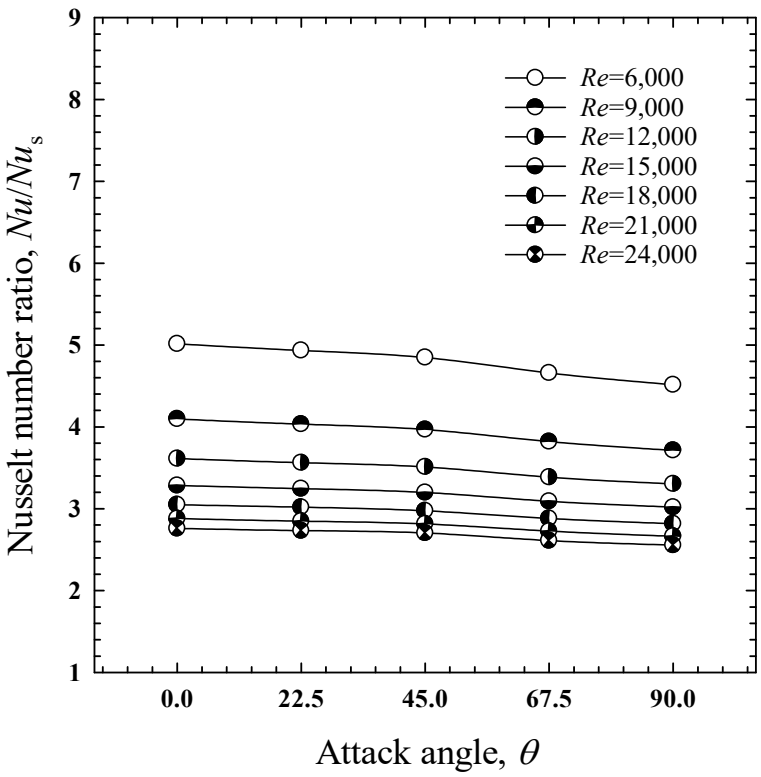

(b) Nu/Nu_s

Figure 4.43. Influence of semi-oval wing perforated V-type baffle (SOW-PVB) at various wing attack angles (θ = 0°, 22.5°, 45°, 67.5° and 90°) on Nusselt number.

4.2.3.2.2 Friction factor results

Figures 4.44 and 4.45 illustrate the influence of installing baffles on friction loss. As the Reynolds number (*Re*) grew, the friction factor dropped for cases. For the whole Reynolds number range, the semi-oval wing perforated V-type baffle (SOW-PVB, θ = 22.5°, 45°, 67.5°, and 90°) showed an advantage over the typical transverse baffle (VB) by causing lower friction loss owing to the presence of a perforation. At a given Reynolds number, the friction factor declined as the relative attack angles (θ) of the wings rose since the wings with larger attack angles caused lower flow obstruction. The mean friction factors induced by the semi-oval wing perforated V-type baffle (SOW-PVB) for attack angles θ = 0°, 22.5°, 45°, 67.5°, and 90° were 16.59, 15.32, 14.22, 13.52, and 13 times of the smooth channel. The average friction factors caused by the installation of typical transverse baffle (VB) were 8.23%, 16.59%, 22.57%, and 27.31% higher than that of the semi-oval wing perforated V-type baffle (SOW-PVB) with θ = 22.5°, 45°, 67.5°, and 90°, respectively.

4.2.3.2.3 Thermal performance factor results

Figure 4.46 displays the thermal performance factor (*TPF*), which is based on the identical pumping power criterion against the Reynolds number. Evidently, as the Reynolds number rose, the thermal performance factor (*TPF*) tended to fall. This suggests that, in terms of overall energy savings, the usage of the semi-oval wing perforated V-type baffle (SOW-PVB) is more viable at lower Reynolds numbers. For the whole Reynolds number range, the channels with the semi-oval wing perforated V-type baffle (SOW-PVB) possessed thermal performance factors (*TPF*) above unity (1.11 to 1.92) which signified its potential for overall energy saving. In comparison with typical transverse baffle (VB), the semi-oval wing perforated V-type baffle (SOW-PVB) with θ = 22.5°, 45°, and 67.5° offered higher thermal performance factors (*TPF*) than those the VB. Interestingly, the semi-oval wing perforated V-type baffle (SOW-PVB) with θ = 45° offered the greatest thermal performance factor. Although the semi-oval wing perforated V-type baffle (SOW-PVB) was less efficient for heat transfer enhancement than the one with θ = 45°, its lower friction loss showed a dominant effect in promoting thermal performance. It can be seen that the semi-oval wing perforated V-type baffle (SOW-PVB) with θ = 45° had a slightly lower heat transfer rate than the semi-oval wing perforated V-type baffle (SOW-PVB) with θ = 22.5° and typical transverse baffle (VB) by about 1.14% and 2.73%, respectively, while exhibiting a significantly reduced friction factor of 7.72% and 16.59%. Therefore, the semi-oval wing perforated V-type baffle (SOW-PVB) with θ = 45° is the most favorable in minimizing pumping power. The highest thermal performance factors offered by the semi-oval wing perforated V-type baffle (SOW-PVB) with θ = 0°, 22.5°, 45°, 67.5° and 90° were 1.12-1.87, 1.14-1.9, 1.15-1.92, 1.13-1.88, and 1.11-1.85, respectively. In addition, the semi-oval wing perforated V-type baffle (SOW-PVB) with θ = 45° gave higher thermal performance factor than semi-oval wing attack angles of θ = 0°, 22.5°, 67.5° and 90° up to 2.21-2.62%, 0.93-1.20%, 1.75-20.3%, and 2.93-3.48%, respectively.

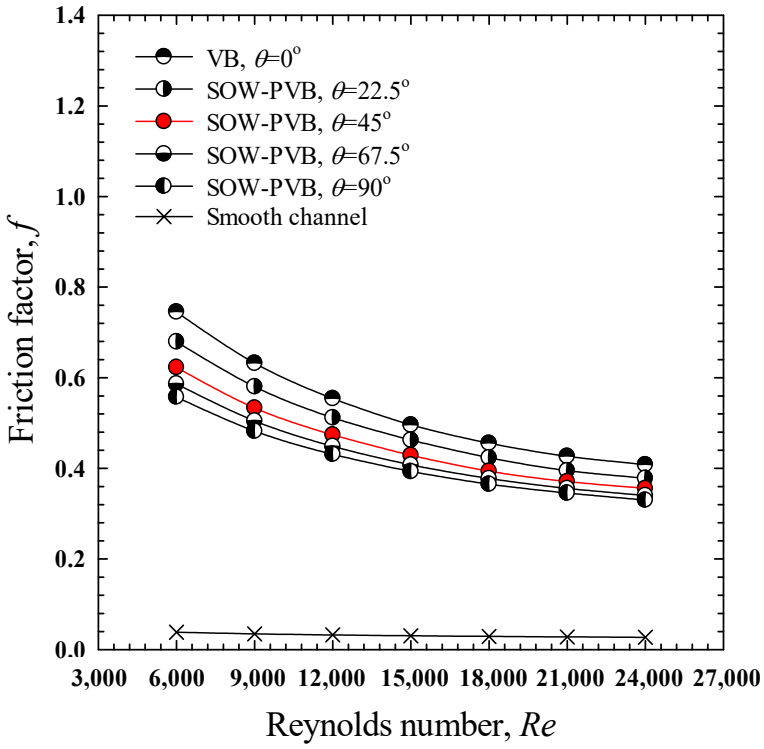

(a) f

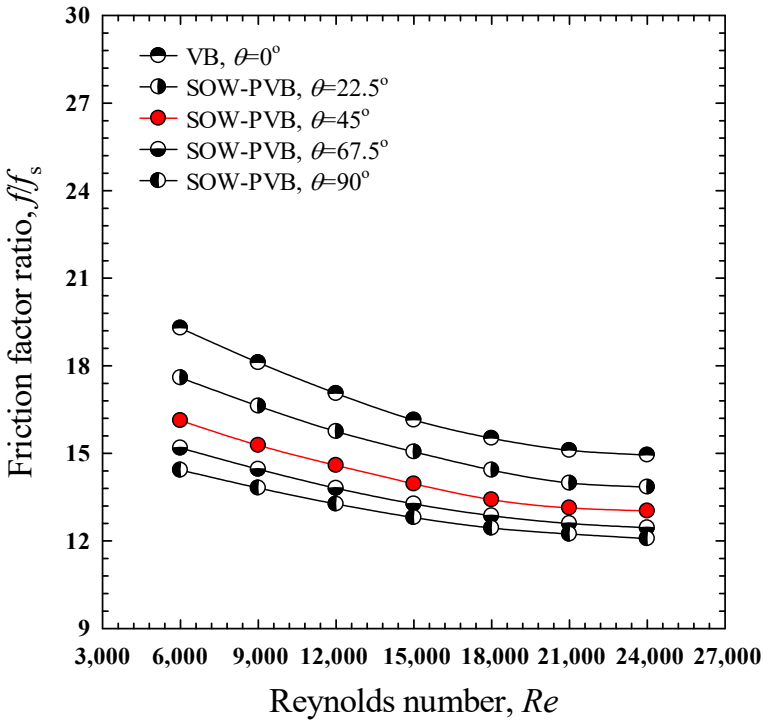

(b) f/f_s

Figure 4.44. Influence of semi-oval wing perforated V-type baffle (SOW-PVB) at various Reynolds number (*Re*) on friction factor.

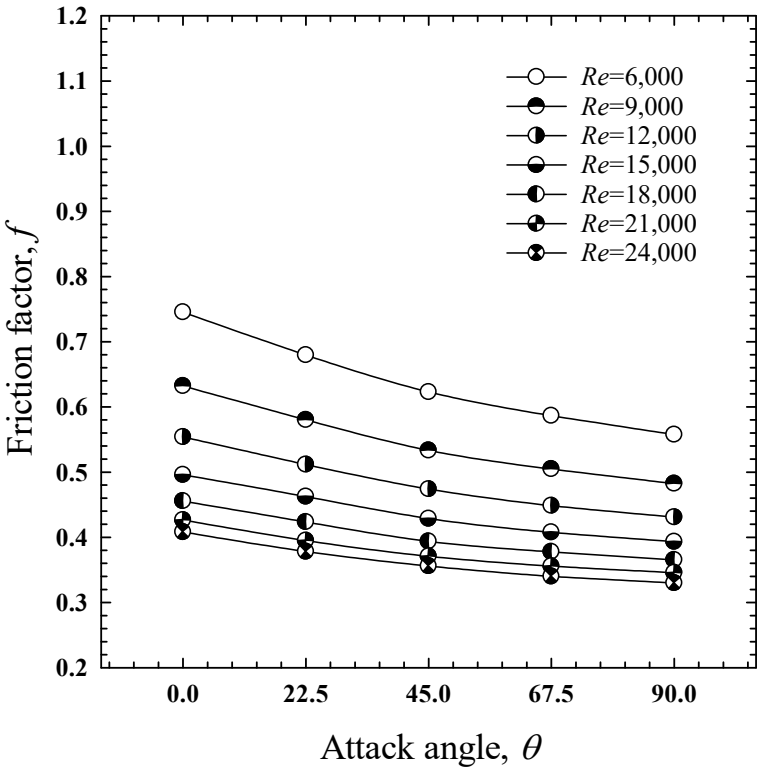

(a) f

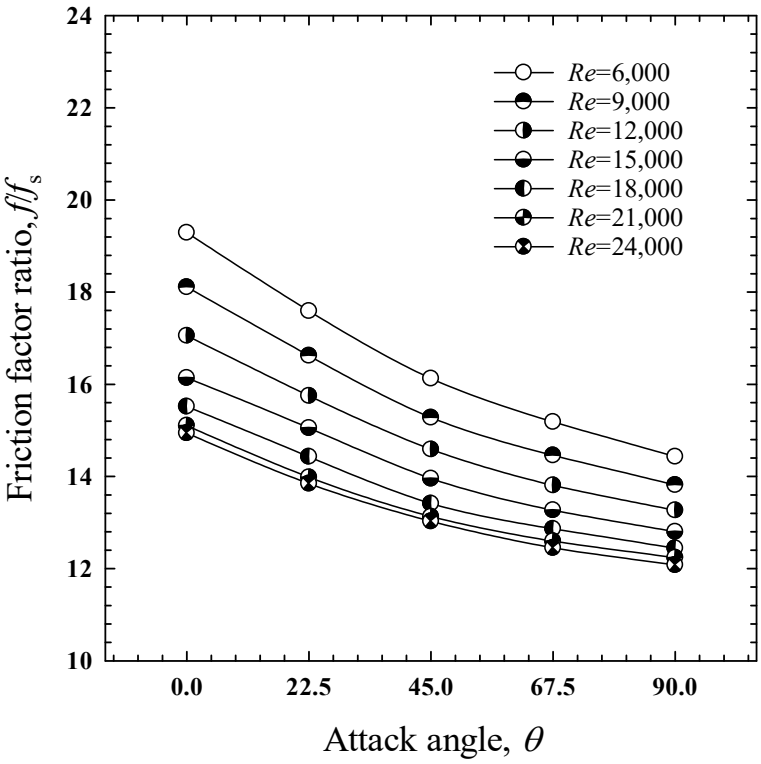

(b) f/f_s

Figure 4.45. Influence of semi-oval wing perforated V-type baffle (SOW-PVB) at various wing attack angles (θ = 0°, 22.5°, 45°, 67.5° and 90°) on friction factor.

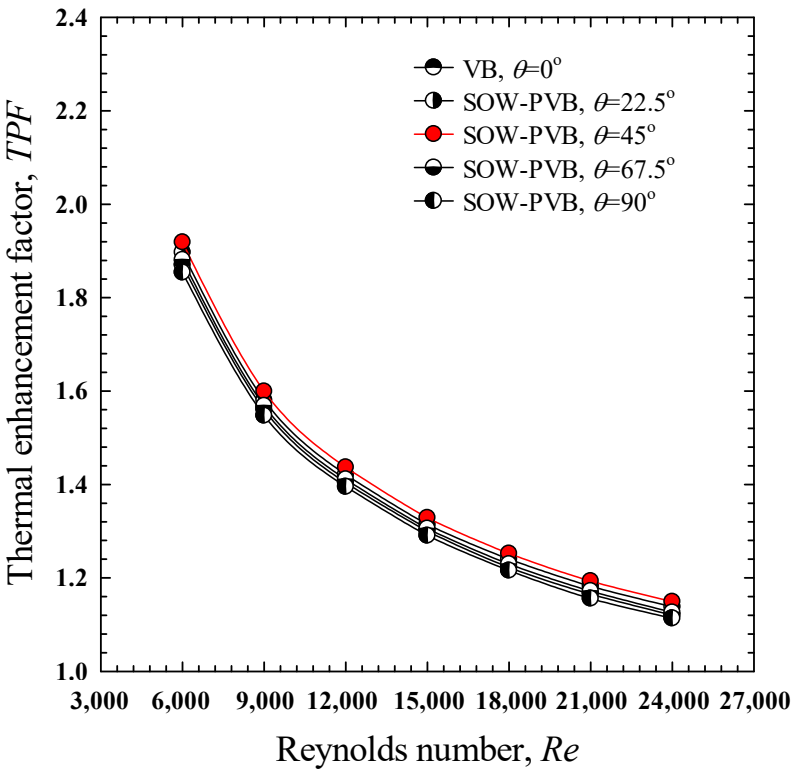

(a) *Re* & *TPF*

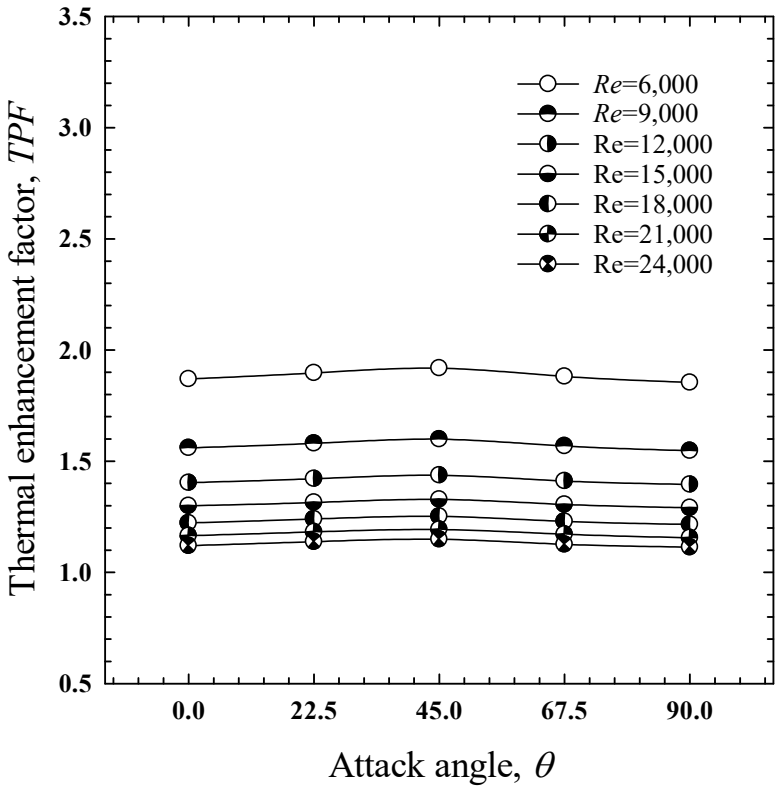

(b) *θ* & *TPF*

Figure 4.46. Influence of semi-oval wing perforated V-type baffle (SOW-PVB) at various wing attack angles (θ = 0°, 22.5°, 45°, 67.5° and 90°) on thermal performance factor.

4.2.3.2.4 Empirical correlations

Least square regression analysis was utilized to develop the experimental results for the Nusselt number (*Nu*), friction factor (*f*), and thermal performance factor (*TPF*) of a channel installed with semi-oval wing perforated V-type baffle (SOW-PVB). The fluid properties (Reynolds number and Prandtl number) and semi-oval wing attack angle (θ) were taken into account. Below are the resultant empirical correlations.

Empirical correlation of Nusselt number (Nu)

$$Nu = 7.242Re^{0.379}Pr^{0.4}(90 + \theta)^{-0.127} \tag{4.46}$$

Empirical correlation of friction factor (f)

$$f = 132.627Re^{-0.415}(90 + \theta)^{-0.354} \tag{4.47}$$

Empirical correlation of thermal performance factors (TPF)

$$TPF = 46.454Re^{-0.366}(90 + \theta)^{-0.009} \tag{4.48}$$

In Figs. 4.47(a-c), the experimental data (Nu_{exp}, f_{exp} and TPF_{exp}) are displayed against the predicted data (Nu_{pred}, f_{pred} and TPF_{pred}) obtained from the correlations. The Nusselt number (*Nu*), friction factor (*f*), and thermal performance factor (*TPF*), respectively, the differences between experimental data and predicted data are ±3.3%, ±2.7%, and ±3.8%, respectively. The insignificant differences indicate that the empirical correlations are applicable for predictions.

Note that above empirical correlations are suitable for the systems with air ($Pr \cong 0.71$) as the working fluid when semi-oval wing attack angle (θ) between 22.5° and 90° and Reynolds number between 6,000 and 24,000.

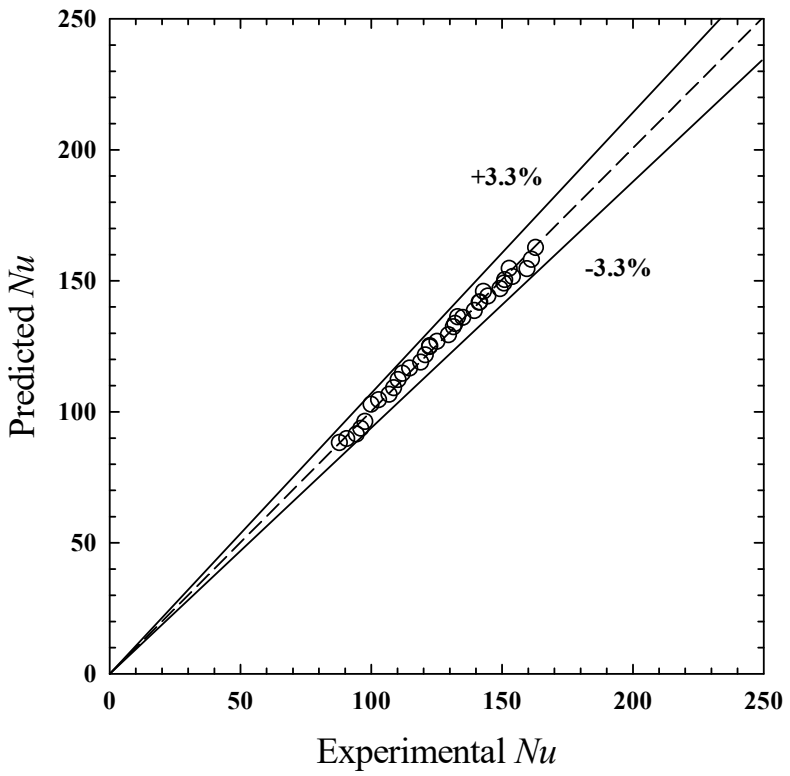

(a) Nu_{exp}, & Nu_{pred}

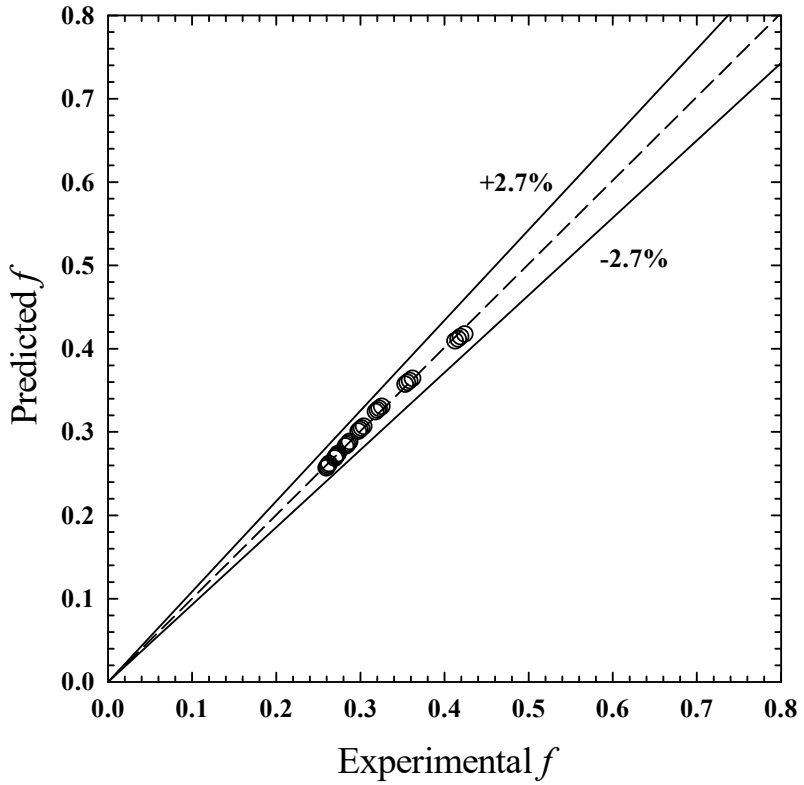

(b) Nf_{exp} & f_{pred}

Figure 4.47. Experimental results & predicted values of the empirical correlations.

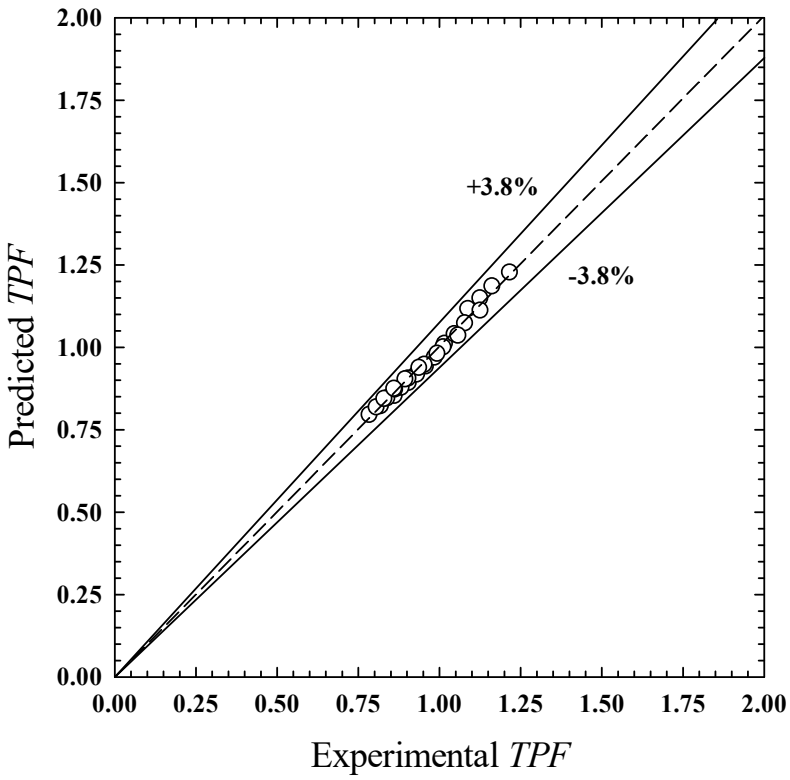

(c) TPF_{exp} & TPF_{pred}

Figure 4.47. Experimental results & predicted values of the empirical correlations. *(continued)*

4.2.3.3 Square-wing perforated V-type baffle

4.2.3.3.1 Heat transfer results

Local Nusselt number distributions at *Re* = 6,000 are shown in Figs. 4.48 and 4.49. These distributions reveal the reasons behind the enhanced heat transfer by different baffles. Clearly, the typical V-type baffles (VBs) caused the strongest reattachment on the heating wall since the fluid flow was forced in only one direction. However, the square-wing perforated V-type baffles (SW-PVBs) gave lower reattachments because some fluid portions flowed through the wings. These fluid portions are subsequently reattached to the small areas as minor reattachments (Fig. 4.48). As the attack angle increased, both major and minor reattachments became weaker since more fluid was directed to flow upward. Figures 49(a-b) also showed that the minor reattachments caused by square-wing perforated V-type baffle (SW-PVB) with the small attack angles of 22.5° and 45° were signified by the presence of separated peaks of local Nusselt numbers. However, at attack angles of 67.5° and 90°, the peaks of minor reattachments were not visible. It is most likely that the weak reattachments were concealed by the major ones.

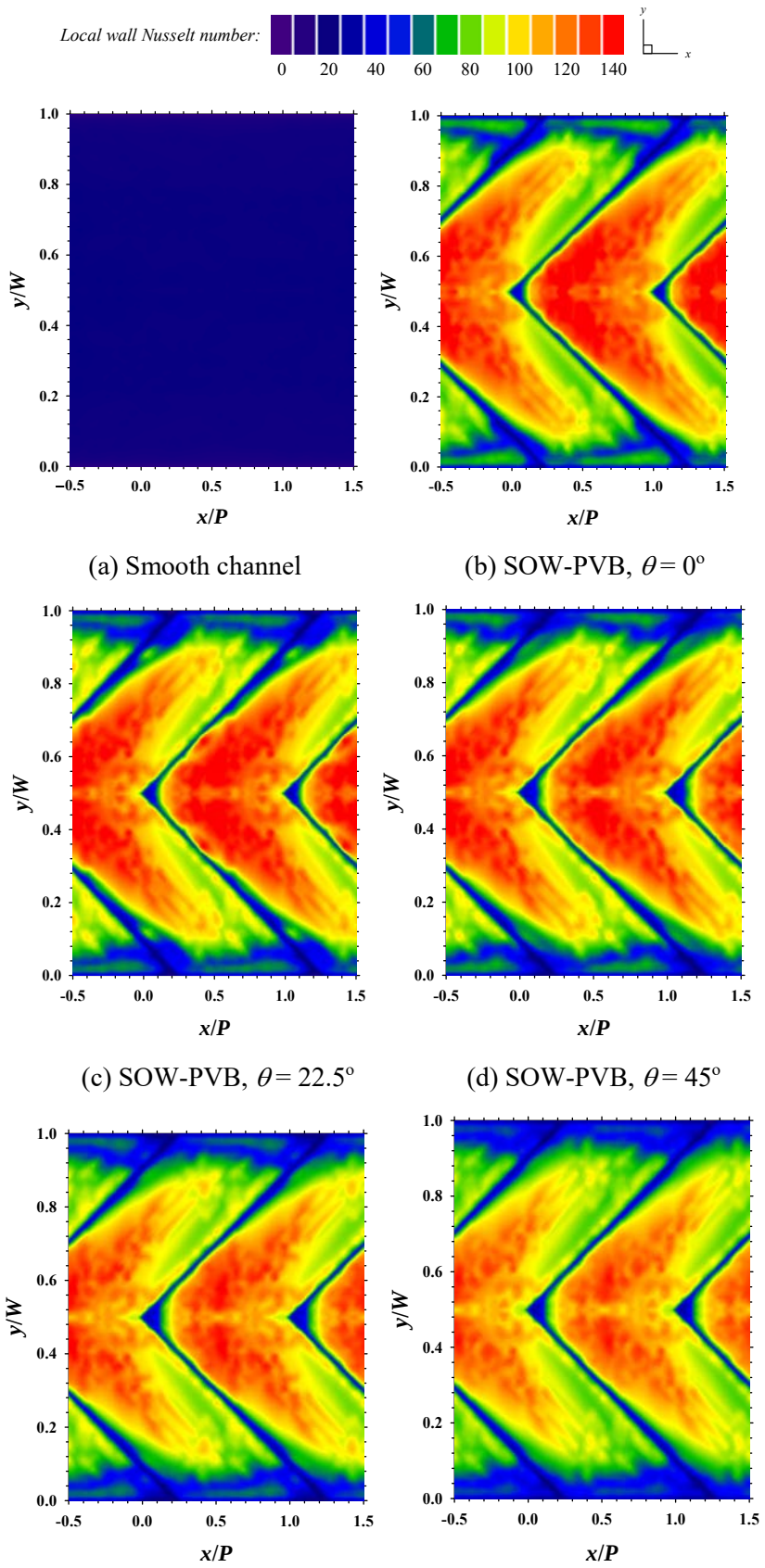

(a) Smooth channel

(b) SOW-PVB, $\theta = 0^{o}$

(c) SOW-PVB, $\theta = 22.5^{o}$

(d) SOW-PVB, $\theta = 45^{o}$

(e) SOW-PVB, $\theta = 67.5^{o}$

(f) SOW-PVB, $\theta = 90^{o}$

Figure 4.48. Influence of square-wing perforated V-type baffle (SW-PVB) at various wing attack angles ($\theta = 0^{o}$, 22.5^{o}, 45°, 67.5^{o} and 90°) on local heat transfer distribution.

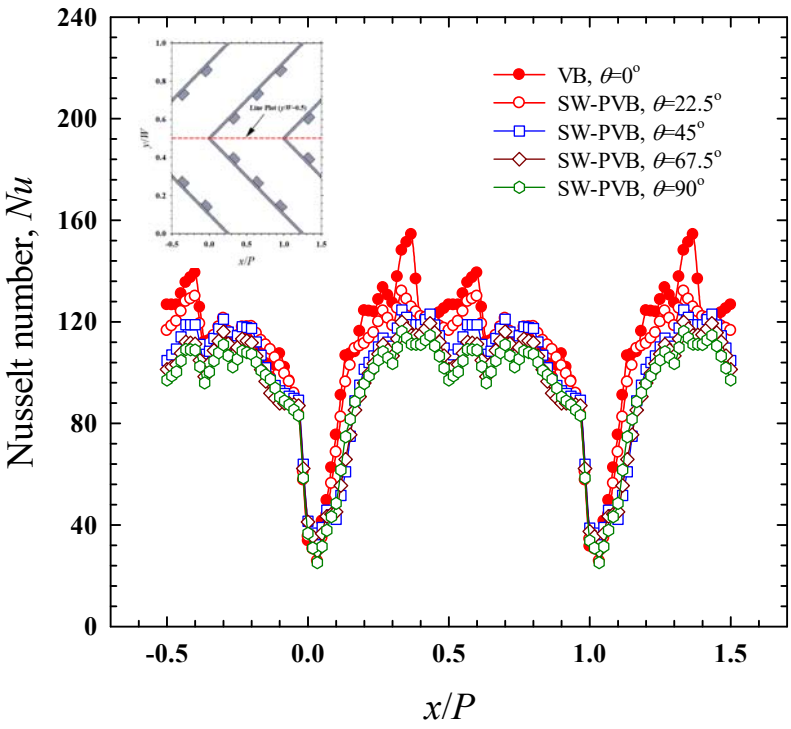

(a) $y/W = 0.5$

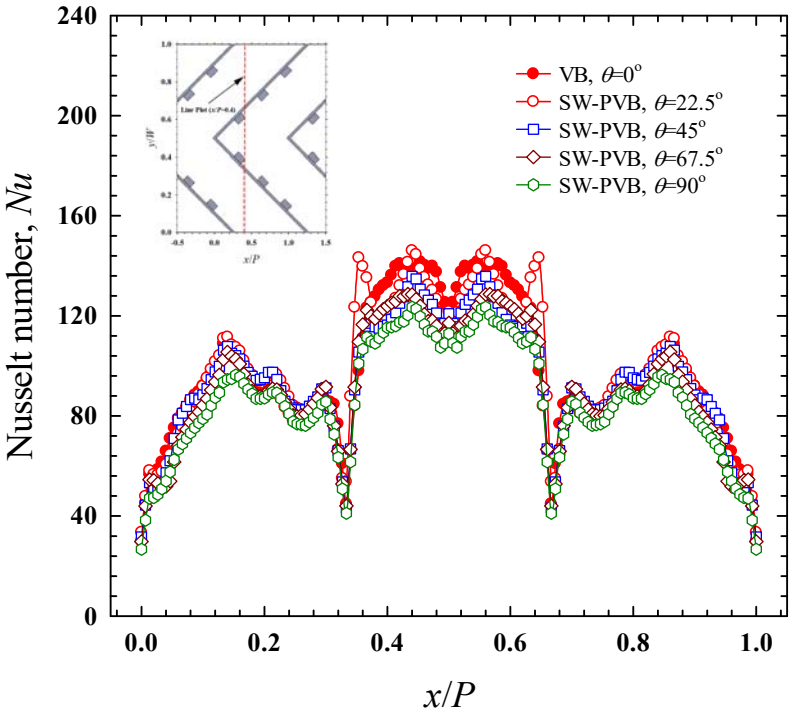

(b) $x/P = 0.4$

Figure 4.49. Normalized of Nusselt number of square-wing perforated V-type baffle (SW-PVB) at various wing attack angles ($\theta = 0^o$, 22.5^o, 45°, 67.5^o and 90°).

Figures 4.50 and 4.51 depict the influences of square-wing perforated V-type baffle (SW-PVB) with various attack angles (θ) on enhanced heat transfer. It can be found that the Nusselt number ratio (Nu/Nu_s) decreased with the Reynolds number (Re). This is as a greater Reynolds number yields a thinner boundary layer. Thus, the effect of the boundary disruption is less significant. Under similar operating conditions, heat transfer rates were boosted significantly by applying square-wing perforated V-type baffle (SW-PVB) compared to those of a plain/smooth channel. Because the baffles improve turbulent flow, the thermal and hydrodynamic boundary layers are thinner. Quantitative comparison demonstrates that the Nusselt numbers of the channel with square-wing perforated V-type baffle (SW-PVB) with $\theta = 0°$, 22.5°, 45°, 67.5° and 90° were respectively, 176-401%, 175-398%, 172-389%, 163-369%, and 157-354% over than those of the plain/smooth channel.

The SW-PVBs with smaller attack angles (θ) provided superior heat transfer enhancement to those with larger attack angles (θ). Under the current scope, the mean Nusselt numbers (Nu) of the channel with square-wing perforated V-type baffle (SW-PVB) of $\theta = 0^o$ (solid V-type baffle) were found to be around 0.29-0.75%, 1.28-2.54%, 5.02-6.96%, and 7.54-10.47% higher than those of square-wing perforated V-type baffle (SW-PVB) of $\theta = 22.5^o$, 45°, 67.5^o and 90°, respectively.

4.2.3.3.2 Friction factor results

The relationship among the friction factor ratio (f/f_s) and Reynolds number (Re) is illustrated in Figs. 4.52 and 4.53. With a flow blockage, the friction factors (f) of the square-wing perforated V-type baffle (SW-PVB) channels were greater than that of the smooth channel ($f/f_s > 1.0$). Generally, friction factor ratios increased with the Reynolds number. Friction factors tended to increase with the attack angle (θ) since more baffles occupied the channel. Quantitative comparisons demonstrate that the friction factors (f) associated with the square-wing perforated V-type baffle (SW-PVB) having $\theta = 0°$, 22.5^o, 45°, 67.5^o and 90° were respectively, 14.94-19.29, 13.96-17.81, 13.17-16.31, 12.52-15.32, and 12.12-14.54 times higher than those of a plain/smooth channel.

Friction factors of square-wing perforated V-type baffle (SW-PVB) at the smallest attack angle, $\theta = 22.5^o$ were approximately 5.96-9.25%, 11.34-16.24%, and 15.11-22.48% higher than those at the larger square-wing attack angles of $\theta = 45^o$, 67.5^o and 90°, respectively. Furthermore, the square-wing perforated V-type baffle (SW-PVB) with $\theta = 22.5^o$, 45°, 67.5^o and 90° showed an advantage in lowering the friction factor by 5.61-7.66%, 11.79-15.48%, 15.94-20.57%, and 18.69-24.61%, respectively, compared to solid V-type baffles ($\theta = 0^o$).

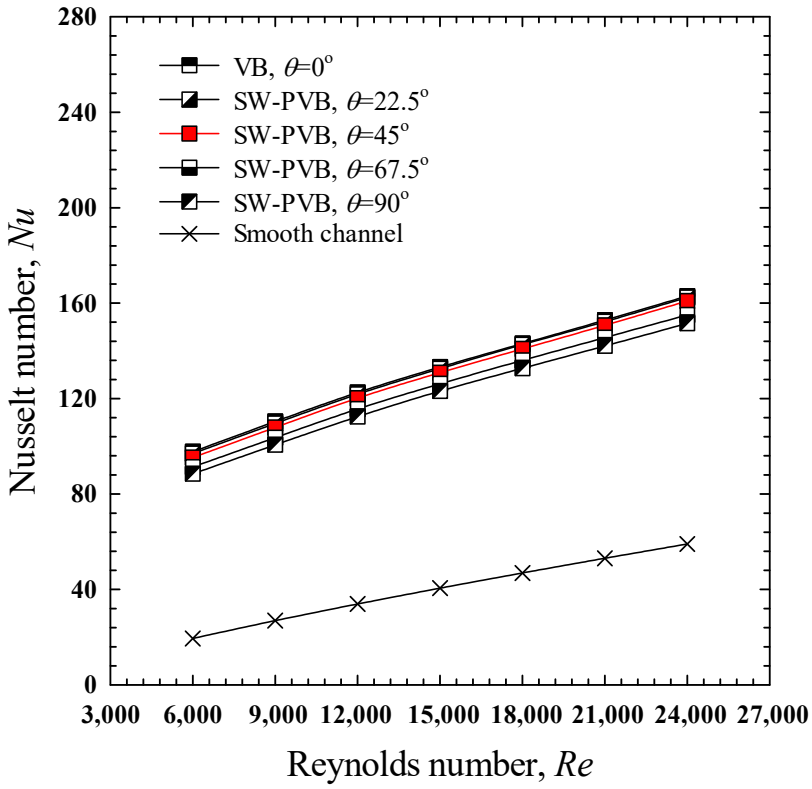

(a) *Nu*

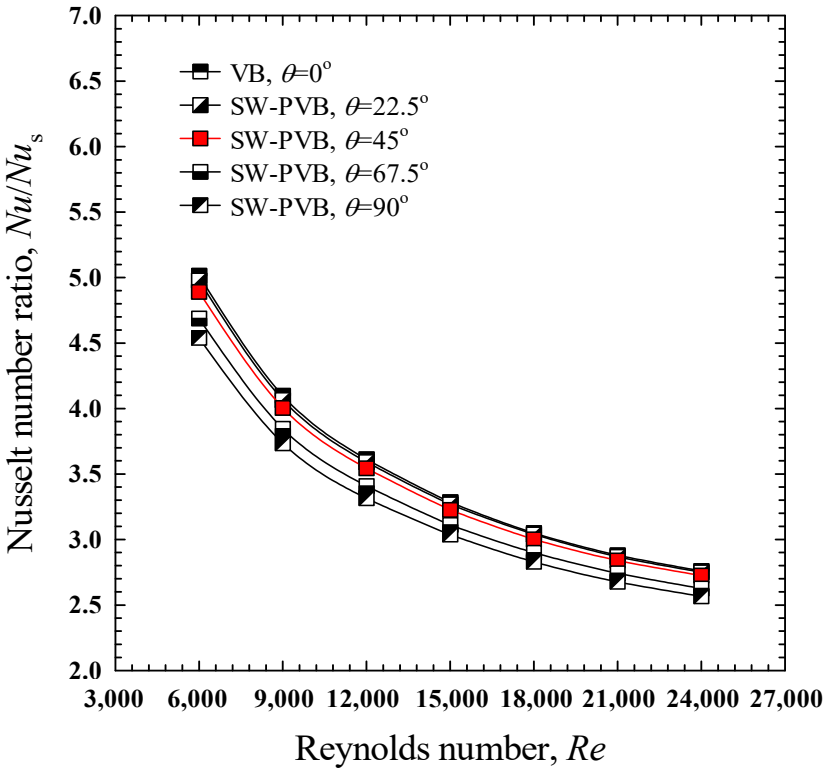

(b) Nu/Nu_s

Figure 4.50. Influence of square-wing perforated V-type baffle (SW-PVB) at various Reynolds numbers (*Re*) on average Nusselt number.

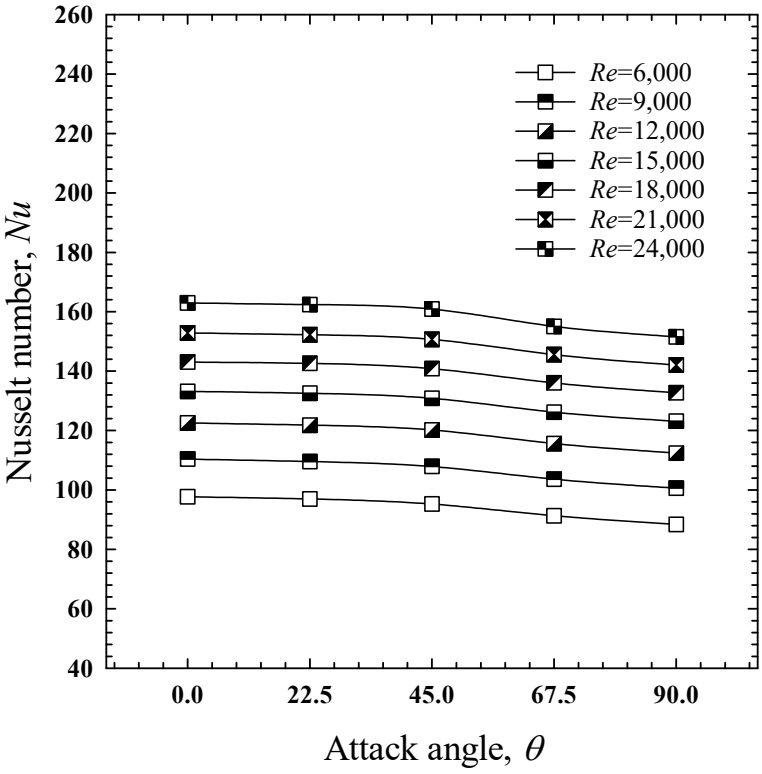

(a) *Nu*

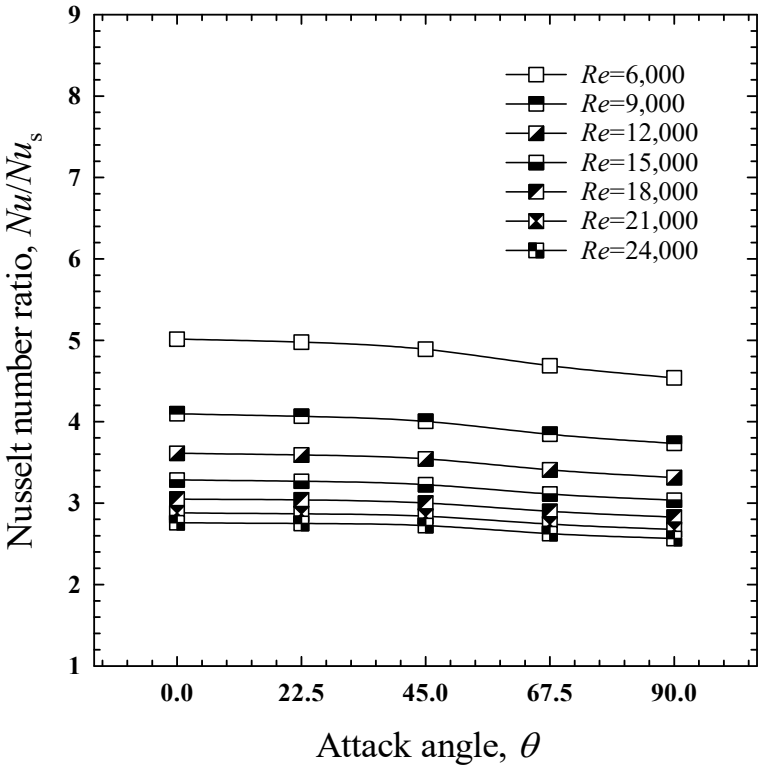

(b) Nu/Nu_s

Figure 4.51. Influence of square-wing perforated V-type baffle (SW-PVB) at various wing attack angles (θ = 0°, 22.5°, 45°, 67.5° and 90°) on Nusselt number.

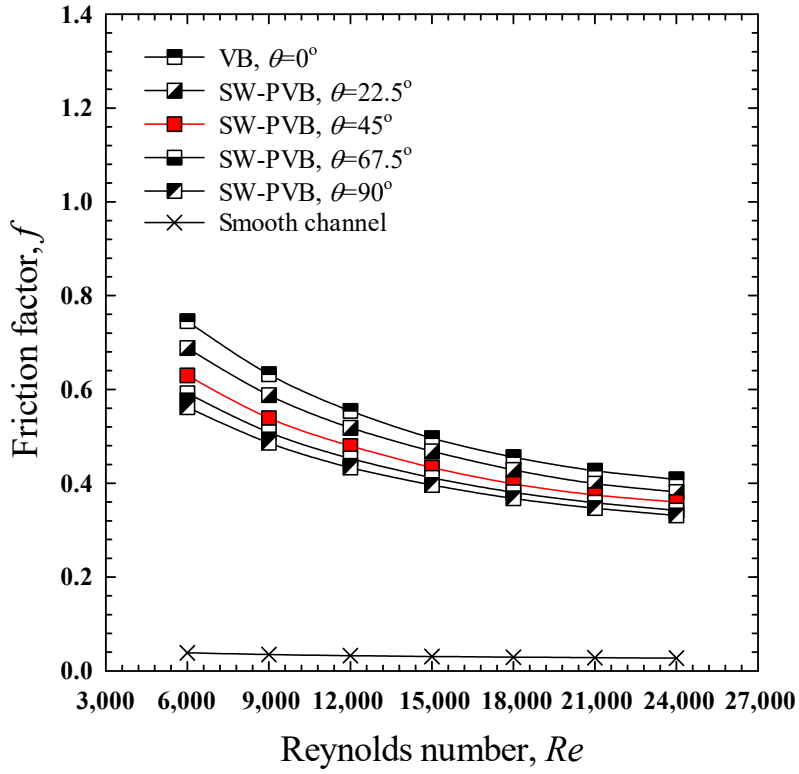

(a) f

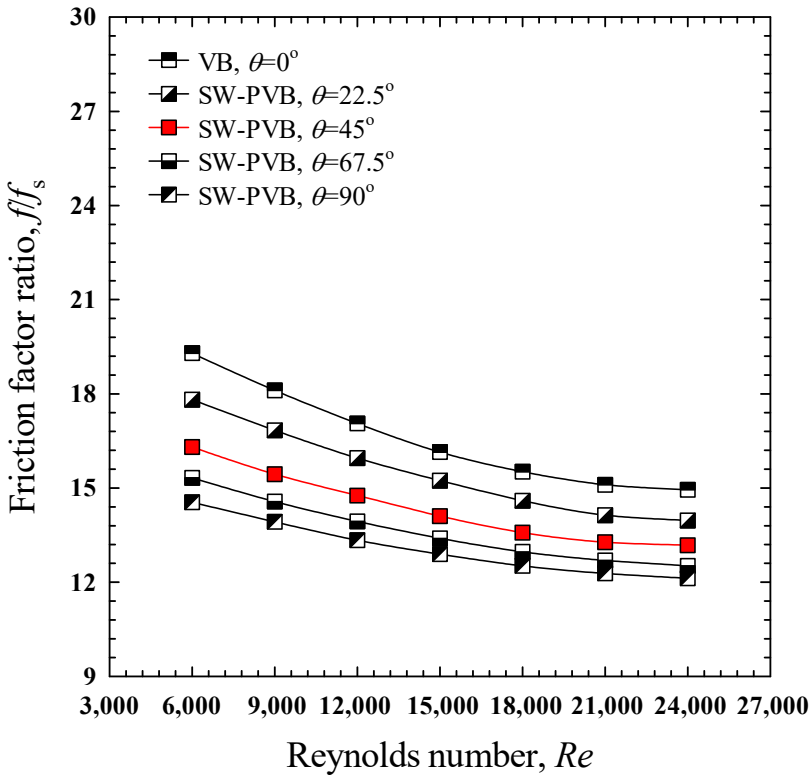

(b) f/f_s

Figure 4.52. Influence of square-wing perforated V-type baffle (SW-PVB) at various Reynolds numbers (*Re*) on friction factor.

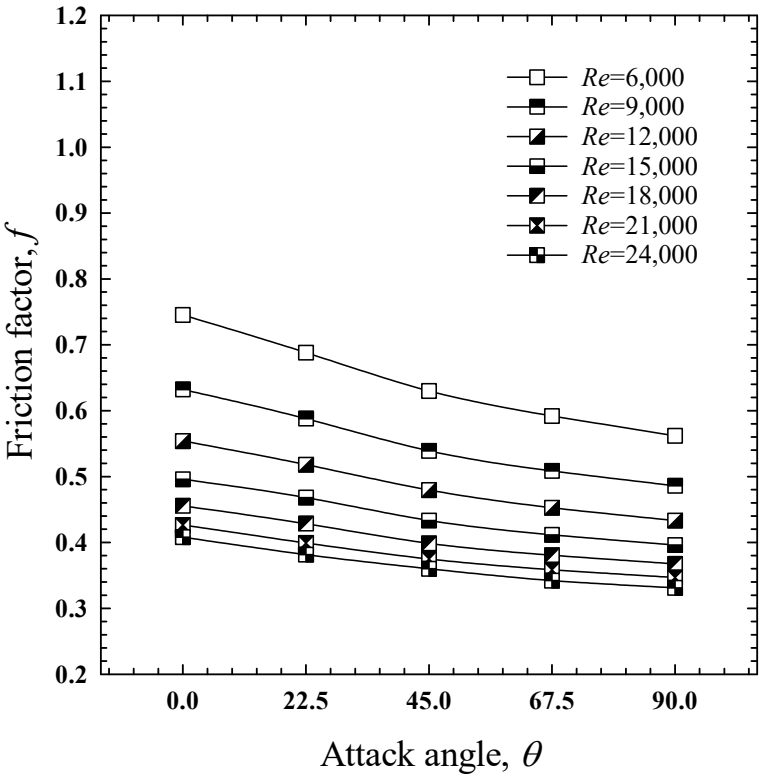

(a) f

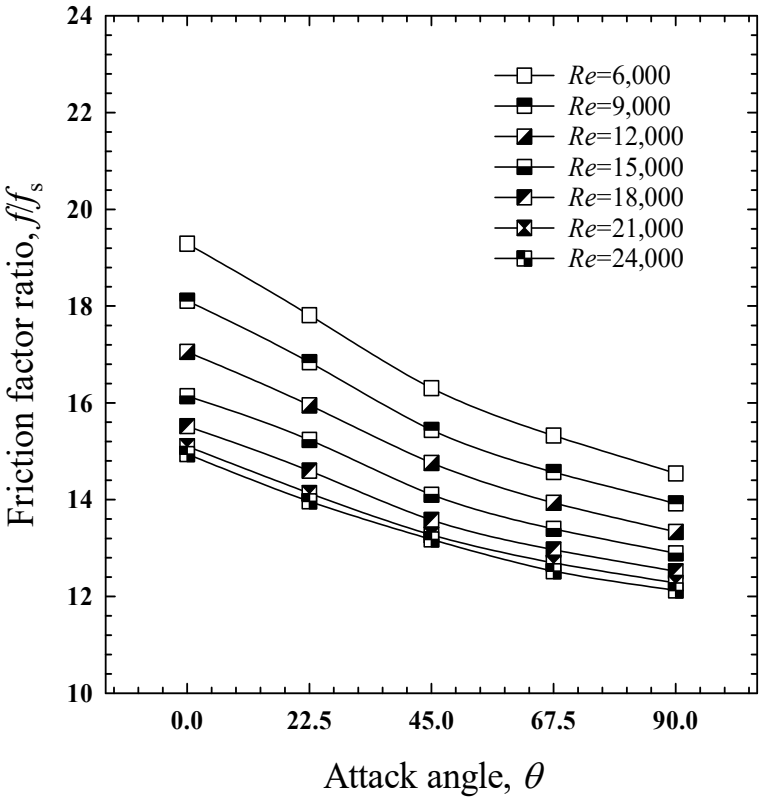

(b) f/f_s

Figure 4.53. Influence of square-wing perforated V-type baffle (SW-PVB) at various wing attack angles (θ = 0°, 22.5°, 45°, 67.5° and 90°) on friction factor.

4.2.3.3.3 Thermal performance factor results

At an identical pumping power, thermal performance factor (*TPF*) was assessed from Nusselt number ratio (Nu/Nu_s) and friction factor ratio (f/f_s). Figure 4.54 demonstrates variation of the thermal performance factor with the Reynolds number (*Re*) for square-wing perforated V-type baffle (SW-PVB) at various square-wing attack angles (θ). In all present studies, the thermal performance factor (*TPF*) declined as *Re* rose. According to these findings, operating at a lower *Re* is more feasible in terms of energy savings. The thermal performance factor (*TPF*) given by the square-wing perforated V-type baffle (SW-PVB) with attack angles of θ = 22.5° and 45° were greater than those given by the typical V-type baffles, primarily due to the lower pressure drop penalty. Nevertheless, the square-wing perforated V-type baffle (SW-PVB) yielded lower Nusselt numbers. However, the thermal performance factor (*TPF*) given by the square-wing perforated V-type baffle (SW-PVB) having attack angles of θ = 67.5° and 90° were less than those of the typical V-type baffles since the square-wing perforated V-type baffle (SW-PVB) yielded significantly lower Nusselt numbers. Among all square-wing perforated V-type baffle (SW-PVB) utilized, those with θ = 45° offered the greatest thermal performance factor (*TPF*). This is due to the optimal compromise between improved heat transfer rate and greater friction loss. At the lowest *Re* of 6,000, the highest thermal performance factor (*TPF*) was 1.86, 1.91, 1.93, 1.88, and 1.85 for baffles with θ = 0° (solid V-type baffle), 22.5°, 45°, 67.5° and 90°, respectively. In other words, the baffles with θ = 45° yielded higher thermal performance factor (*TPF*) than the ones with θ = 0°, 22.5°, 67.5° and 90° by up to 2.75-3.14%, 1.01-1.37%, 1.94-2.17%, and 3.13-3.71%, respectively.

4.2.3.3.4 Empirical correlations

Experimental Nu_{exp}, f_{exp} and TPF_{exp} data were performed as a function of *Re*, *Pr* and square-wing attack angle (θ). The resulting Nu_{pred}, f_{pred} and TPF_{pred} correlations are demonstrated in Eqs. (4.12), (4.13) and (4.14). Figures 4.55(a-c) show verification of the predicted data (Nu_{pred}, f_{pred} and TPF_{pred}) from the correlations with experimental data. Deviations of Nusselt number (*Nu*), friction factor (*f*) and thermal performance factor (*TPF*) were all within ±3.5%, ±2.4% and ±3.9%, which were not significant. Therefore, it is suggested that the present correlations are applicable for predicting Nusselt number (*Nu*), friction factor (*f*) and thermal performance factor (*TPF*) under similar conditions.

Empirical correlation of Nusselt number (Nu)

$$Nu = 7.128Pr^{0.4}Re^{0.378}(90 + \theta)^{-0.121} \quad (4.49)$$

Empirical correlation of friction factor (f)

$$f = 131.244Re^{-0.417}(90 + \theta)^{-0.347} \quad (4.50)$$

Empirical correlation of thermal performance factors (TPF)

$$TPF = 45.886Re^{-0.366}(90 + \theta)^{-0.005} \quad (4.51)$$

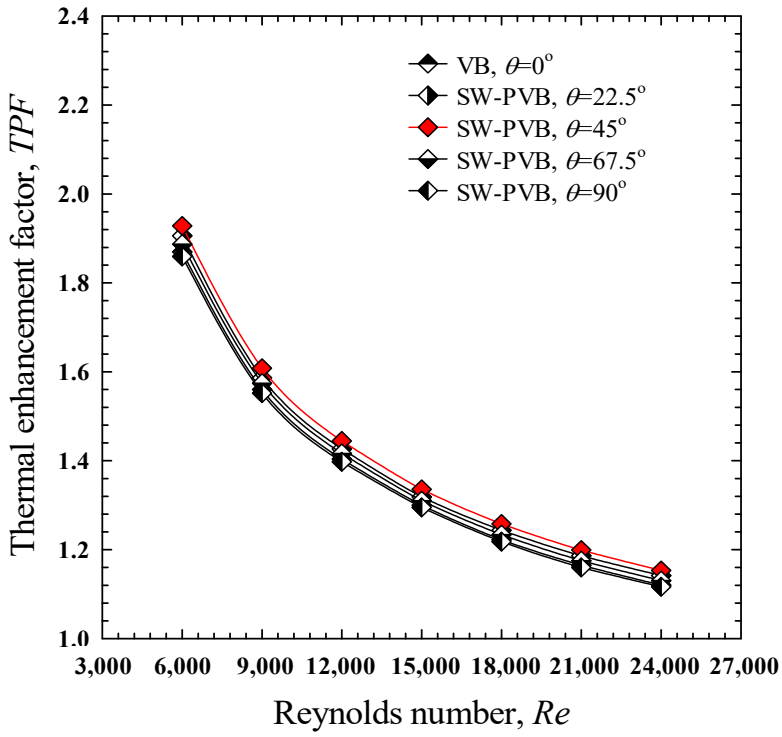

(a) *Re* & *TPF*

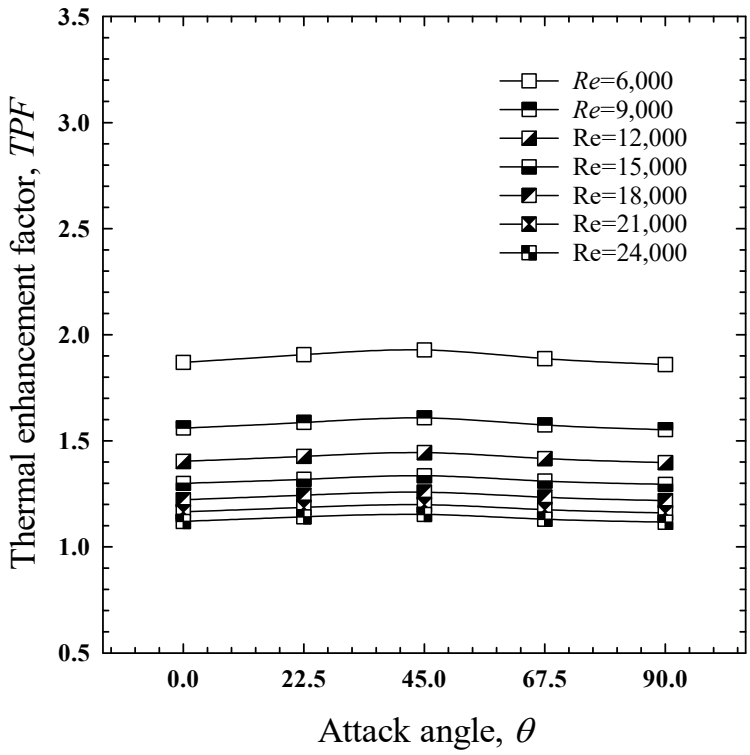

(b) *θ* & *TPF*

Figure 4.54. Influence of square-wing perforated V-type baffle (SW-PVB) at various wing attack angles (θ = 0°, 22.5°, 45°, 67.5° and 90°) on thermal performance factor.

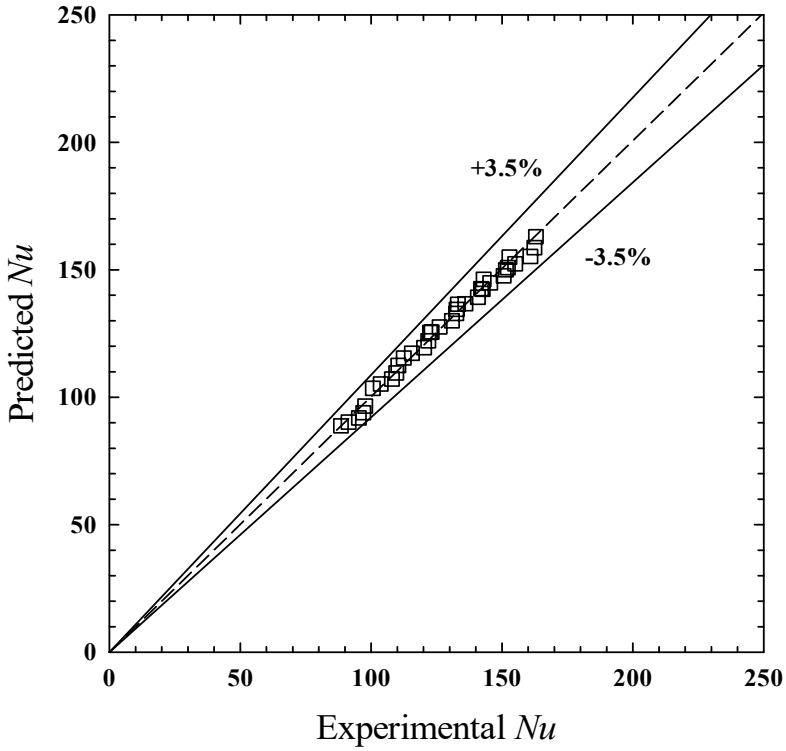

(a) Nu_{exp}, & Nu_{pred}

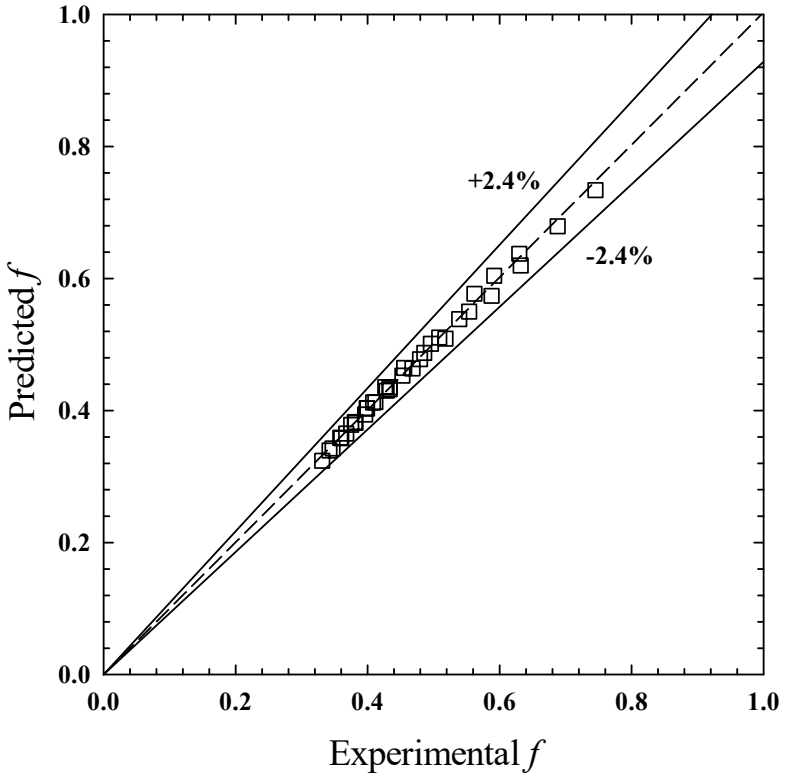

(b) Nf_{exp} & f_{pred}

Figure 4.55. Experimental results & predicted values of the empirical correlations.

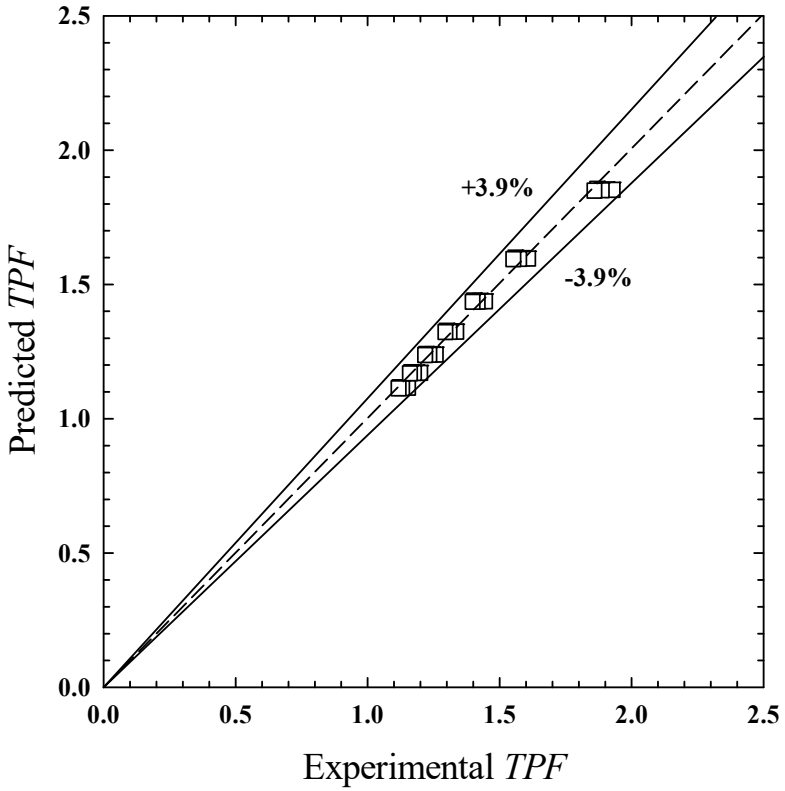

(c) TPF_{exp} & TPF_{pred}

Figure 4.55. Experimental results & predicted values of the empirical correlations. (*continued*)

4.3 Comparison with the relevant works

In Figure 4.56, the thermal performance factors (*TPF*) for the square-winged transverse baffle (SW-PB, θ = 45°) and square-wing perforated V-type baffle (SW-PVB, θ = 45°) are compared to those for previously modified transverse baffles of various designs. Such designs include inclined perforated baffles (baffle height ratio of 0.5, baffle pitch ratio of 10, hole position ratio of 0.266 and open area ratio of 12%) [10], inline/staggered perforated baffles (perforation ratio of 40%) [11], staggered and partially tilted perforated baffles (tilt angle of 45° and perforation ratio of 40%) [17], and V-shaped perforated baffles (*e/H* = 0.285-0.6, *P/e* = 1.0-4.0, and open area ratio of 12-44%) [22]. According to Fig. 4.56, inclined perforated baffles [10] had better thermal performance (*TPF*) than others. The thermal performance (*TPF*) values offered by the current square-wing perforated transverse baffles (SW-PBs, θ = 45°) were moderate compared to V-shaped perforated baffles [22] while the square-wing perforated V-type baffle (SW-PVB) performed better thermal performance. It is noteworthy that the thermal performance (*TPF*) of the SW-PB and square-wing perforated V-type baffle (SW-PVB) was greater than those of the inline/staggered perforated baffles [11], and staggered and partially tilted perforated baffles [17], while it was lower than those of inclined perforated baffles [10] for all Reynolds number and V-shaped perforated baffles [22] at the low Reynolds numbers.

Kumar *et al.* [19]

El Habet *et al.* [20]

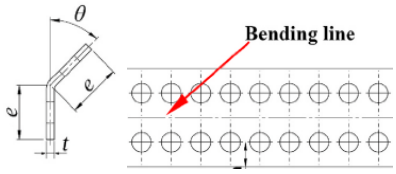

El Habet *et al.* [21]

Chamoli and Thakur [22]

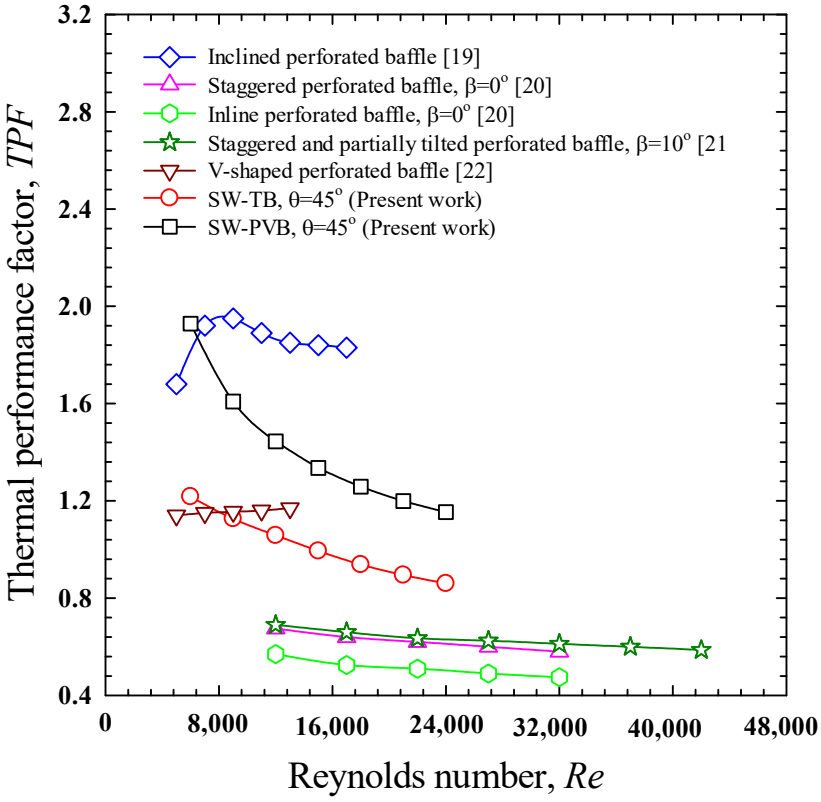

Figure 4.56. Comparison of the current results and those reported in previously published articles.

4.4 Nomenclature

A	area, m^2
B	dark blue
c	specific heat, J kg^{-1} K^{-1}
C	coefficient of the orifice meter
d_1	outside diameter of an orifice plate, m
d_2	inside diameter of an orifice plate, m
D	diameter, m

e	baffle height, m
f	friction factor
G	green
h	heat transfer coefficient, W m^{-2} K^{-1}
H	height of test channel, m
	or hue
I	intensity
k	thermal conductivity of fluid, W m^{-1} K^{-1}
L	length of test section, m
Nu	Nusselt number
$\dot{m}$	mass flow rate, kg s^{-1}
S	saturation
P	baffle pitch, m
	static pressure, Pa; perimeter of the duct or channel, m
Pr	Prandtl number
ΔP	pressure drop, Pa
Q	heat transfer rate, W
R	red
Re	Reynolds number
t	baffle thickness, m
T	temperature, ^{o}C
TPF	thermal performance factor
V	average air velocity, m s^{-1}
w	height of baffle, m
W	width of test section, m

Greek Symbols

θ	attack angles, ^{o}
ρ	fluid density, kg m^{-3}
μ	fluid dynamic viscosity, kg s^{-1} m^{-1}
ν	kinematics viscosity, m^2 s^{-1}

Subscripts

abs	absorption
avg	average
b	bulk
bs	blue start
c	cross-section

d	discharge
exp	experimental
h	hydraulic
hs	heating surface
i	inlet
o	outlet
pred	predicted
rs	red start
s	surface
	or smooth channel
w	wall
x	*x*-axis
y	*y*-axis

Abbreviations

AC	alternating current
ANSI	American national standards institute
ASME	American society for mechanical engineering
HSI	hue-saturation-intensity color system
HTE	heat transfer enhancement
PLA	polylactic acid
RGB	red-green-blue color system
RTD	resistance temperature detector
SW-PVB	square wing perforated V-type baffle
DW-PVB	delta wing perforated V-type baffle
SOW-PVB	semi-oval wing perforated V-type baffle
TLC	thermochromic liquid crystal
VB	V-type baffle

References in chapter 4

1 ASME, Standard Measurement of fluid flow in pipes using orifice, nozzle and venture. ASME MFC-3M-1984, United Engineering Center 345 East 47th Street, New York, 1984, 1-56.

2 Stasiek J, Stasiek A, Jewartowski M, Collins MW. Liquid crystal thermography and true-colour digital image processing. Optics & Laser Technology. 2006;38:243-256.

3 Mehta B, Khandekar S. Measurement of local heat transfer coefficient during gas-liquid Taylor bubble train flow by infra-red thermography. International Journal of Heat and Fluid Flow. 2014;45:41-52.

4 Baughn JW. Liquid crystal methods for studying turbulent heat transfer. International Journal of

Heat and Fluid Flow. 1995;16:365-375.

5 Grassi W, Testi D, Vista DD, Torelli G. Calibration of a sheet of thermosensitive liquid crystals viewed non-orthogonally. Measurement. 2007;40:898-903.

6 Yan WM, Liu HC, Soong CY, Yang WJ. Experimental study of impinging heat transfer along rib-roughened walls by using transient liquid crystal technique. International Communications in Heat and Mass Transfer. 2005;48:2420-2428, June.

7 Abdullah NA, Talib RA, Jaafer AA, Salleh MAM, Chong WT. The basics and issues of thermochromic liquid crystal calibrations. Experimental Thermal and Fluid Science. 2010;34:1089-1121.

8 Kumar R, Chauhan R, Sethi M, Kumar A. Experimental study and correlation development for Nusselt number and friction factor for discretized broken V-pattern baffle solar air channel. Experimental Thermal and Fluid Science. 2017;81:56-75.

9 Nuntadusit C, Wae-Hayee M, Bunyajitradulya A, Eiamsa-ard S. Thermal visualization on surface with transverse perforated ribs. International Communications in Heat and Mass Transfer. 2012;39:634-639.

10 Kumar R, Kumar A, Chauhan R, Sethi M. Heat transfer enhancement in solar air channel with broken multiple V-type baffle. Case Studies in Thermal Engineering. 2016;8:187-197.

11 Maithani R, Saini JS. Heat transfer and friction factor correlations for a solar air heater duct roughened artificially with V-ribs with symmetrical gaps. Experimental Thermal and Fluid Science. 2016;70:220-227.

12 An American National Standard, Measurement of fluid flow in pipes using orifice, nozzle and venture. ASME MFC-3M-2004, United Engineering Center, 345 East 47th Street, New York, 1-56, 2004.

13 Duffie JA, Beckman W.A. Solar Engineering of Thermal Processes, Wiley Inter Science publications, New York, 1980, pp. 398-402.

14 Webb RL, Kim NH. Principles of Enhanced Heat Transfer. 2nd ed., Taylor & Francis, New York, 2005, p. 785.

15 Kline SJ, McClintock FA. Describing Uncertainties in Single Sample Experiments. Mechanical Engineering. 1953;75:3-8.

19 Incropera F, Dewitt PD. Introduction to Heat Transfer, 3rd edition, John Wiley & Sons Inc., 1996,

16 Patankar SV, Liu CH, Sparrow EM. Fully developed flow and heat transfer in ducts having streamwise-periodic variations of cross-sectional area. Journal of Heat Transfer - Transactions of ASME. 1998;98:1109-1151.

17 Patankar SV. Numerical heat transfer and fluid flow. McGraw-Hill, New York, 1980.

18 Launder BE, Spalding DB. The numerical computation of turbulent flows. Computer Methods in Applied Mechanics and Engineering. 1974;3:269-289.

19 Kumar R, Nadda R, Kumar S, Razak A, Sharifpure M, Aybar HS, Saleel CA, Afzal A. Influence of artificial roughness parametric variation on thermal performance of solar thermal collector: An experimental study, response surface analysis and ANN modelling. Sustainable Energy Technologies and Assessments. 2022;52:102047.

20 El Habet MA, Ahmed SA, Saleh MA. Thermal/hydraulic characteristics of a rectangular channel with inline/staggered perforated baffles. International Communications in Heat and Mass Transfer. 2021;128:105591.

21 El Habet MA, Ahmed SA, Saleh MA. The effect of using staggered and partially tilted perforated baffles on heat transfer and flow characteristics in a rectangular channel. International Journal of Thermal Sciences. 2022;174:107422

22 Chamoli S, Thakur NS. Correlations for solar air heater duct with V-shaped perforated baffles as roughness elements on absorber plate. International Journal of Sustainable Energy. 2016;35:1-20.

Publication lists

1) Smith Eiamsa-ard, Arnut Phila, Khwanchit Wongcharee, Varesa Chuwattanakul, Monsak Pimsarn, Naoki Maruyama and Masafumi Hirota, Thermal Visualization and Performance Analysis in a Channel Installing Transverse Baffles with Square Wings, *Energies*, Vol. 15(22), Article no. 8736, November 2022, 19 pages, DOI: 10.3390/en15228736.

2) Smith Eiamsa-ard, Arnut Phila, Khwanchit Wongcharee, Monsak Pimsarn, Naoki Maruyama, Masafumi Hirota, Thermal evaluation of flow channels with perforated-baffles, *Energy Reports*, Vol. 9, May 2023, pp. 525-532, DOI: 10.1016/j.egyr.2023.01.064.

3) Smith Eiamsa-ard, Arnut Phila, Monsak Pimsarn, Naoki Maruyama, Masafumi Hirota, Heat transfer mechanism and thermal performance of a channel with square-wing perforated transverse baffles installed: Effect of square-wing location, *Journal of Thermal Analysis and Calorimetry*, Vol. 148, May 2023, pp. 3835-3849, DOI: doi.org/10.1007/s10973-022-11937-w.

4) Smith Eiamsa-ard, Arnut Phila, Chinaruk Thianpong, Varesa Chuwattanakul, Naoki Maruyama, Masafumi Hirota, Enhanced heat transfer performance in channel with delta-wing - perforated V-type baffles, *Journal of Thermal Analysis and Calorimetry*, Vol. 148, October 2023, pp. 11283-11301, DOI: doi.org/10.1007/s10973-023-12452-2

5) Smith Eiamsa-ard, Arnut Phila, Khwanchit Wongcharee, Monsak Pimsarn, Naoki Maruyama, Masafumi Hirota, Thermal evaluation of flow channels with perforated-baffles, *The 3rd International Conference on Power, Energy and Electrical Engineering (PEEE 2022)*, Paper ID: PEEE22-111, November 18-20, 2022, Barcelona, Spain.

6) Smith Eiamsa-ard, Arnut Phila, Pitak Promthaisong, Naoki Maruyama, Masafumi Hirota, Heat transfer in a channel installed with semi-oval wing perforated V-type baffles, *Heat Transfer Engineering*, Accepted to publication.

CHAPTER 5
Conclusions

5.1 Heat transfer enhancement of semi-circular wing perforated V-type baffle: Numerical investigation

A numerical study examined the enhancement of the heat transfer mechanism and flow topology of a channel contained with semi-circular wing perforated V-type baffles (SCW-PVBs). The main findings are:

1. The impingement introduced multi-spot cooling-temperature zones with reasonable pressure loss. Moreover, the impinging jets also strengthened the thermal disruption and fluid mixing behind the V-shaped baffle.
2. Dead zones became smaller at larger BR because the fluid flow through semi-circular holes and fluid mixing were facilitated. Moreover, the main vortex strength increased with increasing BR, the thermal boundary layer was more severely disrupted and thus, there was more efficient heat transfer through the channel wall.
3. At the PR = 0.5, the main vortex flow and the flow of the impinging jets could access the whole area of the channel wall. The boundary layer was drastically disturbed, particularly the area attacked by the main vortex flow.
4. As the PR increased, vortex intensity became weaker. Thus, there was a large area that the main vortex flow could not access leading to poor heat transfer, especially, at the PR = 2.0.
5. As wing attack angles (θ) increased from 5° to 10°, the fluid flow through the semi-circular holes was promoted resulting in better fluid mixing and a smaller dead zone (high wall temperature behind the baffles reduced). Consequently, the heat transfer behind the baffles was enhanced. However, the strength of the main vortex flow was simultaneously diminished. Thus, the heat transfer of the area that was attacked by the main vortex flow became smaller. The effect of changing θ from 10° to 15° on heat transfer behavior was similar to that from 5° to 10°. However, it is noteworthy that the heat transfer behind the baffles was only slightly improved.

5.2 Heat transfer enhancement of square-winged transverse baffle: Experimental investigation

The heat transfer enhancement behaviors of square-winged transverse baffles (SW-TB) were experimentally investigated using a thermochromic liquid crystal (TLC) sheet. This part aimed to examine the effects of SW-PBs and their wing attack angles (θ = 0° (solid V-shaped baffle), 22.5°, 45°, 67.5°, and 90°) and wing positions (h/e = 0.92, 0.83, 0.75, and 0.67) on heat transfer, friction loss and thermal performance characteristics in the enhanced channel. The important findings of this investigation are summarized as follows:

1. Square-winged transverse baffles (SW-TBs) promoted recirculation flow and induced multiple impinging flows behind each baffle. This allowed better contact between the fluid flow and the channel wall, and thus more efficient heat transfer.
2. The impingement intensity tended to increase as the wing location becomes lower. This can be explained by the fact that the lower wing locations (h/e = 0.67 and 0.75) bring the bulk fluid closer to the bottom wall, leading to stronger impingement and better contact between them.

5.3 Heat transfer enhancement of delta/square/semi-oval wing perforated V-type baffles: Experimental investigation

These experiments measured the heat transfer rates, friction factors, and thermal performance factors of a channel into which delta/square/semi-oval wing perforated V-type baffles (DW-PVBs/SW-PVBs/SOW-PVBs) were attached on the bottom of the heated wall. Thermochromic liquid crystals (TLCs) were used to acquire the temperature distribution on the heat transfer surface. The effects of Reynolds number and semi-oval wing attack angle (θ) on Nusselt number, friction factor, and thermal performance factor were examined. The following are the research findings of this part.

1. Utilization of DW-PVBs/SW-PVBs/SOW-PVBs significantly enhanced heat transfer. Moreover, pressure losses were diminished as compared to the use of typical solid V-shaped baffles. The modified baffles with small attack angles (θ = 22.5°and 45°), gave high Nusselt numbers and friction factors while the ones with larger attack angles (θ = 67.5°, and 90°) exhibited weak multiple impinging jets behind the baffle and small impinged zones, leading to inefficient heat transfer.
2. Among the DW-PVBs/SW-PVBs/SOW-PVBs utilized, the ones with θ = 22.5° showed the highest heat transfer enhancement, while the ones with θ = 45° offered the highest thermal performance factors.
3. Under constant pumping power situations, the modified baffles (DW-PVBs/SW-PVBs/SOW-PVBs) with θ = 22.5°, 45°, and 67.5° yielded greater *TPF* values than the solid V-shaped baffles (θ = 0°).
4. Installation of DW-PVBs/SW-PVBs/SOW-PVBs may be not the most effective approach for improving thermal performance. Innovative engineering design can be implemented for further improvement in a future work.